

NITRIC OXIDE IN A DIESEL ENGINE:
LASER-BASED DETECTION AND
INTERPRETATION

Nitric oxide in a diesel engine: laser-based detection and interpretation

Genie Gertruda Maria Stoffels

Thesis Katholieke Universiteit Nijmegen - Illustrated

With references - With summary in Dutch

ISBN 90-9012846-8

NUGI 812

Subject headings: combustion diagnostics / diesel engine

nitric oxide / laser-spectroscopic techniques / imaging

Cover: Image by the author. Excitation/emission spectrum recorded from the running engine at 42° aTDC (P=10 bars, T=850 K) showing the nitric oxide fluorescence and interfering oxygen fluorescence. False colour representation of figure 2.14.

NITRIC OXIDE IN A DIESEL ENGINE:
LASER-BASED DETECTION AND
INTERPRETATION

EEN WETENSCHAPPELIJKE PROEVE OP HET GEBIED VAN DE
NATUURWETENSCHAPPEN, WISKUNDE EN INFORMATICA

PROEFSCHRIFT

TER VERKRIJGING VAN DE GRAAD VAN DOCTOR
AAN DE KATHOLIEKE UNIVERSITEIT NIJMEGEN,
VOLGENS BESLUIT VAN HET COLLEGE VAN DECANEN
IN HET OPENBAAR TE VERDEDIGEN
OP DINSDAG 14 SEPTEMBER 1999,
DES NAMIDDAGS OM 1.30 UUR PRECIËS

DOOR

GENIE GERTRUDA MARIA STOFFELS

GEBOREN OP 5 NOVEMBER 1969
TE WIJCHEN

PROMOTOR : PROF. DR. J.J. TER MEULEN

CO-PROMOTERES : DR. N.J. DAM

DR. W.L. MEERTS

MANUSCRIPTCOMMISSIE : PROF. DR. G.J.M. MEIJER

PROF. DR. IR. R.S.G. BAERT
TECHNISCHE UNIVERSITEIT EINDHOVEN

PROF. DR. K. KOHSE-HÖINGHAUS
UNIVERSITÄT BIELEFELD, DUISLAND



This work has been made possible by financial support of the 'Nederlandse Organisatie voor Toegepast-Natuurwetenschappelijk Onderzoek' (TNO) and the 'Stichting Technische Wetenschappen' (STW), applied science division of the 'Nederlandse Organisatie voor Wetenschappelijk Onderzoek' (NWO) and the technology programme of the Ministry of Economic Affairs.

Aan mijn ouders

Voorwoord

Mijn proefschrift is af!

Voor U liggen de resultaten van mijn onderzoek. Zo'n vijf jaar geleden startte ik hiermee in het verbrandingslab op de tweede verdieping van de N2-vleugel. Ongeveer twee jaar later verhuisde ik naar het nieuwe diesellab in de Graalburcht waar ik, samen met 'mijn jongens' van het Dieselteam, naar hartelust lawaai kon maken. Hier zijn uiteindelijk de meeste experimenten uitgevoerd die in dit proefschrift beschreven zijn. Ik heb dit werk natuurlijk niet alleen gedaan. Op deze plaats wil ik dan ook iedereen bedanken die, op directe of indirecte wijze, heeft meegewerkt aan mijn onderzoek en proefschrift.

Om te beginnen de leden van het Dieselteam en de 'bewoners' van de Graalburcht:

Mijn promotor, Hans ter Meulen, die ondanks dat hij geen Graalburchtbewoner is, het dieselonderzoek op de voet volgt en altijd weer enthousiast is bij het zien van nieuwe resultaten. Zijn kritische blik op het werk heeft zeker bijgedragen tot het welslagen van het onderzoek en de totstandkoming van dit proefschrift.

Mijn, mij-altijd-pestende co-promotor, UPD Nico Dam. Onze vele discussies over de meetresultaten en de interpretatie daarvan, maar ook over paddestoelen en andere zin en onzin, zijn voor mij erg verhelderend geweest; vooral als ik er weer eens niets van snapte/begreep. Mede door al zijn commentaar, met 'plezier' met rode pen in mijn concepten gekriebeld, is mijn proefschrift geworden zoals het is. Zijn nevenfunctie als spellingchecker voorkwam dat er niet overal *flourescence* staat.

Mijn andere co-promotor, tevens financieel manager en netwerkbeheerder van onze afdeling, Leo Meerts, met niet aflatende belangstelling voor het dieselgebeuren. Zijn bezoeken aan de Graalburcht, de discussies over velerlei onderwerpen en de BBQ in zijn achtertuin na het afdelingsuitstapje gaven de wetenschap een sociaal karakter.

Leander, helaas geen bewoner van de Graalburcht of lid van het Dieselteam, is onmisbaar geweest in de beginfase van mijn onderzoek. Hij heeft met veel enthousiasme een oude tweetakt motor uit een grasmaaimachine opgelapt en deze grondig omgebouwd tot 'mijn dieselmotor'.

Onze technicus, Charles, die in *SolidWorks* de nieuwe cilinderkop van mijn motor ontwierp en telkens trots weer showde hoe mooi je die in drie dimensies kon draaien. Hij bood altijd weer een helpende hand als de motor het weer eens niet deed of als een venster kapot was.

Erik-Jan, mijn opvolger, die meet in de grote DAF-motor en daarbij vijandig zijn optiek en uitlijning veilig probeert te stellen door overal briefjes op te plakken met '*Don't touch, you will meet EJ*'. Het lawaai dat de DAF-motor maakt valt overigens nog wel mee vergeleken met de herrie van de radio van zijn rode Alfa.

René, die als eerste ‘niet-dieselmotor-OIO’ het geweld in de Graalburcht kwam versterken met zijn flowexperimenten. *The Wall* zal voor mij onlosmakelijk verbonden blijven met de Graalburcht.

Marianna, bondgenote in de strijd tegen de mannen, bij wie ik altijd even mijn hart kon luchten, zomaar tussendoor of tijdens het hardlopen. Ooit maken wij nog een handleiding: ‘*How to deal with Nico*’ voor alle nieuwkomers.

De Deense top-Batavier Nicholas, de Duits/Engelse Penelope, toegelaten tot de vrouwenkamer, en de Roemeense Ph.D. studente Angela waarmee de vele zinnige en onzinnige discussies in de Graalburcht een internationaal karakter kregen.

Patrick voor het uitstapje in de SRS-wereld, mijn eerste artikel, en Sander, computerspecialist bij uitstek, voor het fantastische computerprogramma voor de bewerking van de plaatjes van mijn ‘dubbelpulsexperiment’, hoofdstuk 3 van dit proefschrift, en de overige studenten die de Graalburcht hebben bevolkt, de roetonderzoekers Arjen en Nassia, pico-puls-producent Floris, O₂-thermometerspecialist Jeroen, taggingexpert Tim en vlam-foto-akoesticus Jan Matthijs.

Tot slot de eerste dieselpromovendus, mijn voorganger Dr. Theo Brugman uit wiens brein de naam Dieselteam is ontsproten. Hij bracht mij de beginselen van laserdiagnostiek in motoren bij. Zijn grote wens was deel uit te maken van de corona, om mij een ‘makkelijke’ vraag te kunnen stellen, maar dit heeft hij helaas niet meer kunnen doen. Wel weet hij nu alle antwoorden.

Buiten de Graalburcht, maar niet minder belangrijk:

Alle medewerkers van de instrumentmakerij, de glasinstrumentmakerij, de quick-service, de zelf-service en de afdelingen elektronica, grafische vormgeving en computer- en communicatiezaken.

Also I want to thank Dave Rickeard, James Banister and Jill Duff from the Esso Research Centre in Abingdon, UK, for their fruitful collaboration.

Gerard Meijer, Rik Baert and Katharina Kohse-Höinghaus are gratefully acknowledged for their careful proofreading of the manuscript.

Voor de prettige sfeer op onze afdeling, ook ‘buiten’ het werk, wil ik bedanken alle medewerkers van de ‘oude’ afdeling Molecuul- en Laserfysica, met name elektronicaspecialist Frans van Rijn, Jörg, Robert KD, Jules, Adrian, Koen, André Ep, Marcel, Harold, Erko, Maarten, Richard, Rienk, Iwan en alle medewerkers en studenten van de huidige groepen Molecuul- en Laserfysica I en II en Toegepaste Fysica: de technici Chris, John, Cor en Eugène die altijd wel een oplossing hadden voor de problemen op elektronisch en technisch gebied, Magda en Ine voor hun hulp bij administratieve kwesties en verder Rogier, Robert S, Ivan, Frank, Bas, Maarten, Michiel, Karen, Martina, Jack, Bernard, Ralph, Dave, Gerard, Gert, Giel als collega, Mike, Rick, Rudy, Deniz, Hans P, Rob, Andrei, André vR, veiligheidsinspecteur Frans H, Jos, Sacco, Tim, Stefan, Brenda, Edi, Sergio, Iulia, Luc-Jan, Rik, Monique en alle anderen.

Uiteraard zijn er ook buiten de wetenschappelijke wereld veel personen die minstens even belangrijk zijn geweest. Al mijn vrienden, kennissen en familieleden wil ik hier dan ook bedanken voor hun steun en interesse, ook al was het vaak moeilijk te begrijpen waar ik mee bezig was. Een aantal wil ik speciaal noemen:

Paranimf Carolien voor het steeds weer moeten aanhoren van mijn gemopper over mislukte metingen, kapotte lasers en het vervelende schrijven. Onze zwem-, wandel-, schaats- en fiets-

avonden hielpen altijd weer de ellende even te vergeten.

Mijn vrienden uit mijn studietijd: Paranimf Karen, ik heb veel van haar geleerd en ben blij dat ook zij haar promotieonderzoek bij ons op de afdeling kon beginnen, en Eric met jullie dochter Marit en natuurlijk Johan en verder Peter, Paul en Erno, ik hoop dat ook jullie proefschriften snel af zijn.

Rest mij enkel nog mijn ouders en mijn broertjes te bedanken. Antoon, ver weg in Suriname en Bas iets dichterbij in Tilburg, jullie zijn fijne broers. Pap en Mam, fijn dat ik altijd op jullie hulp kan rekenen en dat er altijd een veilige thuishaven is. En tot slot natuurlijk Giel voor veel meer dan ik hier ooit op kan schrijven.

Mensen, allemaal bedankt!

Contents

1 Diesel combustion: an introduction	1
1.1 The ‘rational engine’	2
1.2 General introduction	3
1.3 The combustion process in a diesel engine	7
1.3.1 Combustion phases	8
1.3.2 Established view of the diesel combustion process	10
1.3.3 New ideas about the diesel combustion process	12
1.3.4 The established view compared to the new ideas	14
1.4 Formation of nitric oxide	16
1.4.1 Thermal NO (Zeldovich NO)	17
1.4.2 Prompt NO (Fenimore NO)	19
1.4.3 NO generated via nitrous oxide	19
1.4.4 NO production from fuel nitrogen	20
1.4.5 Formation of NO ₂	20
1.5 Formation and oxidation of soot	21
2 Laser-based diagnostics in a diesel engine	23
2.1 Introduction	24
2.2 Experimental setup	27
2.2.1 The engine	27
2.2.2 Engine characteristics	31
2.2.3 Optical setup	34
2.3 Optical diagnostics	36
2.3.1 Spontaneous light emission	36
2.3.2 Laser induced light emission	38
Quantification of LIF	39
2.3.3 Elastic light scattering	44
2.4 Spontaneous light emission	44
2.4.1 Dispersed flame emission	45
2.4.2 Flame emission images	46
2.5 Spectroscopy in a diesel engine	50
2.5.1 Nitric oxide and oxygen	50
2.5.2 Dispersed fluorescence spectra	55
2.5.3 Saturation	58
Appendix	59

3	A method to assess the local attenuation coefficient by Mie scattering using two counterpropagating laser beams	61
3.1	Introduction	62
3.2	Theory	64
3.2.1	Double image method	64
3.2.2	Single image method	67
3.2.3	Transmission	68
3.3	Experimental setup	69
3.3.1	Double image method	69
3.3.2	Single image method	70
3.3.3	Transmission	71
3.4	Results and Discussion	71
3.4.1	Double image method	71
3.4.2	Single image method	75
3.4.3	Transmission	77
3.4.4	Flame emission	80
3.5	Conclusion	81
	Appendix	81
4	Semi-quantitative nitric oxide densities from spatially averaged dispersed fluorescence spectra	83
4.1	Introduction	84
4.2	Experimental Method	86
4.2.1	Engine	86
4.2.2	Details of test fuels	87
4.2.3	Optical setup	87
4.3	Results and Discussion	87
4.3.1	Engine characteristics	87
4.3.2	Dispersed fluorescence spectra	88
4.3.3	NO density	90
4.3.4	Effect of engine conditions	94
4.4	Conclusion	96
	Appendix	97
5	Nitric oxide distributions in relation to temperature and chemical composition inhomogeneities	101
5.1	Introduction	102
5.2	Theory	103
5.3	Experimental setup	106
5.4	Results and Discussion	108
5.4.1	NO fluorescence distributions	108
	Raw data	108
	Laser intensity	110
	Temperature	111
5.4.2	NO density distributions	115

Temperature distributions	116
Collisional decay rate distributions	118
Discussion	119
5.4.3 Reproducibility	120
5.4.4 Integrated NO density	121
5.5 Conclusion	125
Appendix	126
6 Summary and outlook	129
6.1 Summary	129
6.2 Outlook	133
References	139
Samenvatting	147
Curriculum Vitae	151
Publications	153

Chapter 1

Diesel combustion: an introduction

Abstract

This introductory chapter starts with a historical note about the invention of the diesel engine, followed by a short description of its operating cycle. The established view of the combustion process occurring in the combustion chamber of a diesel engine, as well as some recent modifications are described. The nitric oxide (NO) and soot formed during combustion are the most important polluting components in the exhaust gases of the diesel engine. A literature-based overview of the chemical pathways involved in the NO formation and a possible pathway for the formation of soot are given. Finally, a short preview is provided of this thesis, in which the Laser Induced Fluorescence (LIF) detection technique is applied to observe NO molecules inside the cylinder of an optically accessible two-stroke diesel engine.

1.1 The ‘rational engine’

Rudolf Diesel (1858-1913) patented an engine in 1892 that, in his view, was not just an improvement on existing heat engines, but a machine of an entirely new kind [1]. It was an engine that was built on scientific, rational principles and Diesel fully expected that this ‘rational engine’ would replace the steam engine, used for heavy transportation those days, completely.

Many inventors, long before Diesel, were trying to find a working fluid that would provide the possibility to make a more efficient and smaller engine, compared to the complicated steam engine, the efficiency of which was at most only 7%. The steam engines used water, raised to steam, as a working fluid to transfer the energy of the combustion, that took place outside the engine, to the cylinder, where the steam did its work by expanding against a piston. Air would be a good candidate to use as working fluid because it is readily available and it contains oxygen so that the combustion could take place inside the engine. The first successful internal combustion engine, burning coal gas with a thermal efficiency of 14%, was introduced in 1867. The Otto engine, called after its inventor Nicolaus Otto, was widely used in passenger cars at the time Diesel started thinking about a new heat engine.

The unique aspect of Diesel’s approach was his conviction that his new engine could realize the ideal Carnot cycle, that was first described in 1824 by the French pioneer in thermodynamics Nicolas Carnot. In his engine the pressure should rise only due to the compression of air and ignition of injected fuel should occur only as a result of the high pressure and temperature (in Otto engines ignition has to be initiated). After this autoignition the combustion should continue and add heat isothermally in accordance with the ideal of Carnot. Diesel had calculated that his engine could have an efficiency of 73% for almost all fuels if the combustion process occurred isothermally. He published his ideas in 1893 in a book entitled: *Theory and Construction of a Rational Heat Engine to Take Place of the Steam Engine and of All Presently Known Combustion Engines*.

However, soon after his first experiments in 1893, Diesel found out that an internal combustion engine can never realize the Carnot cycle because too large amounts of air are required to keep the combustion isothermal. Nevertheless, in 1897, after four years of struggling with the required high pressures and the problem of how to inject fuel into the compressed air, Diesel presented his first engine. It was a one-cylinder engine with a thermal efficiency of 26% and a maximum compression of 30 bars, which was a spectacular result. During the next years the engine was further developed with a large step forward in 1920 when the fuel-injection systems were perfected.

Thus, the diesel engine as it is today is quite different from the original Carnot engine as it was proposed by Diesel. However, the essential features of the combustion engine are still the same: It is a high-compression engine in which fuel is injected in air near the end of the compression stroke and is ignited by the heat of the compression. The invention of the diesel engine is a rather unique story in the history of technology, as it started with an idea in which pure science was applied to engineering. Although the scientific ideal of the inventor could not be realised, the invention of the diesel engine has caused a revolution in heavy road transportation in the last century.

1.2 General introduction

In internal combustion engines, like Otto engines (also called spark-ignition (SI) or gasoline engines) and diesel engines (also called compression-ignition (CI) engines), combustion takes place inside the engine after fuel is injected in the combustion chamber. Fuel can be injected either directly into the combustion chamber (Direct Injection (DI)) or into a prechamber, separated from the main combustion chamber (Indirect Injection (IDI)). In the latter case combustion starts in the prechamber and due to the resulting pressure rise burning gases and fuel are driven into the main combustion chamber. An Otto engine uses a spark plug to initiate the combustion, whereas in a diesel engine ignition occurs as a result of the high pressure and temperature.

The thermal energy produced by the combustion is transformed into mechanical energy. A piston moves back and forth in the cylinder and transmits the power generated by the combustion through a connecting rod and crank mechanism to the crankshaft as shown in figure 1.1a. A movement of the piston from its uppermost position (Top Dead Centre (TDC)) to its lowest position (Bottom Dead Centre (BDC)), or vice versa, is called a stroke. Positions in between are denoted in degrees crank angle (Θ), with TDC defined as zero degrees crank angle. Crank angles between TDC and BDC are commonly referred to as ‘after TDC’ (aTDC) whereas crank angles between BDC and TDC are referred to as ‘before TDC’ (bTDC). The volume of the cylinder is a minimum (clearance volume V_c) when the piston is at TDC, whereas it is a maximum (V_t) when the piston is at BDC. As in the two-stroke engine the combustion gases can leave the cylinder once the exhaust opens an effective volume (V_e) is determined by the position of the exhaust port. The difference between the effective volume and the clearance volume is

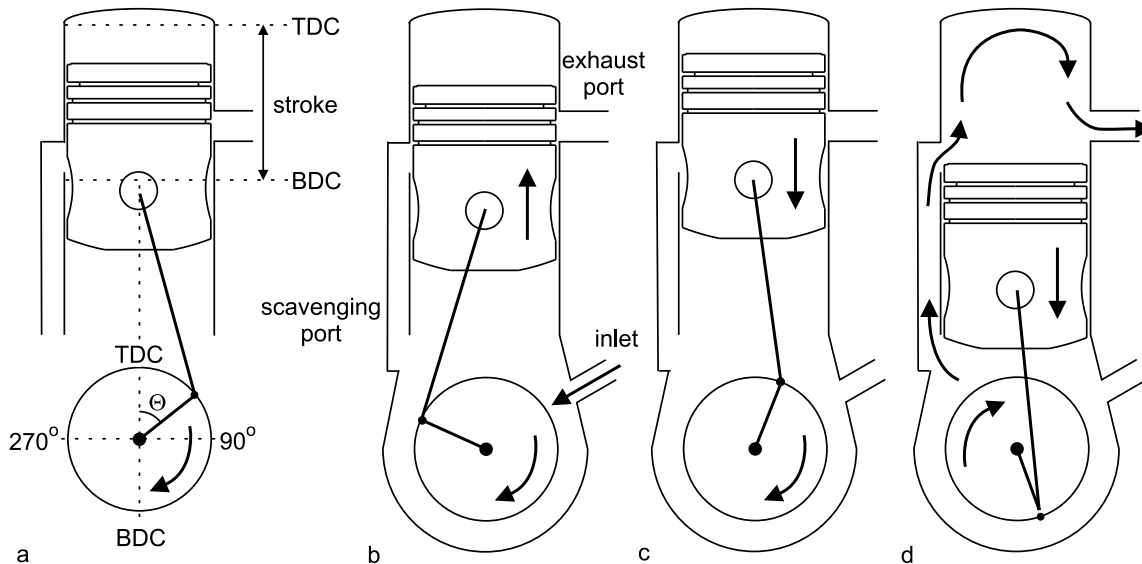


Figure 1.1: a) Basic geometry of the internal combustion (two-stroke) diesel engine. TDC and BDC indicate the uppermost and lowest position of the piston. The two-stroke operating cycle showing b) the compression stroke, c) the expansion stroke and d) the scavenging process.

called the displaced or swept volume (V_d)¹. One complete combustion cycle comprises, besides the fuel injection and combustion, also the refreshment of the cylinder contents (burned gases have to leave the cylinder, while fresh air has to go in).

The total combustion cycle can take place during two or four strokes. The first engines were four-stroke engines in which each cylinder requires four strokes of the piston (*i.e.* two revolutions of the crank shaft) for a complete process that produces one power stroke. In short, the cycle starts with an intake stroke in which the piston moves down and fresh air is let into the cylinder through an inlet valve that closes just after the piston has passed BDC. Following is a compression stroke in which the piston moves up, compressing the air in the cylinder. Just before the piston is at TDC fuel is injected and autoignition initiates the combustion process. In the subsequent expansion stroke, the high-pressure high-temperature combustion gases drive the piston down again. As in this stroke the piston does its work by forcing the crank to rotate, it is often called the power stroke. When the piston reaches BDC the exhaust valve opens and the combustion gases can leave the cylinder when the piston, in the exhaust stroke, moves up again to TDC. The inlet valve opens when the piston approaches TDC, and just after TDC, when the exhaust valve is closed, the cycle starts again.

To get a higher output from a given engine size the two-stroke engine was developed. In addition, it has a simpler construction as the inlet and exhaust valves, on top of the cylinder, are replaced by an exhaust port in the cylinder wall and a scavenging port that is connected with the crank case (see figure 1.1). These ports, which are located near BDC and of which the exhaust port is placed a bit higher than the scavenging port, are opened and closed by the motion of the piston. This engine requires only two strokes (*i.e.* one revolution of the crank shaft) to produce one power stroke. A compression stroke starts when the piston moves up, closing the scavenging and exhaust ports, followed by a compression of the air in the cylinder (figure 1.1b). During this stroke also fresh air is drawn into the crank case through an inlet. Similar to the four-stroke engine, combustion occurs if the piston approaches TDC and the piston moves down in an expansion or power stroke (figure 1.1c). Once the piston reaches the exhaust port the combustion gases start to leave the cylinder. When the scavenging port is opened as well, the fresh air, compressed in the crank case, flows into the cylinder and drives out the combustion gases (scavenging, figure 1.1c).

Although passenger cars are usually powered by an Otto engine the diesel engine is used world wide for heavy transportation. It offers significant fuel economy advantages over other power plants used for road transportation, because of its high thermal efficiency (up to 40%; for an Otto engine it is about 30%) and because the heavy oil it consumes is relatively cheap. Compared to Otto engines, diesel engines have low carbon monoxide (CO) emissions, but, as a result of the high pressure and temperature required for the autoignition of diesel combustion, the emission of nitric oxides (NO_x) is higher. In addition, the large hydrocarbons (HC) present in the diesel fuel are partly transformed into soot particles.

Soot particles and NO_x are the most important polluting components in the exhaust gases of a diesel engine. NO_x participates in chain reactions that remove ozone from the stratosphere, re-

¹These volumes are important for the determination of the compression ratio (ϵ) of the engine defined as [2]

$$\epsilon = \frac{\text{effective cylinder volume}}{\text{minimum cylinder volume}} = \frac{V_d + V_c}{V_c} = \frac{V_e}{V_c}.$$

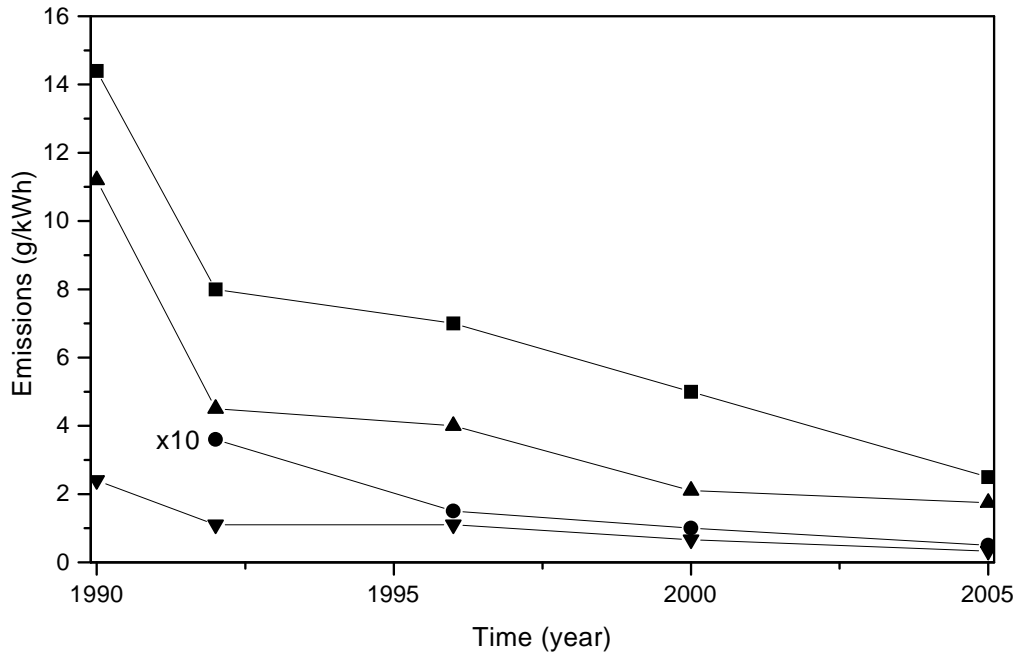


Figure 1.2: Euro emission standards for new trucks: NO (■), soot (●), CO (▲) and hydrocarbons (▼).

sulting in an increased amount of ultraviolet radiation reaching the surface of the earth. It reacts with OH radicals in the upper layers of the troposphere to HNO_2 and HNO_3 , which contribute to acid rain. Furthermore, in combination with the unburned hydrocarbons, it plays a role in the formation of smog [3]. Soot particles cause severe air pollution and, especially the small ones, are a risk for human health as they can penetrate into the lungs and remain there [4]. Because of the damage soot particles and NO_x cause to the environment, ever stricter legislation is introduced for their emissions, as shown in figure 1.2. In order to meet the legislative standards, knowledge of origin, timing and location of the formation of nitric oxide² (NO) and soot particles during the diesel combustion process is important. However, in spite of this importance only little is known about the combustion and emission formation processes in a diesel engine. To understand these processes a clear description of how diesel combustion proceeds (including the temporal and spatial formation of polluting components) inside a diesel engine is required. Such a description is important as a tool in interpreting experimental measurements and in developing predictive numerical models for diesel engines. It will be needed by engine designers who have to meet the ever more stringent emission standards while they want to improve the engine efficiency at the same time.

The combustion in a diesel engine is a very complex, turbulent, heterogeneous, three-dimensional, multiphase process that occurs in a high temperature and high pressure environment [2]. In addition, the details of the process depend on the characteristics of the fuel, on the design of the engine's combustion chamber, on the fuel injection system and on the engine's

²Nitric oxide, NO, is the dominant oxide of nitrogen formed during combustion. The often used chemical symbol NO_x refers to the sum of NO and NO_2 .

operating conditions. To obtain information about the way the combustion and the formation of soot particles and NO proceed, measurements have to be performed under realistic conditions, preferably in a running diesel engine. Due to the recent development of advanced laser-based diagnostics, detailed measurements of the physical and chemical processes occurring during diesel combustion inside the combustion chamber of a running diesel engine are now possible.

The objective of the experiments presented in the current work is the development of a laser-based measurement technique for semi-quantitative determination of the NO density, with both spatial and temporal resolution, during the combustion in a diesel engine. Ultimately, the technique developed during this project should be useful for diagnostics of realistic, commercial diesel engines. Therefore, the operating conditions of the research engine used for this work have been kept as realistic as possible, implying mainly that *i*) standard, commercial diesel fuel is used and *ii*) the engine is operated steadily running. As most important tool in this method the Laser Induced Fluorescence (LIF) detection technique is used to observe NO molecules inside the combustion chamber of an optically accessible diesel engine. In short this technique involves electronic excitation of NO molecules by laser radiation followed by detection of the ensuing fluorescence. The intensity of the fluorescence is a measure for the density of NO molecules. However, although the fluorescence intensity is proportional to the NO density, the proportionality constant includes several spectroscopic and experimental factors. Evaluation of these factors results in expressions that depend on the local conditions in the combustion chamber (*i.e.* pressure, temperature, laser intensity, gas mixture), which in general are not known. Therefore, additional experiments have to be performed to obtain the unknown quantities and a detailed processing of the observed NO LIF signal is required before it can be interpreted as a NO density.

This general introduction is followed by a description of the established view of the diesel combustion process occurring in a diesel engine and some recent modifications. Included are the important aspects concerning the formation of NO and soot. At the end of this chapter the pathways important for the nitric oxide formation are summarised, as well as those involved in the formation of soot particles.

Chapter 2 starts with a short overview of several laser-based diagnostic techniques that are frequently used to study combustion processes, and some applications to diesel engines, as reported in literature, are given. It includes a short review of previous NO LIF measurements that were performed on optically accessible diesel engines. This is followed by a detailed description of the optically accessible diesel engine the current experiments are performed on, the engine characteristics, and an overview of the different optical setups applied. A more detailed description of the LIF technique and the other optical techniques used in the experiments is given. The flame emission, dispersed in its different wavelength components, as well as images showing the flame development during the combustion are presented. Finally, an analysis of the laser spectroscopy of NO in a diesel engine is given, with an emphasis on its interference with oxygen (O₂).

In the experiment described in chapter 3 a method is developed to reconstruct the local laser intensity in the combustion chamber of the running engine from a distribution of the elastically scattered laser radiation. This method is validated by comparing its results to an exact method in which the local laser intensity is reconstructed by making use of two elastic scattering images, recorded from two laser beams which traverse the engine in opposite direction. Additionally, the total transmission of the laser radiation through the combustion chamber of the firing engine

is derived from these distributions.

The results of the first NO LIF experiments are given in chapter 4 in which dispersed fluorescence spectra of NO are presented. They show NO fluorescence throughout the whole combustion stroke starting around TDC. The intensity of the NO dispersion peaks of these spectra provides information about the spatially averaged NO density, present in the probe volume within the cylinder. The factors, all depending on the in-cylinder conditions, that are required to translate the observed fluorescence intensity into a semi-quantitative NO density are derived. Using these processing factors relative NO densities as a function of crank angle for different engine conditions (compression ratio, load and fuel) are obtained. Furthermore, the NO dispersion spectra give information about the wavelengths of the fluorescence bands of NO and O₂ obtained from the running engine. From these spectra a fluorescence band of NO free from O₂ fluorescence, that can be used to obtain spatially resolved NO distributions, is determined.

NO LIF distributions measured through a narrow-band reflection filter to eliminate O₂ fluorescence are the subject of chapter 5. To translate them into semi-quantitative NO density distributions the position dependence of the processing factors is derived. The observed NO density distributions are discussed with an emphasis on the assumptions that are made with respect to the uniformity of the temperature and gas mixture to obtain the distributions.

Finally, a summary of the most important results and the assumptions made in the interpretation of the NO fluorescence yield is given in chapter 6. In addition, an outlook is given in which it is discussed to what extent the developed method meets the objectives of this study, and how it can be improved.

1.3 The combustion process in a diesel engine

The total combustion process inside a diesel engine involves both premixed and diffusion reaction zones. Initially a premixed burn occurs because some fuel and air have mixed already before autoignition occurs. This is followed by a mixing controlled burn which is dominated by diffusion burning, but can contain some premixed burn as well. A division of the combustion process into four separate phases characterised by combustion type, based on the concept of the heat release rate, is described below in section 1.3.1.

Such a division of the total combustion process will not give an answer on how the diesel combustion process starts and develops and how polluting components are formed. To give a good description of the complex processes occurring during diesel combustion, measurements have to be performed under realistic diesel engine conditions. But, prior to the relatively recent development of advanced laser techniques, it was not possible to perform detailed measurements on the combustion processes occurring within the reacting diesel fuel jet. Some information about the fuel jet penetration and spread of the combustion zones could be obtained from recording the natural flame emission. However, the spatial resolution is limited because the signal is integrated along the line of sight and the information is not species specific or quantitative. Sampling probes could provide quantitative species specific data but they are perturbing, have a limited temporal resolution and provide only information about one specific small volume. As detailed information about the diesel combustion process is limited, the description of the diesel combustion process initially was derived from studies of spray combustion in furnaces and gas turbines [5, 6]. In this description it was assumed that the quasi-steady portion of the diesel

combustion process, after the premixed burn, behaves similar to the other spray combustion processes. This view (the ‘old view’) of the diesel combustion process is given in section 1.3.2.

The development of advanced laser-based diagnostics allowed to study the processes occurring inside a reacting fuel jet. Such experiments have provided a lot of new information on the diesel combustion and pollutant formation processes, that is partly in contradiction with the traditional description of diesel combustion. The first experiments indicating that the diesel combustion process is different from the old view were experiments combining LII and elastic scattering experiments that showed that soot was present also at positions where it was not expected according to the old view and that no fuel droplets were present outside the liquid fuel jet [7]. A lot of these recent results were acquired by Dec and co-workers using several planar imaging and natural flame emission diagnostics in an optically accessible DI diesel engine of the heavy duty size class running on a low-sooting fuel. Dec has combined the results of these data, including liquid-phase fuel distributions [8, 9], quantitative vapour-fuel/air mixture images [9, 10], poly-aromatic hydrocarbon (PAH) distribution images, soot concentrations [11–14], soot particle size distributions [13, 14], images of the diffusion flame structure [15], and natural chemiluminescence images of the autoignition [13] to arrive at a detailed modified view of the temporal and spatial evolution of a reacting diesel fuel jet [16]. This alternative view, which describes mainly the beginning of the combustion in much more detail than the old view, is summarised in section 1.3.3, including some more recent results with respect to the NO formation [17] and the autoignition [18]. It should, however, be noted that thus far the model is derived from results that were obtained from one particular engine operated at one typical condition on a special low-sooting fuel. The larger amounts of soot produced by the use of a commercial diesel fuel reduced the optical transparency of this engine rapidly, which precluded to obtain in-cylinder measurements. In addition, as till now insufficient information is available about the later part of the combustion, the model only gives a full description of the first part of the combustion process (the later part can only be estimated). Also, the effects of swirl and wall interactions are neglected.

1.3.1 Combustion phases

Based on the heat release rate different phases, characterised by burning type, can be distinguished in the total diesel combustion process occurring in a DI diesel engine. The heat release rate is defined as the rate at which the chemical energy of the fuel is released by the combustion process. It can be obtained from the in-cylinder pressure as a function of crank angle by calculations based on the first law of thermodynamics and use of the ideal gas law [2]. Four phases, each controlled by different physical or chemical processes, can be distinguished in the heat release rate. The relative importance of each phase depends on the combustion system used and the engine operating conditions, but they are common to all diesel engines.

Typical in-cylinder pressure and heat release rate curves for the compression and expansion stroke of a direct injection diesel engine are given in figure 1.3. During the compression stroke, starting at the moment the exhaust and inlet ports (or valves) close, air is compressed to a pressure of about 40 bars and a temperature of about 850 K. (These are the values that would be reached if no combustion would occur.) Towards the end of the compression stroke fuel is injected into the cylinder (Start Of Injection (SOI) in figure 1.3). The fuel is injected at high pressure through one or more small holes in the injector tip of the fuel injection system,

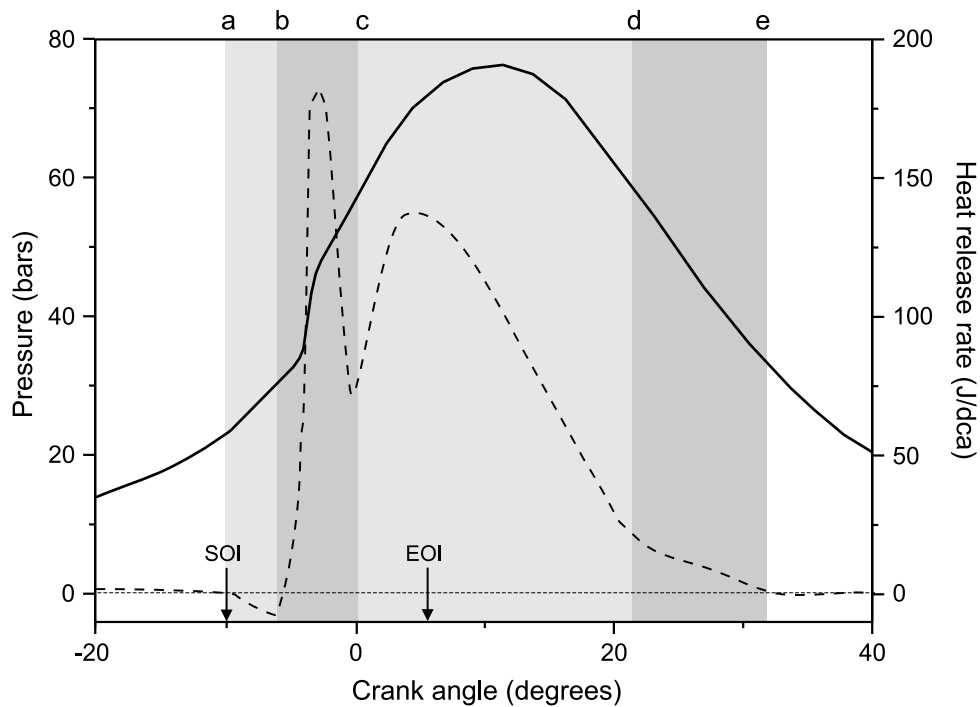


Figure 1.3: Typical in-cylinder pressure (solid curve) and heat release rate (dashed curve) as a function of crank angle for a direct injection diesel engine. Indicated are the start of injection (SOI), end of injection (EOI) and the different phases in the combustion process; the ignition delay period (a-b), the premixed combustion phase (b-c), the mixing controlled combustion phase (c-d) and the late combustion phase (d-e); (dca = degree crank angle).

forming jets at high velocities. The liquid fuel jet penetrates into the combustion chamber, where it breaks up and evaporates, and the fuel vapour mixes with the high temperature, high pressure air. Due to this fuel vaporisation the in-cylinder air initially cools slightly, causing the negative heat release rate just after the start of injection. As the air temperature and pressure are above the fuel's ignition point, spontaneous ignition (autoignition) of the already mixed fuel and air initiates the combustion process. This period, between the start of fuel injection and the start of combustion, is called the ignition delay period (a-b in figure 1.3).

At the ignition point the premixed fuel/air mixture starts burning, producing the fast initial rise in the heat release rate. Also, the temperature and pressure quickly rise above the temperature and pressure reached in the motored (non-firing) engine as combustion of the fuel air mixture occurs. This phase, in which combustion of the fuel vapour that has mixed with air during the ignition delay period proceeds rapidly, is denoted as the premixed combustion phase (b-c in figure 1.3). The heat release rate shows a pronounced spike during the premixed combustion phase, because the premixed fuel burns rapidly and is depleted quickly.

This spike is then followed by a second, broader maximum which is due to mixing controlled combustion and is commonly referred to as the mixing controlled combustion phase or the diffusion burning phase (c-d in figure 1.3). The jet penetrates further into the combustion chamber and burns at its edges as a turbulent diffusion flame with a yellow-white or orange colour due to the presence of carbonaceous particles. Fuel injection stops (End Of Injection

(EOI) in figure 1.3), but mixing of the air in the cylinder with burning and already burned gases continues throughout the combustion and expansion processes. This period, lasting about 20 degrees crank angle, is the main heat release period.

Normally 80% of the total fuel energy is released in the mixing controlled and the premixed combustion phase. The residual fuel energy will be released at a lower rate during the late combustion phase (d-e in figure 1.3).

As the exhaust opens the in-cylinder pressure drops and combustion gases can flow out of the cylinder. Once the inlet opens, air flows into the cylinder and the burned gases, displaced by this fresh air, continue to flow out of the exhaust port (so-called scavenging).

1.3.2 Established view of the diesel combustion process

The basic concepts of the established view of diesel spray combustion are given in a paper by Faeth [6]. Upon injection the liquid fuel jet penetrates into the high pressure, high temperature environment of the combustion chamber. The model envisages the diesel jet as having a cold, fuel-rich core, surrounded by a mixture that contains fuel droplets and vapourised fuel, with a decreasing amount of fuel from the centre of the spray to the edge. Autoignition and the initial premixed burn are expected to occur towards the edge of the spray in regions where the equivalence ratio³ ranges from near stoichiometric to up to about 1.5 [2, 19]. Subsequently, the diffusion flame develops rapidly throughout the mixture in the close-to-stoichiometric regions.

It is, however, not specified if the combustion occurs in many small diffusion flames around individual fuel droplets or in one single, large diffusion flame sheath surrounding the periphery of the spray, being fed by the fuel vapour from many droplets. In a paper by Chui *et al.* [20] a sheath-type combustion is suggested for diesel diffusion flames, but this view is not generally accepted. The Bosch Automotive Handbook [21], for example, suggests that diesel combustion starts in regions around individual droplets that contain a flammable mixture.

Since this description does not deal directly with the nitric oxide and soot formation processes during diesel combustion some possibilities to account for this are presented, mainly based on theoretical ideas but in combination with observed features. The regions where soot is expected to form are derived from the knowledge that soot formation results from fuel that is broken up into soot precursors at temperatures above about 1300 K in combination with the assumption that soot forms under nearly stoichiometric conditions [2]. That is, for soot to be formed mixing of the fuel with the hot in-cylinder air only is not sufficient and heating from the combustion is required as well. Therefore, soot particles are assumed to form in regions where the temperature is sufficiently increased by the combustion and the mixture is nearly stoichiometric. At the fuel-rich side of the diffusion flame these conditions are met. Therefore, soot is

³The fuel/air equivalence ratio (Φ) is defined as the ratio of the actual fuel/air ratio $(F/A)_{\text{actual}}$ and the stoichiometric fuel/air ratio $(F/A)_{\text{stoich}}$ (at stoichiometric conditions there is just enough oxygen for conversion of all fuel into completely oxidised products) as [2]

$$\Phi = \frac{(F/A)_{\text{actual}}}{(F/A)_{\text{stoich}}},$$

in which the fuel/air ratio is given by $(F/A) = (\dot{m}_{\text{fuel}}/\dot{m}_{\text{air}})$ with \dot{m}_{fuel} and \dot{m}_{air} the fuel and air mass flow rates, respectively. This implies for stoichiometric mixtures $\Phi = 1$, for fuel-rich mixtures, in which there is insufficient oxygen to oxidise all the fuel, $\Phi > 1$, and for fuel-lean mixtures, in which excess air is present, $\Phi < 1$.

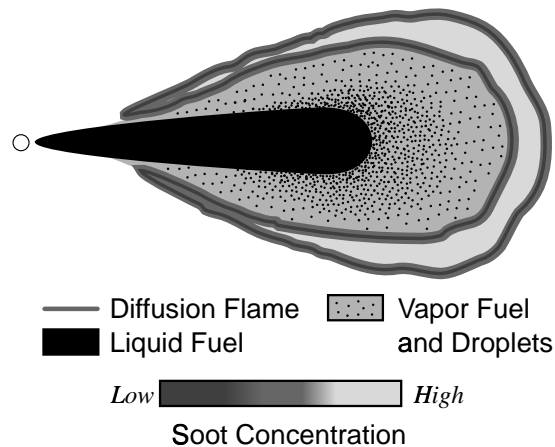


Figure 1.4: Schematic representation of the established view of the diesel combustion process, showing a cross section through the middle plane of a fuel jet. A fuel core (black) is surrounded by fuel droplets and fuel vapour (grey). The diffusion flame is located around the jet periphery with soot at the fuel-rich side. (From Dec [16]; reproduced with permission from SAE paper no. 970873 © 1997, Society of Automotive Engineers, Inc.)

expected to form at the inner side of the diffusion flame around the jet periphery, starting at the positions where autoignition occurs. Because of stoichiometry, the initial fuel-rich premixed burn is not expected to be an important source for soot formation. Later on, soot oxidises in the flame zone when it contacts unburned oxygen.

Nitric oxide is expected to form in the high temperature regions in both the flame front and the burned gases via the thermal NO mechanism (see section 1.4.1). Formation rates then are the highest in the close-to-stoichiometric regions at high temperature [2], that is, at the edge of the diffusion flame. Therefore, NO formation, like soot formation, is expected in the diffusion flame zone, but at the lean side where more oxygen is present.

Dec has summarised this view of the DI diesel combustion in a schematic picture which is reproduced in figure 1.4 [16]. It has to be taken into account that this schematic represents only a general view, that often is used to show how diesel combustion proceeds. The picture of diesel combustion might be more complex, but the available information is not sufficient for a full description, and more detailed experimental data are needed in order to arrive at a better, more complete description of the diesel combustion process. Figure 1.4 shows a cross section through the centre of a fuel jet. A region of dense fuel droplets, possibly with an intact liquid stream near the injector, is seen (black). Around this fuel core a region of more disperse, vapourising droplets and vapour fuel is present (grey). In the case of a sheath-type combustion the diffusion flame is formed around the jet periphery, where fuel and air mix. Around the jet periphery on the fuel-rich side of the reaction zone soot formation is expected. For the case of droplet combustion the flame zone consists of a lot of small flamelets around individual droplets or clusters of droplets. Now soot is expected to form around each droplet within the individual diffusion flamelets. However, as interaction with the gas flow around the droplets could extinguish the flamelets before soot burnout, the soot distribution around the periphery will be more homogeneous, similar to that for the sheath flame case.

1.3.3 New ideas about the diesel combustion process

Because the established view of diesel combustion is not able to explain a number of recent experimental data obtained by laser diagnostic techniques, an alternative ‘conceptual model of diesel combustion’ was developed by Dec [16]. This new model is able to reconcile the experimental data known at that time, but it should be noted that the data used in the model are obtained from one specific test engine operated at only one typical operation condition with a special, low-sooting fuel⁴. Furthermore, the model only gives a full description of the first part of the combustion, from the start to the end of the fuel injection (*i.e.* just after the beginning of the mixing controlled burn). As not sufficient data are available about the last part of the mixing controlled burn only an estimated picture is given for that part. Additionally, the model presents an average description of the events occurring in a single cycle in the absence of wall interactions and swirl; variations in distributions, shapes, size and time can occur from cycle to cycle.

After the start of the injection a fuel jet penetrates into the combustion chamber. At the side of the injector (upstream) the jet mainly contains liquid fuel whereas at the leading end (downstream) the hot air causes the fuel to evaporate at the edges of the liquid fuel jet. Thus, around the liquid fuel jet a region that contains vapour fuel develops. This region first starts along the sides of the jet around 2° aSOI (after SOI). The vapour fuel region becomes larger during further penetration of the jet. The liquid fuel jet will have reached its maximum length when the hot air, penetrating into the jet, is sufficient to vaporise all the fuel around 3° aSOI. However, the vapour region continues to grow and a head vortex, which is typical for a penetrating gas jet, develops at the leading end of the jet. The vapour-fuel/air mixture in the head is relatively uniform with an equivalence ratio varying between 2 and 4. Although the exact time and position of the autoignition are not well known, it is expected that autoignition starts in the head of the fuel jet shortly after the fuel injection between 2° and 3.5° aSOI. By 4.5° aSOI autoignition is seen to have occurred throughout the whole volume of the vapour-fuel/air mixture in the leading part of the jet. At 5° aSOI, just after the time the heat release rate curve starts to rise, fuel breaks down due to the rising temperature (‘cracking’) and large PAHs are seen, uniformly distributed in the head of the jet. This indicates that the rapid rise in the heat release rate is the result of combustion occurring in this fuel-rich mixture. NO cannot yet be seen during this fuel-rich premixed burning.

After this point, around 6° aSOI, soot formation starts. Initially, very small soot particles are found in large parts of the fuel jet. Hereafter, at about 6.5° aSOI, soot is found in the whole region of the vapour fuel jet. However, no soot is seen in a region just a few millimetres downstream of the liquid fuel region. The diffusion flame shows up at 6.5° aSOI. It is located at the periphery of the jet and formed by the products of the fuel-rich premixed burn and the air around it. Just after the diffusion flame has formed the first NO is seen in a thin layer around the jet periphery. Due to the heat of the diffusion flame the liquid fuel region becomes somewhat shorter. During the rest of the premixed burn the jet becomes larger and continues to penetrate into the combustion chamber. The diffusion flame stays at the jet periphery where a thin reaction zone exists. As a result of the flame larger particles are formed at the inner side of the flame, whereas in the central part of the vapour fuel region only small particles are seen. For the whole sooting region an increase in soot particles is seen, with the largest increase in

⁴The engine runs at 1200 rpm, so that 1° crank angle corresponds to 139 μ s.

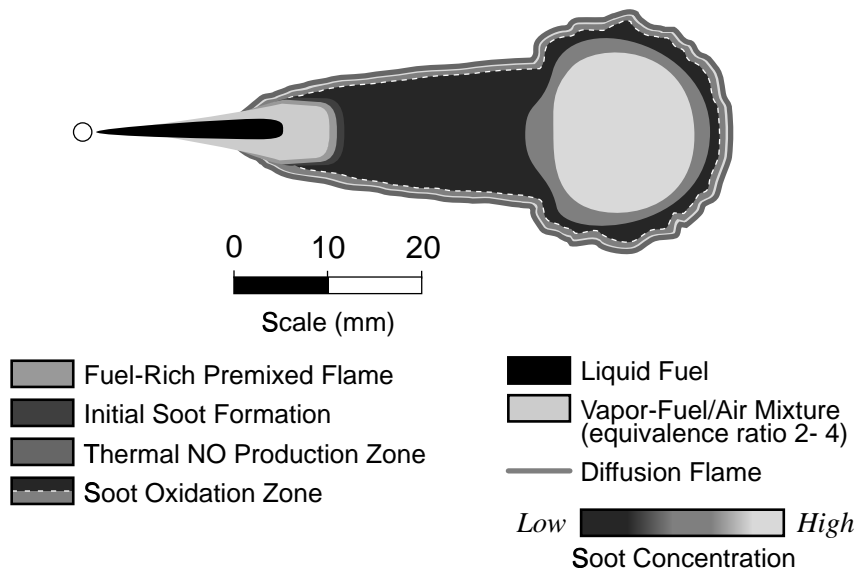


Figure 1.5: Schematic representation of the alternative view, that comprises the new ideas about the diesel combustion process, showing a cross section through the middle plane of a fuel jet, typical for the first part of the mixing controlled burn. A liquid fuel jet (black) is surrounded by a vapour-fuel/air mixture (light grey). Soot particles are present throughout the whole plane, starting a few millimetres downstream from the liquid fuel jet (initial soot formation) with the largest concentration and particle size in the head vortex indicated in a linear grey scale ranging from black (minimum) to white (maximum). A fuel-rich premixed flame is expected between the vapour-fuel/air mixture and the first soot particles. The diffusion flame is located around the jet periphery. At the inner side of the diffusion flame soot oxidation occurs, whereas at the air side of the flame thermal NO production occurs. (From Dec [16]; reproduced with permission from SAE paper no. 970873 © 1997, Society of Automotive Engineers, Inc.)

the head vortex. In addition, the particles in the head vortex are much larger, even larger than those at the jet periphery. NO stays present just outside the sooting region of the jet on the lean side of the diffusion flame.

After all premixed fuel has burned and the combustion becomes mixing controlled the overall features of the jet change only little. However, the jet still continues to penetrate into the combustion chamber and the head vortex, in which the soot concentration and the soot particle size increase further, continues to grow as well. Soot oxidation is almost certainly occurring in the diffusion flame because this is the only significant source of high concentrations of OH radicals, which are assumed to be the most important species for soot oxidation [15]. Oxygen, that also plays a role in soot oxidation, is mainly present in the diffusion flame as well. In addition, the formation of NO continues around the jet periphery.

Figure 1.5 shows a picture that is representative for the fuel jet in the first part of the mixing controlled burn till the end of the fuel injection. In black the liquid fuel is shown and in light grey the relatively uniform vapour-fuel/air mixture surrounding the liquid. Starting from the injector small particles appear suddenly at a small distance downstream from the liquid jet (initial soot formation). During the way down to the end of the fuel jet these soot particles become larger and

their concentration increases. In the head vortex, where soot particles accumulate, the highest soot concentration and the largest soot particles are found. Also, larger particles are seen at the periphery of the jet at the fuel rich side of the diffusion flame. At the inner side of the diffusion flame soot oxidation occurs, whereas at the air side of the flame thermal NO production occurs.

Although the diesel combustion process is described in much more detail by the alternative model, some uncertainties still exist. One of the main questions is to what extent the low-sooting fuel results will hold for real diesel fuel as well. Besides this, it is unknown how the early formation of small soot particles occurs over the whole region of the jet just after the end of the liquid fuel jet. For the present one expects that a fuel-rich premixed flame is present at a small distance downstream from the liquid fuel just before the first soot appears (see figure 1.5). This flame would result from the relatively uniform, fuel-rich combustible mixture at an equivalence ratio of 2-4 that is formed downstream the liquid fuel when the last liquid is vaporised by the hot air in which it penetrates. Such a flame would be perfect for the initial formation of small soot particles, since it contains a lot of fuel and it is sufficiently hot for soot formation. This theory is supported by the fact that the concentration and size of the soot particles increase towards the end of the spray.

Other uncertainties exist about the later part of the combustion, after the time period this model is devised for. In addition, since this description is derived from data obtained at one engine condition, it is not known what the influence of the engine conditions on the reacting fuel jet is. Therefore, more experiments are required to investigate the effect of other engine conditions on the combustion process. It is also necessary to obtain information on the combustion process in an engine running on a commercial diesel fuel, that produces much more soot, instead of a special low-sooting fuel. Furthermore, the effects of wall interactions and swirl should be included in the model.

1.3.4 The established view compared to the new ideas

By comparing the established view of the diesel combustion process to the new ideas large differences with respect to the description of premixed and mixing controlled combustion phases are found. The main differences concern the features of the combustion process related to the autoignition, the liquid fuel phase, the premixed burn, the nature of the diffusion flame and the soot formation. In summary these differences are given in table 1.1.

<i>phenomenon</i>	<i>established view</i>	<i>new ideas</i>
autoignition	local	global
liquid fuel	jet & droplets	only jet
premixed flame	$\Phi \approx 1$	$\Phi \approx 2 - 4$
diffusion flame	'fresh' fuel	decomposed fuel
soot formation	jet periphery	whole jet volume

Table 1.1: *The established view of the diesel combustion process compared to the new ideas about the process.*

In the generally accepted description of the diesel combustion process these aspects are thought to occur in the way as summarised below. First, autoignition occurs only at a few positions in the mixture that are almost stoichiometric, mainly at the periphery of the jet. These positions correspond to the positions where the first soot is formed and therefore the first flame emission is seen. Second, liquid fuel emanates from the injector and fuel droplets are present near (sheath-type) or within (droplet flame) the combustion zone. Third, the initial premixed burn occurs towards the edge of the spray in regions where the mixture is nearly stoichiometric. Fourth, the diffusion combustion proceeds as a more or less classical liquid (non-premixed)-fuel/air diffusion flame at the jet periphery. Fifth, soot formation occurs mainly at the fuel-rich side of the diffusion flame in a sort of shell around the jet periphery.

According to the new ideas about the diesel combustion process these aspects are to be described differently. First, autoignition occurs throughout the whole volume of the vapour-fuel/air mixture before the first soot is seen. Second, the liquid fuel core is short and no fuel droplets are present outside the liquid fuel jet, so that the fuel present in the combustion zone is in the vapour phase only. Third, during the premixed burn combustion occurs under fuel-rich conditions at equivalence ratios ranging from 2 to 4. Fourth, also before the diffusion burning all fuel first undergoes rich premixed combustion. The diffusion flame, finally, occurs between the products of the fuel-rich premixed combustion and air at the periphery of the jet. Fifth, the fuel-rich premixed combustion initiates the early formation of small soot particles just downstream the vapour-fuel/air region. Thereafter, in the mixing controlled phase, soot particles are present throughout the whole fuel jet, increasing in size and concentration towards the end of the jet.

The conceptual model of the diesel combustion process also includes experimental data about the formation of soot and NO, in contrast to the established description. Soot formation would start after an expected, but not proven, fuel-rich premixed flame just downstream of the liquid fuel jet, in the products of the rich combustion. Then soot formation and particle growth continue while the soot moves down the jet to the head vortex and/or to the diffusion flame. Hereafter, soot oxidation occurs in the diffusion flame.

Nitric oxide formation is found not to occur during premixed combustion, including the initial premixed burning phase just after autoignition and the expectedly fuel-rich premixed flame at a small distance downstream of the liquid fuel during the mixing controlled burn [17]. This is explained by the fact that in the premixed burn little oxygen is present and the adiabatic flame temperatures are below those required for thermal NO production. In addition, the equivalence ratio in the region of the premixed burn is in between 2 and 4, which is too high for significant NO production (only little NO is formed at equivalence ratios above 1.8 [22]). However, it is possible that HCN is produced and that this 'fixed nitrogen' will be converted to NO at a later time in the diffusion flame. Formation of NO is seen at the lean side of the diffusion flame around the jet periphery where temperatures are high and oxygen is present, which are ideal conditions for thermal NO production. The fact that NO during this part of the combustion is seen at the diffusion flame should, however, not be taken as an indication that most of the NO is produced only when the diffusion flame is present. Thermal NO production is a relatively slow process and might possibly continue in the later part of the combustion in the hot post combustion gases after the end of the actual combustion. In addition, NO can be formed in the diffusion flame by the conversion of fixed nitrogen resulting from the fuel-rich premixed combustion.

1.4 Formation of nitric oxide

Nitrogen oxides, NO_x , that are formed during the combustion of fossil fuel in air, are mainly NO (nitric oxide), NO_2 (nitric dioxide) and N_2O (nitrous oxide). During diesel combustion at high pressures and temperatures almost all NO_x is in the form of NO. Much of the NO_2 present in the emission of engines results from oxidation of NO at atmospheric pressure via [23]



In the combustion of fuels that contain no (or only little) nitrogen the NO is formed from molecular nitrogen in the air. Many complex reaction paths play a role in the formation (and destruction) of nitrogen oxides during the combustion process. An example of a detailed reaction mechanism comprising 51 species and over 200 reactions is that of Miller and Bowman [22]. Three important chemical pathways for NO formation can be identified, that are distinguished by the reaction involved in the breaking of the N_2 bond (the rate determining step in the NO

Reaction (mechanism)	Rate constant ($\text{cm}^3/\text{mol s}$) (T in K)	Ref.
<i>Thermal NO</i>		
$\text{O} + \text{N}_2 \rightarrow \text{NO} + \text{N}$	$k_1^+ = 7.6 \times 10^{13} \exp(-38000/T)$	[2]
$\text{NO} + \text{N} \rightarrow \text{O} + \text{N}_2$	$k_1^- = 1.6 \times 10^{13}$	[2]
$\text{N} + \text{O}_2 \rightarrow \text{NO} + \text{O}$	$k_2^+ = 6.4 \times 10^9 T \exp(-3150/T)$	[2]
$\text{NO} + \text{O} \rightarrow \text{N} + \text{O}_2$	$k_2^- = 1.5 \times 10^9 T \exp(-19500/T)$	[2]
$\text{N} + \text{OH} \rightarrow \text{NO} + \text{H}$	$k_3^+ = 4.1 \times 10^{13}$	[2]
$\text{NO} + \text{H} \rightarrow \text{N} + \text{OH}$	$k_3^- = 2.0 \times 10^{14} \exp(-23650/T)$	[2]
<i>Prompt NO^\dagger</i>		
$\text{CH} + \text{N}_2 \rightarrow \text{HCN} + \text{N}$	$k_4^+ = 4.3 \times 10^{12} \exp(-11060/T)$	[24]
<i>NO via N_2O</i>		
$\text{N}_2 + \text{O} + \text{M} \rightarrow \text{N}_2\text{O} + \text{M}$	$k_5^+ = 1 \times 10^{14} \exp(-9100/T)^\ddagger$	[26]
$\text{N}_2\text{O} + \text{M} \rightarrow \text{N}_2 + \text{O} + \text{M}$	$k_5^- = 8 \times 10^{14} \exp(-29850/T)$	[26]
$\text{N}_2\text{O} + \text{O} \rightarrow 2\text{NO}$	$k_6^+ = 1 \times 10^{14} \exp(-14200/T)$	[26]
<i>Formation/destruction of NO_2</i>		
$\text{NO} + \text{HO}_2 \rightarrow \text{NO}_2 + \text{OH}$	$k_7^+ = 2.1 \times 10^{12} \exp(-241/T)$	[22]
$\text{NO}_2 + \text{O} \rightarrow \text{NO} + \text{O}_2$	$k_8^+ = 1.0 \times 10^{13} \exp(+300/T)$	[22]
$\text{NO}_2 + \text{H} \rightarrow \text{NO} + \text{OH}$	$k_9^+ = 3.5 \times 10^{13} \exp(+755/T)$	[22]

[†] Only the reaction that splits the triple nitrogen bond is given.

[‡] Dimension: $\text{cm}^6/\text{mol}^2 \text{ s}$.

Table 1.2: Rate constants of reactions important for the NO and NO_2 formation and destruction.

formation) [22, 24, 25]. These are the mechanisms of *i*) thermal NO, *ii*) prompt NO and *iii*) NO generated via N₂O. The amount of NO formed through each of these mechanisms depends on the temperature, pressure and equivalence ratio of the flame. Prompt NO or its precursors can only be formed in the flame front, whereas thermal NO and NO via N₂O can be formed in both the flame front and the post-flame gases. If, in addition, the fuel contains a significant amount of nitrogen (*e.g.* coal) NO can be formed also from this fuel-bound nitrogen [22, 24]. Each of these four mechanisms will be shortly discussed below. Additionally, the conversion of NO to NO₂ in the combustion chamber (important for light load diesel engines as used in the present work) is described.

1.4.1 Thermal NO (Zeldovich NO)

In many combustion processes the oxidation of atmospheric molecular nitrogen (N₂) by the ‘thermal’ mechanism is an important source of NO_x emissions. The formation pathway of thermal NO is often called the Zeldovich mechanism, after Y.B. Zeldovich, who postulated the mechanism. The three elementary reactions that comprise the formation of thermal NO in combustion of near-stoichiometric fuel-air mixtures are [2, 22, 24]



The forward and backward reaction rate constants, k_i^+ and k_i^- , respectively, for these reactions are given in table 1.2. Reaction 1.2 has a high activation energy due to the strong triple bond in the N₂ molecule, and because of this it is the rate limiting step in the thermal NO formation. It is sufficiently fast only at high temperatures (that is why this way to form NO is called the *thermal* NO mechanism).

From reactions 1.2 to 1.4 the rate of NO formation can be derived. Assuming quasi-equilibrium for reactions 1.3 and 1.4, and assuming thermal decomposition of molecular oxygen to be the main source of O-atoms, the initial NO formation rate follows as [2]

$$\frac{d[\text{NO}]}{dt} = k_x(T) [\text{O}_2]_e^{\frac{1}{2}} [\text{N}_2]_e \frac{\text{mol}}{\text{cm}^3\text{s}}, \quad (1.5)$$

in which $[\text{X}]_e$ denotes the equilibrium concentration of the species X in mol cm⁻³ and $k_x(T) = 6 \times 10^{16} T^{-\frac{1}{2}} \exp(-69090/T)$ (T in Kelvin).

For thermal NO formation in a diesel engine the critical period is when the temperatures of the burned gases are at a maximum. That part of the mixture which burns early in the combustion (before TDC) is especially important since it is compressed to a higher temperature, increasing the NO formation rate as combustion proceeds and cylinder pressure increases. After the peak pressure the temperature of the burned gas decreases due to expansion of the cylinder volume and due to mixing with cooler gases, resulting in decreasing thermal NO formation rate. The NO formation rate is the highest at stoichiometric conditions.

Using equation 1.5 the initial NO formation rate in the two-stroke engine can be estimated, using equilibrium concentrations $[\text{N}_2]_e$ and $[\text{O}_2]_e$ based on the amount of N₂ and O₂ in the unburned air. Figure 1.6a shows the initial NO formation rates as a function of crank angle

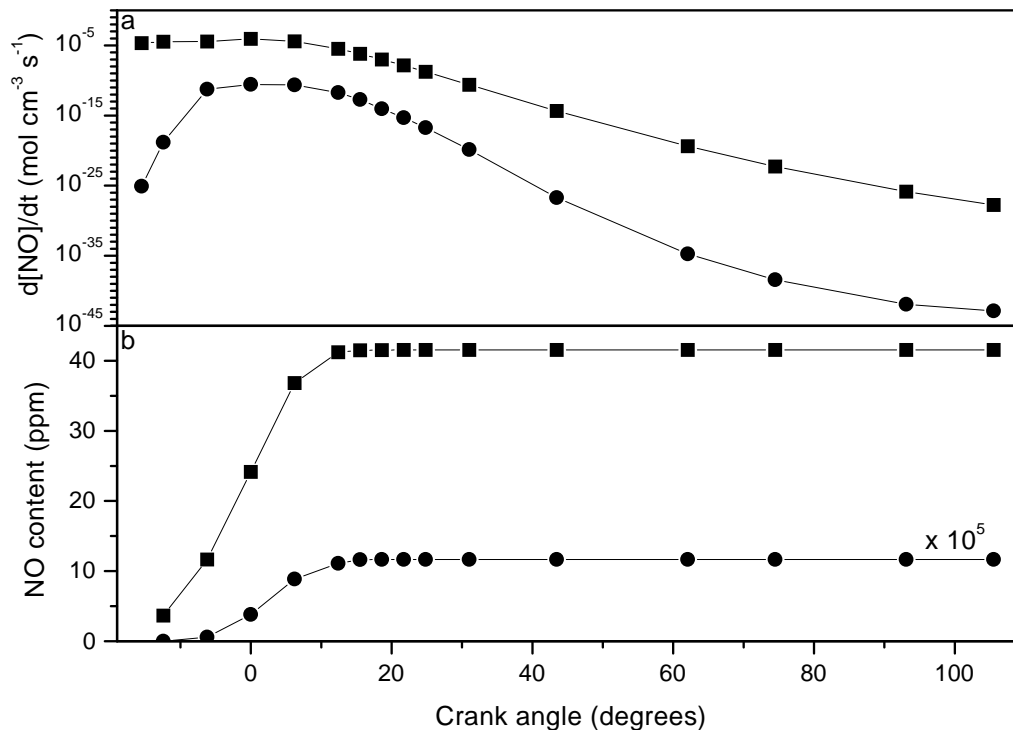


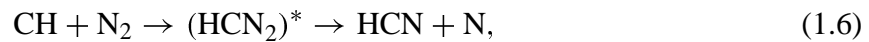
Figure 1.6: a) Calculated initial NO formation rate in the two-stroke engine using equation 1.5 for both the mean gas temperature (●) and the soot temperature (■) using equilibrium concentrations $[\text{N}_2]_e$ and $[\text{O}_2]_e$. b) NO content for both the mean gas temperature (●) and the soot temperature (■) calculated from the initial formation rate taking into account the reaction volume and time.

for two temperatures, the mean gas (●) and the soot temperature (■). These temperatures will be discussed further in chapter 2; see figure 2.4d. The total amount of NO that is formed during the combustion till a specific crank angle can be calculated by taking into account the time and volume available for the NO formation reactions and is given in figure 1.6b. The time is determined by the start of the combustion ($\approx 15^\circ$ bTDC) and the engine speed (20 Hz; $139 \mu\text{sec}$ per degree crank angle), whereas the volume is determined by the volume involved in the NO formation. For the mean gas temperature this is the total volume. However, for the soot temperature this is a smaller part which is not really known. A volume of 10% of the total volume at every crank angle is assumed in figure 1.6b. The NO content curves show that thermal NO is rapidly formed during the early combustion due to the high temperature and that after about 15° aTDC the NO formation is negligible.

For the mean gas temperature it is found that the amount of NO present in the cylinder at the moment the exhaust opens (105° aTDC) is only 0.1 ppb whereas for the soot temperature it is 40 ppm. Clearly, the mean gas temperature is way too low to cause any significant contribution to the NO_x emissions, but the hot regions in the actual flame zone can be expected to be responsible for at least part of the total NO formed. It must, of course, be kept in mind that the contribution on which figure 1.6 is based can only give an order of magnitude estimate.

1.4.2 Prompt NO (Fenimore NO)

In combustion of hydrocarbon fuels, especially under fuel-rich conditions, the prompt NO mechanism can be important. This rapidly formed NO is called prompt NO as this way of NO formation occurs mainly in regions near the flame zone. The mechanism of prompt NO formation was postulated by C.P. Fenimore (hence the alternative name Fenimore NO) and is more complicated than the thermal NO mechanism. Prompt NO formation in hydrocarbon flames is initiated by the rapid reaction of hydrocarbon radicals with N_2 resulting in amines or cyano-compounds that react further to form NO [22, 24]. Although it is not fully understood which hydrocarbon is responsible for prompt NO, it is expected that CH is a major contributor. Since CH is present only at the flame front [22], this would imply that also the prompt NO formation is confined to the flame front, in contrast with the thermal NO. CH reacts with N_2 forming metastable $(HCN_2)^*$ which subsequently forms hydrocyanic acid (HCN) and N-atoms,



with an effective rate constant k_4^+ that is given in table 1.2. Both the N-atom and the CN-radical, formed by thermal decomposition of HCN, react with O-atoms and OH-radicals to form NO via several complex pathways [22].

Fuel-rich conditions favour prompt NO formation because C_2H_2 , a precursor of the CH-radical, is abundantly present, but only little prompt NO is formed at equivalence ratios above 1.8 [22]. The rate-limiting step in prompt NO formation is the formation of HCN. However, the activation energy of this reaction is much lower (about 92 kJ/mol) than the activation energy (319 kJ/mol) of the reactions producing thermal NO. Therefore, in contrast to thermal NO, prompt NO is also formed at relatively low temperatures (down to about 1000 K). For the diesel engine prompt NO formation should occur during the premixed burn, which is fuel-rich, or in the flame front of the diffusion flame. It is also possible that during the premixed combustion only HCN is formed that will be converted to NO at a later time in the combustion.

1.4.3 NO generated via nitrous oxide

Formation of NO via N_2O (nitrous oxide) starts with a reaction analogous to the first reaction of the thermal NO mechanism, in which an O-atom reacts with molecular nitrogen. However, as was first postulated by Wolfrum [26], the product of this reaction may be N_2O if a third molecule M is present to stabilise the collision complex,



The rate constants for the forward and backward reactions, k_5^+ and k_5^- respectively, are given in table 1.2. This reaction has a low activation energy (76 kJ/mol) and becomes more important at higher pressures because it is a three-body reaction. Subsequently, the N_2O may react with O-atoms to form NO,



with a rate constant k_6^+ also given in table 1.2. The NO formation rate can be written as [26]

$$\frac{d[NO]}{dt} = k_g [O][N_2], \quad (1.9)$$

where k_g is an effective rate constant that increases at higher pressures and that, at temperatures below 1700 K, is larger than the rate constant that determines the thermal NO formation [26] (at higher temperatures it approaches the thermal formation rate). Because reaction 1.7 has a smaller temperature dependence than reaction 1.2 from the Zeldovich mechanism, the N_2O mechanism becomes a significant contributor at low temperatures, where the formation of thermal NO is suppressed, and under lean conditions, where the formation of CH is suppressed leading to less prompt NO. Therefore, under circumstances of lean premixed combustion at high pressure and low temperature NO generated via N_2O is an important pathway.

1.4.4 NO production from fuel nitrogen

The nitrogen chemically bound in the fuel (fuel-bound nitrogen) is another source in the formation of NO by combustion of fossil fuels. It is most important in coal combustion, because coal contains about 0.5-2.0 mass-% [22] chemically bound nitrogen, whereas liquid fuel typically contains 0.07 mass-% [2]. During combustion the fuel nitrogen, that can exist as amines and ring compounds (*e.g.* pyridine), is converted, usually quite fast, to precursors of NO. The most important nitrogen-containing species are ammonia (NH_3) and hydrocyanic acid (HCN), the latter is also being formed in the prompt NO mechanism. These compounds oxidise, usually rapidly, to NO via several complex reaction pathways [22].

The conversion of fuel nitrogen to NO is strongly dependent on the initial amount of nitrogen in the fuel/air mixture and on the stoichiometry of the mixture. Relatively high conversion ratios are found for lean and stoichiometric mixtures whereas the conversion ratios are lower for rich mixtures. They are only weakly dependent on temperature, in contrast to the strong temperature dependence of thermal NO. Although diesel fuel can contain some nitrogen, this fuel-bound nitrogen will not contribute significantly to the total amount of NO that is formed [2].

1.4.5 Formation of NO_2

At typical flame temperatures the NO_2/NO ratios should be small considering chemical equilibrium, but in diesel engines the ratio can be higher. This NO_2 is assumed to result from the reaction of NO with HO_2 [2, 22],



Significant HO_2 concentrations are found in the lower-temperature regions of the flame and can react with NO that is transported by diffusion from the high temperature regions to the low temperature regions. NO_2 conversion back to NO may occur via



The rate constants of these reactions are also given in table 1.2. The reactions removing NO_2 are fast and NO_2 will convert back rapidly to NO if high radical concentrations are present. However, if the NO_2 formed in the flame is mixed with colder gases, these last reactions will not take place due to a decrease in the radical concentrations. This is the reason why relatively high NO_2/NO ratios are found in light load diesel engines where cooler regions, that inhibit the conversion back to NO, are more abundant [27].

1.5 Formation and oxidation of soot

The formation of soot during combustion is the result of an incomplete combustion of the hydrocarbons in the fuel, which occurs under conditions of local oxygen deficiency. It is an extremely complicated process in which a sort of gaseous-solid phase transition takes place where the final solid phase (*i.e.* the soot) exhibits no unique chemical or physical structure [28]. Soot formation comprises chemically and physically different processes like the formation and growth of large aromatic hydrocarbons and their transition to so-called primary particles, the coagulation of these small species into larger particles, and the growth of solid particles due to attachment of gas-phase species to the surface. Most of the information about soot formation is obtained from measurements in simple premixed flames, shock tubes and combustion bombs. Although a model that gives a general description of the soot formation process in all different combustion environments is not yet available, some models exist for specific aspects and combustion processes [2, 24, 28, 29]. Below, only a short overview of one possible soot formation process is given, and some aspects, important for the specific case of diesel combustion, are summarised.

In diesel engines soot particles are expected to form during a few milliseconds from fuel hydrocarbons in the temperature range of 1300–2800 K and at pressures between 50 and 100 bars [2]. Since these temperatures are above those of the in-cylinder air before combustion, heat from the combustion is required to initiate the soot formation process. This multi-step process probably starts with the hydrocarbons in the fuel breaking up into small hydrocarbon radicals. These radicals form small hydrocarbons which react to larger ones, of which the polycyclic aromatic hydrocarbons (PAHs) are an important group, as they are the most important precursors of soot. An important channel in the formation of PAHs starts with the formation of acetylene, C_2H_2 , from hydrocarbon radicals. The C_2H_2 reacts with CH or CH_2 to C_3H_3 , pairs of which can form the first ring, benzene C_6H_6 . Subsequently, the molecule grows by further reactions with C_2H_2 to a large PAH. Coagulation of larger PAH molecules initiates growth in the third dimension, and the first very small particles are formed, often called nuclei, with a diameter of about 2 nm. This way a large number of very small particles, that are the precursors of the later formed soot, may be produced.

The bulk of the soot is formed as a result of particle growth which, during the early stages, occurs due to both coagulation, where particles collide and coalesce, and surface growth, which occurs by gas phase species attaching to the surface. Surface growth reactions lead to an increase in the soot volume fraction but does not change the number of particles, whereas by coagulation the number of particles decreases and the soot volume fraction remains constant. If the individual particles are still small both processes will result in particles of approximately spherical shape. These processes of particle growth result in primary soot particles, called spherules, containing some 10^5 carbon atoms at a H/C ratio of about 0.1 and a typical diameter between 20 and 30 nm. If surface growth has stopped, coagulation of spherules continues and as many as a few thousand of these spherules may agglomerate into clusters or chains forming soot particles with a typical diameter between 100 and 150 nm [2].

Besides soot formation, during all phases of the formation process soot oxidation occurs as well. Soot particles or soot precursors are destroyed due to oxidation by species as O_2 , O or OH in or near the flame. A large fraction of the soot formed is oxidised within the cylinder before the exhaust opens. The final emission of soot from the engine depends, of course, on both formation and oxidation rates.

Chapter 2

Laser-based diagnostics in a diesel engine

Abstract

The optically accessible two-stroke diesel engine, which the experiments are performed on, is described, as well as its characteristics and the optical setups. The optical techniques used to study the NO formation inside the cylinder of the engine are explained, including a discussion about the effects of Rotational Energy Transfer (RET) on the obtained NO Laser Induced Fluorescence (LIF) signals. To derive a temperature of the glowing soot particles the spontaneous flame emission is used. In addition, two dimensional images of the flame emission, showing the flame development during the stroke, are presented. The chapter ends with a discussion about the NO spectroscopy in the diesel engine. Excitation/emission spectra recorded from a flame and from the running engine are given. They show the interference of NO and O₂ fluorescence and can be used to select wavelengths suitable for the excitation and detection of NO inside the combustion chamber. Finally, examples of dispersed fluorescence spectra recorded from the running engine are shown.

2.1 Introduction

Powerful lasers in combination with fast intensified detection systems are widely used to study the physical and chemical processes occurring during combustion. Laser-based optical diagnostics can be highly selective, sensitive and non-intrusive. They allow spatially and temporally resolved detection of specific chemical species and quantum states (a requirement for the determination of a temperature) within complex, reactive, turbulent environments [30–33]. The results of these spectroscopic techniques give information about the distributions of various important parameters such as gas composition, temperature and density.

For the specific case of diesel combustion, laser-based diagnostics allow to obtain information about (almost) all aspects of the combustion process, from autoignition to pollutant formation. By combining results obtained simultaneously using several different techniques, relations can be established between different features of the combustion. During the last decade, laser-based optical diagnostics have been applied by several research groups to obtain such information under more or less realistic combustion conditions and in a variety of optically accessible engines (both diesel and spark-ignition (SI) engines) [7–18, 34–54]. The major experimental problem in using laser diagnostics in optically accessible engines is the soot that reduces optical transparency due to both window fouling and attenuation of the laser intensity within the combustion chamber. Therefore, in almost all experiments a substitute or low-sooting fuel was used to reduce the soot formation and, therefore, to increase the optical transparency. Furthermore, in some experiments extra oxygen was added to the intake air, which can reduce the soot production drastically, but at the same time increases the NO production. It should also be noticed that in most of the experiments, the optically accessible engine was operated in skip-fired mode (*i.e.* firing only every n^{th} cycle) in order to reduce the temperature of the cylinder. The most commonly used laser techniques are Laser Induced Fluorescence (LIF), Laser Induced Scattering (LIS) (*i.e.* Rayleigh/Mie scattering), Laser Induced Incandescence (LII), and Raman scattering. Detection of the chemiluminescence and the natural flame emission (including the two colour method) should be mentioned as well, since, although they are not laser-based, these techniques are often used to obtain additional information necessary to characterise the combustion process.

Below, the different techniques and their specific applications are mentioned shortly and some references to literature are given. As the objective of this work is the visualisation of NO densities using the LIF technique some more attention will be given to this specific case.

Among the manifold of optical techniques the LIF technique has the sensitivity to provide temporally and spatially resolved information about specific molecules present in combustion processes. The LIF technique is a two-step process involving electronic excitation by laser radiation followed by detection of the ensuing fluorescence. It is widely used to obtain in-cylinder NO density distributions from optically accessible engines [17, 34–41].

Andresen *et al.* [35] showed that it is possible to detect NO molecules inside an optically accessible engine by the LIF technique, using an excitation wavelength of 193 nm to excite the NO molecules, like it was done in atmospheric flames before. Dispersed fluorescence spectra of NO were presented, as well as NO fluorescence distributions recorded from a SI engine running on iso-heptane (C_8H_{18}). However, NO fluorescence could only be seen around BDC (1 bar) as at higher pressures the intensity of the laser beam was too much attenuated.

NO fluorescence distributions at higher pressures (5 and 10 bars), averaged over 30 en-

gine cycles and also recorded using 193 nm excitation, were presented by Arnold *et al.* [36]. The distributions were obtained from a transparent DI passenger car diesel engine, running on *n*-heptane to keep the engine optically transparent. It was mentioned that for a quantitative analysis of the fluorescence signal the effects of pressure should be taken into account.

Alataş *et al.* [37] succeeded in measuring NO fluorescence distributions throughout almost the whole engine cycle using 226 nm excitation of NO. However, a 50/50 mixture of iso-octane and *n*-tetradecane was used as fuel and the DI diesel engine, with a square combustion chamber, was a research engine running in skip-fired mode in order to reduce soot production. In addition, oxygen-enriched intake air (30%) had to be used to increase the NO concentration and to reduce the soot concentration even more. Although the start of the NO formation could not be resolved and the results were not processed for changing pressure, temperature and laser intensity during the stroke it was concluded that NO formation starts early during the combustion and stops not later than 40 degrees crank angle. Furthermore, it was concluded that the greatest problem in acquiring the NO images is the attenuation of the laser radiation.

The LIF imaging technique, using 193 nm laser radiation to excite the NO molecules, was applied for the first time to an optically accessible IDI diesel engine running on commercial diesel fuel by Brugman *et al.* [34, 38]. To keep the engine transparent, oxygen was added to the intake air (20%), and a special UV transparent, chemically inert lubricant was used. NO fluorescence images, averaged over 50 engine cycles, and excitation spectra up to pressures of about 5 bars as a function of load and crank angle were reported. NO fluorescence images could not be obtained at higher pressures (*i.e.* smaller crank angles) because the windows were blocked by the piston. Additionally, curves of the total amount of NO in the engine, obtained by integrating the signal of the images, were presented. Both the fluorescence images and the NO curves were processed for the change in laser intensity. In order to obtain semi-quantitative information about the amount of NO present in the cylinder effects of the changing pressure and temperature during the stroke were also taken into account.

Nakagawa *et al.* [39] applied the LIF technique to a single jet DI diesel engine running on a mixed fuel (50/50 iso-octane/*n*-tetradecane and 40/60 ethylalcohol/*n*-dodecane mixtures) in skip-fired mode. Reported were NO fluorescence images, averaged over five laser shots and using 226 nm excitation, that showed the location of NO relative to the reacting fuel jet, but the start and end of the NO formation could not be determined. However, to obtain these results significant oxygen enrichment of the intake air (between 21 and 35%) was required to reduce the soot production and enhance the NO signal. The results were not processed for changing pressure, temperature and mixing. Moreover, no spectroscopic evidence was presented for the absence of O₂ fluorescence in the images.

The most recent paper by Dec and Canaan [17] presented temporally and spatially resolved NO distributions from a DI diesel engine recorded by single-shot LIF imaging in which NO molecules were excited at 226 nm. Here, a low-sooting fuel was used and the engine was operated skip-fired. Additionally, a curve of the total amount of NO in the combustion chamber was given, obtained by integrating the NO fluorescence signal over a representative sector of the combustion chamber. In order to determine the total in-cylinder NO content the fluorescence signal was corrected for the effects of the changing pressure, temperature and mixing during the stroke. However, no corrections were made for the attenuation of the laser intensity or induced fluorescence on its way through the combustion chamber as the authors claim that it can be neglected. The results showed that NO formation does not start during the premixed

burn (which is fuel-rich), but begins around the periphery of the fuel jet just after the diffusion flame forms. During the burn-out phase NO remains along the track of the fuel jet and the NO formation continues in the hot post-combustion gases, after the diffusion flame has gone out.

Besides NO distributions OH radical distributions in diesel combustion are obtained using the LIF technique as well [15, 35, 36, 39, 43]. These distributions give information about the location of the diffusion flame. During diesel combustion the OH radicals are mainly present in a narrow region at the flame front (the reaction zone) because three body recombination reactions that reduce the high flame front OH concentrations to equilibrium levels occur rapidly at diesel engine pressures. It was found that the diffusion flame is located around the periphery of the jet [15].

Detection of the natural flame luminosity, LIS and LII, are commonly used techniques for the visualisation of soot in diesel flames [7, 11, 12, 14, 43–46]. The natural flame luminosity is generally accepted to arise from glowing soot particles (except perhaps during the very early stage of combustion; see *e.g.* [13]). Its spatial distribution and (spectral) intensity therefore provide an experimentally straightforward, albeit not necessarily easily interpretable, way of learning something about the soot production. The LIS technique detects the radiation of the laser beam that is elastically scattered by the soot particles (and, in fact, by any other kind of particles as well). The principle of the LII technique is based on the detection of the radiation emitted by soot particles that are rapidly heated by the absorption of laser light from a high-power laser. These techniques (or combinations of them) provide information about the distribution of soot particles and of various aspects of soot including particle sizes, number densities, and soot volume fractions during the whole combustion process.

In addition, laser induced Rayleigh scattering allows the investigation of the liquid and vapour phases of the diesel jet. It can be used to obtain the structure of the liquid diesel fuel spray, as well as to obtain quantitative distributions of the fuel vapour concentration during the diesel combustion process [8, 9, 47, 48]. The fuel/air ratio at a single point in the spray region of an evaporating diesel spray is also determined by the use of instantaneous multi-species Raman scattering [49]. This technique uses an imaging spectrometer to detect simultaneously the relative intensities of Raman scattered signals from a (substitute) fuel molecule ($C_{16}H_{32}$) and nitrogen (N_2).

The two colour method, which is not laser-based, can be used to determine soot concentrations and temperatures [33, 50–54]. In this method the thermal radiation at two different wavelengths is detected and the flame temperature or soot concentration is determined from the ratio of their intensities. Another technique that is not laser-based but needs an intensified fast detection system is the detection of the chemiluminescence which provides information about the autoignition. Here, the early, relatively weak natural light emitted by molecules (OH, C_2 , CH) that are excited by exothermic chemical reactions that are specific for the initial combustion is detected [13, 18].

2.2 Experimental setup

2.2.1 The engine

Measurements were performed on a one-cylinder, two-stroke, direct injection (DI) diesel engine (Sachs). The engine was modified quite considerably, as described below, in order to provide full optical access during the whole cycle. As a result, it may not be very representative for typical production engines, but it is well suited for the evaluation of laser diagnostics, one of the aims of the present work. The modified engine is schematically shown in figure 2.1 and its specifications are given in table 2.1.

Optical access to the combustion chamber is obtained by replacing the original cylinder

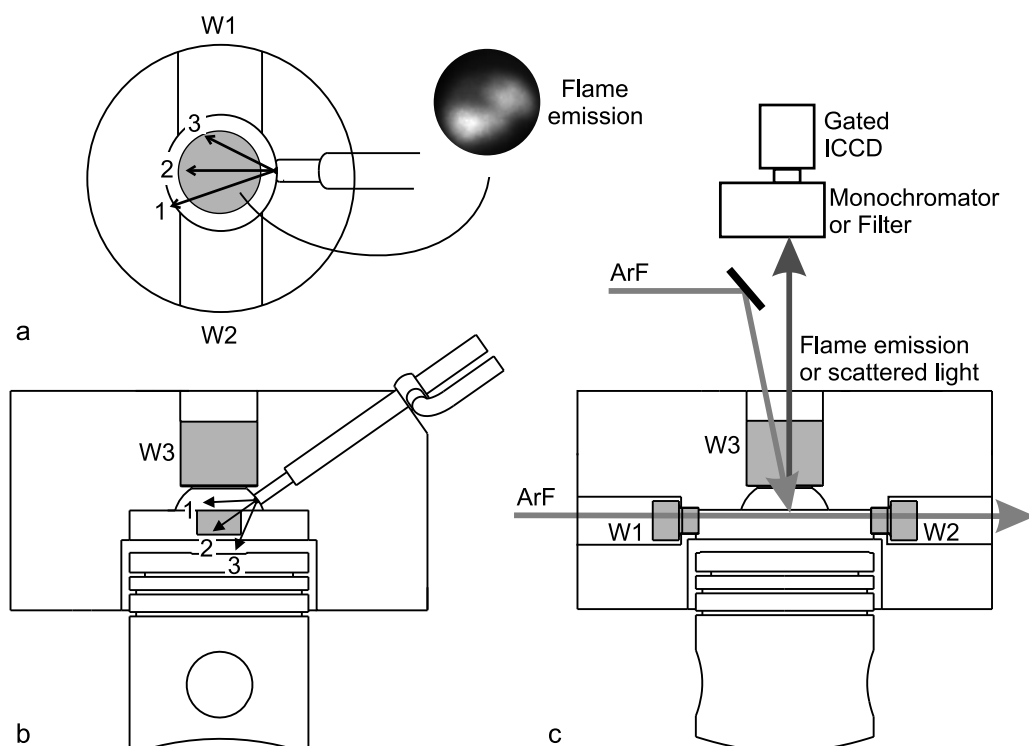


Figure 2.1: Schematic view of the modified two-stroke diesel engine and the optical setup. The engine is optically accessible by the two windows in the side wall (side windows, W1 and W2) and the window in the top of the cylinder head (top window, W3). a) Top view of the engine showing the top window, the piston and the location of the injector. The spray directions of the three sprays are indicated (arrows 1-3). Also shown is an image of the natural flame emission. b) Side view of the two-stroke engine showing the position of the injector at an angle of 35 degrees with respect to the piston surface and the directions of the three sprays. c) The ArF excimer laser beam enters the combustion chamber through the top window (W3) or traverses the combustion chamber through the side windows (W1 and W2). The induced fluorescence is detected through the top window by a gated, intensified CCD camera, positioned behind either a filter (for imaging) or a monochromator (for dispersed fluorescence). Natural flame emission images are recorded through the top window using the CCD camera in kinetics mode and without a filter.

Engine Make	Sachs
Engine Type	Two-stroke, One-cylinder, DI diesel
Bore	81.5 mm
Stroke (effective)	80 mm (55 mm)
Cylinder capacity (effective)	412 cc (308 cc)
Fuel injection	direct, 3 hole injector
Exhaust port opening	105° aTDC
Intake port opening	121° aTDC

Table 2.1: Specifications of the modified engine.

head by a new water-cooled cylinder head in which quartz windows are mounted. The quartz used is Suprasil I, of which a piece of 25 mm thickness has an internal transmission of about 75% for 193 nm radiation. Because a two-stroke engine has no in- and outlet valves a window (diameter 25 mm; thickness 35 mm) could be mounted centrally in the top of the cylinder head (top window; W3 in figure 2.1). Through this cylindrical top window the central 25 mm of the combustion chamber can be seen. The top window could be replaced by a pressure transducer (AVL QC32) for time-resolved in-cylinder total pressure measurements. Two other windows are rectangular (clear aperture $25 \times 10 \text{ mm}^2$; thickness 25 mm) and are mounted in the side wall of the cylinder head (side windows; W1 and W2 in figure 2.1). These side windows are placed diametrically in such a way that a laser beam can enter the combustion chamber through one of them and leave it through the other one. Because of the high pressure and temperature that are reached during the combustion the mounting of the windows has caused some problems. Windows broke as a result of high local stress and seals were burned away. However, after several trials these problems were solved. The opening hole for the top window in the cylinder head has a diameter of 25 mm, whereas the top window itself has a diameter of 35 mm, which gives the possibility to use a seal of 5 mm width between the window and the cylinder head. Because this broad seal reduces the surface stress, a relatively hard annealed copper seal, which

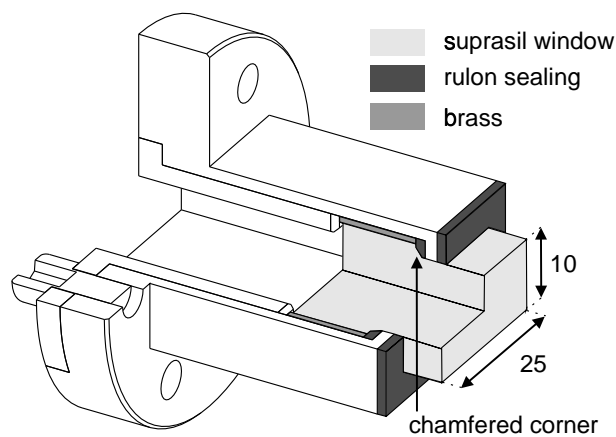


Figure 2.2: Mounting of the side windows.

is not burned away (like polymer seals), is used. The design of the mounting of the side windows is shown in figure 2.2. To strengthen the side windows the corners are chamfered and flame polished. They are packed in brass and mounted in separate holders, which are mounted in the cylinder head. This construction provides the possibility to take out the side windows easily for cleaning. The sealings between the windows and the holder, and between the holder and the head are made of rulon. Because the temperature at the position of the side windows is not as high as it is at the position of the top window, the rulon does not burn away.

A modified piston with a slot of 0.5 mm depth and 25 mm width in its upper surface is used. This slot allows the laser beam to traverse the combustion chamber during the whole engine cycle, even if the piston is in its uppermost position (0° degrees crank angle, defined as Top Dead Centre (TDC)).

As the top window is mounted at the original position of the fuel injector, fuel is injected through a specially designed three hole injector which is placed in the cylinder head at an angle of 35 degrees with respect to the piston upper surface, as shown in figure 2.1b. The middle one of the three sprays is directed in line with the injector. The other two sprays are in the same plane at an angle of 35 degrees in outward direction with respect to the middle spray. The injector is rotated 30 degrees around the injector axis with respect to a vertical plane containing the injector axis, in order to avoid that one of the sprays (number 3 in figure 2.1) would hit the laser beam entrance window (W1). However, the laser beam exit window is hit directly by one of the other sprays (number 1 in figure 2.1). As a result, when using side window illumination (see section 2.2.3), the laser beam passes over the spray in the first-encountered half of the cylinder (spray number 3 in figure 2.1) and passes through the spray region in the second half. Fuel injection starts at 27° bTDC with an injection pressure of 170 bars. The original scavenging ports are closed in order to avoid that soot particles present in the crank case can flow into the measurement volume where they would strongly attenuate the laser beam. The fresh air required for the combustion is added through a new inlet from outside. A small overpressure of about 0.2 bars is used to improve scavenging. In this modified situation the exhaust opens at 105° aTDC and the inlet at 121° aTDC. Because conventional lubricant oil is not UV transparent an alternative, chemically inert, UV transparent oil (Fomblin Y25, Ausimont S.P.A.) is used. An electric water-cooled brake (Zollner & Co) is connected to the flywheel of the engine and provides various load conditions.

In spite of all modifications the engine can be operated in steady-state (*i.e.* not skip-fired)

Engine speed	1200 rpm
Injection timing	27° bTDC
Intake air pressure	1.2 bars (absolute)
Intake air temperature	320 K (estimated)
Compression ratio	12.4 - 14.4
Load	0.44 - 0.88 kW
Fuel	Standard commercial diesel fuel (2 types, numbered 1 and 2; see table 2.3)

Table 2.2: Operating conditions of the modified engine.

at 1200 rpm (20 Hz; one degree crank angle correspondes to 139 μ s) at standard commercial diesel fuel for 20 minutes. Window fouling turned out to be relatively unimportant. The top window (W3) is burned clear by the combustion itself (although it became slightly dull in the long run), whereas the side window (W1) used to couple in the laser beam is kept clear by ablation by the excimer laser beam. The laser beam exit window (W2), however, becomes black by soot because it is hit directly by one of the sprays and the laser intensity left at this window is not high enough to clean it by ablation.

Since, the lubricating qualities of the oil are not so good, the engine is operated only at low load varying between 0.44 kW and 0.88 kW, to reduce wear. As a result of the modifications to allow optical access the compression ratio, varying between 12.4 and 14.4, is lower than for typical diesel engines. For the measurements the engine is operated on two different diesel fuels at various loads and compression ratios which are summarised in table 2.2. The two fuels selected are standard commercial automotive diesel fuels, meeting the European EN590 specification. Details of the test fuels are given in table 2.3. The main differences between them are that fuel 2 has a narrower distillation, lower T95, lower sulphur content, and higher cetane number than fuel 1. Most experiments are performed at the same operating conditions. If it is not mentioned explicitly the engine is running with a compression ratio of 13.4 on diesel fuel 2 and loaded by 0.44 kW. Only in the experiments performed to study the effects of fuel, compression ratio and load on the NO production (chapter 4) these parameters are varied.

<i>Fuel Code</i>	<i>Fuel 1</i>	<i>Fuel 2</i>
Density (g/ml)	0.8242	0.8233
Distillation ($^{\circ}$ C)		
IBP [†]	166	184
T10	194	215
T50	235	250
T90	326	292
T95	347	309
FBP [‡]	364	327
Sulphur (%m/m)	0.16	0.02
Cetane Number	47.1	53.2
Aromatics HPLC (%m/m)		
1-ring	15.1	14.0
2-ring	2.9	2.6
3-ring	0.7	0.2
Total	18.7	16.8
Viscosity (cSt at 40 $^{\circ}$ C)	2.04	2.25

[†] IBP = Initial Boiling Point

[‡] FBP = Final Boiling Point

Table 2.3: Details of the commercial diesel fuels used in the experiments.

2.2.2 Engine characteristics

To characterise the modified engine it is necessary to obtain some information about the engine parameters at different engine conditions. The in-cylinder pressure of the engine as a function of time is measured using a water-cooled pressure transducer (AVL QC32). The output of this transducer is sent to a charge amplifier whose output is averaged over 100 engine cycles by a digital oscilloscope (Le Croy 9361).

As an example the pressure curve of the motored (non-firing) engine, reaching a pressure of 42 bars at TDC, is given in figure 2.3a (solid curve). This corresponds to a compression ratio of 14.4, which can be calculated on the assumption that the cylinder contents behave as an ideal gas and using the ideal gas law for adiabatic expansion ($PV^\gamma = C$, $\gamma = 1.4$). The ideal gas model ($PV \propto T$) can also be used to derive a temperature curve from the pressure curve. The temperature curve, that is obtained on the assumption of a mean gas temperature of 320 K as the exhaust closes, is given in figure 2.3b (solid curve). It shows a maximum temperature of about 850 K at TDC.

The in-cylinder pressure curve of the firing engine running on diesel fuel 1 and loaded by 0.44 kW is given in figure 2.4a (solid curve). A maximum pressure of 76 bars is reached at 1° aTDC. At 105° aTDC, as the exhaust opens, the pressure is 2 bars. The derivative of the pressure curve with respect to the crank angle, $dP/d\Theta$ (*i.e.* the change in pressure per degree

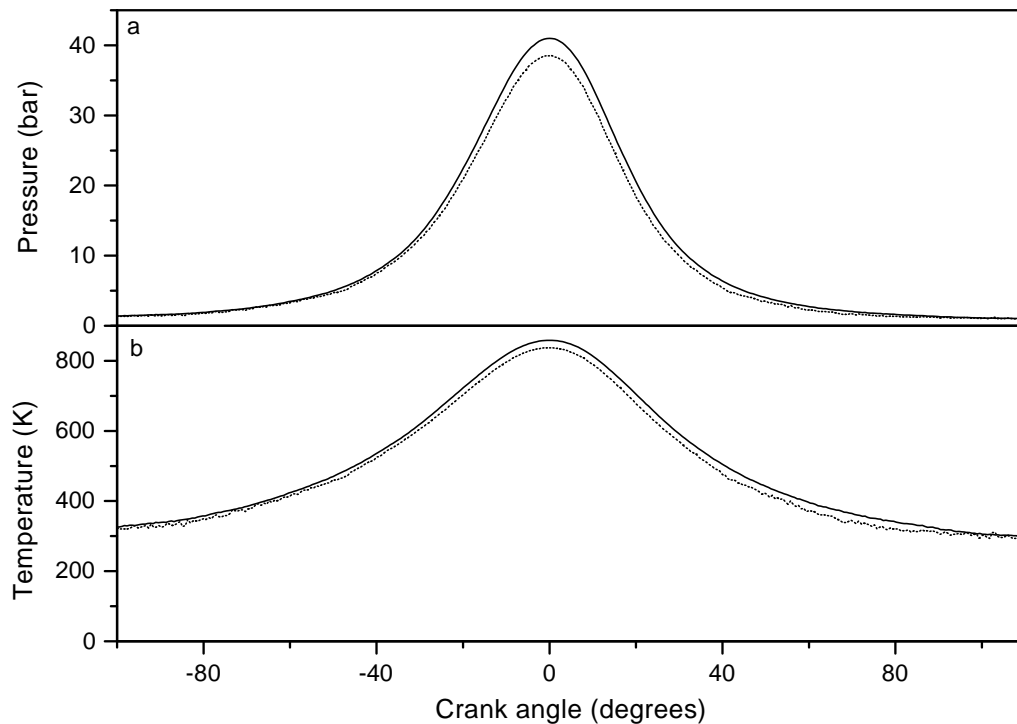


Figure 2.3: Parameters of the motored (non-firing) engine with a compression ratio of 14.4 (solid curves) and 13.4 (dotted curves). a) Pressure, b) Temperature calculated by using the ideal gas law.

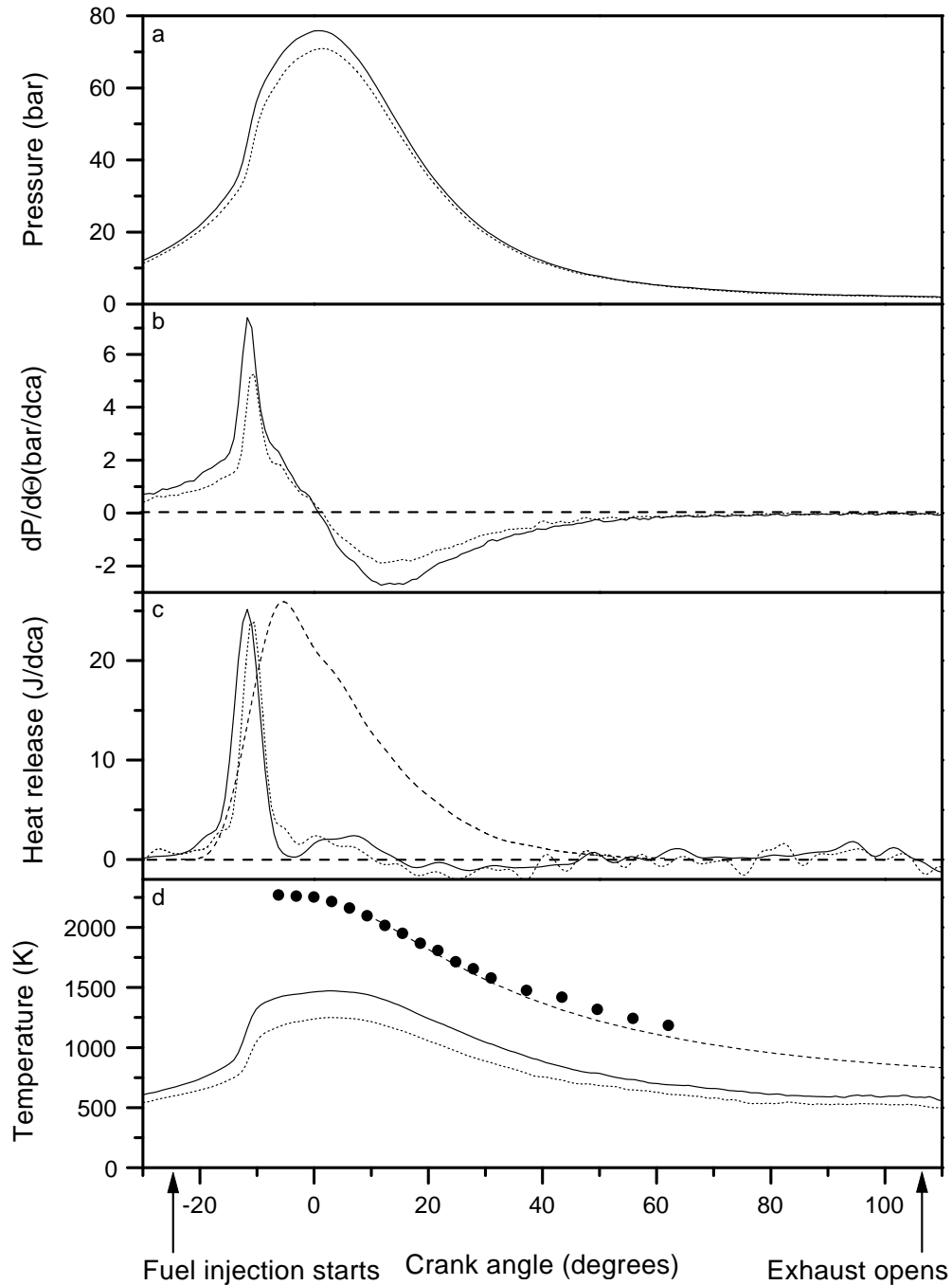


Figure 2.4: Parameters of the modified diesel engine running steadily on diesel fuel 1 loaded by 0.44 kW, at a compression ratio of 14.4 (solid curves) or 13.4 (dotted curves). a) Pressure, b) Derivative of the pressure with respect to crank angle, c) Heat release (solid and dotted curves). Integrated intensity (arb. units) of the natural flame emission (dashed curve). d) Mean gas temperature derived from the heat release (solid and dotted curves). Soot temperature derived from the spectrum of the natural flame emission (●). The dashed curve is an extrapolation based on adiabatic expansion of an ideal gas during the later part of the stroke, matched to the intermediate part of the measured data.

crank angle) is given in figure 2.4b (solid curve). The maximum rate of change in pressure is 7.4 bars/dca^1 , which is quite high. This indicates that at the start of the combustion much premixed fuel is present in the cylinder which starts burning at once. The rate of release of the chemical energy of the fuel (the rate of fuel burning) through the combustion process is called the heat release rate. The heat release rate can be calculated from the pressure curve, its derivative and the volume curve using the laws of thermodynamics on the assumption of an ideal gas inside the cylinder and neglecting crevice flows [2]. The calculated heat release is given in figure 2.4c (solid curve); the total heat released amounts to 180 J per cycle. Combustion starts around 15° bTDC as can be seen from the sudden rise of the pressure curve to above the motored engine level. Also, the derivative of the pressure curve, $dP/d\Theta$, shows a spike at this position. Natural flame emission can be observed till around 60° aTDC. The integrated intensity of the observed flame emission is included in figure 2.4c (dashed curve). Evidently, the visible combustion continues long after the main contribution to the heat release. The average temperature of the gas inside the whole cylinder can be derived from the heat release curve. The mean gas temperature curve that is obtained on the assumption of an air temperature of 320 K at the moment the exhaust port closes is given in figure 2.4d (solid curve). Till the combustion starts at 15° bTDC the mean gas temperature follows the temperature curve of the motored engine. As the combustion starts the temperature in the firing engine rises suddenly. It reaches a maximum of 1470 K a few degrees after TDC. As the exhaust opens the temperature has dropped to 580 K.

If the engine conditions change the characteristics of the engine also change. To get an impression of the change in the parameters if the compression ratio is lowered to 13.4, the parameters for this case are also given in figure 2.3 and figure 2.4 (dotted curves). In agreement with the lower compression ratio of 13.4 the maximum pressure for the motored engine is 38 bars. The maximum pressure in the firing engine is also lower, 71 bars, which results in lower values for the derivative of the pressure, the heat release and the mean gas temperature. As a result of the lower pressure and temperature, combustion is seen to start around 1 degree crank angle later. The engine characteristics also change if a higher or lower load is applied. A higher load gives a higher peak pressure whereas a lower load lowers the peak pressure. The other parameters show a similar behaviour. Changing the fuel does not significantly change the parameters of the engine.

The shapes of the pressure curve, its derivative and the heat release indicate that the engine conditions are far from optimal. The pressure change per degree crank angle is high at the start of the combustion due to a large amount of premixed fuel that burns in a very short time. The pressure curve shows a maximum close to TDC. This results in a heat release rate that shows a relatively large contribution from the premixed combustion and little diffusion burning. However, at normal operating conditions (high load, high speed) the engine wear would increase dramatically caused by the use of the alternative lubricant. In the experiments the load and engine speed are kept low and the injection timing is advanced, resulting in a larger amount of premixed fuel and a higher peak pressure and temperature.

¹dca = degree crank angle.

2.2.3 Optical setup

The laser used in most of the experiments is a pulsed tunable excimer laser consisting of two laser tubes in an oscillator-amplifier configuration (Compex 350T; Λ -Physik). The output of this laser, operated on ArF, is tunable between 192.9 nm and 193.9 nm and has a linewidth of 1 cm^{-1} . The laser delivers a beam with a rectangular cross section ($25 \times 3 \text{ mm}^2$) in 20 ns pulses with an energy of maximally 350 mJ at the laser exit. Calibration of the laser radiation wavelength is achieved by monitoring the induced fluorescence from NO in an oxy-acetylene flame [55].

Depending on the measurements the laser beam is coupled into the engine through the top window (W3) or through one of the side windows (W1), as schematically indicated in figure 2.1c. If the side windows are used the laser beam is focussed down to a thin sheet of about 0.1 mm thickness which traverses the combustion chamber parallel to the piston upper surface; it is located within the slot when the piston is at TDC (*i.e.* 12 mm below the top window). The laser illuminates the whole area beneath the top window resulting in a measurement area of nominally $25 \times 0.1 \text{ mm}^2$ (diameter \times thickness; in practice this will be larger due to scattering of laser light within the cylinder and a somewhat diffuse inside surface of the entrance window).

Scattered laser radiation is always detected through the top window by a gated CCD camera (576×384 pixels) equipped with an image intensifier (ICCD-576G/RB-E; Princeton Instruments) and a quartz $f/4.5$ 105 mm objective (Nikon). The camera output is digitised by a controller (ST-138; Princeton Instruments) and sent to a computer for further processing. For imaging the laser sheet is coupled into the engine through the side window, so that the fluorescence is detected in a direction perpendicular to the laser sheet by the CCD camera placed behind a filter to single out the wavelength of interest. This results in an image that contains spatial information of the plane of interest as shown in figure 2.5a. The camera may also be mounted directly behind an imaging monochromator (1200 gr/mm holographic grating blazed at 250 nm (Chromex 250i)), at the position of the exit slit, as part of an Optical Multichannel

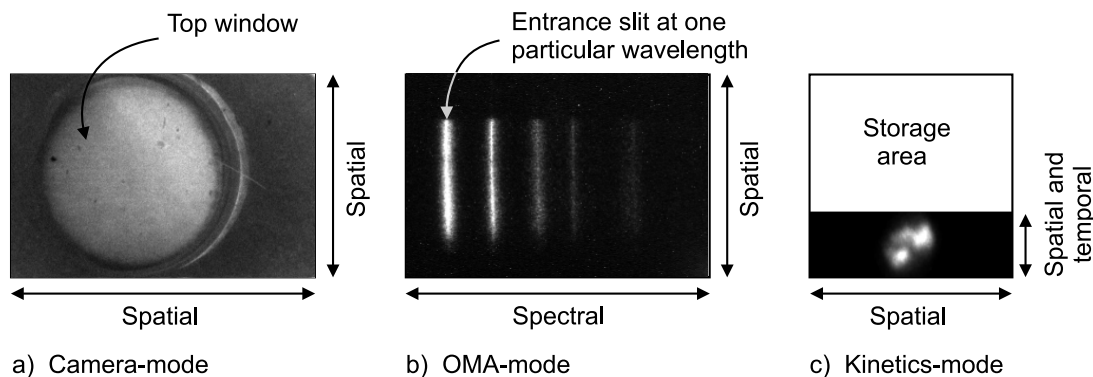


Figure 2.5: Comparison of the three modes in which the CCD camera is used. a) Camera-mode resulting in images containing spatial information in two directions; b) OMA-mode resulting in images that contain spatial information only in the direction along the slit and spectral information along the other axis; c) Kinetics-mode resulting in a series of images obtained at very short time intervals during one stroke.

Analyzer (OMA) setup, to spectrally disperse the fluorescence. In this way the camera records images that contain spatial information only in the direction along the slit while spectral information is obtained along the other axis as shown in figure 2.5b. A dispersed fluorescence spectrum can be obtained from this image by integrating the intensity in the direction along the slit. This way of detection is mainly used in combination with the setup in which the laser beam is coupled into the engine through the top window. The laser and camera system are synchronised to the position of the piston with an accuracy of 0.6 degree crank angle.

The advantage of the side window setup is that spatial distributions of NO can be observed. But, because the laser beam has to travel 25 mm before it enters the observation area it is already strongly attenuated due to absorption by and scattering off droplets and soot particles present in the combustion chamber. This problem of attenuation of the laser beam is partly circumvented by coupling in the laser beam through the top window, so that it enters the combustion chamber directly in the observation area. A disadvantage, however, is that part of the spatial resolution is lost, as fluorescence is now obtained from the whole volume that is illuminated by the laser beam integrated in vertical direction (that is, along the line of sight of the detector). The vertical extent of the probe volume depends on the penetration depth of the laser radiation, which is determined by the density of the scattering particles and/or the position of the piston. Also, the intensity of the back-scattered radiation from the window becomes a matter of concern, as fluorescence is detected in a nearly backward direction. To suppress the contribution of this back-reflected radiation a normal incidence 193 nm mirror is mounted in front of the collection optics. This mirror suppresses the contribution of the 193 nm radiation by three orders of magnitude and transmits all radiation above 203 nm.

During the measurements images or dispersed fluorescence spectra are generally averaged over several engine cycles. Due to averaging the signal to noise ratio is increased and cycle to cycle variations are averaged out. Therefore, the spectra represent an average density of NO and the images contain information about average distributions in which the gradients and boundaries between components are smeared out. Since the average information is found to reproduce, images and spectra of measurements at different crank angles, recorded under the same engine conditions can be compared. In addition, relations between different quantities obtained in separate measurements can still be demonstrated. However, differences between the individual combustion cycles cannot be obtained using averaged data. To get cycle-resolved results single laser pulses have to be used. But, in that case results of different crank angles cannot be compared so easily as due to the irreproducibility of the combustion process the amount of NO and the distributions can vary every engine cycle. Therefore, to relate different quantities and aspects of the combustion process it would be necessary to measure them simultaneously if single laser pulses are used.

In order to follow the combustion process as a function of crank angle during one and the same stroke images or spectra have to be acquired very fast after each other. This requires a high repetition rate laser system as well as a fast detection system (or several lasers and cameras). For laser-based measurements this would require a laser that has a repetition rate of at least a factor 10 to 50 faster than the speed of the engine, which is not available at the moment. As a fast detection system for images an intensified CCD camera can be used in the so-called kinetics mode. To this end a CCD camera with a movable mask in front of the photocathode on the image intensifier is used (ICCD-512-T; Princeton Instruments) with a $f/3.5$ - $f/4.5$ 28-70 mm objective (Nikon). In kinetics mode, an image is projected on a narrow strip at one end

of the image intensifier and the rest of the intensifier is masked and used as a storage area, as shown in figure 2.5c. After recording an image the rows in the illuminated area are shifted to the masked part of the photocathode and a new image can be recorded in the exposed part. The time between the images is determined by the frequency that is used to open the gate again. However, the minimum time is determined by the number of rows in the unmasked area and the time required to shift a row (minimal $1.6 \mu\text{s}$ for this particular detection system). If, for example, 50 rows of the total of 512 rows are unmasked, 10 images can be acquired with a minimum time of $80 \mu\text{s}$ between the images. The camera in kinetics mode is used to obtain single shot images of the natural flame emission, which is also detected through the top window, at different crank angles during one stroke. This way the flame development during one stroke can be followed and differences between different strokes can be seen.

2.3 Optical diagnostics

To study the NO formation inside the cylinder of the two-stroke diesel engine mainly the LIF technique is applied. In addition, elastic scattering of the laser radiation is used to obtain information about the local intensity of the laser radiation in the running engine. The spontaneous emission of the flames (natural flame emission) is observed in order to get information about the flame structure and the temperature of the soot particles. Brief descriptions of the different optical techniques, with an emphasis on the aspects important for the investigation of the combustion process inside the two-stroke engine, will be given below. More extended descriptions can be found in the literature [30–33].

2.3.1 Spontaneous light emission

Just detecting the spontaneous light emission from the flame is probably the most straightforward optical technique to get some information about the combustion process. In diesel engines with highly sooting, luminous, non-transparent flames the spontaneous emission is dominated by the thermal black (or grey) body emission from incandescent soot particles that are heated to flame temperatures. This emission has a broad spectral distribution with an intensity that is a function of the temperature and the soot volume fraction [33].

However, it should be noted that besides this strong soot luminosity the spontaneous light emission also contains a relatively weak natural emission from gaseous combustion products (mainly OH, CH and C_2 radicals), due to a process called chemiluminescence [13, 18]. Chemiluminescence arises from combustion radicals, which are raised to an excited state by exothermic chemical reactions and then subsequently decay back to their ground state by emitting a photon. The wavelength of the photon is characteristic for the emitting molecule and as such it provides information about the chemical reactions that occur. Because chemiluminescence is produced directly by the exothermic reactions that play a role in the early combustion (*i.e.* before soot is formed) it gives information about the location (in both space and time) of the initial combustion (autoignition). Subsequent to the early combustion, soot formation is induced by the rising temperature and luminous soot appears. Although chemiluminescence continues to occur throughout the whole combustion process, the intense yellow-white emission from the incandescent soot particles completely dominates over the weaker chemiluminescence as soon

as soot formation has started (the emission from soot particles is about three orders of magnitude stronger than the early chemiluminescence [18]). It is important to realize that it is almost always soot emission that is detected experimentally, and since soot is formed only after the onset of the combustion, the moment of first visible soot luminosity does not indicate the ignition of the combustion.

By the use of a fast detector such as a gated CCD camera this spontaneous flame emission can be detected with both spatial and temporal resolutions. The obtained signal per pixel represents the integrated natural flame emission along the line of sight from a volume with a diameter determined by the magnification of the imaging optics used and a depth depending on the soot concentration. In the case of high soot concentrations only soot near the surface of the flame contributes to the flame emission whereas at lower soot concentrations also soot inside the flame contributes.

If the spontaneous light emission of the flame is dispersed in its different wavelength components, information is provided about the origin of the emission. In the case of the two-stroke engine, dispersing the emission results in a smooth, structureless spectrum dominated by the thermal grey body radiation from the incandescent soot particles. The wavelength dependence of the intensity of the emission depends on the temperature of the grey body. Therefore, the spectrum representing the thermal radiation as a function of wavelength can be used to derive a temperature of the glowing soot particles. It has been shown that if the soot particles are small this temperature is also a good measure for the flame temperature [56]. Note that by using the whole spectrum to determine the temperature the principle of the two colour method, which is based on the detection of the thermal radiation at only two different wavelengths, is extended to a continuous range of wavelengths [33, 50, 51].

In general, a black body emits radiation over a range of wavelengths with an intensity $I_b(\lambda, T)$, given by Planck's Law as a function of temperature, T , and wavelength, λ ,

$$I_b(\lambda, T)d\lambda \propto \frac{d\lambda}{\lambda^5(\exp(\frac{hc}{\lambda kT}) - 1)}, \quad (2.1)$$

where h is Planck's constant, c the velocity of light and k the Boltzmann constant. In general, however, soot particles cannot be treated as black bodies; they rather behave like grey bodies. The radiation, $I_g(\lambda, T)$, emitted by a grey body at a given wavelength and temperature, is less than that of a black body. The monochromatic emissivity, ϵ , of a body at a wavelength λ is given by

$$\epsilon(\lambda, T) = \frac{I_g(\lambda, T)}{I_b(\lambda, T)} < 1. \quad (2.2)$$

The emissivity of the soot particles in the diesel flame is in general independent of temperature but not independent of the wavelength and can be approximated by [33, 57]

$$\epsilon_\lambda = 1 - \exp\left(-\frac{KL}{(\lambda/\lambda_0)^\alpha}\right), \quad (2.3)$$

where K is an absorption coefficient depending on the soot concentration in the flame, L is the optical path length of the radiation and λ_0 is a reference wavelength. The value of the parameter α depends on the physical and optical properties of the soot in the flame. For the visible wavelength range $\alpha = 1.38$ is a suitable value [58].

2.3.2 Laser induced light emission

A common technique for laser-based diagnostics of combustion processes is Laser Induced Fluorescence (LIF) detection. Because of its great sensitivity LIF is very useful to obtain information about minority species with high spatial and temporal resolution [30–32]. This technique, schematically illustrated for the NO molecule in figure 2.6, is based on the principle that molecules can only absorb and emit radiation (photons) of very specific and characteristic wavelengths (energies). In the visible or UV spectral range absorption of a photon results in a promotion of the molecule to an electronically excited state. The excited molecule will decay back to the electronic ground state on a time scale of typically nanoseconds, which is accompanied by emission of a photon (fluorescence or radiative decay) in a random direction. As the molecule can decay to more than one (ro)vibrational level the fluorescence will contain several wavelengths. However, not all excited molecules will decay by emitting a photon, because there are competing non-radiative pathways, generally due to collisions with neighbouring molecules. These processes reduce the fluorescence yield, and become more important with increasing pressure.

An excitation spectrum can be obtained by scanning the excitation laser wavelength and recording the intensity of the total fluorescence (or one of the fluorescence wavelengths bands). Each time the excitation wavelength matches an allowed transition in the molecule, this will result in a fluorescence peak in the spectrum. Alternatively, by recording the fluorescence dis-

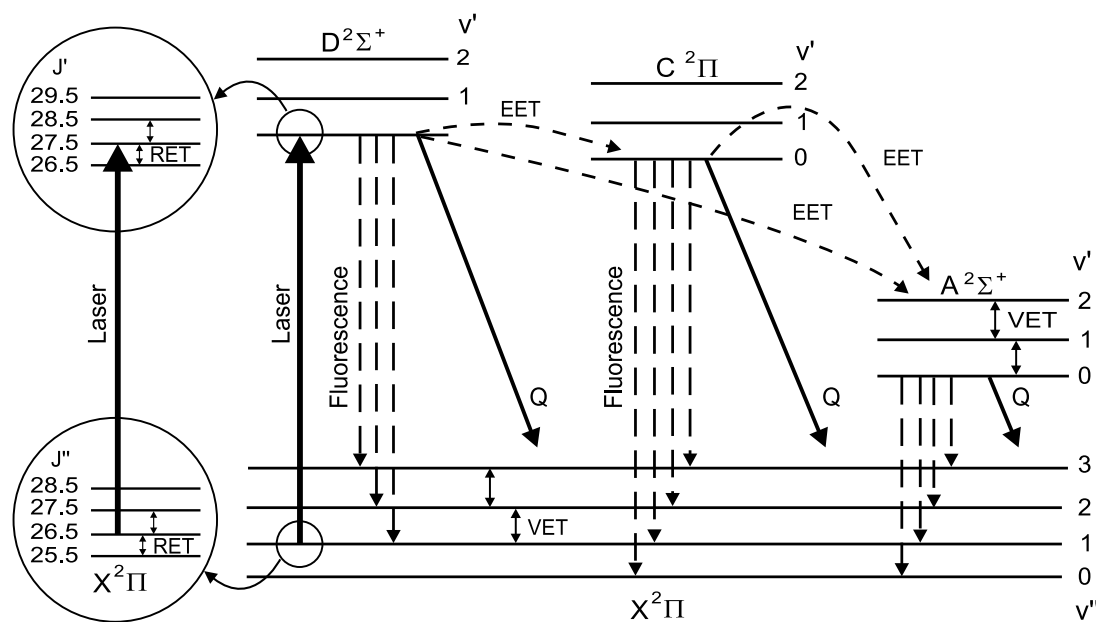


Figure 2.6: Schematic energy level diagram showing the principle of Laser Induced Fluorescence (LIF) and competing processes. Excitation of the $R_1(26.5)$ transition in the $D^2\Sigma^+(v'=0) \leftarrow X^2\Pi(v''=1)$ band of NO is shown (upward arrow) together with the relevant depopulating processes (downward arrows), including fluorescence (dashed), quenching (Q); (solid), electronic energy transfer (EET); (short dashed), vibrational energy transfer (VET) and rotational energy transfer (RET); (bidirectional arrows). Level distances are not to scale.

persed in its different wavelength components, while the laser wavelength is fixed at a specific transition of the molecule of interest, a so-called dispersion spectrum is obtained. Each fluorescence peak in a dispersed fluorescence spectrum corresponds to a radiative decay channel at a certain wavelength, characteristic for the excited molecule. Both excitation and dispersion spectra can be used to demonstrate the presence of a specific molecule. However, the possibility of spectroscopic interference by other molecules that are present in the measurement volume has always to be taken into account.

Excitation spectra and dispersed fluorescence spectra can be obtained simultaneously during one excitation wavelength scan using an Optical Multichannel Analyzer (OMA) system. A dispersed fluorescence spectrum can be recorded and stored for each excitation wavelength while the light source is scanning. This results in a fluorescence signal as a function of both the excitation and dispersed fluorescence wavelength. The fluorescence intensity at every combination of excitation and dispersed fluorescence wavelength can be represented in *e.g.* a two-dimensional image in which the fluorescence intensity is represented in a grey or false colour scale. Individual excitation and dispersion spectra can be extracted from this so-called excitation/dispersion spectrum by taking appropriate cross sections through the image (examples follow in section 2.5.1).

Quantification of LIF

The translation of fluorescence signal into absolute number densities of the probed molecules is usually not straightforward because of the dependence of the fluorescence signal upon the physical environment. In principle, if there were no fluorescence losses (*e.g.* at low density), the fluorescence yield would be proportional to the number of excited molecules, with a proportionality constant that would not depend on the environmental conditions (pressure, temperature, gas composition, etc.) under which the measurement is performed. In general, however, there are other possible decay mechanisms that also depopulate the excited state (figure 2.6). The electronically excited state might be predissociated, or the excited molecule might decay via collisions. The fraction of excited molecules that fluoresces is given by the so-called Stern-Vollmer factor, $A^*/(A+P+Q^*)$, in which A , P , and Q^* denote rate constants for total radiative decay, predissociation and non-radiative decay of the electronically excited state, respectively. A^* is the radiative decay rate for the transitions which are observed within the bandwidth of the detection system. While A and P are molecular constants of the excited state, the value of Q^* depends upon pressure, temperature and composition of the environment. For NO predissociation does not play a role and in the case that NO is excited at high pressure and temperature (that is, under conditions typical for combustion in a diesel engine) $Q^* \gg A$, so $A+P+Q^* \approx Q^*$ [30]. Thus, the interpretation of the LIF signal depends upon the value of Q^* which will be determined by collisions of the excited molecules with neighbouring molecules. In other cases, however, for example for oxygen (O_2) in the electronically excited $B^3\Sigma_u^+$ -state, $P \gg Q^*$ and $P \gg A$ and the Stern-Vollmer factor reduces to A/P , independent of pressure and temperature. Due to this effect O_2 fluorescence can be used to determine temperatures, as discussed briefly in chapter 6.

The quenching term Q^* includes several different non-radiative decay channels that are a result of intermolecular collisions. A number of different collisional energy transfer processes can be distinguished: *i*) Electronic Energy Transfer (EET) to another electronically excited state,

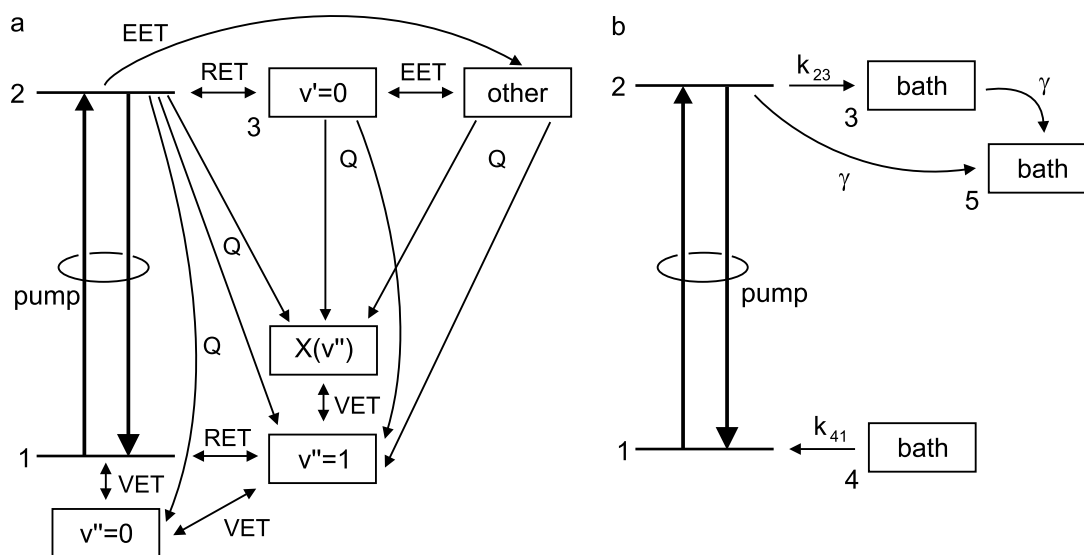


Figure 2.7: a) Detailed level scheme including the various collisional energy transfer processes that affect the LIF yield. b) Simplified level scheme used in the model.

ii) Vibrational Energy Transfer (VET) within a given excited electronic state, iii) Rotational Energy Transfer (RET) within a given vibrational state and iv) Quenching (Q) to the electronic ground state. After one of the first three processes the molecule remains electronically excited and still can decay to the ground state, which again can be non-radiative or radiative, but then at a different wavelength. RET and VET can take place in the ground state as well where they influence the population of the initial state. These different energy transfer processes are included in figure 2.6.

The various collisional energy transfer processes affect the LIF yield in different ways. This will be discussed here for the specific case of NO excited on the $R_1(26.5)/Q_1(32.5)$ transition in the $D^2\Sigma^+(v'=0) \leftarrow X^2\Pi(v''=1)$ band around 193 nm, combined with fluorescence detection in the $D^2\Sigma^+(v'=0) \rightarrow X^2\Pi(v''=3)$ band at 208 nm. The fluorescence is detected without rotational resolution. This detection scheme can be modelled using the rate equation approach and one of the energy level schemes shown in figure 2.7. The most detailed and, therefore, somewhat obscure level scheme of figure 2.7a, includes all energy transfer processes mentioned above explicitly. The laser radiation transfers population between levels 1 and 2 at a pumping rate $B_{12}I = B_{21}I$ (assuming equal degeneracy for both levels). RET causes a depopulation of the excited level 2 and a replenishment of the ground level 1. VET processes maintain the thermal equilibrium between the vibrational states. Therefore, VET can be neglected in the excited state (where $v'=0$ is populated), but it might still be of some importance in the ground state ($v''=1$), at least at higher pressures. Quenching and EET processes, finally, remove population out of the electronically excited D-state to the electronic ground state or to other electronically excited states ($A^2\Sigma^+$ and $C^2\Pi$), respectively. Since the fluorescence is detected without rotational resolution, the instantaneous fluorescence rate is proportional to the sum of the population in levels 2 and 3 ($D(v'=0)$).

As compared to the situation in which there would be no collisional energy transfer at all,

quenching and EET cause a reduction in fluorescence yield, but RET tends to compensate for this, at least in part². In the initially unpopulated $D(v'=0)$ state, RET processes remove molecules from the laser-excited state, thereby making them unavailable for stimulated emission back to the ground state without causing any loss in fluorescence yield. RET processes in the ground state, on the other hand, tend to refill the level depleted by laser excitation, at a rate which is proportional to the deviation from the equilibrium population. Under conditions of strong enough pumping, therefore, it is possible to excite more molecules than were originally present in the ground state 1 (see *e.g.* [59]). The latter effect has recently been shown to potentially cause large errors in temperature determination based on two-line LIF [60], and will also be a matter of concern in LIF-based molecular density determinations.

Based on the above observations, it is possible to collapse the rather involved level scheme of figure 2.7a into the simplified version of figure 2.7b. The laser still couples the levels 1 and 2, and RET processes are incorporated through interaction with two ‘bath’ levels, 3 and 4, the population of which is assumed constant. The fluorescence rate is proportional to the sum of the populations in levels 2 and 3 (together making up the $D(v'=0)$ state). Upper state quenching and EET are combined, giving a total rate γ , and modelled by (one-way) interaction with another bath level 5. VET and quenching directly to the ground electronic state are neglected. This results in the following rate equations for the laser-coupled levels:

$$\dot{N}_1 = -B_{12} I N_1 + B_{21} I N_2 - k_{41} (N_1 - N_1^{eq}) \quad (2.4)$$

$$\dot{N}_2 = +B_{12} I N_2 - B_{21} I N_1 - k_{23} (N_2 - N_2^{eq}) - \gamma N_2 \quad (2.5)$$

and for the remainder of the $D(v'=0)$ state:

$$\dot{N}_3 = k_{23} N_2 - \gamma N_3. \quad (2.6)$$

The equilibrium populations $N_i^{eq} = N_i(t = 0)$ are $N_1^{eq} = 1$, $N_2^{eq} = N_3^{eq} = 0$. These rate equations allow an analytical solution for the fluorescence yield resulting from a constant intensity laser pulse of duration τ_p (see Appendix), which can then be used to assess the sensitivity of the fluorescence yield to the individual model parameters.

In the following the two excitation configurations that were used in the experiment will be considered (see figure 2.1). In what will be called the top illumination setup the laser beam enters the combustion chamber through the top window, and therefore immediately enters the observation volume (seen by the camera). In case of the other setup, the side illumination scheme, the laser beam enters the combustion chamber through a side window and has to traverse about 30% of the combustion chamber before entering the observation volume. As a result, the intensity levels (and therefore the pump rates $B_{12}I$) are higher in the top illumination scheme than in the side illumination scheme.

As a general result, the calculated fluorescence signal (equation 2.17) is nearly linear with laser intensity, under the conditions of the engine experiments. In figure 2.8a a measure, Δ , for the deviation of the fluorescence signal from linearity with the laser intensity, defined as

$$\Delta(I_0) = \frac{S_{\text{LIF}}(I_0) - \left. \frac{\partial S_{\text{LIF}}}{\partial I} \right|_{I_0} I_0}{S_{\text{LIF}}(I_0)}, \quad (2.7)$$

²In general, RET tends to establish thermal equilibrium between the rotational level populations of any vibronic state.

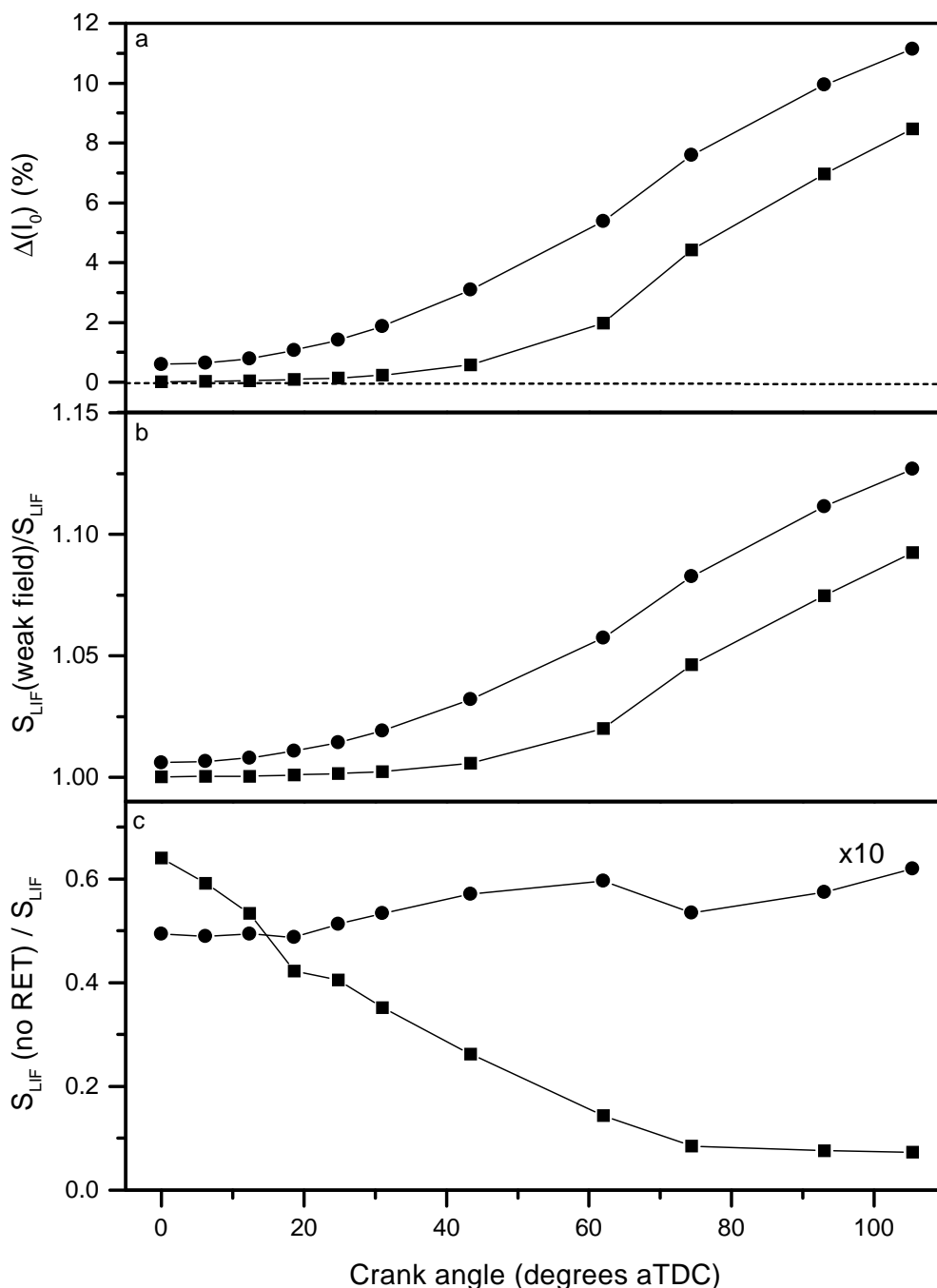


Figure 2.8: a) Deviation of the fluorescence signal from linearity (equation 2.7) for side illumination (■) and top illumination (●). b) Ratio of the fluorescence yield calculated in the weak field limit (Appendix, equation 2.18) to that using the full model (Appendix, equation 2.17) for side illumination (■) and top illumination (●). c) Ratio of the fluorescence yield calculated by neglecting RET in the full model (Appendix, equation 2.18 with $k_{23} = k_{41} = 0$) to that using the full model (Appendix, equation 2.17) for side illumination (■) and top illumination (●).

is plotted for both experimental configurations, using formula 2.17 from the Appendix and parameter values as appropriate for the engine (laser intensity and collision rates)³. The figure shows that the deviations from linearity are reasonably small for the side illumination setup, always less than 2% for $\Theta \lesssim 60^\circ$ aTDC and increasing only for $\Theta \rightarrow$ BDC. The increase for larger Θ is caused by the decrease in laser attenuation, and therefore larger saturation by the higher intensities at increasing Θ . For the top illumination setup the deviations from linearity are larger, also due to larger saturation by the high intensity levels closely below the entrance window.

As mentioned in the Appendix, LIF yields are often interpreted in the weak field limit. The present model allows to assess the error made by that approach, and this is illustrated in figure 2.8b for the case of the two-stroke engine. Shown in the figure is the ratio of the fluorescence yield calculated in the weak field limit (Appendix, equation 2.18) to that using the full model (Appendix, equation 2.17). It can be seen that for both setups the weak field limit slightly overestimates the fluorescence yield, but that the difference decreases closer to TDC; it stays below 5% for $\Theta \lesssim 60^\circ$ aTDC (top illumination) or $\Theta \lesssim 80^\circ$ aTDC (side illumination).

The fact that using the weak field limit would, in the case considered here, imply only a modest overestimate of the fluorescence yield, does not mean that RET processes are unimportant. On the contrary, as shown in figure 2.8c, the presence of RET may increase the fluorescence yield by as much as a factor of 20. The net effect of RET is about constant for the top window illumination setup, and becomes progressively more important for the side illumination setup for larger crank angles. This is explained by the fact that the importance of RET becomes more pronounced at higher intensities. In case of the top illumination setup, there is always high laser intensity available within the observation volume, whereas in the side illumination setup the laser beam suffers some intensity loss on its way through the first (invisible) part of the combustion chamber. This intensity loss is larger for smaller crank angles.

At first sight, it might seem surprising that, when RET implies such an enormous enhancement of the fluorescence yield, the use of the weak field limit (in which RET would play only a minor role) still results in only relatively small deviations from the full model calculations. The reason for this is to be found in some fortuitously compensating effects. In the ground state, on the one hand, RET is neglected but so is also the depletion of the lower level 1. Sticking to the weak field solution even if the intensities are actually too high for that, in a sense therefore corresponds to assuming an infinitely fast RET rate k_{41} out of an infinitely large bath 4. Similarly, although in the weak field limit RET is neglected in the upper electronic state, so is also the stimulated emission back to the ground state by the laser, and the weak field assumption essentially corresponds to assuming an infinitely fast RET rate k_{23} into a perpetually empty bath 3.

In summary, therefore, carrying on the weak field limit into the strong field regime actually corresponds to using the full model with infinitely fast rotational relaxation rates (k_{41} and k_{23}) into infinitely large bath states (3 and 4). This also explains why figure 2.8b shows the weak

³In the top illumination case, $S_{\text{LIF}}(I_0)$ has to be replaced by an integral over the penetration depth,

$$\int_0^{z_p} S_{\text{LIF}}(I_0(z)) dz,$$

with z_p the vertical distance between top window and piston upper surface.

field limit to always overestimate the fluorescence yield. In practice, considering the relatively small errors made, the weak field limit will be used in the subsequent chapters. The results of figures 2.8a and 2.8b will, however, be kept in mind.

2.3.3 Elastic light scattering

As a laser beam traverses the combustion chamber elastic scattering of the laser radiation can be observed. The elastically scattered radiation has the same wavelength as the laser radiation and results from scattering off fuel vapour, liquid fuel and oil droplets and/or soot particles. When the diameter of the scattering particles is small compared to the laser wavelength this elastic scattering is called Rayleigh scattering, whereas it is denoted by Mie scattering if the diameter of the scattering particles is large. As the scattering cross sections for Mie scattering often are much larger than those associated with fluorescence, the intensity of the elastic Mie scattering tends to be much larger than that of the inelastic fluorescence. The cross section for elastic scattering depends on the particle size. For particles within the Rayleigh limit it is proportional to the particle diameter to the sixth power [61]. However, for larger particles the relation between particle size and intensity is much more complex. Consequently, recording the scattered light provides only qualitative information of where scattering particles are, or are not, present in the combustion chamber. (Note that combining scattering experiments with Laser Induced Incandescence (LII) allows to obtain quantitative information about particles sizes and densities [11–13].)

Due to the scattering the laser intensity is attenuated on its way through the combustion chamber. In addition, absorption by soot particles and oil and fuel droplets plays an important part in the decrease of the laser intensity. As the intensity of the elastically scattered radiation is proportional to the laser intensity, images of the elastically scattered radiation can be used to reconstruct the local laser intensity inside the running engine (chapter 3).

2.4 Spontaneous light emission

Based on the combustion-induced pressure rise seen in the engine characteristics (figure 2.4) it follows that combustion starts around 15° bTDC. Flame luminosity, as observed through the top window, can indeed be detected from about 15° bTDC onwards, up to about 60° aTDC. To the unaided eye, the flames have a white colour which results from the burning of soot particles that are formed in a fuel rich spray. It indicates that the natural emission of the flames results from highly sooting flames with temperatures around 2000-2500 K [2]. This is, however, only a rough estimate; a more accurate soot temperature can be derived from the spectrally dispersed spontaneous flame emission (section 2.4.1). Information about the structure of the flames follows from two-dimensional flame emission images (section 2.4.2).

2.4.1 Dispersed flame emission

The visible flame luminosity is predominantly due to glowing soot particles. Its spectral distribution is a function of the temperature of the soot, and can serve as kind of a soot thermometer, by comparison to the well known black or grey body radiation distribution curves as described in section 2.3.1. To obtain a temperature of the soot particles the spontaneous flame emission of the two-stroke engine coming through the top window is dispersed into its different wavelength components by a dispersion prism and recorded with a CCD camera as shown in the upper left of figure 2.9. Two slits (S) are used to define the position that the emission is obtained from. A lens (L; $f = 200$ mm) is used to focus the dispersed emission on the intensified CCD camera. It is used with a bellows in between the lens and the camera to enlarge the image in order to fill the whole CCD chip.

Spectra of the dispersed flame emission, obtained with a gate width of 500 ns and averaged over 200 engine cycles are recorded for all crank angles at which it can be observed. They represent an average emission signal from a narrow strip (1×25 mm²) through the centre of the top window. Frequency calibration is achieved by recording the well known emission lines produced by a mercury lamp which was placed on top of the engine. The spectral response function of the setup was calibrated using a quartz tungsten-halogen calibration lamp (Oriol Instruments; 63358-M).

A few of these dispersed flame emission spectra are given in figure 2.9. The first spectrum

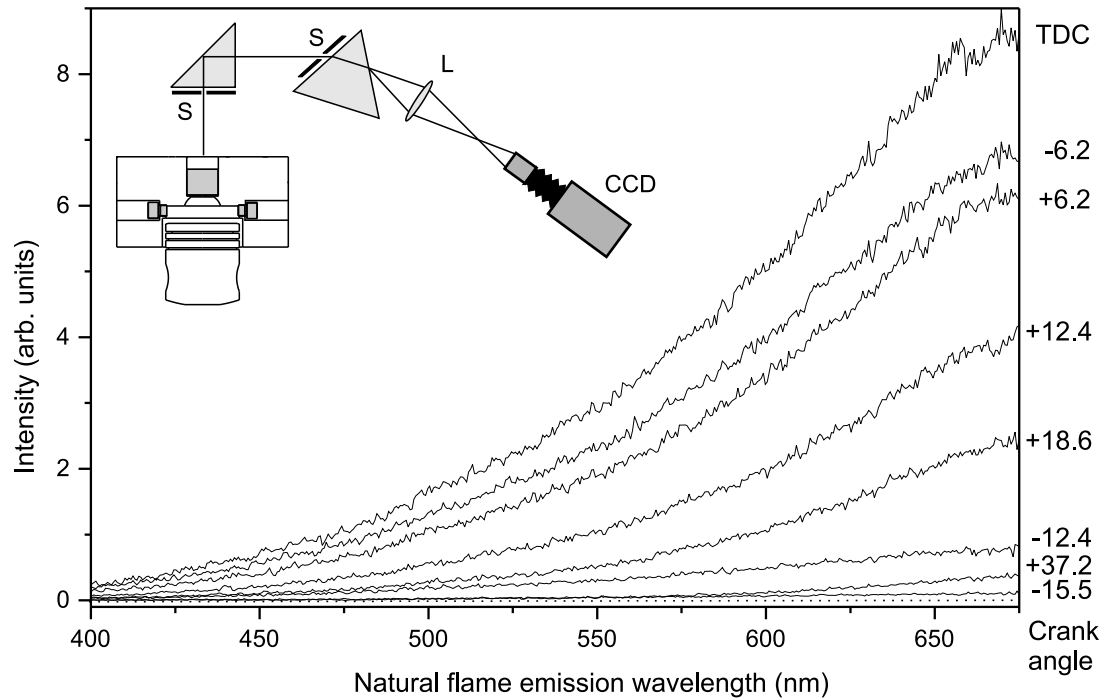


Figure 2.9: Spontaneous light emission from the flames dispersed in its different wavelength components for several crank angles as indicated in the figure (+ and – refer to angles after and before TDC, respectively). The experimental setup used to disperse the flame emission is shown in the upper left; S=slit; L=lens.

of the natural flame emission can be observed at 15° bTDC. The intensity increases almost linearly till just before TDC, after which it decreases till at around 60° aTDC the last visible flame emission can be observed. The spectra show no fine structure due to chemiluminescence of excited molecules. This indicates that the spontaneous flame emission indeed is dominated by grey body radiation of incandescent soot particles in this wavelength range. If a specific molecule would contribute significantly to the flame emission, an emission peak at a wavelength characteristic for the molecule would show up. This can easily be observed for *e.g.* C_2 , CH and OH in Otto engines, where the thermal radiation from the soot is much lower than in diesel engines [35]. For diesel engines OH fluorescence has been seen around 310 nm (which is below the wavelength range of figure 2.9), but its intensity is small compared to the strong grey body emission that dominates the spectrum at wavelengths above 340 nm [18].

The observed flame emission spectra can be fit to Planck's Law combined with the emissivity given in equation 2.1 and equation 2.3, respectively, to obtain information about the value of KL and the temperature of the incandescent soot particles⁴. The spectra can be fit well to black body (Planck) curves, the addition of the grey body term giving no improvement. Apparently, the KL -value for the flames in this engine is high, resulting in an emissivity of the soot particles of almost unity. The temperatures derived from the soot spectra by fitting them to black body curves is shown in figure 2.4d (●). The dashed curve in this figure is an extrapolation based on adiabatic expansion of an ideal gas ($\gamma = 1.36$, for the combustion stroke) during the last part of the stroke, matched to the experimental data around 15° aTDC.

The soot temperature reaches a maximum of about 2250 K around TDC, and is always much higher than the mean gas temperature derived from the heat release rate (figure 2.4d). From this it follows that the cylinder contents are not in thermal equilibrium. The soot temperature represents the temperature of the locally present soot whereas the mean gas temperature represents the average temperature of the gas inside the whole cylinder. As soot particles are formed during the combustion where the temperature is locally high and not yet in equilibrium with the whole cylinder contents, the soot temperature is expected to be higher than the mean gas temperature [53]. The measured soot temperature is in agreement with the (empirical) temperature following from the colour of the flame emission. The white colour indicates a temperature of carbon particles in the flames of 2000-2500 K [2].

2.4.2 Flame emission images

Recording two-dimensional images of the emission from incandescent soot particles that are formed in the flames provides information about the spatial structure of the flames. However, usually a CCD camera needs about 300 ms to record one image, which is not fast enough to follow the combustion during one single stroke. By using an intensified CCD camera in kinetics mode images can be acquired very fast after each other (0.1-1 ms) which gives the possibility to follow the evolution of the flame during one stroke. By using an ICCD camera in kinetics mode with a gate width of 200 ns single shot images of the spontaneous flame emission of the two-stroke engine are obtained as a function of crank angle.

Figure 2.10 (bottom four rows) shows four series of nine single shot images obtained every 3.6 degrees crank angle (0.5 ms) of the same stroke, covering the time span that the flame

⁴It has been shown that if the soot particles are small this temperature is also a good measure for the flame temperature [56].

emission is clearly visible from 11.3° bTDC till 17.5° aTDC. The series are not obtained from successive strokes. The time between them, determined by the read out time of the camera is about 3 seconds. The images show the flame emission in the central 25 mm of the combustion chamber, integrated over a depth determined by the soot concentration in the flame. The position of the side windows, W1 and W2, the injector (i), and the directions of the fuel sprays are indicated in the figure. The illuminated part of the photocathode corresponds to 50 pixel rows on the CCD chip, so the spatial resolution is $0.5 \times 0.5 \text{ mm}^2$. Till around 60° aTDC flame emission can still be seen, but, its structure does not change much any more. Also the flame emission averaged over ten cycles is given in figure 2.10 (top row). The intensities of all series are individually scaled (linear grey scale, ranging from black (minimum) to white (maximum)) in such a way that the intensities of the images within a series can be compared. The percentage given in front of each series indicates the total integrated intensity of the series compared to the intensity of the average series. It can be used as a measure for the intensity variation between the different series. From the individual series it can be seen that there is a large variation in the structure and intensity of the flames for different engine cycles. The averaged series (10 cycles), however, are found to reproduce for different measurements.

To get more detailed information about the start of the combustion, similar series of images are taken, beginning at the start of the combustion and with smaller delay times between the images. Four series of single shot images of the spontaneous flame emission during the first part of the combustion taken every 0.9 degree crank angle ($83 \mu\text{s}$) are shown in figure 2.11 (bottom four rows). Also the flame emission averaged over ten cycles is given (top row). First flame emission occurs between 15° bTDC and 14° bTDC. Although in every series the behaviour of the combustion is again different, some similarities during the progress of the combustion can be seen. The first emission from soot is seen to start almost always at two different places, probably resulting from two of the three sprays that are closest to the top window (sprays 1 and 2, note that spray 3 cannot be seen as it angles downward out of the field of view). Mostly one emission spot, at the side of the laser exit window (W2), is seen first, followed by a second emission spot, located near the side of the injector, a few tenths of a degree later (see arrows in figure 2.11). As the combustion continues the intensity increases almost linearly and the two flame emission spots slowly merge into one another, but the two flames can still be distinguished, even at 17.5° aTDC. These two emissions move in a counterclockwise direction, most clearly seen in figure 2.10. This indicates that there is a certain swirl inside the cylinder in counterclockwise direction.

The total integrated intensity of an image is a measure for the intensity of the spontaneous flame emission. For the series of images given in figure 2.10 the total integrated intensity as a function of crank angle is given in figure 2.12. This figure shows clearly the variation of the intensity of the flames, but the shape of the curves does not change drastically between the different strokes. The most intense part of the combustion is reached at a slightly different crank angle for every stroke, varying by about 3 degrees around 2° bTDC. For comparison with the heat release the total integrated intensity of the observed flame emission (an average of the curves of figure 2.12) is included in figure 2.4c as well.

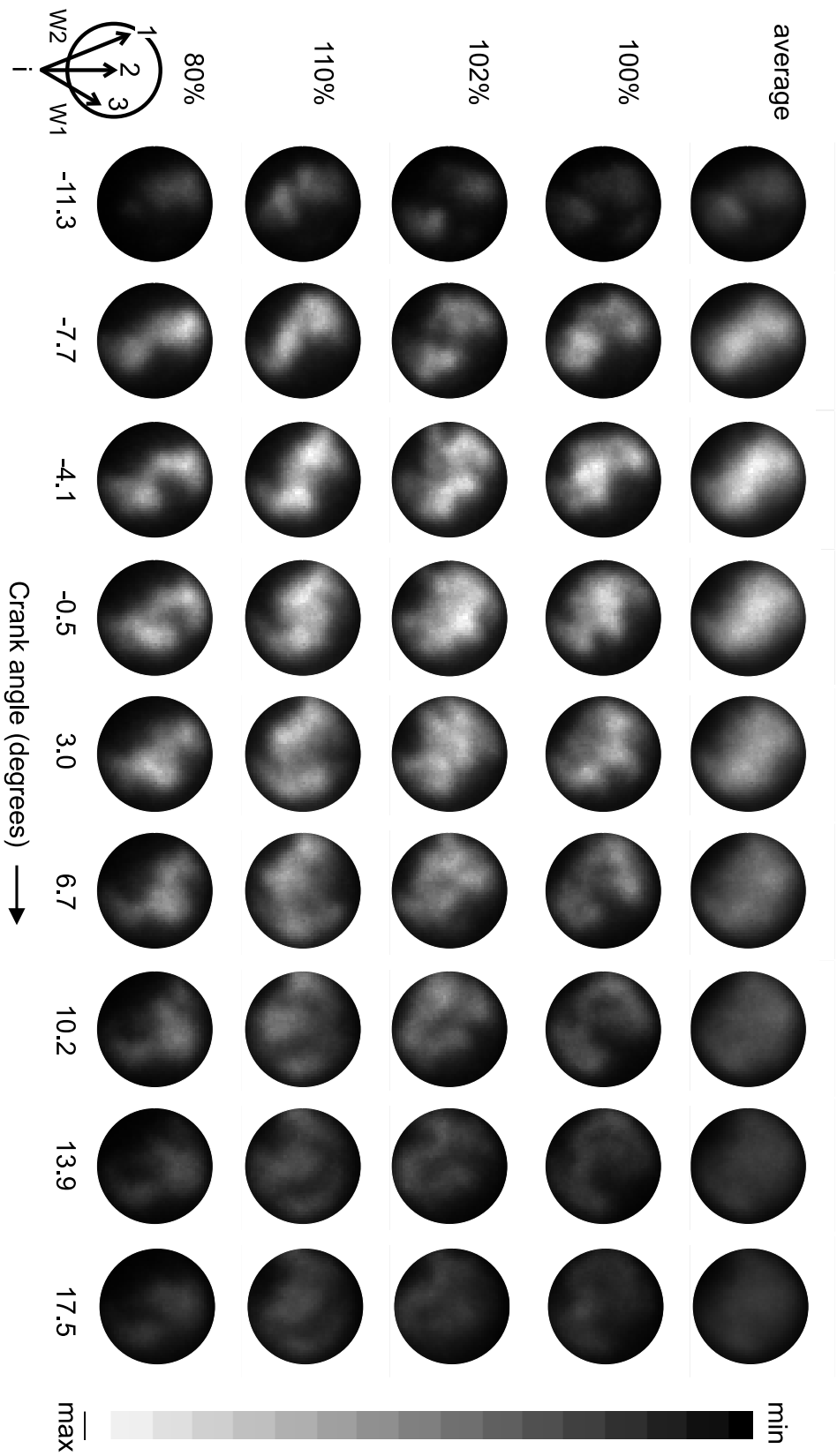


Figure 2.10: Four series of single shot images of the spontaneous flame emission, during that part of the stroke that flame emission is clearly visible, obtained every 3.6 degrees crank angle of the same stroke (bottom four rows) and the average flame emission (top row). The intensities in all series are individually scaled and represented in a linear grey scale, ranging from black (zero intensity) to white (maximum intensity). The percentage given for each series indicates the total integrated intensity of the series compared to the total integrated intensity of the average series. The position of the side windows, W1 and W2, and the injector (i) and the directions of the fuel sprays are indicated in the lower left.

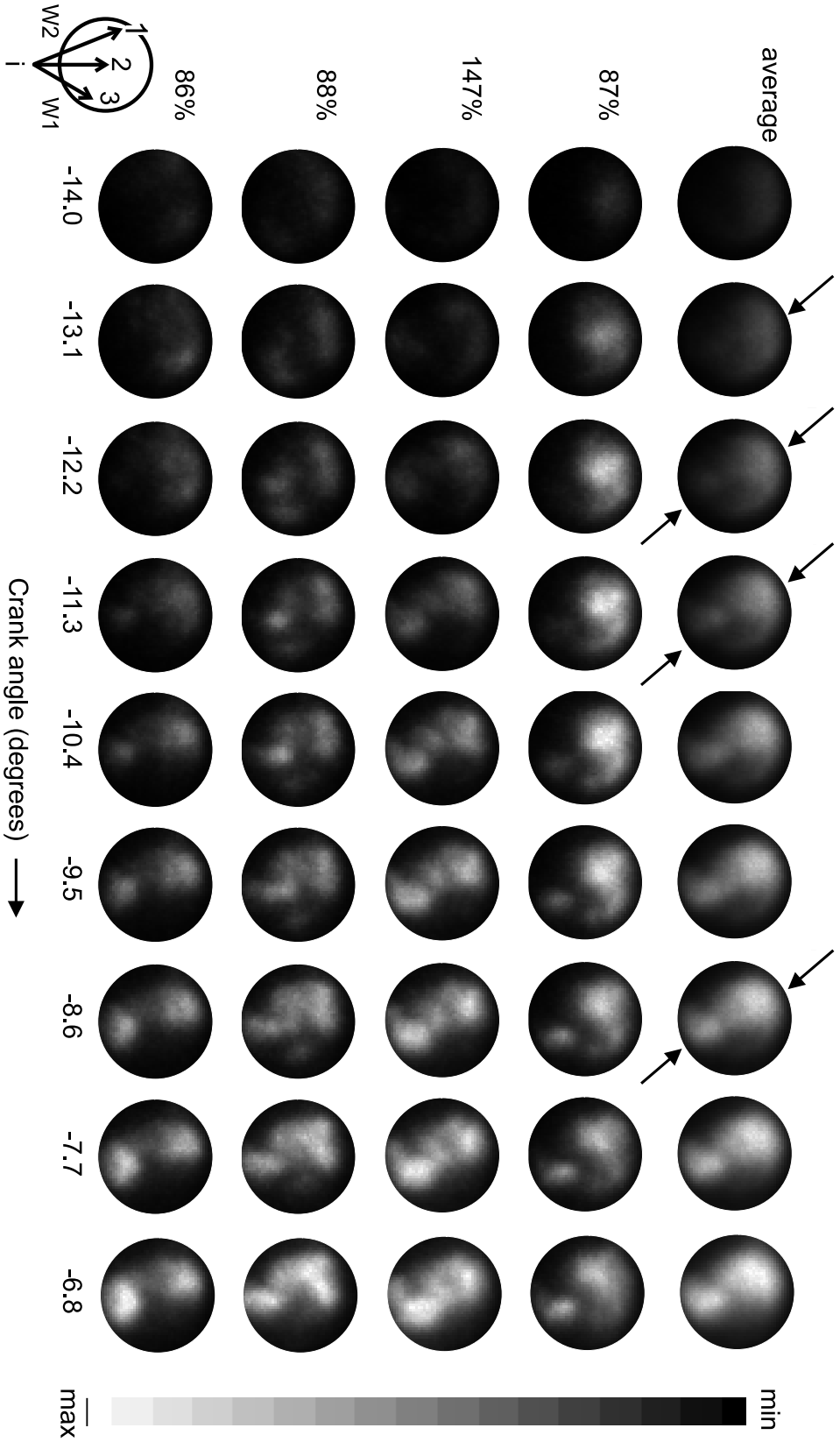


Figure 2.11: Four series of single shot images of the spontaneous flame emission at the start of the combustion, obtained every 0.9 degree crank angle of the same stroke (bottom four rows) and the average flame emission (top row). Otherwise as in figure 2.10. The arrows are explained in the text.

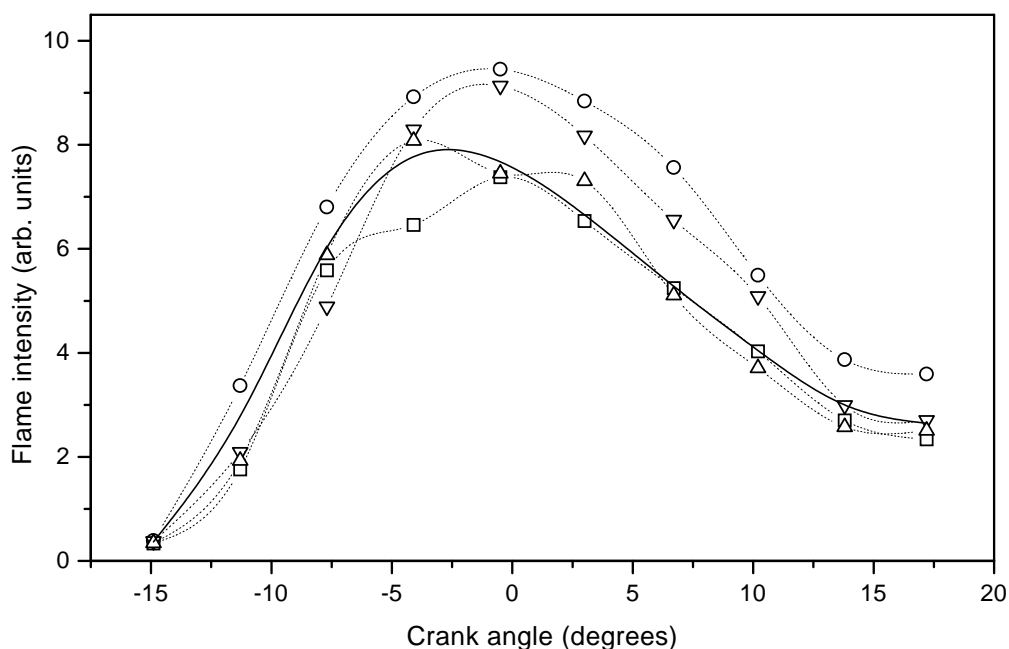


Figure 2.12: Total integrated intensity of all series of single shot images of the spontaneous flame emission given in figure 2.10. The solid line represents the average intensity. The symbols (\square , \circ , ∇ , \triangle) correspond to the different individual series of figure 2.10 from top to bottom, respectively.

2.5 Spectroscopy in a diesel engine

2.5.1 Nitric oxide and oxygen

To detect NO in combustion processes by means of the LIF technique various wavelengths can be used for excitation and detection. One frequently used wavelength is 226 nm, which can be used to reach the lowest electronic state of NO by making a transition in the $A^2\Sigma(v'=0) \leftarrow X^2\Pi(v''=0)$ band. Less often used is the 248 nm radiation of an excimer laser operated on KrF to excite the NO molecules to the $A^2\Sigma(v'=0)$ -state starting from the second vibrational level of the ground state ($X^2\Pi(v''=2)$).

In this work the 193 nm radiation of an ArF excimer laser is used to excite the NO molecules in the $D^2\Sigma^+(v'=0) \leftarrow X^2\Pi(v''=1)$ band. The excitation spectrum of this transition and the dispersed fluorescence spectrum of the $D^2\Sigma^+(v'=0) \rightarrow X^2\Pi(v'')$, measured in an atmospheric flame with an ArF excimer laser are well known [55, 62]. Figure 2.13 shows an excitation/dispersion spectrum recorded in an oxy-acetylene flame using the ArF excimer laser to excite the NO and the OMA setup to detect the induced fluorescence. The camera gate width is 40 ns and the entrance slit of the monochromator is set to 25 μm . The excitation laser wavelength is directed along the ordinate (λ_{exc}) and ranges from 51648 cm^{-1} to 51719 cm^{-1} . The dispersed fluorescence in the wavelength range between 200 and 230 nm is represented along the abscissa (λ_{fl}). The fluorescence intensity at every $\lambda_{exc}/\lambda_{fl}$ combination is represented in a linear grey scale ranging from black (zero intensity) to white (maximum intensity). The excitation range

covers many rovibrational transitions of the $\text{NO } D^2\Sigma^+(v'=0) \leftarrow X^2\Pi(v''=1)$ band. By integrating the signal over a small range around $\lambda_{fl} = 208 \text{ nm}$ (corresponding to $D(v'=0) \rightarrow X(v''=3)$ fluorescence) an excitation spectrum is obtained. This spectrum is also given in the figure. All lines belong to the $D^2\Sigma^+(v'=0) \leftarrow X^2\Pi(v''=1)$ transition of NO. The four strongest lines result from the coinciding R_1 and Q_1 branches, as indicated in the figure. The P_1 lines partly overlap the R_1/Q_1 lines in this frequency region but their intensity is less.

The dispersed fluorescence spectrum shown in the same figure (along the top) results from excitation of NO at the $R_1(26.5)/Q_1(32.5)$ transition. It shows two progressions. Not only fluorescence out of the directly excited $D(v'=0)$ -state to the $X(v''=2-5)$ -states is observed (201, 208, 216 and 225 nm), but, due to rapid EET from the D-state to the C-state, also fluorescence from the $C(v'=0)$ -state to the $X(v''=2-5)$ -states is observed (204, 212, 220 and 229 nm). The C-state progression is shifted to the red (by about 5 nm) and has the same Franck-Condon pattern as the D-state owing to the similarity of their potential energy curves. At 225 nm also fluorescence from the $A(v'=0)$ -state to the $X(v''=0)$ -state could be present. However, as it coincides with a fluorescence band out of the D-state it cannot be distinguished. It should also be noted that the D-state fluorescence bands are spectrally broad, in spite of the selective excitation of only two or three rotational energy levels. The peaks on each of the dispersed fluorescence bands can be ascribed to band heads of the different rotational branches. This indicates the occurrence of a considerable amount of RET in the upper state.

In the engine, however, the pressure, temperature and gas mixture are different from those in the flame. In order to select the best wavelengths for excitation and detection of NO inside the engine, excitation and dispersion spectra have to be obtained from the engine. This results in excitation/dispersion spectra that, at first sight, look quite different from the ones recorded from the flame. An excitation/dispersion spectrum recorded in the running engine at 42° aTDC ($P = 10 \text{ bars}$, $T_{gas} = 850 \text{ K}$), in which the wavelength ranges are the same as for the spectrum obtained from the flame (figure 2.13) is shown in figure 2.14. This spectrum is obtained by coupling in the laser beam through the top window and detecting the fluorescence through the top window as well (gate width 50 ns, slit 50 μm). This spectrum is measured in about 15 minutes while the laser radiation was scanned over 70 cm^{-1} . The spectrum does not show any attenuation of the intensity during this scan indicating that window fouling does not occur during the measuring time. The strong feature at $\lambda_{fl} = 207.8 \text{ nm}$ is an artefact of the measurement setup, probably due to Raman scattering of the quartz top window. (Note that this feature slightly shifts to the red, as the excitation wavelength scans to the red, their frequency difference remaining constant. This would be expected for a feature due to Raman scattering.) Below $\lambda_{fl} = 204 \text{ nm}$ the contribution of the fluorescence signal is suppressed by the normal incidence 193 nm laser mirror used to block the elastically scattered laser radiation. Although the excitation and dispersed fluorescence wavelength ranges of figures 2.13 and 2.14 are the same, the most prominent fluorescence progressions are at completely different $\lambda_{exc}/\lambda_{fl}$ combinations. In fact, all strong fluorescence features in figure 2.14 can be ascribed to the Schumann-Runge bands of oxygen. Nitric oxide fluorescence out of the D-state is present as well, but much weaker and more diffuse (at $\lambda_{fl} = 208, 216 \text{ and } 225 \text{ nm}$). Apparently, the conditions in the engine are such that O_2 fluorescence, at least at this particular crank angle, strongly interferes with the NO fluorescence. The excitation and dispersion spectra shown in the margin of figure 2.14 demonstrate, however, that the contribution of the two components can still be separated by a proper choice of excitation and detection wavelengths.

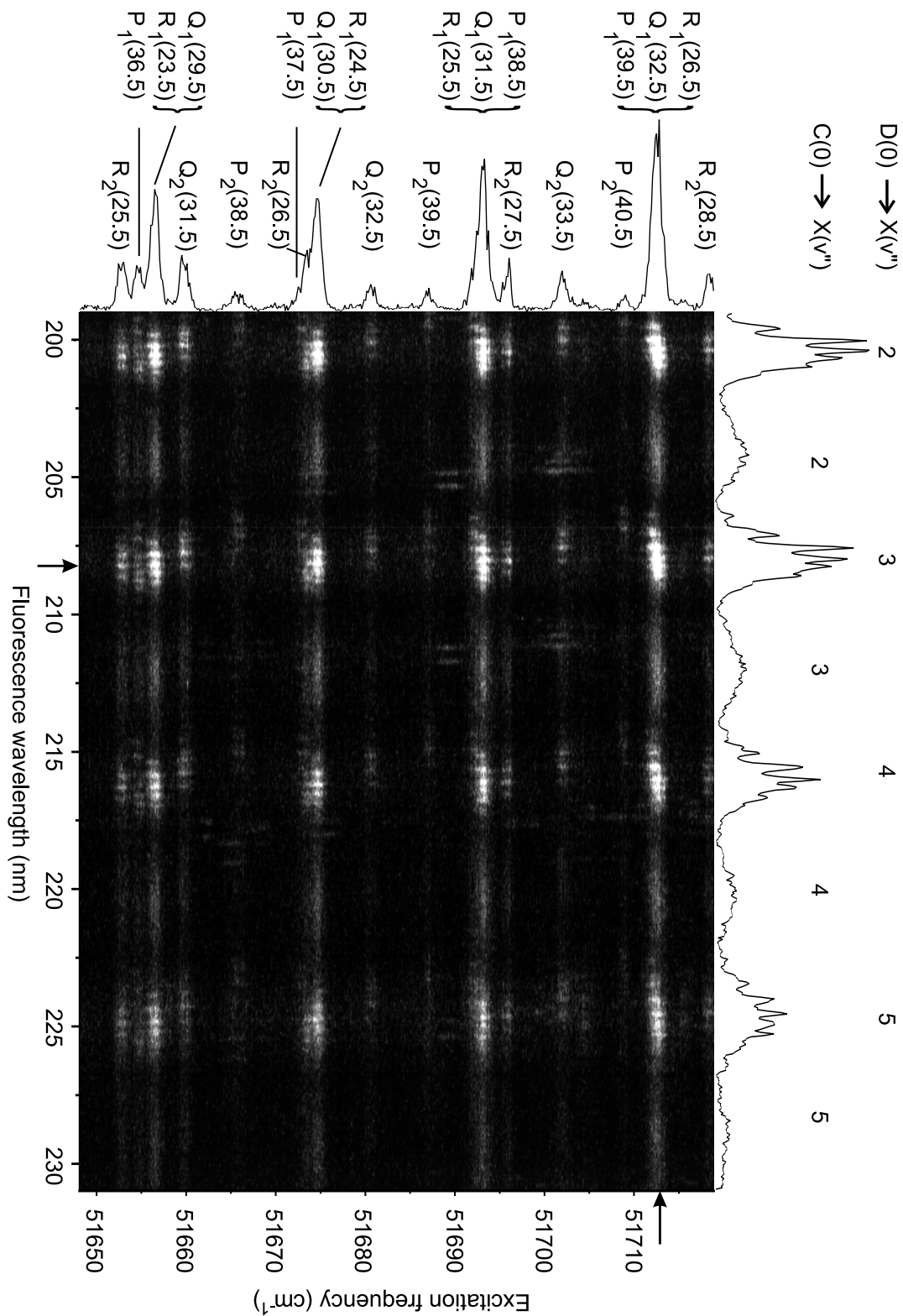


Figure 2.13: An excitation/dispersion spectrum obtained from an oxy-acetylene flame. The fluorescence intensity at every $\lambda_{exc}/\lambda_{fl}$ combination is represented in a linear grey scale ranging from black (zero intensity) to white (maximum intensity). The spectra shown along the margins are obtained at the positions indicated by the arrows.

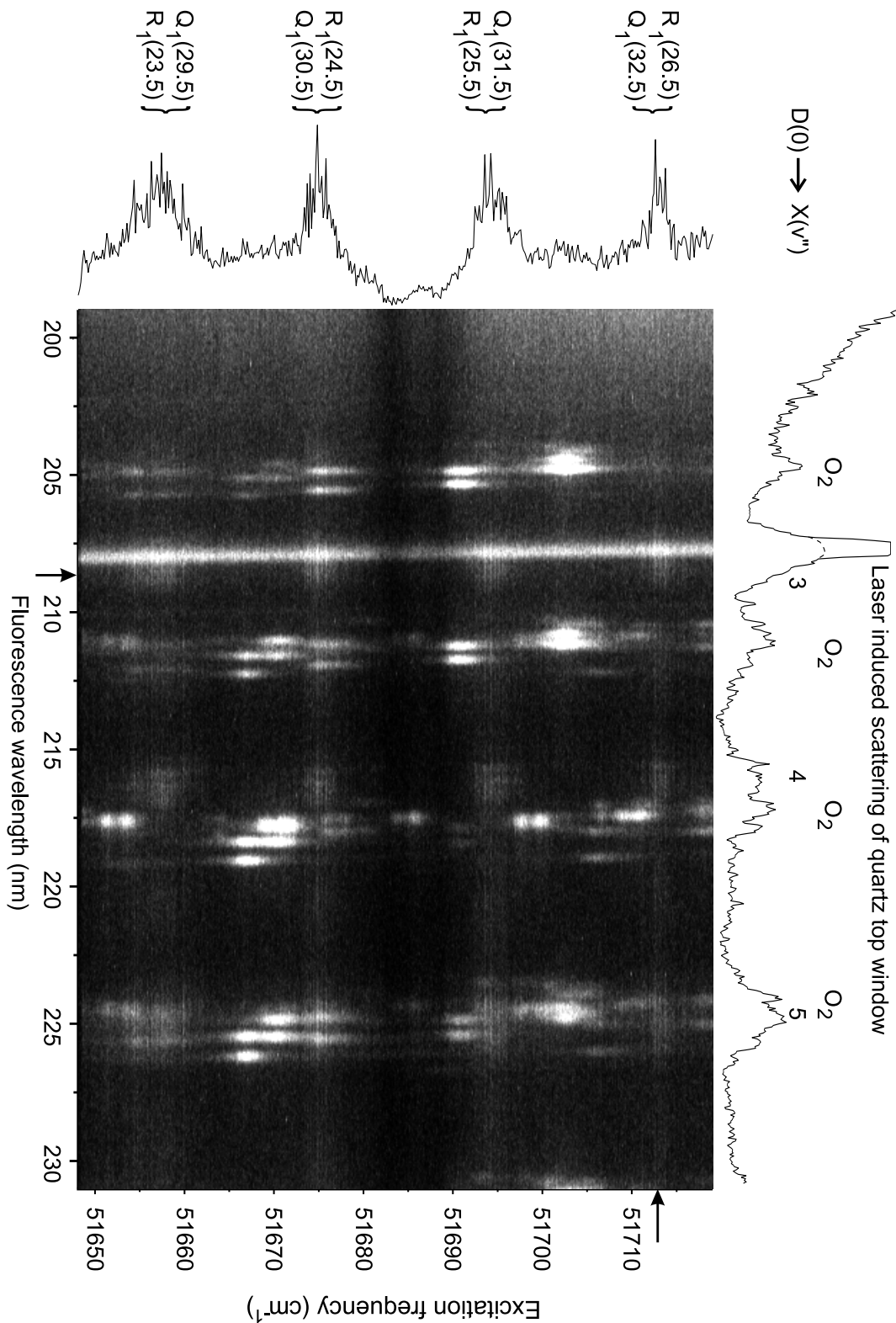


Figure 2.14: An excitation/dispersion spectrum recorded in the engine at 42° aTDC ($P = 10$ bars, $T_{gas} = 850$ K). Otherwise as in figure 2.13. The strong feature at $\lambda_{fl} = 207.8$ nm is an artefact due to the quartz top window. Below $\lambda_{fl} = 204$ nm the contribution of the fluorescence signal is suppressed by a normal incidence 193 nm laser mirror in front of the collection optics.

The O₂ transitions that can be excited within the tuning range of an excimer laser operated on ArF belong to the Schumann-Runge B³Σ_u⁺ ← X³Σ_g⁻ system. The vibrational ground state (v''=0) can be excited to the B(v'=4)-state via several rotational transitions, causing large absorptions in the intensity profile of the excimer laser radiation when transmitted through air. In addition, transitions in the B(v'=10,11) ← X(v''=2) and B(v'=14,15,16) ← X(v''=3) bands can be observed. The corresponding dispersed fluorescence spectra extend to the visible wavelength range, reaching vibrational levels in the X-state as high as v''=35 [63–66]. At high temperatures the O₂ spectrum becomes so dense that it is almost impossible to avoid O₂ excitation completely (see *e.g.* [65]). Therefore, even if the laser frequency is off-resonant for an O₂ excitation, some fluorescence of O₂ will still be observed. Also, some O₂ fluorescence is seen which is induced by the broad-band fraction of the excimer laser radiation. This O₂ fluorescence interferes in the NO spectra (it partly overlaps the NO fluorescence bands) and becomes stronger when temperatures are higher, because O₂ is excited from the vibrationally excited X(v''=2 or 3)-states, as can be seen in figure 2.14. Around λ_{exc} = 51685 cm⁻¹ the laser intensity reaching the engine is relatively weak, causing dark horizontal bands at λ_{exc} in figure 2.14, due to absorption on the rotational R(21) and P(19) lines of the B(v'=4) ← X(v''=0) transition of O₂ present in the air through which the laser beam is transmitted.

In emission the O₂ fluorescence is seen around 205 nm, 211 nm, 217.5 nm and 225 nm. It is characterised by narrow doublet structures due to fast predissociation of the upper state [63–65]. This predissociation causes excited O₂ molecules to dissociate before significant RET has occurred, so that, contrary to the rather broad NO fluorescence, the O₂ fluorescence consists of only two closely spaced lines originating from the directly excited level. (At still higher pressures upper state RET has been observed for O₂ as well [67].) However, as several O₂ transitions can be excited simultaneously the total O₂ fluorescence signal consist of several doublets, causing some broadening. At 225 nm the NO fluorescence coincides with the O₂ fluorescence. At 208 nm and 216 nm, however, the NO fluorescence can be distinguished from that of O₂ in case of appropriate resolution of the dispersed fluorescence. Fluorescence resulting from O₂ excited from the vibrational ground state (B(v'=4) ← X(v''=0)) is not seen in the engine or flame spectra. This is partly because the frequency that excites this transition is already partly absorbed by O₂ in the ambient air. Also, the oscillator strength for transitions starting from v''=0 is less than for transitions from v''=2,3 and the B(v'=4)-state dissociates fast [65].

In the NO excitation spectrum included in figure 2.14 the strong R₁/Q₁ lines can still be recognised. The apparent increase in background signal is the result of the gaps between the closely spaced lines disappearing due to pressure broadening of the spectral lines. Also, the transition frequency can shift by collisions with neighbouring molecules. At the engine conditions at which this spectrum is obtained (P = 10 bars, T_{gas} = 850 K) the transition frequencies are red-shifted by about 1.5 cm⁻¹ as compared to the corresponding atmospheric flame spectrum. However, due to increased pressure broadening the excitation frequency is relatively insensitive to the actual value of the pressure shift. In the dispersed fluorescence spectrum almost only NO fluorescence from the directly excited D-state is observed (besides the O₂ fluorescence). Fluorescence from the C-state is hardly detectable any more at this crank angle.

The spectrum of figure 2.14 can be used to select suitable wavelengths for excitation and detection of NO inside the combustion chamber of the engine. The interference from hot O₂ has to be minimised whereas the NO signal is preferred to be maximal. The R₁(26.5)/Q₁(32.5)

excitation line at $\lambda_{exc} = 51712.5 \text{ cm}^{-1}$ (193.377 nm) turns out to be a good one, as O_2 excitation is almost avoided (only O_2 fluorescence induced by the broad-band laser radiation is seen) and NO fluorescence is relatively strong. For detection of NO the $\text{D}(v'=0) \rightarrow \text{X}(v''=3)$ fluorescence band at 208 nm is in principle the best one, as the nearest O_2 fluorescence signals are at 205 nm and 211.5 nm. However, if the laser beam is coupled into the engine through the top window, the signal (obtained through the same window) also contains a contribution caused by non-resonant scattering by the top window itself at 207.8 nm.

During the NO measurements the laser radiation is fixed at the wavelength position of the $\text{R}_1(26.5)/\text{Q}_1(32.5)$ transition. The laser is tuned to resonance by monitoring the induced fluorescence from NO in the oxy-acetylene flame shifted by a known amount to get in resonance with the NO transition under engine conditions.

2.5.2 Dispersed fluorescence spectra

A series of dispersed fluorescence spectra averaged over 100 engine cycles in the wavelength range between 200 nm and 265 nm is given in figure 2.15. These spectra are obtained by coupling in the laser beam (exciting the $\text{R}_1(26.5)/\text{Q}_1(32.5)$ NO transition) through the top window and detecting the induced fluorescence, also through the top window, by the OMA system (50 μm entrance slit). The peak at 207.8 nm and the rise in intensity above 250 nm seen in all spectra, both result from laser induced emissions of the top window. The fact that all spectra show spectral structure (either NO or O_2 fluorescence) indicates that fluorescence can be obtained throughout the whole stroke, even at TDC where pressure and temperature are high. The series of spectra shows the O_2 fluorescence mostly induced by the broad-band radiation of the excimer laser as can be seen from the many O_2 fluorescence peaks of different transitions of O_2 ($\text{B}(v'=14,15,16) \rightarrow \text{X}(v'')$ and $\text{B}(v'=10,11) \rightarrow \text{X}(v'')$) arising around TDC. In addition, they show the interference of O_2 fluorescence with the NO fluorescence resulting from the excited D-state as well as from the A-state and C-state populated by EET.

At 19° bTDC almost no fluorescence is seen, whereas at 16° bTDC many narrow fluorescence peaks arise, all resulting from hot O_2 . The O_2 fluorescence appears suddenly on approaching TDC as can be seen in figure 2.16. This figure presents four spectra, with 0.6 degree crank angle between them, showing the rise of the O_2 fluorescence within 1.8 degree crank angle. The sudden appearance of O_2 fluorescence is due to the fast rise in temperature at the start of the combustion. As the combustion continues, the O_2 fluorescence intensity remains almost constant till around 40° aTDC; it then decreases and after 62° aTDC no O_2 fluorescence is seen any more because of the small population of the $v''=2$ and 3 states as a result of the lower temperature.

Fluorescence from NO is seen first around TDC at 235 nm. It results from both the directly excited $\text{D}(v'=0)$ -state and the $\text{A}(v'=0)$ -state, the latter being populated out of the D-state due to rapid EET. At increasing crank angles several broad NO fluorescence bands appear beside the narrow O_2 fluorescence peaks. From around 35° aTDC onwards the structure of the spectra gets dominated by NO fluorescence of increasing intensity. Fluorescence resulting from the $\text{D}(v'=0)$ -state to the $\text{X}(v''=3,4)$ -states is seen at 208 nm (red shoulder of the quartz Raman scattering peak) and 216 nm (blue side of the O_2 peak), respectively. (The fluorescence to the $\text{X}(v''=2)$ -state at 201 nm cannot be seen as its contribution is suppressed by the 193 nm laser mirror in front of the collection optics.) At 225 nm the $\text{D}(v'=0) \rightarrow \text{X}(v''=5)$ and $\text{A}(v'=0)$

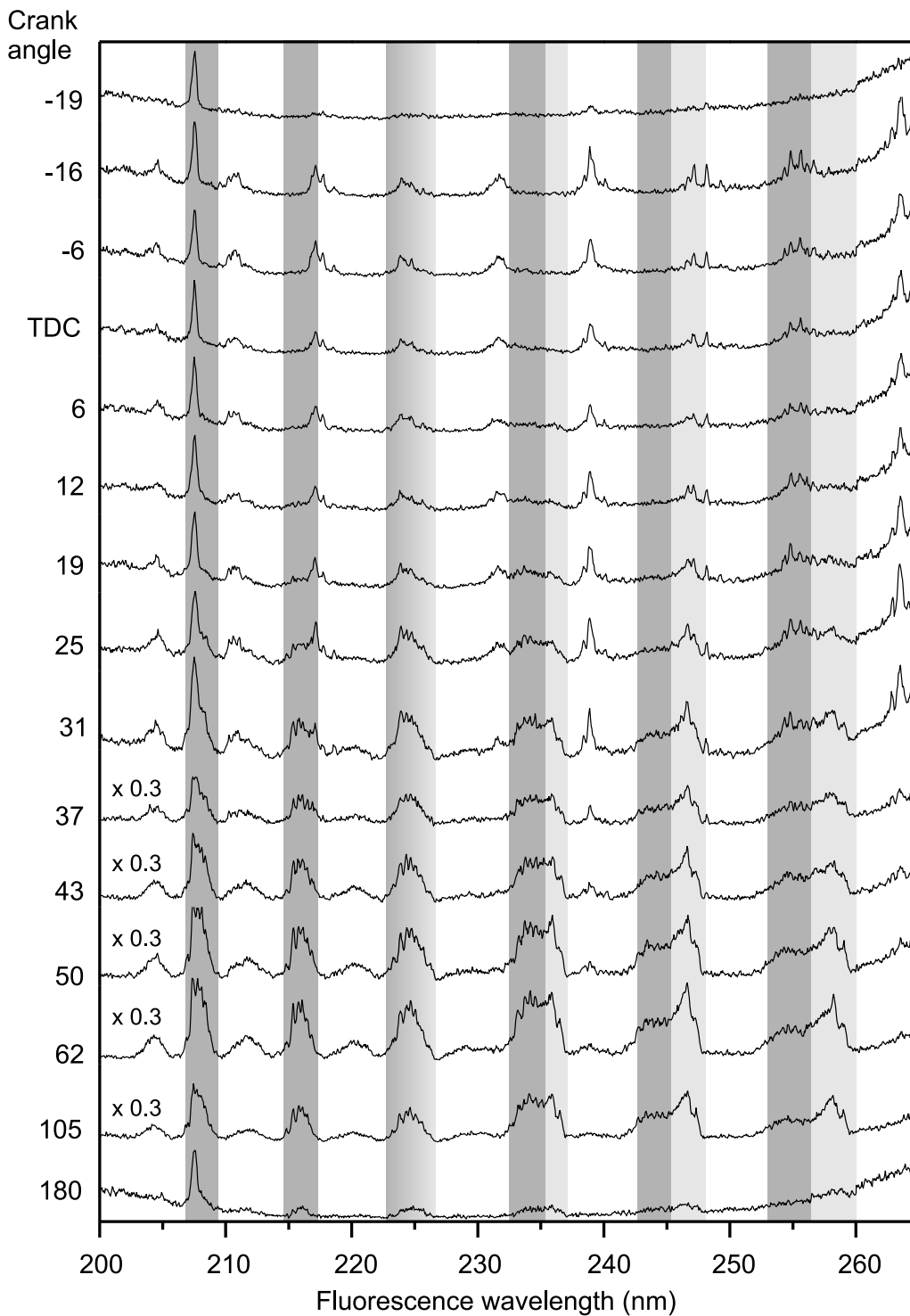


Figure 2.15: A series of dispersed fluorescence spectra (averaged over 100 engine cycles) obtained from the two-stroke engine, showing the interference between NO and O₂ fluorescence. All spectra are at the same scale unless indicated otherwise. The persistent peak at 207.8 nm is an artefact due to the top window. The dark grey bands indicate the positions of the $D^2\Sigma^+(v'=0) \rightarrow X^2\Pi(v''=3-8)$ bands and the light grey bands the positions of the $A^2\Sigma^+(v'=0) \rightarrow X^2\Pi(v''=0-3)$ bands of NO.

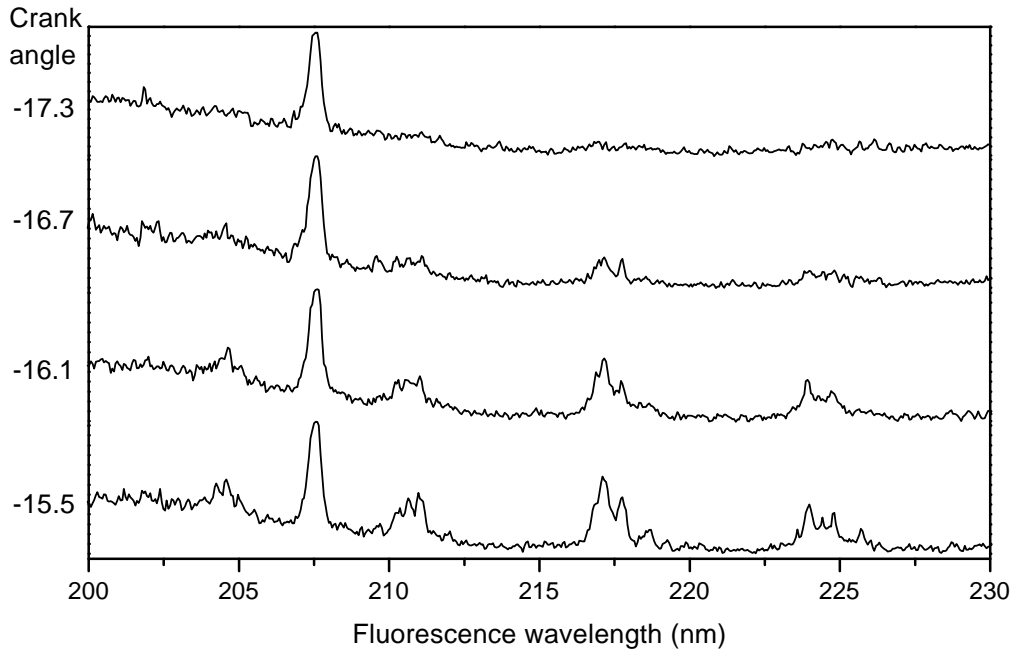


Figure 2.16: Four dispersed fluorescence spectra obtained from the two-stroke engine showing the sudden appearance of O_2 fluorescence due to the fast rise in temperature at the start of the combustion. The peaks around 205, 211, 217.5 and 225 nm can be ascribed to fluorescence from several transitions in the ($B(v'=14,15,16) \rightarrow X(v'')$ and $B(v'=10,11) \rightarrow X(v'')$) bands. The persistent peak at 207.8 nm is an artefact due to the top window.

$\rightarrow X(v''=0)$ fluorescence bands of NO coincide with an O_2 fluorescence band ($B(v'=10) \rightarrow X(v''=7)$). At higher wavelengths, fluorescence from the NO $D(v'=0)$ -state to the $X(v''=6,7,8)$ -states is seen at 234, 244 and 254 nm, respectively. Red shifted from these D -state fluorescence bands is fluorescence from the NO $A(v'=0)$ -state to $X(v''=1,2,3)$ -states, observed at 236, 246.5 and 258.5 nm, respectively. The broad emission signals seen at 204, 212, 220 and 229 nm can be attributed to NO fluorescence from the $C(v'=0)$ -state, populated by EET, to the $X(v''=2-5)$ -states. Some of these NO fluorescence bands also coincide with O_2 fluorescence. In these regions only the shape of the peaks changes during the stroke from a narrow structure around TDC (characteristic for O_2) to a broad, rippled structure towards BDC (characteristic for NO).

These series of spectra show that EET is an important process in the engine as many strong fluorescence peaks are seen from the $C(v'=0)$ -state and the $A(v'=0)$ -state. These states are not directly excited and fluorescence can only arise because these states are populated due to rapid EET. The spectrum obtained at BDC (180° aTDC) shows only little NO fluorescence, indicating that almost all NO has been removed by scavenging. At the moment the exhaust closes, at 105° bTDC, and the next compression stroke starts, all previously formed NO is expected to be flushed out of the combustion chamber.

The NO dispersed fluorescence spectra provide information on the amount of NO present inside the probed volume of the cylinder. The integrated intensity of the NO fluorescence band can be used to obtain an in-cylinder NO density (chapter 4). The spectra also provide information about the position of NO fluorescence bands and O_2 fluorescence peaks using an excitation

wavelength of 51712.5 cm^{-1} obtained from the running engine. This information is necessary to determine a fluorescence band of NO free from O_2 fluorescence for imaging of NO distributions (chapter 5).

2.5.3 Saturation

The dependence of the fluorescence signal on the pulse energy of the excimer laser can be derived from dispersed fluorescence spectra. To this end dispersed fluorescence spectra, averaged over 100 engine cycles, are obtained at 74° aTDC for different laser pulse energies. The laser beam is coupled into the engine through the top window and fluorescence is coupled out also through the top window and detected by the OMA system. Fluorescence from O_2 is absent from these spectra (compare figure 2.15). The integrated fluorescence yield as a function of the laser pulse energy (measured directly in front of the engine entrance window) is shown in figure 2.17 (●). The solid line is a linear fit to the measured data. It can be concluded that the fluorescence yield depends linearly on the laser pulse energy. In itself, such a linear dependence is no guarantee for the absence of saturation (see *e.g.* [68]). Saturation generally occurs when the optical pumping is strong enough to induce ‘considerable’ changes in the equilibrium populations of the molecular levels that are coupled by the pump. In molecules, RET is the fastest process that maintains thermal equilibrium. Thus, as long as RET rates are faster than the pump rate, saturation effects will not be evident, even for laser fluences that would lead to considerable saturation if RET were absent. (The effect of RET on the fluorescence signal is discussed in section 2.3.2.) Therefore, saturation effects will be neglected in the following chapters.

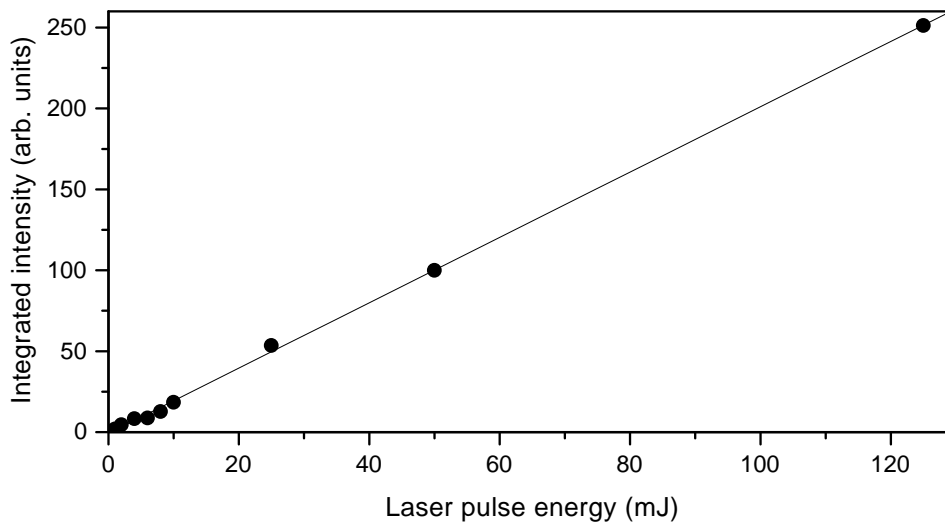


Figure 2.17: The dependence of the integrated fluorescence yield on the pulse energy of the excimer laser derived from dispersed fluorescence spectra (●). The solid line is a linear fit to the data points.

Appendix

The rate equations 2.4 – 2.6 of section 2.3.2 can be solved analytically, yielding

$$N_1(t) = A_1 \exp[-\alpha_+ t] + A_2 \exp[-\alpha_- t] + A_3 \quad (2.8)$$

$$N_2(t) = B_1 \exp[-\alpha_+ t] + B_2 \exp[-\alpha_- t] + B_3 \quad (2.9)$$

$$N_3(t) = k_{23} \exp[-\gamma t] \left[\frac{B_1}{\gamma - \alpha_+} (\exp[(\gamma - \alpha_+) t] - 1) + \frac{B_2}{\gamma - \alpha_-} (\exp[(\gamma - \alpha_-) t] - 1) + \frac{B_3}{\gamma} (\exp[\gamma t] - 1) \right], \quad (2.10)$$

in which a constant pump rate has been assumed. The constants are given by

$$A_1 = + \frac{a_2 - (k_{23} + \gamma)\alpha_-}{(\alpha_+ - \alpha_-)a_2} B_{12} I \quad B_1 = - \frac{a_2 - k_{41}\alpha_-}{(\alpha_+ - \alpha_-)a_2} B_{12} I \quad (2.11)$$

$$A_2 = - \frac{a_2 - (k_{23} + \gamma)\alpha_+}{(\alpha_+ - \alpha_-)a_2} B_{12} I \quad B_2 = + \frac{a_2 - k_{41}\alpha_+}{(\alpha_+ - \alpha_-)a_2} B_{12} I \quad (2.12)$$

$$A_3 = + \frac{k_{41}(B_{12} I + k_{23} + \gamma)}{a_2} \quad B_3 = - \frac{k_{41}B_{12} I}{a_2} \quad (2.13)$$

and

$$\alpha_{\pm} = 1/2 \left(a_1 \pm \sqrt{a_1^2 - 4a_2} \right) \quad (\in \mathbb{R}) \quad (2.14)$$

$$a_1 = (B_{12} + B_{21}) I + k_{41} + k_{23} + \gamma \quad (2.15)$$

$$a_2 = k_{41}B_{21}I + (B_{12}I + k_{41})(k_{23} + \gamma) \quad (2.16)$$

The total fluorescence yield S_{LIF} (number of photons emitted in a specific vibronic band with spontaneous emission rate constant A^*) induced by a constant intensity laser pulse of duration τ_p then follows as

$$\begin{aligned} S_{\text{LIF}} &= \int_0^{\tau_p} A^* \left[N_2(t, I) + N_3(t, I) \right] dt + \int_{\tau_p}^{\infty} A^* \left[N_2(t, I=0) + N_3(t, I=0) \right] dt \\ &= A^* \left[\frac{B_1}{\alpha_+} (1 - \exp[-\alpha_+ \tau_p]) + \frac{B_2}{\alpha_-} (1 - \exp[-\alpha_- \tau_p]) + B_3 \tau_p \right] + \\ &\quad A^* k_{23} \left[\frac{B_1}{\gamma - \alpha_+} \left[\frac{1}{\alpha_+} (1 - \exp[-\alpha_+ \tau_p]) - \frac{1}{\gamma} (1 - \exp[-\gamma \tau_p]) \right] + \right. \\ &\quad \left. \frac{B_2}{\gamma - \alpha_-} \left[\frac{1}{\alpha_-} (1 - \exp[-\alpha_- \tau_p]) - \frac{1}{\gamma} (1 - \exp[-\gamma \tau_p]) \right] + \right. \\ &\quad \left. \frac{B_3}{\gamma} \left[\tau_p - \frac{1}{\gamma} (1 - \exp[-\gamma \tau_p]) \right] \right] + \frac{A^*}{\gamma} \left[N_2(t = \tau_p) + N_3(t = \tau_p) \right]. \end{aligned} \quad (2.17)$$

The Einstein coefficient for absorption, B_{12} , was taken from LIFBASE [69], by adding together the coefficients for the coincident $R_1(26.5)$ and $Q_1(32.5)$ transitions, yielding

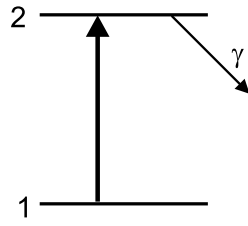


Figure 2.18: *Simplified level scheme used in the weak field limit.*

$B_{12} = 3.23 \text{ nsec}^{-1}/(\text{MW}/(\text{cm}^2\text{cm}^{-1}))$. Neglecting a small difference in degeneracy, $B_{21} = B_{12}$ will be assumed. The RET processes in ground and excited state are here assumed to behave similarly⁵, with a rate constant of $k_{23} = k_{14} = 10^5 \text{ sec}^{-1}\text{Pa}^{-1}$ at room temperature [70]. For the non-radiative decay rate constant γ a similar value is taken [71]. Furthermore, all collisional rate constants will be assumed to possess the same pressure and temperature dependence, given by $k \propto P/\sqrt{T}$. This particular equation is discussed in the Appendix of chapter 4. The value of A^* is irrelevant here, since it is merely a proportionality factor. The laser pulse duration $\tau_p = 20 \text{ nsec}$. All crank angle dependent pressure and temperature values are taken from figure 2.4, using the mean gas curve of figure 2.4d for the temperature.

In the weak field limit, the excitation laser power produces only a negligible perturbation of the population of the lower state level. In this limit, both RET and stimulated emission can be neglected and the simplified level scheme of figure 2.7b reduces to the even more simplified level scheme of figure 2.18. The expression for the fluorescence yield then reduces to

$$S_{\text{LIF}}^{\text{WF}} = \frac{A^*}{\gamma} (1 - \exp[-B_{12} I \tau_p]) \approx \frac{A^*}{\gamma} B_{12} I \tau_p, \quad (2.18)$$

the last step under the condition that $B_{12} I \tau_p \ll 1$. Equation 2.18 is the one that is usually used in the interpretation of LIF signal strengths.

⁵As far as known there are no published data on RET in the NO D(v'=0)-state.

Chapter 3

A method to assess the local attenuation coefficient by Mie scattering using two counterpropagating laser beams

Abstract

Two-dimensional laser induced fluorescence distributions of specific molecules within the combustion chamber of a running diesel engine can be interpreted quantitatively, provided that a number of additional parameters is known. One of the most elusive of these is the local illumination intensity distribution over the field of view, dealt with in this chapter. A method to derive the spatially resolved attenuation coefficient is developed, using two elastic light scattering images, recorded simultaneously from the same area within the engine, but illuminated from opposite directions (double image method). Although exact in principle, this method requires considerable experimental expenditure, and for this reason a more approximate method using only a single elastic scattering image is described as well (single image method). The single image method requires the total transmission losses over the engine's combustion chamber as input. Since the experimental determination of transmission faces its own difficulties, it is described in a separate section. The results of the single image method are compared against those of the double image method. Finally, they are compared against images of the natural emission of the cylinder contents during combustion.

3.1 Introduction

Laser-based optical diagnostics can be used to characterise combustion processes in great detail. They are appreciated for their ability to combine non-intrusiveness with sensitivity and selectivity for specific chemical species and quantum states [30]. As such they have been applied to both open flames and internal combustion engines [31,32]. Laser Induced Fluorescence (LIF) is a diagnostic technique that has the sensitivity to provide spatially and temporally resolved information on minority species in combustion processes. The measurement principle of this technique involves electronic excitation of the molecules of interest by laser radiation and detection of the induced fluorescence. By using a sheet of laser light and recording the fluorescence by a gated CCD camera in a direction perpendicular to the plane of the laser sheet, two-dimensional distributions of the species of interest can be obtained. Two-dimensional LIF has been used to demonstrate the presence of a large number of specific small molecules in a variety of combustion environments [31,32]. Spatially resolved detection of the laser induced fluorescence provides information on the local density of the molecule of interest, but in general this information is hard to quantify. In principle, if the transition is not saturated, the fluorescence intensity is proportional to the intensity of the laser beam, the density of the molecules in the probed state and the fraction of excited molecules that fluoresces at the right wavelength. The proportionality constant, however, depends strongly on the local conditions in the observation point, like pressure, temperature and chemical composition. For a two-dimensional measurement, fluorescence quenching and temperature might be inhomogeneous as the local conditions within the observation volume can be different at each position. In addition, the local laser intensity will generally vary over the field of view, due to scattering and absorption. In practice, the laser intensity distribution within a certain measurement volume is difficult to assess. In general, when LIF is to be applied to practical combustion devices, factors that determine the laser intensity in the measurement volume comprise *i*) losses due to the (often limited) optical access to the combustion, *ii*) extinction between the access ports and the actual observation area and *iii*) extinction within the observation area itself. Although the last two loss factors, in principle, are caused by the same processes, they should be distinguished in the analysis. In the following, several published attempts to deal with this problem will be discussed, and subsequently the specific problem of NO detection inside the combustion chamber of a running diesel engine by means of UV LIF will be considered.

Stepowski [72] developed a technique in which the fluorescence signal obtained from OH excited by laser light in a flame is quantified by a locally determined absorption between two closely spaced points. To be independent of the local environment, which could be different for the two probed points, a bi-directional laser beam configuration was used. After the first laser beam a second laser beam is sent through the flame along the same path but in opposite direction and with a slight delay. *In situ* calibration of the fluorescence signal is determined from the ratio of the two fluorescence signals induced by the two excitation beams. In this method it is assumed that the attenuation of the laser beam is caused only by absorption by the molecule of interest. Versluis *et al.* [73] have extended this technique and presented a detection scheme for two-dimensional spatially resolved absolute number density measurements of OH radicals in flames. The OH concentration is derived from the ratio of two OH LIF images, which are obtained from two laser beams travelling through the flame along the same path but in opposite direction. By using this bi-directional approach and division of the images on a

pixel-to-pixel basis, quenching rates are eliminated. A disadvantage of this method is the loss in sensitivity, as by the division of both signals the experiment in principle is reduced to an absorption measurement and the sensitivity of the LIF technique is lost.

This method cannot directly be applied to measure absolute concentrations of molecules in diesel engines as the process that reduces the intensity of the laser radiation is more complicated. Whereas in the flame experiments [72, 73] attenuation of the laser intensity is (assumed to be) caused by absorption of the radiation by only the species of interest, this molecular absorption plays only a minor part in the decrease of the laser intensity in the diesel engine. On its way through the combustion chamber, attenuation of the laser beam is mainly caused by scattering off and absorption by soot particles and oil and fuel droplets. Therefore, the laser intensity attenuation depends on the density of scattering and absorbing particles and oil and fuel droplets rather than on the density of the absorbing molecules. Although in this case the method with the two anti-collinear laser beams is not useful to determine the absolute concentration of the molecular species of interest it can, however, be used to determine a local factor for the attenuation of the laser radiation. This local attenuation coefficient is required to calculate the local laser intensity, one of the parameters that is necessary to quantify two-dimensional LIF distributions.

In the present work the technique with the bi-directional laser beam configuration is adapted to obtain an effective attenuation coefficient for the laser intensity which can be used to calculate the local laser intensity. To this end the elastically scattered laser radiation, the intensity of which is proportional to the local laser intensity, is recorded. To be independent of the local scattering circumstances two laser beams are used, the second of which traverses the engine with a short delay (≈ 50 ns) and in opposite direction as compared to the first laser beam. Two cameras are used to record two-dimensional images of the elastically scattered laser radiation. Contrary to the flame experiment [73], in which the images are recorded after each other on the same camera, both images now have to be recorded at nearly the same moment using two laser and camera systems, as the combustion in a diesel engine is very irreproducible. After some manipulation, discussed below, this results in an image representing an attenuation factor for the laser intensity which can be used to reconstruct the local laser intensity.

Using this method in practice for the determination of NO density distributions implies that three images, scattering distributions in both directions and a NO fluorescence distribution, would have to be recorded simultaneously. This is rather complicated, as three camera systems and (at least) two laser beams would have to be used. It would be of interest, if possible, to use only one scattering image to arrive at the local laser intensity. In addition, therefore, a method is developed to extract the local laser intensity from only one scattering image. This method, which will be denoted as the single image method, is checked by comparing its result with that of the method using images obtained from two laser beams travelling through the engine in opposite direction, denoted as the double image method.

Finally, the single image method is applied to elastic scattering images in order to compare them to simultaneously measured flame emission images.

3.2 Theory

In general, images recorded by a CCD camera represent a spatially resolved light scattering efficiency. Assuming that only a thin plane perpendicular to the line of sight of the camera is illuminated, the signal $S(x, y)$ given by any pixel can be written as

$$S(x, y) = G(x, y) n(x, y) \sigma(x, y) I_L(x, y), \quad (3.1)$$

in which (x, y) represent co-ordinates in the illuminated plane, $I_L(x, y)$ denotes the local illumination intensity, $\sigma(x, y)$ is a light scattering cross section, $n(x, y)$ the density of scattering particles and $G(x, y)$ a collection efficiency. The detailed forms of $n(x, y)$ and $\sigma(x, y)$ depend on the actual light scattering mechanism (like *e.g.* LIF, Rayleigh/Mie, Raman), whereas $G(x, y)$ is determined mainly by the experimental setup.

If density distributions, $n(x, y)$, are to be determined from the light scattering images, all other factors in equation 3.1 have to be known. Evaluation of these factors results in expressions that depend on the local conditions (pressure, temperature, laser intensity) and therefore on the position (x, y) . Probably the most elusive factor in equation 3.1 is the local laser intensity $I_L(x, y)$, a factor which cannot be measured directly in a running engine, but in general will not be uniform over the whole field of view. By the use of two elastic scattering images obtained (quasi-)simultaneously from two laser beams which traverse the engine in opposite direction, but along the same path, the local laser intensity can be reconstructed. This method is similar to the method used to obtain absolute OH concentration profiles in flames as reported by Versluis *et al.* [73]. Alternatively, the local laser intensity can be reconstructed from one elastic scattering image if some assumptions are made. Both methods are described below.

3.2.1 Double image method

A schematic top view of the scattering experiment in which the laser sheet traverses the engine from side window W1 to side window W2, called the forward direction, is given in figure 3.1. The x -axis is taken along the laser beam, the y -axis along the width of the laser sheet. The thickness of the light sheet is neglected. Elastically scattered light is measured in a direction perpendicular to the laser sheet (z -direction) between the boundaries $x = 0$ and $x = L(y)$ (determined by the size of the observation window) for the whole width of the laser sheet. As the laser beam propagates in the x -direction, only the intensity decrease in x -direction has to be taken into account¹ and the two-dimensional problem can be reduced to a one-dimensional problem by analysing each line along the x -direction, for a fixed value of y , separately.

The measured intensity of the laser radiation scattered from a position (x, y) generated by the laser sheet traversing the engine in forward direction, $S_{for}(x, y)$, is given by equation 3.1, which can be slightly adapted for this specific situation to read

$$S_{for}(x, y) = C A(x, y) I_{for}(x, y) [n\sigma]_{sca}(x, y), \quad (3.2)$$

in which C is a proportionality constant including a number of experimental parameters like camera sensitivity and losses caused by the optics used for imaging and filtering. $A(x, y)$ is a factor describing the attenuation of the scattered light on its way to the top window as well as the

¹This implies that secondary scattering is neglected; see also the Appendix

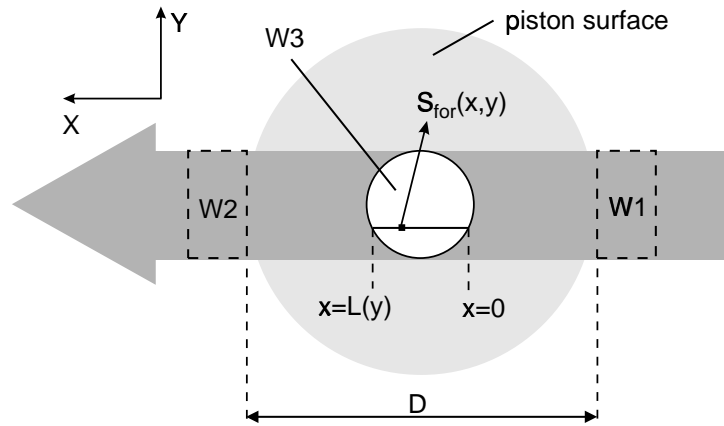


Figure 3.1: Schematic top view of the laser sheet traversing the engine in the forward direction from side window W1 to side window W2. The x-axis is taken along the laser sheet and the signal is obtained in a direction perpendicular to the laser sheet (z-direction) through the top window W3 between the boundaries $x = 0$ and $x = L(y)$. The piston surface with a diameter $D = 81$ mm is also indicated.

losses caused by the top window itself. The factor $[n\sigma]_{sca}(x, y)$ represents the effective contribution of all scatterers at position (x, y) which is actually given by $\sum_j n_{j,sca}(x, y)\sigma_{j,sca}(x, y)$, where the sum is over all different scatterers present and $n_{j,sca}(x, y)$ is the density of scattering particles of a certain type with a scattering cross section $\sigma_{j,sca}(x, y)$. However, in the experiment the contribution of different types of particles cannot be separated, and therefore they are combined into one effective scattering term. The laser intensity along the forward direction, $I_{for}(x, y)$, is given by Lambert-Beer's law as

$$I_{for}(x, y) = I_{for}(0, y) \exp\left(-\int_0^x [n\sigma]_{ext}(x', y) dx'\right), \quad (3.3)$$

in which $I_{for}(0, y)$ is the initial laser intensity at $(x = 0, y)$. Note that this is not the laser intensity at the entrance window of the engine, as the laser beam has to travel through the entrance window and a part of the combustion chamber before reaching the observation area (see figure 3.1). The factor $[n\sigma]_{ext}(x, y)$ is an effective attenuation coefficient for the laser radiation given by

$$[n\sigma]_{ext}(x, y) = [n\sigma]_{sca}(x, y) + [n\sigma]_{abs}(x, y), \quad (3.4)$$

where $[n\sigma]_{abs}(x, y)$ is the effective contribution of absorption to the laser extinction, and which consists of different components, similar to $[n\sigma]_{sca}(x, y)$. Note that, while the scattering is due only to the density and cross section of scattering particles, the attenuation of the intensity of the laser radiation is caused by both scattering and absorption.

If the laser sheet traverses the engine along exactly the same path but in opposite direction, which is called the backward direction, similar equations can be derived. In this case the measured intensity of the scattered radiation, $S_{back}(x, y)$, at a position (x, y) is given by

$$S_{back}(x, y) = C' A(x, y) I_{back}(x, y) [n\sigma]_{sca}(x, y), \quad (3.5)$$

where the proportionality constant C' has not necessarily the same value as C in equation 3.2, but the attenuation factor $A(x, y)$ is the same in both cases. The laser intensity of the backward travelling sheet, $I_{back}(x, y)$, with an initial intensity $I_{back}(L(y), y)$ at $(x = L(y), y)$, is given by

$$I_{back}(x, y) = I_{back}(L(y), y) \exp \left(- \int_{L(y)}^x [n\sigma]_{ext}(x', y) d(-x') \right), \quad (3.6)$$

in which the reverse direction of integration is indicated explicitly.

If the forward and backward scattering signals are recorded simultaneously from the same area, both the loss factors $A(x, y)$ as well as the absorption cross section and density of the scattering particles are the same, and cancel if both scattering signals are divided. Using equations 3.2 to 3.6, the ratio $R(x, y)$ between both scattering signals can be written as

$$\begin{aligned} R(x, y) &\stackrel{\text{def}}{=} \frac{S_{back}(x, y)}{S_{for}(x, y)} \quad (3.7) \\ &= \left(\frac{C' I_{back}(L(y), y)}{C I_{for}(0, y)} \right) \exp \left(- \int_{L(y)}^x [n\sigma]_{ext}(x', y) d(-x') + \int_0^x [n\sigma]_{ext}(x', y) dx' \right) \\ &= \left(\frac{C' I_{back}(L(y), y)}{C I_{for}(0, y)} \right) \exp \left(2 \int_0^x [n\sigma]_{ext}(x', y) dx' - \int_0^{L(y)} [n\sigma]_{ext}(x', y) dx' \right). \end{aligned}$$

Note that after the division of the signals only the part concerning the extinction of the laser radiation is left and the experiment actually is reduced to measuring extinction. Taking the natural logarithm of the ratio of the scattered signals results in

$$\ln R(x, y) = \ln \left(\frac{C' I_{back}(L(y), y)}{C I_{for}(0, y)} \right) + 2 \int_0^x [n\sigma]_{ext}(x', y) dx' - \int_0^{L(y)} [n\sigma]_{ext}(x', y) dx'. \quad (3.8)$$

If the derivative of $\ln R(x, y)$ with respect to x is taken, only the second term on the right-hand side of equation 3.8 contributes, since the other terms are independent of the variable x . Using the Leibnitz theorem for differentiation of an integral this gives

$$\frac{d}{dx} \ln R(x, y) = 2 [n\sigma]_{ext}(x, y), \quad (3.9)$$

which can be rewritten as

$$[n\sigma]_{ext}(x, y) = \frac{1}{2} \frac{d}{dx} \ln \left(\frac{S_{back}(x, y)}{S_{for}(x, y)} \right). \quad (3.10)$$

Thus, an effective attenuation coefficient $[n\sigma]_{ext}$ at any position (x, y) can be determined from two simultaneously recorded elastic scattering images of the same area by calculating the slope

of the natural logarithm of their ratio. As this coefficient is derived without making any assumptions, it gives the exact attenuation for the laser radiation inside the combustion chamber. Moreover, this result is independent of transmission losses in the laser entrance windows, as well as losses in the optical detection pathway. An image of the local laser intensity decrease inside the observation volume in the cylinder can be calculated by integrating $[n\sigma]_{ext}(x, y)$ over the path in the observation volume, for both the forward and backward directed laser beams (using equation 3.3 or 3.6, respectively). The average attenuation coefficient can be extrapolated to estimate the total attenuation over the whole optical path in the combustion chamber.

3.2.2 Single image method

If only one elastic scattering image is available (*e.g.* in forward direction), the local laser intensity can still be extracted from the image if some assumptions are made. First it is assumed that a constant relation exists between the contribution to the attenuation of the laser radiation caused by absorption and by scattering. This assumption is based on the fact that for small enough particles their properties will be determined by the material rather than by exact shape or size [75]. The contributions of scattering and absorption to the attenuation of the laser intensity are assumed to be related by a proportionality constant ξ as

$$[n\sigma]_{sca}(x, y) = \xi [n\sigma]_{abs}(x, y). \quad (3.11)$$

If the approximation of a constant relation between scattering and absorption is used, the laser intensity given in equation 3.3 can be rewritten as

$$I_{for}(x, y) = I_{for}(0, y) \exp\left(-\int_0^x (1 + \xi) [n\sigma]_{abs}(x', y) dx'\right). \quad (3.12)$$

Combining expression 3.12 for the laser intensity with equation 3.2 for the intensity of the scattered laser radiation results in

$$\begin{aligned} S_{for}(x, y) &= C I_{for}(0, y) \xi [n\sigma]_{abs}(x, y) \exp\left(-\int_0^x (1 + \xi) [n\sigma]_{abs}(x', y) dx'\right) \\ &= -\frac{C \xi}{1 + \xi} I_{for}(0, y) \frac{d}{dx} \exp\left(-\int_0^x (1 + \xi) [n\sigma]_{abs}(x', y) dx'\right). \end{aligned} \quad (3.13)$$

Integrating both sides of equation 3.13 results in

$$\int_0^x S_{for}(x', y) dx' = \frac{C \xi}{1 + \xi} I_{for}(0, y) \left(1 - \exp\left(-\int_0^x (1 + \xi) [n\sigma]_{abs}(x', y) dx'\right)\right), \quad (3.14)$$

in which the exponential term represents the local laser intensity decrease inside the observation volume. This intensity decrease can be calculated from the elastic scattering image by integrating the signal if the laser intensity at the beginning of the observation volume $I_{for}(0, y)$

is known. This intensity can be approximated from the total transmission of the laser radiation through the engine. On the assumption of an average attenuation coefficient that does not vary appreciably over length scales corresponding to the size of the observation area, the intensity decrease in the first part of the combustion chamber, that cannot be seen through the window, can be determined.

3.2.3 Transmission

The intensity of the laser radiation, where it enters the observation area at the position $(0, y)$ in the combustion chamber of the engine, is given by

$$I_{for}(0, y) = I_{W1} T_{W1} \exp \left(- \int_{W1}^0 [n\sigma]_{ext}(x', y) dx' \right), \quad (3.15)$$

where I_{W1} is the intensity of the laser radiation before entering the engine (through window W1) and T_{W1} the transmission of the entrance window. Using an average attenuation coefficient, $[\overline{n\sigma}]_{ext}$, equation 3.15 can be rewritten as

$$I_{for}(0, y) = I_{W1} T_{W1} \exp \left(- [\overline{n\sigma}]_{ext} \frac{(D - L)}{2} \right), \quad (3.16)$$

where D is the diameter of the cylinder (see figure 3.1).

The average attenuation coefficient can be obtained from the total transmission of the laser radiation through the combustion chamber of the running engine. For the forward direction the transmission through the combustion chamber of the engine is given by

$$I_{W2} = I_{W1} T_{W1} T_{W2} \exp (-[\overline{n\sigma}]_{ext} D), \quad (3.17)$$

where I_{W2} the intensity of the laser radiation after its way through the firing engine and the two side windows and T_{W2} the transmission of the exit window. Equation 3.17 can be rewritten as

$$[\overline{n\sigma}]_{ext} = -\frac{1}{D} \ln \left(\frac{I_{W2}}{I_{W1} T_{W1} T_{W2}} \right), \quad (3.18)$$

which subsequently can be used in equation 3.16, if one assumes that the *average* attenuation in the whole cylinder is the same as that in the invisible parts (note that $L \approx 0.3D$). However, a disadvantage of this method is that the window transmission, which is difficult to measure, is included in the result.

Alternatively, the average attenuation coefficient of the observation volume, without any contribution from the side windows, can be derived from the double image method. The effective attenuation coefficient, $[n\sigma]_{ext}(x, y)$ from equation 3.10, can be used to calculate an average attenuation of the laser beam over the observation area, which can be assumed to be equal to the average attenuation for the whole path in the combustion chamber.

Using the average attenuation coefficient in the integral of equation 3.14 and integrating over the part of the cylinder that can be seen (*i.e.* $0 < x < L(y)$) results in

$$\int_0^{L(y)} S_{for}(x', y) dx' = \frac{C \xi}{1 + \xi} I_{for}(0, y) \left(1 - \exp \left(-(1 + \xi) [\overline{n\sigma}]_{abs} L(y) \right) \right), \quad (3.19)$$

which can be rewritten as

$$I_{for}(0, y) = \frac{1 + \xi}{C \xi} \left(1 - \left(\frac{I_{W2}}{I_{W1} T_{W1} T_{W2}} \right)^{\frac{L(y)}{D}} \right)^{-1} \int_0^{L(y)} S_{for}(x', y) dx'. \quad (3.20)$$

If this result for the laser intensity at the beginning of the observation area is used in equation 3.14, an expression for the local laser intensity decrease can be derived

$$\frac{I_{for}(x, y)}{I_{for}(0, y)} = 1 - \left(1 - \left(\frac{I_{W2}}{I_{W1} T_{W1} T_{W2}} \right)^{\frac{L(y)}{D}} \right) \frac{\int_0^x S_{for}(x', y) dx'}{\int_0^{L(y)} S_{for}(x', y) dx'}. \quad (3.21)$$

Note that this expression is independent of the exact value of the proportionality constant ξ ; only the assumption of a constant relation between absorption and scattering is used. If the value of ξ is varied, only the absolute values of the laser intensity change, but not the distribution. A method to estimate the value of ξ is given in the Appendix.

3.3 Experimental setup

The engine used in the experiment is an optically accessible one-cylinder two-stroke direct injection diesel engine (bore $D=81$ mm) which is described in detail in chapter 2, section 2.2. The engine is steadily running (*i.e.* not skip-fired) on standard commercial diesel fuel and ambient (non-oxygen-enriched) intake air. Optical access to the combustion chamber is provided by quartz windows (Suprasil I) in the cylinder head. Two rectangular side windows (W1 and W2; 25×10 mm²; thickness 25 mm) are placed diametrically in the wall in such a way that a laser sheet can enter the combustion chamber through one of them and can leave it through the other. A cylindrical top window (W3; diameter 25 mm; thickness 35 mm) is placed centrally in the top of the cylinder head.

3.3.1 Double image method

The experimental setup showing the engine, two laser beams and two CCD cameras is schematically given in figure 3.2. The laser systems used are both pulsed (10 Hz) excimer lasers (Compex 350T and EMG 150 MSCT; Λ -Physik) running on ArF delivering radiation tunable between 192.9 and 193.9 nm. Both deliver pulses with a duration of 20 ns, a bandwidth of 1 cm^{-1} and a rectangular beam profile (25×3 mm²). The laser beams are oriented in a horizontal plane parallel to the piston upper surface and shaped into a thin sheet (25×0.5 mm²) by two cylindrical lenses. The laser sheet traversing the engine in forward direction is coupled into the engine through the side window W1 and coupled out through the other side window W2. The second laser sheet going in backward direction is directed anti-collinearly through the engine (coupled in through W2 and out through W1). The sheets spatially overlapped inside the engine. The elastically scattered laser radiation is detected in a direction perpendicular to the laser sheets through the top window by two similar camera systems (figure 3.2). By the use of 193 nm

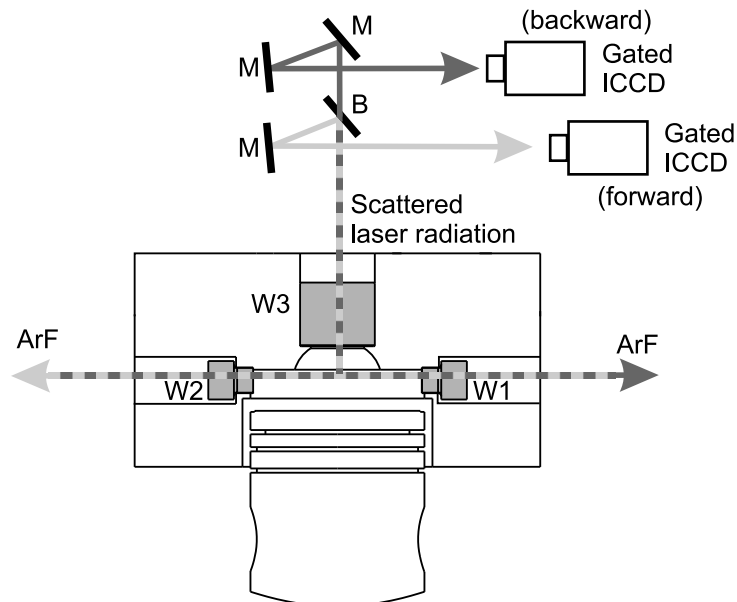


Figure 3.2: Schematic view of the experimental setup. One laser sheet traverses the engine in the forward direction from side window W1 to side window W2, while the other traverses the engine in the backward direction from W2 to W1. Elastically scattered radiation is detected through the top window W3 in a direction perpendicular to the laser sheets by two intensified CCD cameras. B, beam splitter; M, mirror.

optics the contribution of the natural flame emission is completely suppressed. Both cameras are gated intensified CCD cameras (ICCD-576G/RB-E; Princeton Instruments) whose output is digitised (ST-138; Princeton Instruments) and sent to a computer for further processing. The used gate width is 25 ns. The position of the piston, the laser pulses and camera systems are synchronised using a delay generator. The time delay between both lasers is set to 50 ns. This delay is long enough to be able to detect the scattered radiation from both sheets separately, while it is short enough for both scattering signals to originate from essentially the same distribution of scattering particles inside the combustion chamber. For the processing of the images home-developed software is used [74]. For the processing it is important that the images correspond to exactly the same field of view, as small misalignments may introduce artificial structure in the result. Proper alignment of the images was achieved using separately recorded images of a highly structured reference picture put into the engine instead of the top window.

3.3.2 Single image method

In the present experiment the single image method is applied to the elastic scattering images obtained with the setup described above, in order to be able to compare the results with those obtained using the double image method. But, in general, the single image method will be applied to an image of the elastically scattered radiation recorded simultaneously and from the same area as a fluorescence image of NO. For this purpose, although the setup used to obtain two scattering images simultaneously could be used, the experiment can also be done using only one laser system. If the laser is tuned to a NO resonance, the NO fluorescence and

elastically scattered radiation can be obtained from the same laser pulse with different filters (one transmitting NO fluorescence and one transmitting the laser radiation) in front of the two camera systems. If instead of the NO fluorescence the natural flame emission is recorded, the same setup can also be used to obtain one scattering image and one image of the natural flame emission.

3.3.3 Transmission

To obtain information about the transmission of the laser radiation through the combustion chamber, the absolute attenuation of the 193 nm laser radiation through the firing engine and the side windows is measured. The laser beam is coupled in and out through the side windows and the transmitted radiation is detected behind the exit window by a CCD camera. However, as the contribution of the windows, which cannot be measured directly, is still included in the result this method gives the transmission through the combustion chamber in arbitrary units only. Results will be compared with those derived independently from the double image method.

3.4 Results and Discussion

Using the setup with two laser beams propagating in forward and backward direction through the engine and two camera systems, images of the elastically scattered laser radiation were measured in forward and backward direction as a function of crank angle. They will be denoted as forward and backward elastic scattering images. Forward, $S_{for}(x, y)$ (column 1), and backward, $S_{back}(x, y)$ (column 2), elastic scattering images taken at different crank angles are given in figure 3.3. The images are averaged over five engine cycles. The side window W1 is located at the right hand side and W2 at the left hand side of the images, so that in forward direction the laser beam is directed from right to left whereas in backward direction it is directed from left to right (indicated in the figure by the horizontal arrows). The dark spots that are present in all images are the result of dirt on the outside of the top window. However, as the transmission losses due to the top window are included in the factors $A(x, y)$ in equations 3.2 and 3.5, the effect of the dirt will cancel in the determination of the fluorescence ratio (equation 3.8), and the final attenuation factor (equation 3.10) is not affected by this dirt². For crank angles below 37° aTDC no elastic scattering images are presented because the signal becomes too weak.

The images were analysed using both the double image method and the single image method. By comparing the results of both methods, the assumptions made in the single image method can be checked.

3.4.1 Double image method

First, the double image method, described in section 3.2.1, is applied to determine the distribution of the local laser attenuation coefficient, $[n\sigma]_{ext}(x, y)$ (equation 3.10), as a function of crank angle. The distributions, which are given in figure 3.3 (column 3), show a fairly homogeneously distributed attenuation factor over the whole observation area. No places are seen

²Of course, some signal must remain in the images at the location of the dirt, otherwise the ratio in equation 3.10 is not defined.

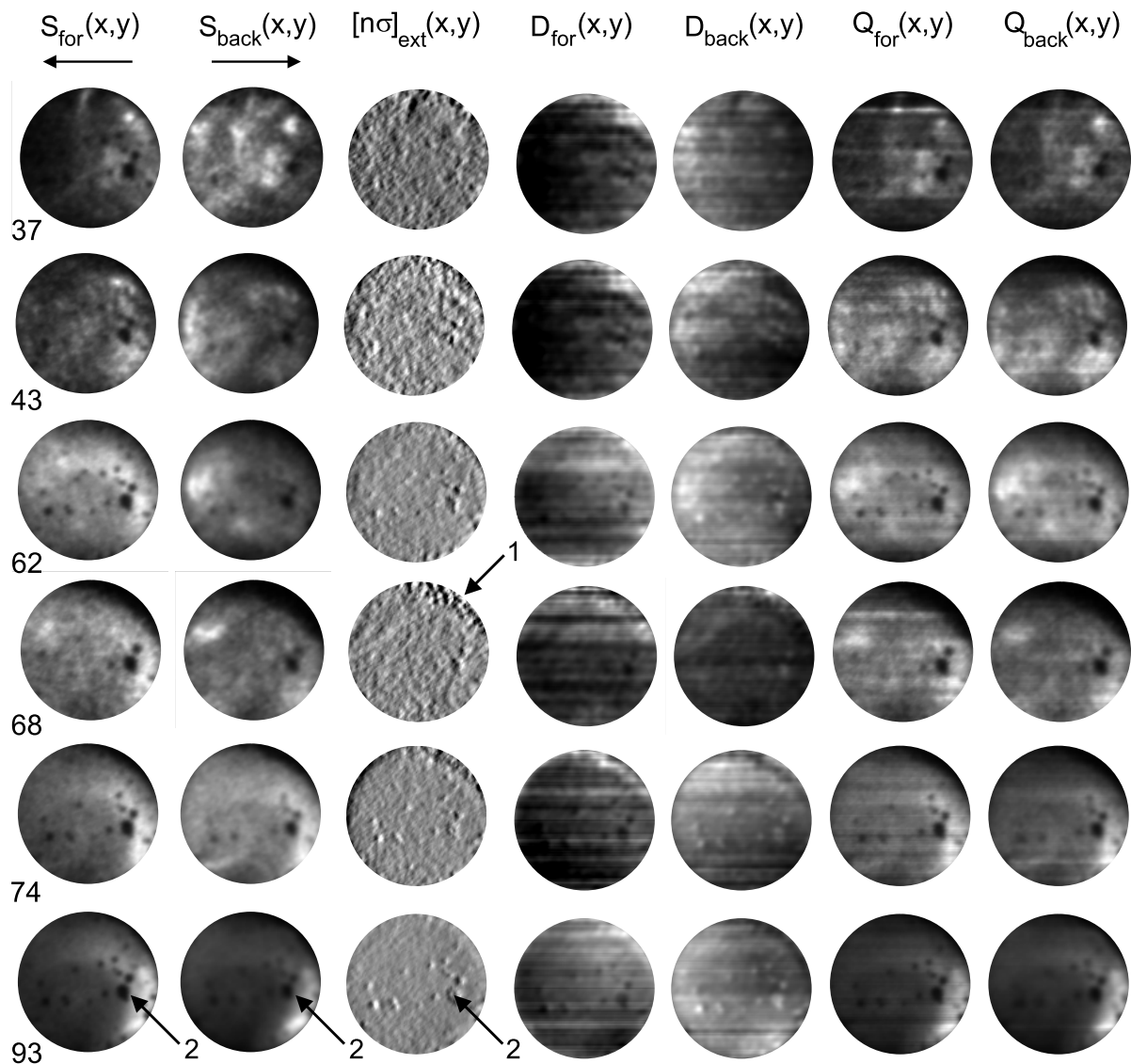


Figure 3.3: Pairs of forward, $S_{for}(x, y)$ (column 1), and backward, $S_{back}(x, y)$ (column 2), elastic scattering images averaged over five cycles obtained at 37, 43, 62, 68, 74 and 93° aTDC. The attenuation coefficient, $[n\sigma]_{ext}(x, y)$ (column 3), derived from the elastic scattering images using the double image method (section 3.2.1). The local laser intensity decrease in forward, $D_{for}(x, y)$ (column 4), and backward, $D_{back}(x, y)$ (column 5), direction obtained from the local attenuation factor. The effective scatterer distributions determined from the forward, $Q_{for}(x, y)$ (column 6), and backward, $Q_{back}(x, y)$ (column 7), elastic scattering image and corresponding laser intensity decrease image. Laser beam directions are indicated in the figure. The dark spots that are present in all scattering images are the result of dirt on the outside of the top window. All images are individually scaled and represented in a linear grey scale ranging from black (zero intensity) to white (maximum intensity). The faint horizontal structure in some of the images is an artefact of the software used for image processing. Arrows are explained in the text.

where the attenuation is significantly stronger or weaker. As expected, the average attenuation coefficient decreases towards BDC as a result of the decreasing density of particles that scatter and absorb the laser radiation. It can be used to obtain the average attenuation of the radiation over the field of view which can be extrapolated to estimate the transmission over the whole optical path in the combustion chamber (see section 3.4.3). The effect of a weak elastic scattering signal on the result is clearly seen in the attenuation factor distribution at 68° aTDC. In the upper right side of the image the signal contains a lot of noise (pock-marked appearance (arrow 1)), resulting from the division of two small signals. Although present in all $[n\sigma]_{ext}(x, y)$ distributions, the one at 93° aTDC most clearly shows that dirt on the observation window may lead to artificial structure in the $[n\sigma]_{ext}(x, y)$ distribution (arrow 2), in spite of the fact that inhomogeneities in the collection efficiency should cancel, as argued in section 3.2.1. The reason why this expected cancellation does not occur completely can probably be found in that the dark spots cause steep intensity gradients in the elastic scattering images, which are amplified by the derivative taken in order to arrive at the $[n\sigma]_{ext}(x, y)$ distribution (equation 3.10). Both noise and small misalignments of the two images may therefore easily lead to structures as those in figure 3.3.

An image of the local laser intensity decrease inside the observation volume in the cylinder can be calculated by integrating the effective attenuation coefficient, $[n\sigma]_{ext}(x, y)$, over the path in the observation volume and taking the exponent of it. Using equation 3.3 results in

$$\exp\left(-\int_0^x [n\sigma]_{ext}(x', y) dx'\right) = \frac{I_{for}(x, y)}{I_{for}(0, y)} \stackrel{\text{def}}{=} D_{for}(x, y). \quad (3.22)$$

$D_{for}(x, y)$ represents the laser intensity decrease in forward direction. For the backward direction, $D_{back}(x, y)$, representing the laser intensity decrease in backward direction, follows from equation 3.6,

$$\exp\left(-\int_{L(y)}^x [n\sigma]_{ext}(x', y) d(-x')\right) = \frac{I_{back}(x, y)}{I_{back}(L(y), y)} \stackrel{\text{def}}{=} D_{back}(x, y). \quad (3.23)$$

The local laser intensity decrease, calculated for both directions of the laser beam, using equations 3.22 and 3.23, is also included in figure 3.3 (columns 4 and 5). As expected, the largest attenuation is found for crank angles closer to TDC. For crank angles $\leq 62^\circ$ aTDC the $D(x, y)$ -images of figure 3.3 show a decreasing intensity along the propagation direction of the laser beam. At higher crank angles, the laser intensity decrease images are more or less uniform. This indicates only weak laser attenuation over the observation area, however the intensity still decreases with about 40% over the field of view for crank angles $\geq 68^\circ$ aTDC. Since 40% transmission loss is a substantial amount, this illustrates the low sensitivity of the double image method applied to this particular combustion device. Interestingly, the dark spots in the original images (arrows 2) show up much less conspicuously in the $D(x, y)$ -images than in the $[n\sigma]_{ext}(x, y)$ -images (column 3), because the integration involved in the calculation of the former cancels the error-amplification of the differentiation required to arrive at the latter.

Dividing the scattering image by the intensity decrease image results, for the forward direction, in

$$\frac{S_{for}(x, y)}{D_{for}(x, y)} = C A(x, y) I_{for}(0, y) [n\sigma]_{sca}(x, y) \stackrel{\text{def}}{=} Q_{for}(x, y), \quad (3.24)$$

in which $Q_{for}(x, y)$ represents an effective scatterer density distribution obtained from the forward directed laser beam. Using the backward scattering image and the intensity decrease image in backward direction leads to a similar expression for $Q_{back}(x, y)$. Note that the effective scatterer distributions $Q(x, y)$ do not reflect the actual $[n\sigma]_{sca}(x, y)$, but are weighted by non-uniformities in both the illumination intensity and the optical detection pathway. Only if both the incident laser intensity and the collection efficiency are uniform, does $Q(x, y)$ reflect the scatterer distribution $[n\sigma]_{sca}(x, y)$. The effective scatterer distributions obtained from both the forward, $Q_{for}(x, y)$ (column 6), and backward, $Q_{back}(x, y)$ (column 7), direction are also given in figure 3.3. For crank angles $\geq 68^\circ$ aTDC the scatterer distributions are almost similar to the elastic scattering images, which results from the fact that the change in laser intensity over the observation area is only small. Also for smaller crank angles the same features are seen although they are less pronounced.

As the backward and forward images are obtained simultaneously from the same area, the factors $[n\sigma]_{sca}(x, y)$ and $A(x, y)$ should be the same. Therefore, if both effective scatterer densities are divided the $[n\sigma]_{sca}(x, y)$ and $A(x, y)$ factors cancel, resulting in

$$\frac{Q_{for}(x, y)}{Q_{back}(x, y)} = \frac{C I_{for}(0, y)}{C' I_{back}(L(y), y)} = C(y). \quad (3.25)$$

Consequently, the scattering images may only differ by a factor $C(y)$, which may vary in y -direction but should be constant in x -direction. The variation in y -direction is a measure for the variation of the intensity difference of the laser beams where they enter the observation area ($x = 0$ and $x = L(y)$). It is found that the effective scatterer distributions obtained from the forward and backward elastic scattering image show hardly any difference in y -direction (compare Q_{for} and Q_{back} in columns 6 and 7 in figure 3.3). This indicates that the intensity of the laser beams in y -direction at the edge of the observation area is almost homogeneously distributed, which is in agreement with the fact that the laser attenuation ($[n\sigma]_{ext}(x, y)$, figure 3.3 column 3), is found to be quite homogeneous over the field of view. The fact that the effective scatterer distributions show structure, in contrast to those of the laser attenuation coefficient (involving scattering and absorption), indicates that the contribution from absorption to the laser attenuation is much larger than the contribution from scattering.

To obtain some information about the variation in the effective attenuation coefficient for different engine cycles three single shot images obtained at 62° aTDC were analysed. For both directions the elastic scattering images, $S_{for}(x, y)$ and $S_{back}(x, y)$ (columns 1 and 2), local attenuation factor, $[n\sigma]_{ext}(x, y)$ (column 3), laser intensity decrease, $D_{for}(x, y)$ and $D_{back}(x, y)$ (columns 4 and 5) and effective scatterer distribution $Q_{for}(x, y)$ and $Q_{back}(x, y)$ (columns 6 and 7) are given in figure 3.4. The elastic scattering images are different for each cycle, which is the result of the irreproducibility of the combustion. The local laser attenuation coefficient is homogeneously distributed for all three cases but the average attenuation coefficient varies and therefore the total transmission of the laser radiation through the engine varies. Also the effective scatterer distributions show different structures resulting from the irreproducibility of

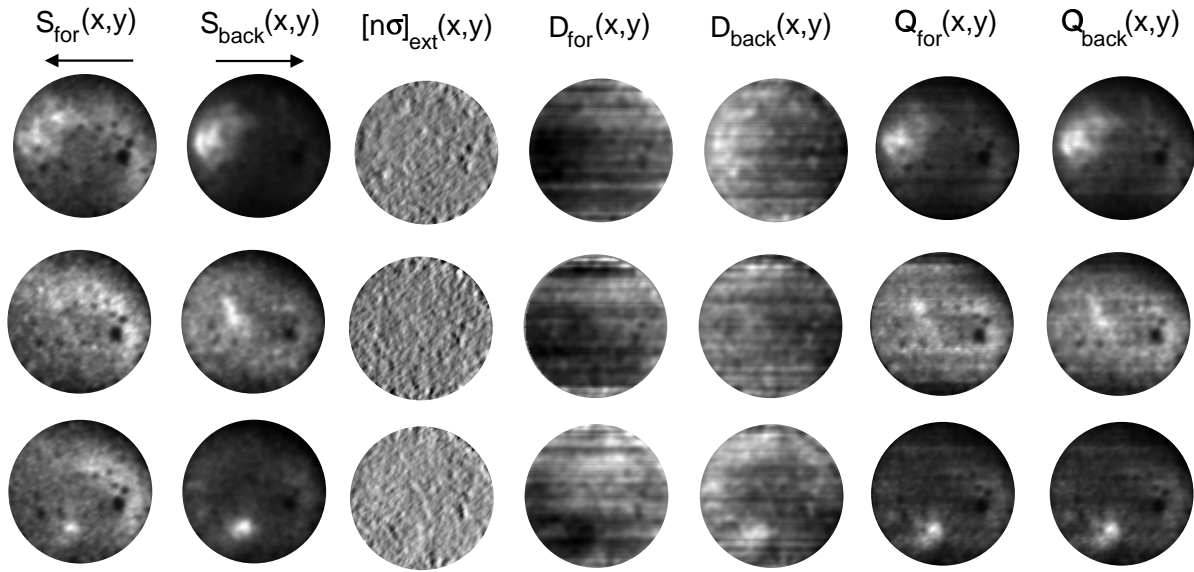


Figure 3.4: Three pairs of single shot elastic scattering images, $S_{for}(x, y)$ and $S_{back}(x, y)$ (columns 1 and 2), obtained at 62° aTDC, the corresponding laser attenuation coefficient, $[n\sigma]_{ext}(x, y)$ (column 3), the laser intensity decrease, $D_{for}(x, y)$ and $D_{back}(x, y)$ (columns 4 and 5), and effective scatterer distributions, $Q_{for}(x, y)$ and $Q_{back}(x, y)$ (columns 6 and 7). Laser beam directions are indicated in the figure. All images are individually scaled and represented in a linear grey scale ranging from black (zero intensity) to white (maximum intensity).

the combustion. In all cases, however, Q_{for} and Q_{back} are very similar, indicating that the laser intensity distribution over the width of the beam is virtually uniform, and that the processing of the forward and backward images yields consistent results.

3.4.2 Single image method

Both forward and backward scattering images can be used separately to obtain the local laser intensity using the single image method described in section 3.2.2 (equation 3.21). The input parameters are the proportionality constant ξ that relates the contributions from absorption and scattering (equation 3.11), and the transmission of the laser radiation through the whole engine.

To illustrate the method and the influence of the input parameters, one pair of single shot images is evaluated for three different values of the transmission of the laser radiation through the whole engine. In figure 3.5 (row 1) one pair of single shot elastic scattering images, $S_{for}(x, y)$ and $S_{back}(x, y)$, recorded at 62° aTDC is given together with the laser intensity decrease images, $D_{for}(x, y)$ and $D_{back}(x, y)$, and effective scatterer distributions, $Q_{for}(x, y)$ and $Q_{back}(x, y)$, obtained using the double image method. Both the forward and backward image were analysed separately with the single image method, using the transmission obtained by the double image method (discussed in section 3.4.3). The results, given in figure 3.5 (row 2), show the laser intensity decrease images as they are derived from one single elastic scattering image using equation 3.21. Also the corresponding effective scatterer distributions $Q_{for}(x, y)$ and $Q_{back}(x, y)$ resulting from the division of the elastic scattering image by the corresponding laser intensity decrease image are given. Comparing the scatterer distributions provides a way

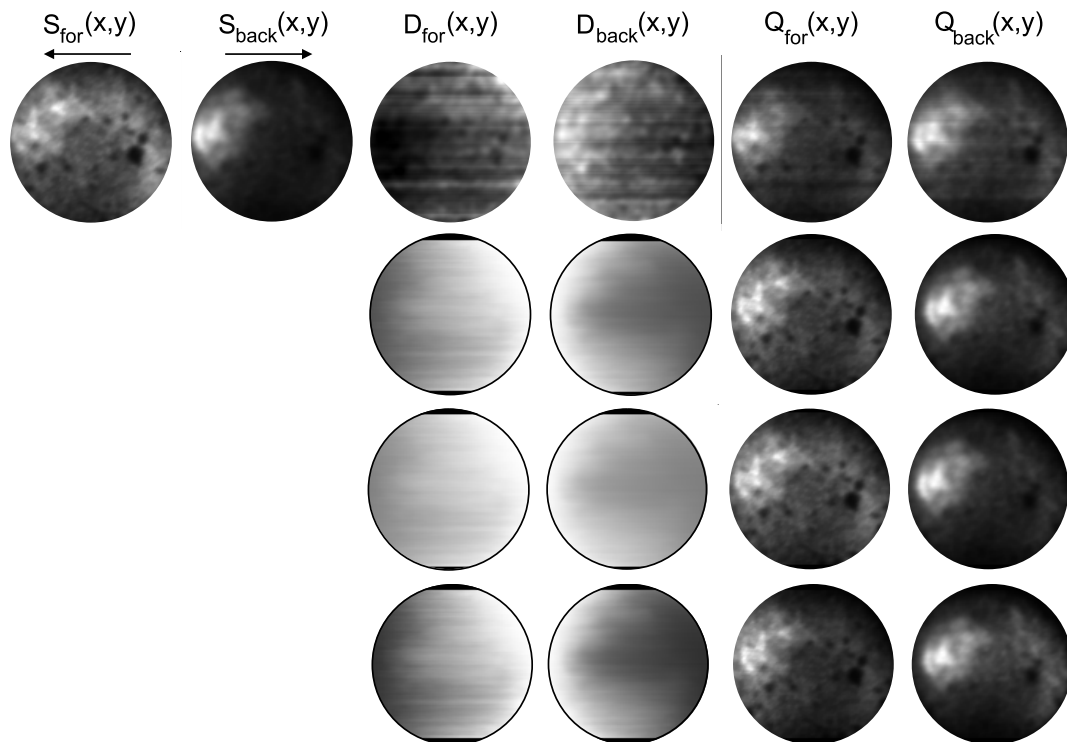


Figure 3.5: One pair of single shot elastic scattering images, $S_{for}(x, y)$ and $S_{back}(x, y)$, obtained at 62° aTDC, laser intensity decrease, $D_{for}(x, y)$ and $D_{back}(x, y)$, and effective scatterer distributions, $Q_{for}(x, y)$ and $Q_{back}(x, y)$, obtained using the double image method (row 1). Laser intensity decrease images and corresponding scatterer distributions obtained from the elastic scattering images using the single image method with a transmission as obtained from the average attenuation coefficient following from the double image method (row 2), a five times higher transmission (row 3) and a five times lower transmission (row 4). Laser beam directions are indicated in the figure. All images are individually scaled and represented in a linear grey scale ranging from black (zero intensity) to white (maximum intensity).

to check the assumptions made in the single image method. The scatterer distributions, obtained independently from each other from simultaneously recorded elastic scattering images by the single image method, should show the same structure along the x -direction (laser beam propagation direction). Differences between them may only occur along the y -direction, because the incident laser intensity distributions for the forward and backward images are not necessarily the same. This is similar to the case where they are obtained using both the forward and backward elastic scattering image in the double image method. As can be seen from a comparison of the upper two rows of figure 3.5, the effective scatterer distributions $Q(x, y)$ obtained by both methods are very similar, and all major features reproduce well. The single image method is less susceptible to the noise than the double image method, as is evidenced by the somewhat greater detail in the $Q(x, y)$ -distributions and, more clearly, by the much smoother $D(x, y)$ -distributions. The latter, of course, is due to the assumption of a constant ξ over the field of view, an assumption that need not be made in the double image method.

In order to estimate the sensitivity of the single image method to the value adapted for the overall transmission, the forward and backward images are analysed using a five times higher

transmission as well as a five times lower transmission than the transmission following from the double image method. The results are also given in figure 3.5 (rows 3 and 4). At first sight little differences are seen when the forward and backward scattering distributions are compared. However, when the distributions obtained from the double image method are divided by the distributions obtained from the single image method gradients along the direction of the laser beam are seen if the transmission is too high or too low. In the case of too high a transmission the scatterer density is about 10% too high at the side the laser beam enters the observation area. If the transmission is too low the density is about 10% too low at the side the laser beam enters the observation area. Although some differences are seen, it can nevertheless be concluded that the results of the single image method are only weakly dependent on the transmission. Changing the transmission within a factor of 2.5 (both smaller and larger) has no significant influence on the result. Here it should be noted that the double image method provides a reliable estimate of the transmission over the observation area. In general, however, a direct determination of transmission through a running engine is quite difficult, as will be discussed below (section 3.4.3).

The exact value of the parameter ξ does not influence the scatterer distribution, as argued above (section 3.2.3), but the single image method *does* require ξ to be constant. Variations in ξ over the field of view would reflect themselves in variations (along the laser beam propagation direction, x) of the effective scatterer distribution reconstructed from both the forward and backward elastic scattering images. As discussed above, such variations do not occur (as long as the proper transmission data are used), so that the assumption of ξ being constant seems to be justified.

As a final comparison between the single and double image methods, the elastic scattering images of figure 3.3 (columns 1 and 2) were evaluated with the single image method, using transmission data obtained by the double image method (discussed in section 3.4.3) and an average value of $\xi = 0.1$ (Appendix). Figure 3.6, which should be compared with figure 3.3, shows the measured elastic scattering images $S_{for}(x, y)$ and $S_{back}(x, y)$ (the same as those in figure 3.3), together with the laser intensity decrease images $D_{for}(x, y)$ and $D_{back}(x, y)$ (columns 3 and 4) as they are derived from one single elastic scattering image using equation 3.21. Also the effective scatterer distributions $Q_{for}(x, y)$ and $Q_{back}(x, y)$ (columns 6 and 7) resulting from the division of the elastic scattering image by the corresponding laser intensity decrease image are given. Comparing the scattering distributions from both the single and the double image method results in the conclusion that they show the same features and that hardly any qualitative differences are seen. This again corroborates the assumption of a constant relation between scattering and absorption, and indicates that the use of the average attenuation coefficient to calculate the transmission is appropriate.

3.4.3 Transmission

The transmission of the 193 nm radiation through the firing engine can be measured directly by detecting the transmitted laser radiation behind the exit window, as described in section 3.3.3. This method gives information about the total absolute attenuation of the laser radiation in the combustion chamber and by the side windows. Therefore, a main disadvantage of this method is the uncertainty in the transmission of the side windows. Several factors play a role in reducing the window transmission. During operation of the engine, the window inner surface

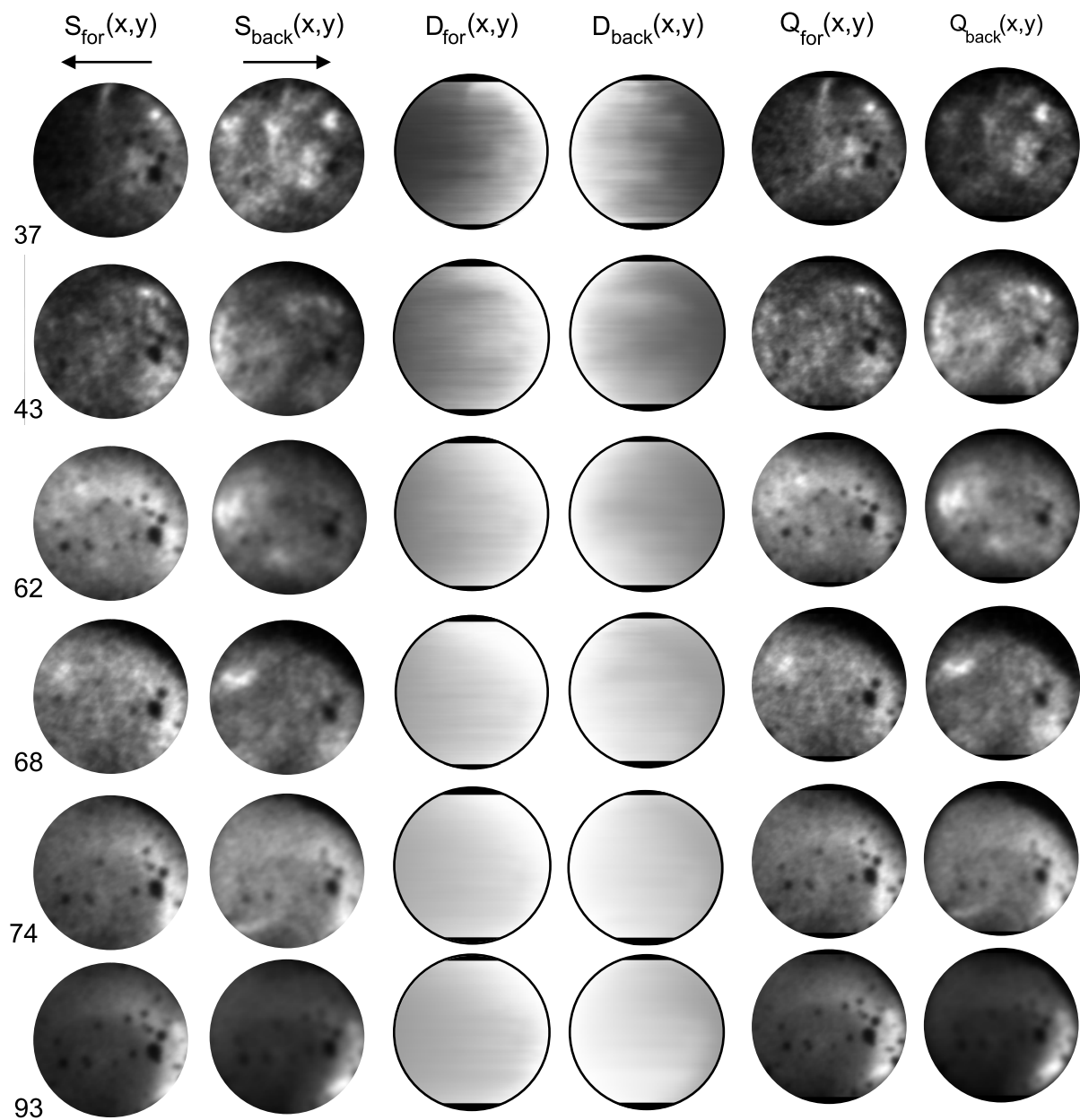


Figure 3.6: Pairs of forward, $S_{for}(x, y)$ (column 1), and backward, $S_{back}(x, y)$ (column 2), elastic scattering images averaged over five cycles obtained at 37, 43, 62, 68, 74 and 93° aTDC. The local laser intensity decrease in forward, $D_{for}(x, y)$ (column 3), and backward, $D_{back}(x, y)$ (column 4), direction obtained by using the single image method (section 3.2.1) with a transmission obtained from the double image method. The effective scatterer distributions determined from the forward, $Q_{for}(x, y)$ (column 5), and backward, $Q_{back}(x, y)$ (column 6), elastic scattering image and corresponding laser intensity decrease image. Laser beam directions are indicated in the figure. All images are individually scaled and represented in a linear grey scale ranging from black (zero intensity) to white (maximum intensity).

becomes soiled by a (thinner or thicker) layer of soot and oil. This may be expected to lead to considerable transmission losses, but is, unfortunately, impossible to measure independently. Moreover, prolonged use of the windows causes their inner surfaces to be slightly etched by the violence of the combustion, leading to some degree of diffusion of the incident laser beam. This again reduces the measured transmission, and should also be taken into account. Thus, although the overall transmission through the whole engine as a function of crank angle can be measured quite accurately, the uncertain window transmission renders an extrapolation of these data to transmission losses over the field of view within the cylinder rather dubious.

More exactly, the transmission can be derived from the average attenuation coefficient $[\overline{n\sigma}]_{ext}$, calculated from the local attenuation coefficient, $[n\sigma]_{ext}(x, y)$, obtained from the double image method in section 3.4.1 and given in figure 3.3 (column 3). Since the attenuation coefficient is seen to be fairly uniform over the observation area, it seems reasonable to assume that the average attenuation coefficient calculated over the observation area will also be valid for the ‘invisible’ parts of the combustion chamber. This transmission is given in figure 3.7 (■) for all measured crank angles. The error bars are based on the spread in the local attenuation coefficients. Also given in figure 3.7 (●) is the transmission calculated from the average attenuation coefficient of the single shot elastic scattering images of figure 3.4. The transmission data obtained from the single shot images show that a large variation in transmission for different cycles can occur, and the analysis of many single shot images indicates that due to the turbulence of the combustion the transmission can vary by a factor of 10. In comparing single cycle results this effect has to be taken into account. However, if images are averaged over several

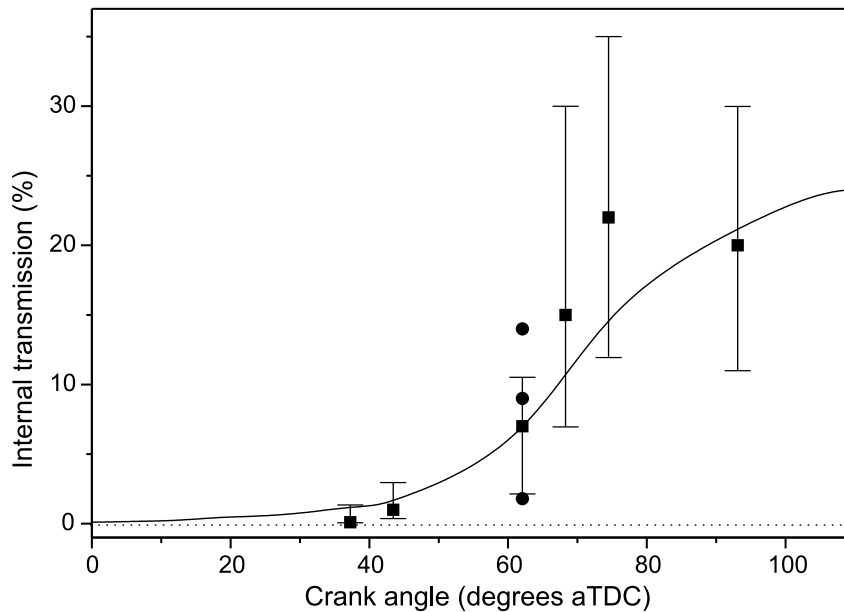


Figure 3.7: Transmission of 193 nm laser radiation through the firing engine (excluding the losses in the side windows) derived from the average attenuation coefficient obtained by the double image method for the averaged scattering images (■) and for the single shot images at 62° aTDC (●). The solid curve is based on direct transmission measurements, scaled to fit the double image data. The resulting scale factor leads to the conclusion that the combined window transmission is only 0.5%.

engine cycles the high and low values cancel and a reproducible value results. The solid curve is based on direct transmission measurements, scaled to fit the double image data. The resulting scale factor leads to the conclusion that the combined window transmission is only 0.5%.

3.4.4 Flame emission

Figure 3.8 shows images of the elastically scattered laser radiation, $S(x, y)$ (column 1), and the natural flame emission, $F(x, y)$ (column 2), recorded at three different crank angles at which both could be obtained simultaneously. They are measured using the setup with one laser beam and two camera systems, and averaged over ten engine cycles. Fuel is injected from the bottom upwards. A gate width of 200 ns was used to record the 22 and 25° aTDC images, whereas for the 31° aTDC images a gate width of 1500 ns was used in order to collect sufficient light from the flame emission. This explains the better signal to noise ratio in the 31° aTDC flame emission image compared to the 22 and 25° aTDC images for which the emission is actually stronger. For 22° aTDC the elastic scattering signal is weak, resulting in a lot of noise. The natural flame emission image represents the integrated flame emission along the line of sight. As the images are obtained at crank angles $\geq 22^\circ$ aTDC the flames have already spread out showing a more homogeneous pattern than expected at the start of the combustion.

The single image method, using a transmission input obtained from figure 3.7, was applied

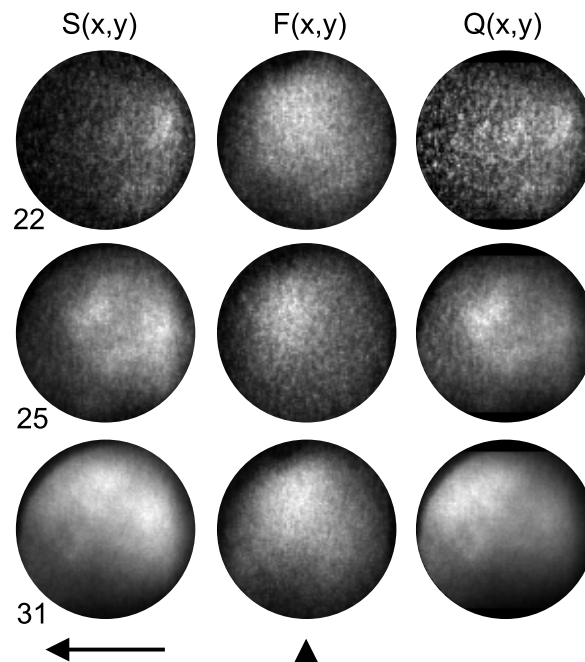


Figure 3.8: Images, averaged over ten engine cycles, of the elastically scattered laser radiation, $S(x, y)$ (column 1), the natural flame emission, $F(x, y)$ (column 2), and the effective scatterer distribution, $Q(x, y)$ (column 3), at 22, 25 and 31° aTDC. The direction of the laser beam is indicated below the scattering images. Fuel is injected from the bottom upwards (black arrowhead). All images are individually scaled and represented in a linear grey scale ranging from black (zero intensity) to white (maximum intensity).

to the elastic scattering images to obtain an image of the effective scatterer distribution, $Q(x, y)$, similar to $Q_{for}(x, y)$ in equation 3.24. The effective scatterer distributions are also given in figure 3.8 (column 3). Due to the processing the signal in the effective scatterer distributions is shifted to the left (in the direction of the laser beam) compared to the elastic scattering images. The flame emission images and the effective scatterer distributions show similar structure. This makes it plausible that the incandescent soot particles present in the flames are mainly responsible for the elastic scattering (and absorption) of the laser radiation.

3.5 Conclusion

A method is developed to obtain the local laser intensity inside the combustion chamber of an optically accessible engine. By the use of two elastic scattering images, obtained from two laser beams which traverse the engine in opposite direction, the local effective attenuation coefficient of the laser intensity over the field of view can be obtained without knowledge of the initial intensity distributions of the laser beams. It is found that the attenuation coefficient is fairly homogeneously distributed over the field of view. The attenuation coefficients are used to reconstruct the laser intensity decrease over the observation area. In addition, an effective scatterer distribution is determined from the elastic scattering image and the corresponding laser intensity decrease image. On the assumption that the average attenuation coefficient over the field of view is valid for the whole cylinder contents the transmission of the laser radiation over the whole optical path in the combustion chamber is determined. This result is compared to the absolute transmission of the laser radiation, including the losses by the windows, measured by detecting the transmitted radiation behind the exit window. Window losses are found to be considerable. Moreover, the transmission of 193 nm laser radiation is found to vary by up to a factor of 10 between individual strokes.

As an alternative, a method is developed to reconstruct the local laser intensity from one single elastic scattering image. The results of both methods are compared and show the same structures indicating that the method using only one scattering image is usable. The single image method is applied to an elastic scattering image in order to compare the determined effective scatterer distribution to a simultaneously measured image of the natural flame emission. It is found that the distribution of the scatterers compares with the flame emission, making it plausible that the laser radiation is scattered mainly by the incandescent soot particles in the flame. These methods can be used to correct planar LIF distributions for laser intensity variations over the field of view.

Appendix

The method in which the local laser intensity is derived from one elastic scattering image is based on the assumption that a constant relation exists between the contribution to the attenuation of the laser radiation caused by absorption and by scattering, *i.e.*

$$[n\sigma]_{sca}(x, y) = \xi [n\sigma]_{abs}(x, y).$$

The proportionality constant ξ can be estimated from the expressions for attenuation, absorption

and scattering efficiencies, Ψ , defined as

$$\Psi = \frac{\sigma}{\pi a^2}, \quad (3.26)$$

where a is the radius of the particle. These expressions are given by Bohren and Huffman [75] in terms of the size parameter, x , and the relative refractive index, m ,

$$x = \frac{2\pi na}{\lambda} \quad \text{and} \quad m = \frac{n_p}{n}, \quad (3.27)$$

where n and n_p are the (complex) refractive indices of the medium and the particle, respectively. In the limit of small particle size ($x \ll \lambda$) the result of the elastic theory can be expanded, resulting in

$$\begin{aligned} \Psi_{ext} = & 4x \operatorname{Im} \left\{ \frac{m^2 - 1}{m^2 + 2} \left(1 + \frac{x^2}{15} \left(\frac{m^2 - 1}{m^2 + 2} \right) \frac{m^4 + 27m^2 + 38}{2m^2 + 3} \right) \right\} \\ & + \frac{8}{3} x^4 \operatorname{Re} \left\{ \frac{m^2 - 1}{m^2 + 1} \right\}^2, \end{aligned} \quad (3.28)$$

$$\Psi_{sca} = \frac{8}{3} x^4 \left| \frac{m^2 - 1}{m^2 + 1} \right|^2, \quad (3.29)$$

$$\Psi_{abs} = \Psi_{ext} - \Psi_{sca}. \quad (3.30)$$

The efficiencies can be calculated if the refractive indices are known. Using the data of Carter *et al.* [76] the refractive index of the soot for 193 nm laser radiation can be determined resulting in $n_p = 0.765 + 1.07i$. The mixture surrounding the particle consists of air, from which some oxygen is consumed by the combustion, and some combustion products. For this medium the refractive index of air, $n \approx 1$ is taken, which results in $m \approx n_p$ and

$$\Psi_{ext} = 4.132x + 0.372x^3 - 2.832x^4, \quad (3.31)$$

$$\Psi_{sca} = 2.87x^4, \quad (3.32)$$

$$\Psi_{abs} = 4.132x + 0.372x^3 - 5.702x^4. \quad (3.33)$$

Using these efficiencies, the ratio between scattering and absorption is given by

$$\xi = \frac{\Psi_{sca}}{\Psi_{abs}} = \frac{x^3}{1.44 + 0.13x^2 - 1.99x^3}, \quad (3.34)$$

which depends on the size parameter x only. Diesel particulate material typically consists of collections of primary particles, ranging in diameter between 15 and 30 nm, agglomerated into clusters of particles [2]. These aggregates vary in diameter between 50 and 220 nm. Based on the data of the particle size distribution given by Heywood [2], an average value of $\xi_{av} = 0.1$ is determined for 193 nm laser radiation. This indicates that the contribution from absorption to the attenuation of the laser radiation is much larger than the contribution from scattering, implying that the effects of secondary scattering may be neglected in the analysis.

Chapter 4

Semi-quantitative nitric oxide densities from spatially averaged dispersed fluorescence spectra¹

Abstract

The formation of nitric oxide (NO) in a diesel engine has been studied as a function of crank angle throughout the whole combustion cycle, using the Laser Induced Fluorescence (LIF) technique. Measurements were performed in an optically accessible one-cylinder, two-stroke, direct injection diesel engine. The engine was operated in steady state at different loads, compression ratios and commercial diesel fuels. A tunable ArF excimer laser beam was used to excite the NO molecules in the $D^2\Sigma^+(v'=0) \leftarrow X^2\Pi(v''=1)$ band at 193 nm. Dispersed fluorescence spectra allowed to discriminate between NO and interfering oxygen fluorescence. From the spectra, a relative measure for the amount of NO present in the probed volume of the cylinder was obtained. This amount was transformed into an in-cylinder NO density/content, taking into account the changes in laser intensity, pressure, temperature and volume during the stroke. The resulting NO density/content curves show a slow start of the NO formation at the beginning of the combustion, gradually rising to a broad maximum to somewhere in between 20° and 50° aTDC. It is concluded that, in this engine, the bulk of NO formation takes place relatively late in the stroke. This suggests that the diffusion burning phase of combustion makes an important contribution to the NO formation, contrary to the model which assumes that NO is formed mainly during the initial premixed burn.

¹Adapted from: G.G.M. Stoffels, E.J. van den Boom, C.M.I. Spaanjaars, N.J. Dam, W.L. Meerts, J.J. ter Meulen, J.C.L. Duff and D.J. Rickeard, "In-cylinder measurements of NO formation in a diesel engine", SAE paper no. 1999-01-1487 (1999).

4.1 Introduction

The diesel engine offers the benefits of high fuel economy and reduced CO₂ emissions. However, compared to gasoline engines, its disadvantage lies in its emissions of nitric oxides (NO_x) and particulate matter (PM), which are facing increasingly stringent regulations in Europe, North America, and the Far East. The chemistry of NO_x formation is thought to be well understood, but the complex physics of diesel injection and combustion makes an analytical approach to understanding nitric oxide (NO) formation in a diesel engine difficult. The objective of this work was to quantify the NO density within a diesel engine cylinder as a function of time throughout the whole combustion cycle using optical diagnostics based on Laser Induced Fluorescence.

Laser-based diagnostics are of interest for the study of combustion processes because they allow non-intrusive, spatially and temporally resolved measurements of specific chemical species [30–33]. The Laser Induced Fluorescence (LIF) technique has the sensitivity to provide information also about several minority species present in combustion processes. This LIF technique is in principle a two step process: electronic excitation of molecules by a laser beam and detection of the ensuing fluorescence. The fluorescence can be dispersed by a monochromator to obtain spectrally resolved information or a filter can be used to single out a specific fluorescence wavelength band. By the use of the Planar LIF (PLIF) technique, which involves excitation by a thin laser sheet and detection of the fluorescence through a filter in a direction perpendicular to the sheet, two-dimensional fluorescence distributions can be obtained. The (P)LIF technique has been used to demonstrate the presence of a large variety of molecular species in combustion processes, but quantification of fluorescence signals is difficult. The fluorescence signal is proportional to the local density of molecules excited by the laser beam that fluoresce at the right wavelength. However, the proportionality constant depends strongly on the local pressure and temperature, the local laser intensity and the chemical composition of the environment. Since most of these parameters are not known and difficult to measure, some assumptions have to be made to obtain quantitative data. Another problem is the possible spectroscopic interference between different molecules.

The LIF technique has been applied before to both spark ignition (SI) engines (see *e.g.* the recent work of Sick *et al.* [41, 77] and references in there) and to diesel engines [17, 37–39] to measure the in-cylinder NO distribution and the in-cylinder NO content. Nakagawa *et al.* [39] applied PLIF imaging to a single fuel jet diesel research engine running on a mixed fuel to minimise soot production. However, to obtain sufficient NO fluorescence oxygen enriched intake air was used. The results showed the location of the NO relative to the reacting fuel jet, but the start and the end of the NO formation are not determined. The data were not corrected for changes in laser intensity, pressure, temperature and mixing to obtain some quantitative information about the amount of NO present in the cylinder.

Recently, an impressive paper by Dec and Canaan [17] presented NO distributions showing the timing and location of NO formation in a direct injection (DI) diesel engine running on a low-sooting fuel, obtained by single-shot PLIF imaging. A tripled Nd:YAG laser pumping a narrow-line optical parametric oscillator (OPO) was used to excite the NO molecules in the $A(v'=0) \leftarrow X(v''=0)$ band at 226.035 nm and the fluorescence of the $A(v'=0) \rightarrow X(v''=1,2,3,4)$ bands was detected. In addition to the NO distributions, a curve of the total averaged NO PLIF intensity as a function of crank angle was shown, obtained by integration of the NO

PLIF signal over a representative sector of the combustion chamber. In order to determine the total in-cylinder NO content the integrated NO PLIF signal was corrected for the effects of pressure, temperature and mixing. However, no attention was given to the attenuation of the laser intensity or the induced fluorescence on its way through the combustion chamber as the authors claim that it can be neglected. It was found that NO formation does not start during the premixed combustion (which is fuel rich), but begins around the fuel jet periphery just after the diffusion flame forms, where it remains until the jet structure begins to disappear. As the burn-out phase continues, NO remains along the track of the fuel jet, and the NO formation continues in the hot post-combustion gases after the end of combustion. The NO content curve shows that only 67% of the NO has formed by the end of the apparent heat release, so NO formation must continue in the post-combustion gases after the diffusion flame has gone out.

For the present chapter, the LIF technique was used to obtain dispersed fluorescence spectra of NO from an optically accessible two-stroke DI diesel engine. The engine was operated in normal mode (*i.e.* not skip-fired) on standard commercial diesel fuel and ambient (non-oxygen-enriched) intake air. Using an excimer laser to excite the NO molecules in the $D(v'=0) \leftarrow X(v''=1)$ band at 193.377 nm, NO fluorescence could be detected during the whole combustion process. Dispersed fluorescence spectra in the wavelength range between 200 nm and 230 nm were obtained as a function of crank angle using a monochromator. The main advantage of dispersed fluorescence spectra over images is that the spectra allow discrimination between NO and oxygen (O_2) fluorescence. When the fluorescence was dispersed into its different wavelength components the interference of NO and O_2 fluorescence could clearly be seen. The spectra allowed to discriminate against O_2 fluorescence and to arrive at a semi-quantitative measure for the amount of NO inside the probed volume of the cylinder as a function of crank angle. These data were processed for the changes in laser intensity, pressure, temperature and volume during the stroke in order to obtain an in-cylinder NO density as a function of crank angle.

A second aim of this experiment was also to make a qualitative/quantitative assessment of the effect on NO production of engine conditions (compression ratio and load) and fuel. To that end, dispersed fluorescence spectra of NO were measured for different engine conditions and fuels.

This chapter begins with a description of the experimental method, including the engine, its operating conditions and the optics used to obtain the dispersed fluorescence spectra. Next the results are presented: the engine characteristics observed, the fluorescence spectra obtained by dispersing the LIF signal, and the translation of the fluorescence yield into a semi-quantitative measure of NO content. These results are discussed in terms of the effects of engine conditions and fuels on NO formation. Finally, the findings of this work are compared with current theoretical and experimental data on of NO in the literature and some conclusions are drawn.

4.2 Experimental Method

4.2.1 Engine

The engine used is a one-cylinder, two-stroke, direct injection diesel engine (Sachs) described in detail in chapter 2, section 2.2. To allow to study the combustion process inside the cylinder the engine is made optically accessible by mounting two quartz (Suprasil I) windows in the cylinder wall (side windows (W1,2 in figure 4.1); $25 \times 10 \text{ mm}^2$, thickness 25 mm) and one in the top of the cylinder head (top window (W3); diameter 25 mm, thickness 35 mm) as shown schematically in figure 4.1. The top window could be replaced by a pressure transducer for time-resolved in-cylinder measurements.

The engine was operated in steady state at 1200 rpm on standard commercial diesel fuel and loaded by an electric water-cooled brake. To study the effect of the engine conditions on the NO production different compression ratios, loads and fuels were used. The operating conditions are summarised in table 2.2.

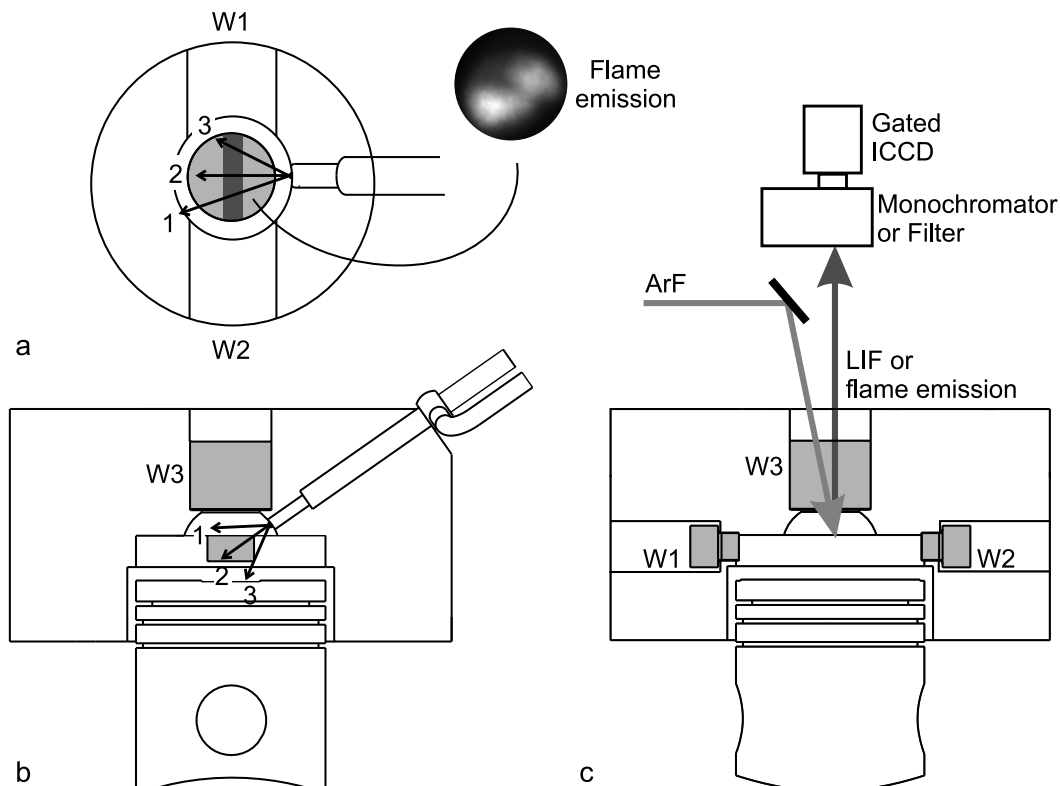


Figure 4.1: Schematical view of the modified two-stroke diesel engine and the optical setup. The engine is optically accessible by two windows in the side wall (side windows; W1,2) and one window in the top of the cylinder head (top window; W3). The ArF excimer laser beam enters the combustion chamber through the top window, illuminating the area indicated by a grey rectangle in a). The induced fluorescence or natural flame luminosity is detected through the top window by a gated CCD camera, positioned behind a monochromator. Spray directions of the three-hole nozzle are indicated (arrows 1–3 in a) and b)); an image of the natural flame luminosity (recorded at TDC) is shown in the insert to figure a).

4.2.2 Details of test fuels

The two fuels selected were standard commercial automotive diesel oil, meeting the European EN590 specification. The details of the test fuels are given in table 2.3. The main differences between them were that fuel 2 had a narrower distillation range, lower T95, lower sulphur content, and higher cetane number than fuel 1.

4.2.3 Optical setup

The optical setup used in the LIF experiments is also indicated schematically in figure 4.1. A pulsed ArF excimer laser (Compex 350T; Λ -Physik), tunable between 192.9 and 193.9 nm with 20 ns pulse duration and a bandwidth of 1 cm^{-1} , was used to excite nitric oxide molecules at the $R_1(26.5)/Q_1(32.5)$ transition in the $D^2\Sigma^+(v'=0) \leftarrow X^2\Pi(v''=1)$ band at 193.377 nm [55]. This transition was selected to minimise interference from vibrationally hot oxygen, that has several strong absorptions within the tuning range of the ArF excimer laser [63–66]. The laser was synchronised to the position of the piston with an accuracy of 0.6 degree crank angle. It was manually tuned to resonance with the NO transition before each measurement cycle; frequency drift during each measurement was less than the laser bandwidth and negligible with respect to the observed NO line widths. A normal incidence 193 nm laser mirror was used in front of the collection optics to suppress the contribution of the elastically scattered radiation.

To obtain dispersed fluorescence spectra, the unfocused, rectangular ($25 \times 3 \text{ mm}^2$) laser beam was coupled into the combustion chamber through the top window, with a pulse energy of 130 mJ, typically. The area illuminated by the laser beam is indicated in figure 4.1a. The ensuing fluorescence was coupled out also through the top window, and detected by a gated (50 ns) intensified CCD camera (ICCD-576G/RB-E; Princeton Instruments) placed behind a monochromator (Chromex 250i; 1200 gr/mm grating, entrance slit width $50 \mu\text{m}$, slit oriented parallel to the length of the illuminated area), which was used to disperse the induced fluorescence in its different wavelength components. This system effectively constitutes an Optical Multichannel Analyser (OMA), whose output was digitised and sent to a computer for further processing. The spectrally resolved fluorescence was averaged over the height of the slit, and therefore represents an average over the whole probe volume.

4.3 Results and Discussion

4.3.1 Engine characteristics

For a good interpretation of the NO fluorescence yield motor parameters like pressure and temperature in the cylinder are important. To obtain some information about these parameters of the modified engine for the different engine conditions, the in-cylinder pressure was measured for all engine operating conditions used in the experiment. These curves were used to calculate the heat release and the mean gas temperature, on the assumption of an ideal gas in the cylinder and neglecting crevice flows [2].

Two typical in-cylinder pressure curves, their derivatives with respect to crank angle and the calculated heat release curves are given in chapter 2, figures 2.4a, b and c, respectively. In these cases the engine was running on diesel fuel 1 and loaded by 0.44 kW. The difference between

the engine conditions was the compression ratio which was 14.4 (solid curve) or 13.4 (dashed curve). Similar curves were obtained at the other engine conditions. In the modified engine the peak pressures, typically 70-75 bars, are already reached at Top Dead Centre (TDC) and at the moment the exhaust opens the pressure has dropped to about 2 bars. The mean gas temperature curves, derived from the heat release curves, are given in figure 2.4d (solid and dashed curves) and show maximum temperatures of 1300-1500 K a few degrees after TDC, dropping to about 500-600 K just before the exhaust opens. Since the mean gas temperature is not necessarily decisive with respect to the NO formation, also the temperature as it can be obtained from the natural flame luminosity [33] (see section 2.4.1) is included in figure 2.4d (■)². This soot temperature has a maximum of about 2250 K and is much higher than the mean gas temperature. The reason for the difference is found in the fact that the cylinder contents are not likely to be in thermal equilibrium. The mean gas temperature represents an average temperature of the gas inside the whole cylinder, whereas the soot temperature represents the temperature of the locally present soot. This latter temperature is obtained from the actual combustion where the temperature is locally high and not yet in equilibrium with the rest of the gas in the cylinder.

4.3.2 Dispersed fluorescence spectra

Dispersed fluorescence spectra were obtained by coupling in the laser beam through the top window while detecting the fluorescence through the same window with the OMA system. The laser induced fluorescence, dispersed into its wavelength components between 200 nm and 230 nm, is shown in figure 4.2 for different crank angles. During the measurement of this series of dispersion spectra, the engine was running on diesel fuel 1 at a compression ratio of 14.4 and loaded by 0.44 kW. The spectra are averaged over 100 engine cycles and represent an average fluorescence signal of a narrow strip ($25 \times \text{ca. } 0.5 \text{ mm}^2$) with a vertical extent depending on the penetration depth of the laser radiation. No background signal from natural flame emission is observed in this wavelength region with the used camera gate width of 50 ns, so that all observed signal is laser induced. The peak at 207.8 nm present in all spectra is an artefact of the measurement setup, caused probably by Raman scattering of the quartz top window. All spectra show spectral structure indicating that fluorescence can be obtained throughout the whole stroke, even at TDC where the pressure and temperature are high and attenuation of the laser radiation is strong.

Around 30° aTDC, a conspicuous qualitative change in spectral structure and intensity is seen. The grey bands in figure 4.2 mark the spectrally broad structures at 208 nm (red shoulder of the quartz phosphorescence peak), 216 nm and 225 nm. These structures can be attributed to NO fluorescence from the directly excited $D(v'=0)$ -state to the $X(v''=3,4,5)$ -states, respectively. (The $D(v'=0) \rightarrow X(v''=2)$ band at 201 nm is suppressed by the 193 nm mirror.) The two weaker emission signals seen at 212.5 nm and 220 nm (for $\Theta \gtrsim 40^\circ$ aTDC) result from NO fluorescence out of the $C(v'=0)$ -state, populated by Electronic Energy Transfer (EET), to the $X(v''=3,4)$ -states. For $\Theta \lesssim 30^\circ$ aTDC, additional peaks at 211 nm and 217.5 nm are present besides the NO signals. These fluorescence features can be ascribed to hot oxygen (O_2). Within the tuning range of an excimer laser operated on ArF a number of O_2 transitions in the Schumann-Runge $B^3\Sigma_u^+ \leftarrow X^3\Sigma_g^-$ system can be excited, the strongest of which start from $v''=2$ or 3 [63–66]. At

²It has been shown that if the soot particles are small this temperature is also a good measure for the flame temperature [56].

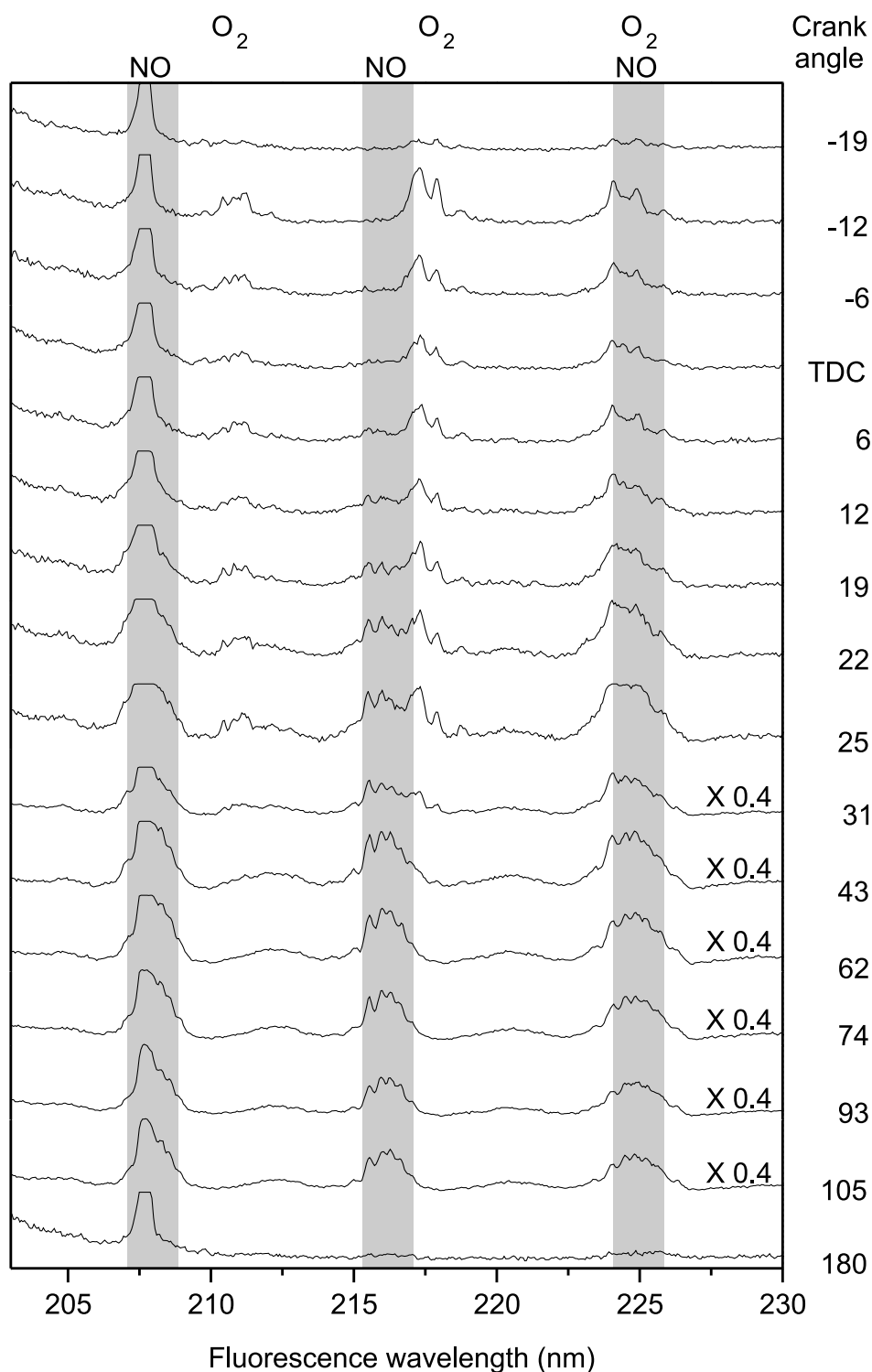


Figure 4.2: Dispersed fluorescence spectra of NO (averaged over 100 engine cycles) at different crank angles obtained from the engine running on diesel fuel 1 at a compression ratio of 14.4 and loaded by 0.44 kW. All spectra are at the same scale unless indicated otherwise. The persistent peak at 207.8 nm is an artefact of the quartz top window. The grey bands indicate the positions of the $D^2\Sigma^+(v'=0) \rightarrow X^2\Pi(v''=3,4,5)$ bands of NO.

the high temperatures that are reached during the combustion around TDC, these vibrationally excited levels are sufficiently populated to give fluorescence signals. When using an ArF laser, completely avoiding O₂ excitation at high temperatures is difficult because all strong NO transitions lie close to some O₂ resonance. The O₂ fluorescence is characterised by narrow doublet structures, due to fast predissociation of the upper state [63–65]. Also the doublet structure seen at 225 nm near TDC is the result of fluorescence of O₂. Around 225 nm, only the shape of the peak changes with increasing crank angle from a doublet structure (characteristic for O₂) for $\Theta \lesssim 30^\circ$ aTDC to a broad, rippled structure (characteristic for NO) for $\Theta \gtrsim 30^\circ$ aTDC, because the fluorescence bands of NO and O₂ coincide in this wavelength region. Although NO fluorescence is the most evident in the spectra for $\Theta \gtrsim 30^\circ$ aTDC, it can already be seen in the spectrum recorded at 6° bTDC. The spectrum at 180° aTDC (BDC) shows no NO fluorescence, indicating that every cycle all NO is removed by scavenging. (For comparison, Bräumer *et al.* found that five cycles were needed to completely remove all NO in their SI engine [78].) At 180° aTDC, no oxygen fluorescence is seen neither, because of the small population of the $v''=2$ and 3 as a result of the low temperature at that moment.

Similar series of spectra, reproducing well, were obtained for several engine runs. Also, dispersed fluorescence spectra were obtained for other engine conditions. They show the same spectral structures and only little difference is seen in the intensity of the NO fluorescence peaks, mainly around TDC. The NO dispersion spectra provide information on the amount of NO present inside the probed volume of the cylinder, which can be used to obtain an in-cylinder NO density. They also provide information about the wavelengths of the fluorescence bands of NO and O₂ obtained from the running engine. This information is necessary to determine a fluorescence band of NO that is free from O₂ fluorescence and can be used for imaging of NO distributions.

4.3.3 NO density

The area below the NO fluorescence peaks in the dispersion spectra (the so-called fluorescence yield) provides information on the amount of NO present inside the probed volume of the cylinder at different crank angles. To compare the fluorescence yields at different crank angles and engine conditions it is necessary to convert them into more quantitative data. However, as almost all NO fluorescence bands are overlapped by O₂ fluorescence, the structures due to O₂ fluorescence have to be taken into account. From this point of view the NO fluorescence band at 208 nm would be best suited for evaluation, but unfortunately it is exactly at this wavelength that interference with a signal originating from the quartz window occurs. Alternatively, the NO peak at 216 nm was used, because it is only slightly mixed with the O₂ fluorescence at 217.5 nm. To determine the contribution of O₂, the peaks in the 12° bTDC spectrum (where only O₂ fluorescence is present) are fitted to Gaussian curves. Because the position and shape of the O₂ peaks do not change during the stroke (a benefit of the fast predissociation of the B-state), this result can be used, together with a proportionality constant for the change in intensity, to determine the O₂ contribution to the emission in the 216–218 nm region at all crank angles. Taking this contribution into account, the NO fluorescence at 216 nm is fitted to a Gaussian curve in order to obtain an NO fluorescence yield. Following this procedure, fluorescence yield curves as a function of crank angle are obtained for the engine at different operating conditions (fuel, load, compression ratio). The fluorescence yield curve obtained from the spectra

presented in figure 4.2 is given in figure 4.3a (open squares, \square). Curves obtained for other engine conditions look rather similar and most of the differences are seen around TDC (discussed below). However, comparison of just the fluorescence yields would be deceptive because they also depend on the pressure, temperature and laser radiation intensity inside the cylinder. These parameters vary during the stroke and for different engine conditions. Therefore, in order to compare the fluorescence yields throughout the stroke and for different engine conditions, they have to be translated into an in-cylinder NO concentration, taking into account the changing in-cylinder conditions. The model used to process the measured fluorescence yield is described in the Appendix.

Two NO density curves as a function of crank angle derived from the fluorescence yield curve in figure 4.3a following the procedure described in the Appendix, are given in figure 4.3b. The difference between the curves is the temperature used in the processing. The \blacksquare -curve results from using the mean gas temperature whereas the \bullet -curve results from using the soot temperature. For comparison these two temperature curves are included in figure 4.3a. For both curves the in-cylinder pressure given in figure 2.4 is used. Under the assumption that the probe volume is representative for the whole cylinder content (see Appendix and figure 4.1c), NO content curves can be derived from the density curves, resulting in figure 4.3c.

Before discussing the shape of the curves in figure 4.3, some discussion concerning possible error sources is appropriate. However, since most of these are systematic errors that appear in all NO content curves they do not affect the relative differences between curves, and NO content curves at different engine conditions can be compared. Because the fluorescence yield curves obtained for several engine runs reproduce well, the accuracy of the obtained NO content curve will be determined mainly by the precision of the fluorescence yield processing method. Although the general relationship between the fluorescence yield and the NO content is well established (equation 1 of the Appendix), some errors will be introduced by the assumptions made in obtaining the different factors that are used in the model. It is, for instance, not clear which temperature has to be used in the processing. Neither the soot temperature nor the mean gas temperature represents the local temperature at the position the NO is measured. During the actual combustion, the relevant temperature is probably higher than the mean gas temperature, as the cylinder contents are not likely to be in thermal equilibrium at that moment. The soot temperature may therefore be a better estimate for the NO temperature in the beginning of the combustion. However, this temperature will likely be too high at the end of the combustion, since the gases cool down faster than the soot particles. Probably, a realistic temperature of the probe volume is somewhere in between the two temperature curves of figure 4.3a. The effect of the two different temperatures is seen in figure 4.3b where NO density curves are given resulting from the same fluorescence yield curve using both temperatures. The use of the mean gas temperature results in a curve that shows a faster rise of the NO density in the early phase of the combustion.

The NO density curve, given in figure 4.3b, shows that NO can first be detected at 6° bTDC and that its density increases throughout the combustion stroke till somewhere in between 20° and 50° aTDC, depending slightly on the temperature used in the derivation. The dip around 20° aTDC is probably not realistic. The subsequent decrease is largely due to the expanding in-cylinder volume, as can be seen from the NO content curves of figure 4.3c. The latter continue to rise up to about 50° aTDC, after which they more or less level off or show a small decrease. Comparison of the NO curves with the engine parameter curves of figure 2.4 leads to

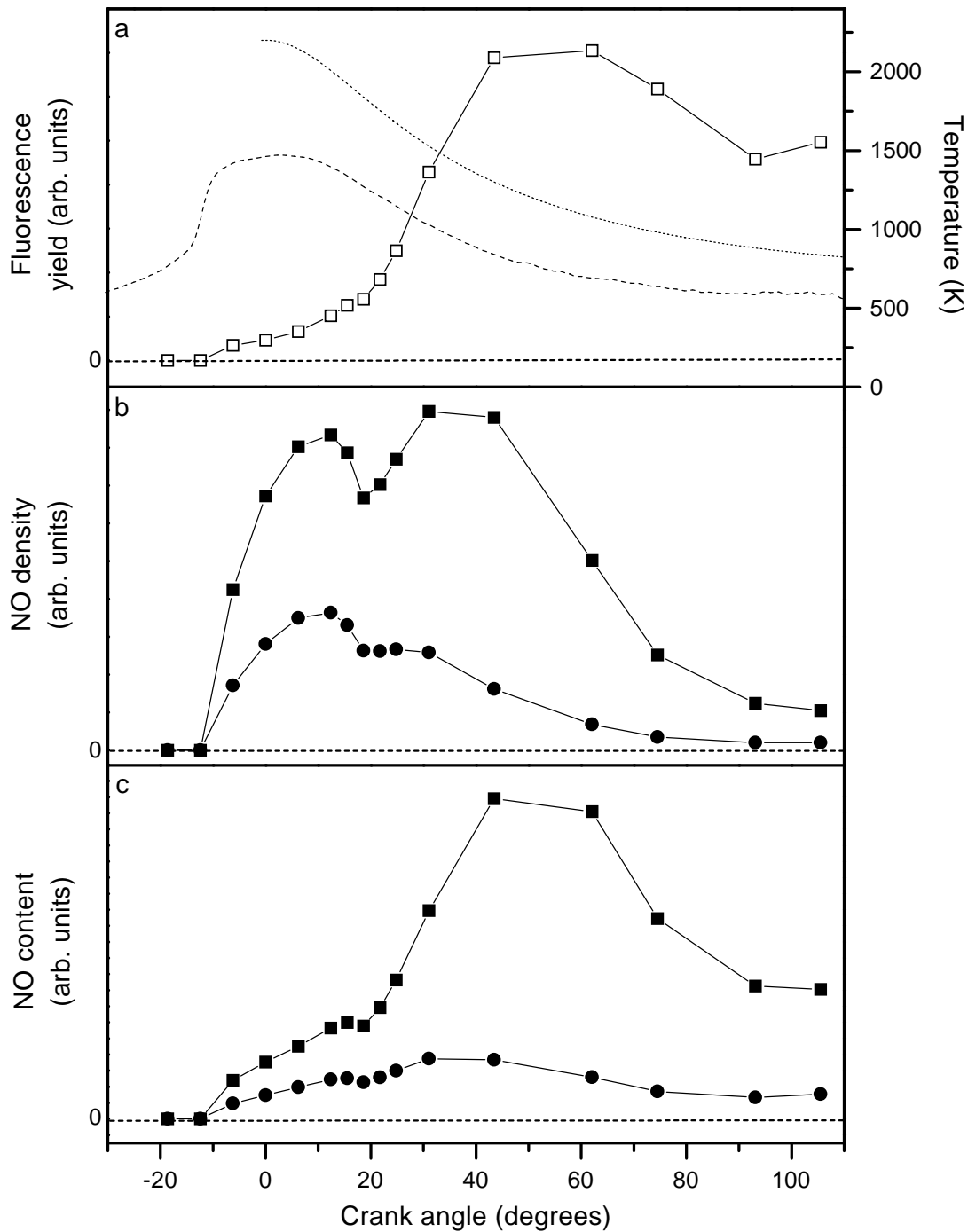


Figure 4.3: a) The integrated NO fluorescence yield obtained from the spectra given in figure 4.2 (\square). The mean gas temperature (dashed line) and the soot temperature (dotted line) obtained at the same engine conditions are also included. b) Corresponding NO density following the procedures described in the Appendix, using either the mean gas temperature (\blacksquare) or the soot temperature (\bullet). c) Corresponding NO content obtained by multiplying the curves in b) by the (crank angle dependent) cylinder volume. Engine running on fuel 1, $\epsilon = 14.4$ and 0.44 kW load.

the conclusion that, in this (considerably modified) engine, the bulk of NO formation does not coincide with the highest pressure and temperature part of the stroke. Neither is any relation seen between the NO formation and the peak of the premixed burn in the heat release curve at 12° bTDC. At this crank angle only O_2 fluorescence is present in the spectra of figure 4.2, indicating that, although there definitely is laser intensity within the cylinder (and note that the O_2 fluorescence in all spectra up to 25° aTDC is about equally strong), the NO density is still below the detection limit. The bulk of NO formation takes place relatively late in the stroke, suggesting that the diffusion burning phase of combustion (starting at 3° aTDC) makes an important contribution to the NO formation. Only little NO production is seen during the initial premixed combustion, which is fuel rich.

The apparently late start of NO formation implied by the NO curves of figure 4.3 may raise the question whether all laser intensity might be absorbed early in the combustion chamber, before reaching the area where NO is formed. Although this possibility cannot unequivocally be excluded (since the laser intensity cannot directly be measured within the cylinder), it is not considered very likely, again because of the presence of the O_2 fluorescence. This fluorescence originates from excitation of O_2 molecules in the $v''=2$ or 3 states. (In fact, the temperature dependence of the O_2 is even stronger than that of the NO fluorescence, because the lower levels involved are at a higher energy in O_2 ($v''=3$ $J''=5/15$ around 5800 cm^{-1}) than in NO ($v''=1$, $J''=26.5/32.5$ around 4300 cm^{-1}). Thus, it is likely that the O_2 fluorescence signal originates mainly in the highest temperature regions within the cylinder, that is, from around the spray edges where the premixed combustion occurs. This is also the region where NO might be expected to form (see images in Dec and Canaan [17]). Therefore, the absence of detectable NO fluorescence in the presence of hot O_2 fluorescence can be taken as an indication that NO formation has not yet begun at 12° bTDC.

This somewhat surprising result is supported by theoretical predictions by the group of Peters [79] and also by recent experimental results from laser imaging techniques from other research groups [17,39]. Nakagawa et al. [39] found that NO was formed on the lean side of the flame, where oxygen is present and the temperature is high. The region where NO is located was found to expand during the combustion, indicating that NO is not formed in the regions where the premixed combustion occurs. Images reported by Dec and Canaan [17] showed that, in the engine used, NO formation starts around the jet periphery just after the diffusion flame forms. It was found that NO remained confined to the edge of the jet until the jet structure disappeared. As the combustion continued, NO formation continued in the hot post-combustion gases, in the trail of the reacting fuel jet. Additionally, Dec and Canaan [17] presented a NO content curve that showed that NO formation does not arise from the premixed combustion but starts just after the diffusion flame forms and continues in the hot post-combustion gases after the end of the combustion. Only 67% of the NO had formed by the end of the apparent heat release. It is also in agreement with data obtained from cylinder gas sampling measurements that showed that NO formation starts somewhat after the beginning of the combustion and rises throughout the combustion process [80].

These results support the expectation that the initial premixed burn is too fuel rich to produce significant NO as discussed in the conceptual model of Dec [16], which is derived from data of several different laser-based diagnostics. However, the results appear to conflict with the models that predict that the initial premixed burn has a large contribution to the NO formation and that the NO_x emissions correlate with the amount of fuel consumed during the initial premixed

burn [24, 81]. Rather, the present results indicate that any correlation of NO_x emission with the fuel consumption during the premixed burn must have another reason. An explanation can be found in the rapid, large rise of the in-cylinder temperature around TDC caused by the premixed burn [17]. The higher air temperature will cause an increase in temperature of the diffusion flame resulting in a higher NO production in the diffusion burning phase. This effect would be larger if the contribution of the premixed burn to the total burn is larger and/or the volume at TDC is smaller. Consequently, it will have more influence in engines with a small bore, as the one used in this experiment (note that in this engine also the premixed burn contributes relatively much to the heat release).

The decrease in NO content at the end of the stroke can possibly be explained by a conversion of NO into NO_2 by oxidation in the colder part of the stroke, which is also predicted by theoretical calculations [79]. A relatively large conversion to NO_2 in this engine, used at a light load, would be consistent with a generally high NO_2/NO ratio at the exhaust occurring in light-load diesel engines, where cooler regions advance the conversion to NO_2 [27].

4.3.4 Effect of engine conditions

To study the effect of different engine conditions on the NO production, the compression ratio (ϵ), fuel and load were varied. Dispersed fluorescence spectra were recorded for the different engine conditions. They were evaluated using the mean gas temperature in the way described in the Appendix in order to obtain NO density curves as a function of crank angle. The NO density curves shown in figure 4.4a are obtained at different compression ratios ($\epsilon=14.4$ (■); $\epsilon=13.4$ (□)), the curves in figure 4.4b result from the engine running on different fuels (fuel 1 (■); fuel 2 (□)), and those in figure 4.4c are obtained from the engine loaded by different loads (0.75 kW (■); 0.88 kW (□)). From the curves in figure 4.4 it can be concluded that changing the engine conditions within these limits has only little influence on the NO production. A higher compression ratio leads to an earlier start of NO formation, as can be seen in figure 4.4a. This also follows from a comparison of the curves of figures 4.4a and c where the NO formation in the situation with the lower ϵ (figure 4.4c) starts much later. A possible explanation for this could be that, for lower compression ratios, the lower temperatures prevailing during most of the combustion cycle reduce all reaction rates, leading to a slower rise of the NO density to above the detection limit. (Note that absolute values in figure 4.4 may not be compared between graphs.) From figure 4.4b it follows that for both fuels NO formation starts at the same crank angle, but the early diffusion burning contributes more to the NO formation in the case of fuel 1. Because NO formation continues longer in the case of fuel 2, the densities reached at the end of the cycle are comparable. The influence of load can be derived from figure 4.4c. A higher load results in a slightly advanced rise of the NO density, which can be the result of the higher temperatures at higher loads, but otherwise the two curves are very similar.

As discussed in the context of figure 4.3, the density curves can be converted to NO content curves, thus removing the effect of the increasing in-cylinder volume. All NO content curves thus derived from figure 4.4 show a slow start of NO formation followed by a steep rise around 30° aTDC and a maximum around 80° aTDC, after which a small decrease follows. This indicates that, for all conditions studied, the NO formation does not arise from the initial premixed combustion but that the diffusion burning phase of combustion makes an important contribution.

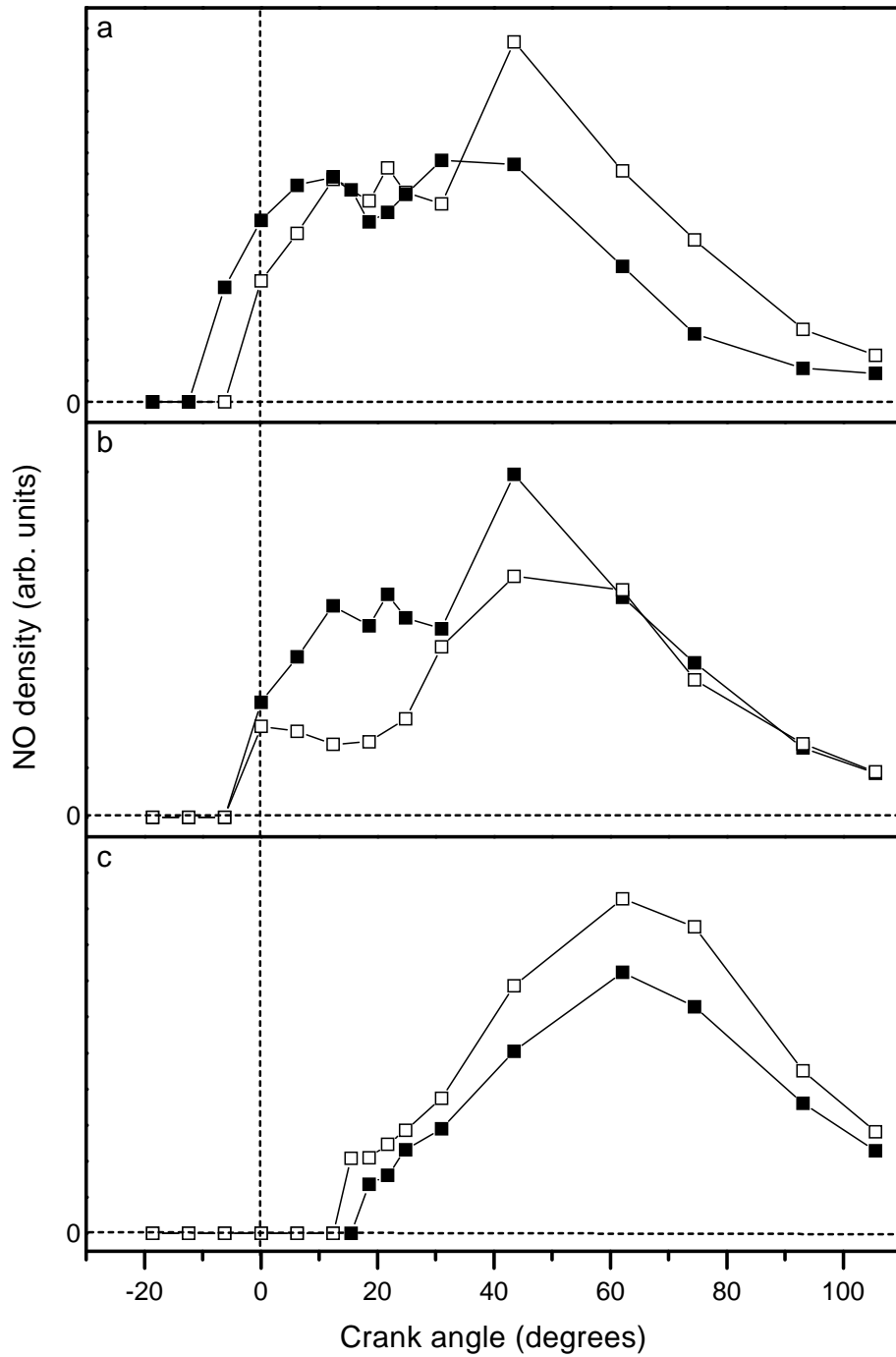


Figure 4.4: NO density curves obtained from the integrated NO fluorescence yield of dispersed fluorescence spectra recorded at different engine conditions.

a) Compression ratio $\epsilon=14.4$ (■) and $\epsilon=13.4$ (□); (fuel 1, 0.44 kW load)

b) Fuel 1 (■) and 2 (□); ($\epsilon=13.4$, 0.44 kW load)

c) Load of 0.75 kW (■) and 0.88 kW (□); ($\epsilon=12.4$, fuel 2)

4.4 Conclusion

The Laser Induced Fluorescence (LIF) technique was used to study the nitric oxide (NO) production inside the combustion chamber of an optically accessible two-stroke diesel engine running on standard commercial diesel fuel. Using 193 nm excitation of NO and detection of the ensuing fluorescence at 216 nm allowed the determination of NO density throughout the whole combustion stroke.

Dispersed fluorescence spectra as a function of crank angle were measured. They show spectral structure resulting from NO fluorescence from 6° bTDC onwards, as well as additional fluorescence resulting from hot oxygen (O_2), partly overlapping the NO fluorescence bands. For crank angles $\lesssim 20^\circ$ aTDC the spectra are dominated by fluorescence from vibrationally hot O_2 ($v''=2,3$), whereas it is almost absent in the spectra at crank angles $\gtrsim 40^\circ$ aTDC. In the evaluation of the measured fluorescence signals, this interfering O_2 fluorescence was taken into account.

From the dispersed fluorescence spectra a relative measure for the amount of NO present inside the cylinder was obtained. In order to compare the amounts of NO throughout the stroke and for different engine conditions, fluorescence spectra were processed for the changing in-cylinder conditions (volume, pressure, temperature and laser radiation intensity). Two different estimates of the local temperature within the probe volume were used.

The resulting NO density curves showed that, for this engine, the density increases throughout the combustion stroke till somewhere between 20° and 50° aTDC. Thereafter, the NO density in the probe volume seems to decrease, however, this is mainly an effect of the expanding cylinder volume as seen from the NO content curves. This indicates that the diffusion burning phase of the combustion makes an important contribution to the NO formation and that NO formation continues in the hot post-combustion gases. This result is in agreement with the recently presented results from the group of Dec [17], showing that NO was formed at the periphery of the jet, starting just after the diffusion flame forms. Towards the end of the stroke a small decline of the NO content curves was seen. This could be due to the conversion of NO to NO_2 in the colder part of the stroke.

In the future, planar LIF will be used to obtain two-dimensional distributions of NO fluorescence, using the O_2 interference-free band at 208 nm. In addition, the LIF method will be applied on a realistic six-cylinder, direct-injection, 11.6 ℓ DAF diesel engine. One of the cylinders is elongated and has been made optically accessible by a window in the piston and windows in the top of the cylinder wall. Also, other excitation/detection schemes will be pursued, notably using 226 nm excitation of NO in the $A(v'=0) \leftarrow X(v''=0)$ band. First measurements using this excitation pathway are currently being evaluated [82].

Appendix: Signal processing

In order to quantify the measured fluorescence yield, all factors concerning the excitation of the molecules and the induced fluorescence resulting from the excited molecules have to be taken into account. For the case of pulsed excitation in which the fluorescence out of the excited state is recorded, the relation between the fluorescence signal S_{LIF} , and the local NO density, ρ_{NO} , can be written as

$$S_{\text{LIF}} = C \int_{\text{V}} A_{\text{F}}(\vec{r}) \wp(\text{P}, \text{T}(\vec{r})) g(\nu_{\text{L}}, \nu_{\text{a}}) f_{\text{v,J}}(\text{T}(\vec{r})) I_{\text{L}}(\vec{r}) \rho_{\text{NO}}(\vec{r}) d^3r \quad (4.1)$$

where the integration is taken over the whole volume seen by the detector. C is a proportionality constant, $I_{\text{L}}(\vec{r})$ is the local intensity of the laser beam and $A_{\text{F}}(\vec{r})$ is a factor describing the attenuation of induced fluorescence on its way to the top window. The Boltzmann fraction, $f_{\text{v,J}}(\text{T}(\vec{r}))$, describes the temperature-dependent population of the probed state. The Stern-Vollmer factor, $\wp(\text{P}, \text{T}(\vec{r}))$, accounts for the competition between radiative and non-radiative (collision-induced) decay of excited molecules, and $g(\nu_{\text{L}}, \nu_{\text{a}})$ is the overlap integral of the laser line profile with the NO absorption spectrum. In the model rotational energy transfer in the ground state is neglected as discussed in chapter 2, section 2.3.2.

In order to extract a NO density from the measured fluorescence yield, all factors in equation 4.1 have to be known. However, although the general relationship between the fluorescence yield and the NO content is clear, most of the individual factors are difficult to obtain. Furthermore, evaluation of these factors results in expressions which depend on the in-cylinder conditions (volume, pressure, temperature and laser intensity) of which particularly the temperature is insufficiently known. The evaluation of the individual factors of equation 4.1 is discussed below for the case of laser illumination and fluorescence detection both through the top window.

Ideally, for the experimental setup of figure 4.1, each (square) CCD pixel collects fluorescence from a square rod parallel to the cylinder axis and extending from the bottom of the top window downwards (z -direction; $z=0$ at the top window). In practice, some averaging will take place due to the finite depth of field of the camera objective ($f/4.5$), as well as some image blurring due to the slightly etched lower surface of the observation window. Neglecting these effects for the present analysis, and taking into account that the spectra in figure 4.2 represent averages over the slit height, equation 4.1 can be rewritten as

$$\begin{aligned} S_{\text{LIF}}(\lambda) &= C(\lambda) \int_{z=0}^{z_p} A_{\text{F}}(z) \wp(\text{P}, \text{T}(z), \lambda) g(\nu_{\text{L}}, \nu_{\text{a}}, z) f_{\text{v,J}}(\text{T}(z)) I_{\text{L}}(z) \rho_{\text{NO}}(z) dz \\ &\approx C(\lambda) \overline{\wp(\text{P}, \bar{\text{T}}, \lambda)} \overline{g(\nu_{\text{L}}, \nu_{\text{a}})} f_{\text{v,J}}(\bar{\text{T}}) \bar{\rho}_{\text{NO}} \int_{z=0}^{z_p} I_{\text{L}}(z) A_{\text{F}}(z) dz \end{aligned} \quad (4.2)$$

in which z_p is the position of the piston upper surface. In the second step several proportionality factors have been replaced by their average values (indicated by overbars), which allows to take them out of the integral. This model, therefore, provides a value for the *average* NO density in the whole volume seen by the detector (the probe volume).

Proportionality constant C: This factor is just a gauge constant including a number of experimental parameters like collection efficiency, window transmission, camera sensitivity, etc. It is constant during the whole combustion stroke.

Local laser intensity $I_L(z)$ and Fluorescence attenuation $A_F(z)$: On their way through the combustion chamber both the laser radiation and the induced fluorescence suffer attenuation, due mainly to absorption by and scattering off soot particles and fuel and oil droplets. The intensity of the laser beam, with an intensity I_0 when it enters the combustion chamber, can be written as

$$I_L(z) = I_0 \exp \left(- \int_0^z \sigma_{ext}(z') n_{ext}(z') dz' \right), \quad (4.3)$$

in which σ_{ext} is an effective extinction cross section and n_{ext} is the density of attenuating particles. A similar equation holds for the fluorescence attenuation, $A_F(z)$. In general, both σ_{ext} and n_{ext} will be a function of position z . The local extinction coefficient is (for this particular setup) an inaccessible parameter, that cannot be measured. An approximation can be made by replacing $\sigma_{ext}(z)n_{ext}(z)$ by its average, $[\overline{n\sigma}]_{ext}$. In this approximation, and combining the equations for I_L and A_F , the integral in equation 4.2 can be written as

$$\int_{z=0}^{z_p} I_L(z) A_F(z) dz \approx I_0 \int_{z=0}^{z_p} \exp(-2 [\overline{n\sigma}]_{ext} z') dz' = \frac{\delta I_0}{2} (1 - \exp(-2 z_p/\delta)) , \quad (4.4)$$

in which a penetration depth δ has been defined as $\delta = 1/[\overline{n\sigma}]_{ext}$. Also, $[\overline{n\sigma}]_{ext}$ has been assumed to be the same at the wavelengths of excitation (193 nm) and fluorescence detection (216 nm in the case of figure 4.2).

A measure for the average extinction coefficient over the whole cylinder can be obtained from transmission measurements of the laser beam, as discussed in chapter 3. These data, given in figure 4.5, show a rise in transmission around 60° aTDC, which coincides with the end of the visible combustion, suggesting that unburned fuel plays a part in the absorption of 193 nm laser radiation. Apart from this, the expansion also reduces the density of soot and other absorbing species, which causes less attenuation of the laser radiation with increasing crank angle. The penetration depth of the laser radiation, defined in equation 4.4, is also included in figure 4.5, as well as the distance between the lower surface of the top window and the upper surface of the piston (z_p).

For the interpretation of the spectra of figure 4.2, we have assumed the *average* extinction coefficient obtained from the transmission measurements to be equal to the *average* extinction coefficient $[\overline{n\sigma}]_{ext}$ of equation 4.4. It has, however, been checked that changing these values by as much as a factor of 10 (both smaller and larger) has relatively little influence on the *shape* of the NO density curves as a function of crank angle (the absolute numbers do change, of course, but these are arbitrary units anyway).

Boltzmann fraction $f_{v,J}(\overline{T})$: The temperature dependent fractional population of the probed state ($v''=1, J''=26.5/32.5$) can be calculated using the well established spectroscopic data of the NO electronic ground state [83]. For the average temperature \overline{T} either the mean gas temperature or the soot temperature has been used.

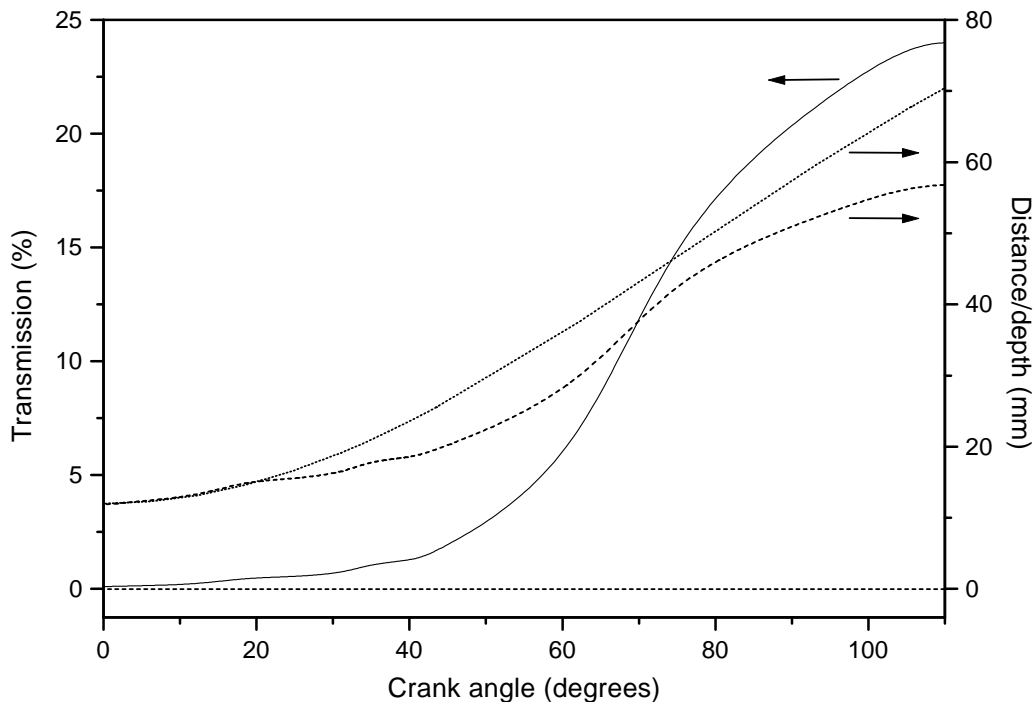


Figure 4.5: Transmission of the laser beam (solid line; $\lambda=193.377$ nm) through the firing engine (based on 0.5% window transmission). It is measured by coupling the laser beam in and out through the side windows and detecting the transmitted radiation behind the exit window. Also included are the penetration depth (δ) defined in equation 4.4 (dashed line), as well as the distance between the lower surface of the top window and the upper surface of the piston (z_p) (dotted line).

Stern-Vollmer factor $\wp(P, \bar{T})$: The competition between the radiative and non-radiative decay channels is described by the Stern-Vollmer factor,

$$\wp(P, \bar{T}, \lambda) = \frac{A_{v'v''}}{\sum_{v''} A_{v'v''} + Q} \approx \frac{A_{v'v''}}{Q}. \quad (4.5)$$

The radiative decay rate, $A_{v'v''}$, can be estimated from the radiative lifetime of the D-state ($\tau=18$ ns [84]) and the Frank-Condon factor for the used fluorescence transition $D(v'=0) \rightarrow X(v''=4)$ at 216 nm (0.076, calculated using a model of Nicholls [85] and the spectroscopic data for NO [83]). The non-radiative decay rate, Q , is caused by intermolecular collisions including both EET ($D \rightarrow C$ and $D \rightarrow A$) and quenching ($D \rightarrow X$). For the A-state, data on quenching are available in literature [71, 86], but little is known for the D-state. Separate measurements in a high temperature, high pressure cell have shown that $D \rightarrow A$ electronic energy transfer induced by collisions with N_2 is a very effective decay channel [82]. Since N_2 is always the major species in the combustion chamber, it is assumed for the moment that the non-radiative decay rate of the $D(v'=0)$ level in the engine is dominated by N_2 collision-induced EET to the A-state, so that the detailed composition of the burning mixture is relatively unimportant³. Therefore,

³Note that N_2 is an inefficient quencher of the $A(v'=0)$ level (see *e.g.* ref. [71]), but that EET plays no role in the non-radiative decay of this (lowest excited) electronic state.

Q can be written as $Q = \bar{v} n_{col} \sigma_{col}$, in which $\bar{v} = \sqrt{8k\bar{T}/\pi\mu}$ is the mean relative velocity of the collision partners at a total density n_{col} ($\propto P/\bar{T}$) and σ_{col} is an effective non-radiative cross section, taken to be independent of pressure and temperature. In the firing engine $Q \gg A$ [30] and therefore

$$\wp(P, \bar{T}) \propto \frac{\sqrt{\bar{T}}}{P}. \quad (4.6)$$

Overlap integral $g(\nu_L, \nu_a)$: The overlap integral can be calculated analytically by assuming Gaussian profiles for both the laser emission ($L(\nu - \nu_L)$) and the NO absorption line ($N(\nu - \nu_a)$), with central frequencies ν_L and ν_a , respectively. A shift in the position of the lines is not taken into account because the laser is tuned to resonance ($\nu_L = \nu_a$), under engine conditions, before each measurement. This results in:

$$g(\nu_L, \nu_a) = \int_0^{+\infty} L(\nu - \nu_L) N(\nu - \nu_a) d\nu \propto \frac{1}{\sqrt{\Delta_L^2 + \Delta_a^2}}, \quad (4.7)$$

in which Δ_L and Δ_a are the widths (FWHM) of the laser emission line and the NO absorption line, respectively⁴. Δ_L is constant (1 cm^{-1}) but Δ_a is affected by the changing pressure and temperature during the stroke. Calculation of Δ_a requires information about the pressure broadening of the NO absorption lines in the $D(\nu'=0) \leftarrow X(\nu''=1)$ band under engine conditions. These data are not available in literature. For the present purpose the functional pressure and temperature dependence of the $A \leftarrow X$ band is taken [87, 88], in combination with a proportionality factor that is derived from own measurements on the $D \leftarrow X$ band in the engine, (section 2.5.1, figure 2.14), yielding

$$\Delta_a = 0.53 P \left(\frac{295}{\bar{T}} \right)^{0.75} \text{ cm}^{-1}, \quad (4.8)$$

with P the pressure in bar and \bar{T} the average temperature in Kelvin.

Following the procedure described above, relative values for the average NO density within the probe volume can be extracted from the fluorescence yield as a function of crank angle. To the extent that the probe volume is representative for the whole cylinder (which seems not unreasonable, in view of the illuminated area indicated in figure 4.1 and the penetration depth of figure 4.5), these density data can be related to an in-cylinder NO content by multiplication with the (crank angle dependent) in-cylinder volume,

$$N_{NO} \propto \overline{\rho_{NO}} V(z_p). \quad (4.9)$$

⁴Under the conditions of the present experiments, pressure broadening is likely to give the dominant contribution to the NO linewidth. Thus, it would be more appropriate to use a Lorentzian instead of a Gaussian lineshape, but this would not lead to analytical results for the overlap integral. Numerical calculations have shown that equation 4.7 gives about 3% too small results, almost independent of crank angle. Since all NO density results reported here are in arbitrary units, such a virtually constant proportionality factor is irrelevant. Note that also a possible contribution of neighbouring NO transitions at high pressure and temperature to the overlap integral is neglected.

Chapter 5

Nitric oxide distributions in relation to temperature and chemical composition inhomogeneities

Abstract

The Planar Laser Induced Fluorescence (PLIF) technique is used to study the spatial and temporal distribution of nitric oxide (NO) inside the combustion chamber of an optically transparent two-stroke diesel engine running on commercial diesel fuel. The NO molecules are excited by a sheet of excimer laser radiation in the $D^2\Sigma^+(v'=0) \leftarrow X^2\Pi(v''=1)$ band at 193.377 nm. Induced fluorescence is detected by a CCD camera through a narrow-band filter in order to single out a NO fluorescence band at 208 nm that is free of oxygen (O_2) fluorescence. Additionally, distributions of the elastically scattered radiation are recorded to reconstruct the local laser intensity, in order to correct the NO fluorescence distributions for the decrease in laser intensity over the field of view. The obtained distributions are transformed into NO density distributions on the assumptions that all other factors in the transformation of NO fluorescence into NO density are uniform over the field of view. The extent to which deviations from uniformity in temperature and fluorescence quenching rate affect the derived NO density distribution is estimated. A measure for the NO density inside the probe volume as a function of crank angle is derived from the fluorescence distributions by integrating the total fluorescence. This fluorescence yield is transformed into a semi-quantitative NO density/content in the cylinder taking into account the crank angle dependence of the engine parameters (pressure, temperature and laser radiation intensity). These NO density/content curves are compared to similar curves obtained from dispersed fluorescence spectra.

5.1 Introduction

Strategies for the reduction of toxic emissions from diesel engines focus on particulates (soot) and oxides of nitrogen (NO_x). Emission control therefore aims at either catalytic exhaust gas after-treatment or at combustion optimisation, where optimisation is taken to imply reduced toxic compound formation while (at least) maintaining combustion efficiency. Combustion optimisation, arguably the more fundamental way of tackling the emission problem, poses a huge challenge both to experimental data acquisition and interpretation, and to theoretical combustion modelling. Non-intrusive optical diagnostics, based on planar Laser Induced Fluorescence (LIF), are used to monitor the amount as well as the distribution of nitric oxide (NO) inside the combustion chamber of a diesel engine.

The measurement principle of the planar LIF (PLIF) technique involves electronic excitation of the molecules of interest by a thin sheet of laser radiation, and detection of the subsequent fluorescence in a direction perpendicular to the sheet by an intensified CCD camera. PLIF has been used to demonstrate the presence of a large number of specific small molecules in a variety of combustion environments, but in general the observed data are very hard to quantify [30–32]. Although in principle the LIF intensity is linearly proportional to the local number density of laser-excited molecules, the proportionality constant depends on the local laser intensity, which is likely to vary over the field of view, and the local physico-chemical environment, involving local temperature, density, chemical composition and possibly spectroscopic interference by other molecules. Therefore, the proportionality constant will depend on the position and a fluorescence distribution cannot immediately be interpreted as a molecular density distribution. Since most of the parameters necessary for the translation of fluorescence into density are usually not known and difficult to assess simultaneously with the (P)LIF measurements, some assumptions have to be made to obtain a molecular density distribution and to quantify data.

The PLIF technique has been applied to both gasoline engines [41, 77] and to diesel engines [17, 37–39] to obtain information about the in-cylinder NO content and the in-cylinder NO distribution. The diesel engines used were often running skip-fired in order to reduce the cylinder temperature [17, 37, 39]. In addition, a low sooting diesel fuel [17, 37, 39] and/or oxygen enriched intake air was used [37–39] to reduce soot production. For this chapter the PLIF technique is used to obtain two-dimensional NO fluorescence distributions within the combustion chamber of a small, optically accessible two-stroke, direct-injection (DI) diesel engine, that is operated in normal mode (*i.e.* not skip-fired) using standard commercial diesel fuel and ambient (non-oxygen-enriched) intake air. Cycle-averaged NO fluorescence distributions as a function of crank angle are recorded by detecting the fluorescence from NO molecules which are excited in the $\text{D}^2\Sigma^+(\nu'=0) \leftarrow \text{X}^2\Pi(\nu''=1)$ band at 193.377 nm using an ArF excimer laser. As it is difficult to completely avoid oxygen (O_2) excitation in this wavelength range, it is necessary to use a narrow-band filter to single out the $\text{D}^2\Sigma^+(\nu'=0) \rightarrow \text{X}^2\Pi(\nu''=3)$ NO fluorescence band at 208 nm, that is not overlapped by O_2 fluorescence. Distributions of the elastically scattered laser radiation are obtained immediately after the NO fluorescence distributions during the same engine run. These are used to process the fluorescence distributions for the change in laser intensity on its way through the cylinder (see chapter 3). In-cylinder NO density distributions are derived by evaluation of the fluorescence distributions taking all location-dependent factors into account. These NO distributions are used to calculate a semi-quantitative NO density or content in the probe volume as a function of crank angle. Therefore the total NO fluorescence in the

image is averaged and processed for the changes in laser intensity, pressure and temperature during the stroke.

This chapter starts with a concise theoretical part giving the relationship between the NO fluorescence yield and the NO density and a description of all factors involved, followed by an experimental part in which the setup is described. The results of the PLIF measurements are presented and translated into NO density distributions which are analysed with an emphasis on the effects of inhomogeneities in temperature and/or chemical composition of the cylinder contents over the field of view. Finally, an in-cylinder NO density/content is derived from the distributions and compared against the results obtained from dispersed fluorescence spectra dealt with in chapter 4, and some conclusions are given.

5.2 Theory

This part concentrates on the evaluation of data recorded with the experimental setup described below, in which images that contain spatially resolved information about NO can be obtained by illuminating a plane by a thin laser sheet and recording the induced fluorescence in a direction perpendicular to it by a CCD camera. For the case of pulsed excitation in which the fluorescence out of the excited state is recorded, the relation between the fluorescence measured by any pixel, $S_{\text{LIF}}(x, y)$, and the corresponding local NO density, $\rho_{\text{NO}}(x, y)$, is given by

$$S_{\text{LIF}}(x, y) = C A_F(x, y) \wp(T, P) g(\nu_a(T, P), \nu_L) f_{v,J}(T) I_L(x, y) \rho_{\text{NO}}(x, y), \quad (5.1)$$

in which (x, y) represent the coordinates in the illuminated plane, with the x -axis taken along the direction of the laser beam and the y -axis along the width of the laser sheet. C is a proportionality constant, mainly determined by the experimental setup, $f_{v,J}(T)$ is the Boltzmann fraction that describes the temperature dependent fractional population of the probed state and $g(\nu_a(T, P), \nu_L)$ is the overlap integral of the laser line profile with the NO absorption spectrum. The Stern-Vollmer factor, $\wp(T, P)$, describes the competition between the radiative and non-radiative decay, $I_L(x, y)$ is the local laser intensity and $A_F(x, y)$ is a factor describing the attenuation of the induced fluorescence on its way out of the engine.

In order to extract a two-dimensional NO density distribution, $\rho_{\text{NO}}(x, y)$, from a measured NO fluorescence image, all other factors in equation 5.1 have to be known. Unfortunately, most of these factors are difficult to obtain. In addition, their evaluation often results in expressions that depend on the local circumstances (pressure, temperature, laser intensity) at the position (x, y) , which in general are not sufficiently known. The pressure as a function of crank angle in the running engine is known well and is expected to be uniform over the whole field of view. The temperature, on the other hand, is difficult to determine and in general cannot be expected to be the same over the whole field of view. Furthermore, the laser intensity depends on the position, as it is attenuated on its way through the combustion chamber. Consequently, most of the individual factors in equation 5.1 will depend on the position (x, y) as well as on the crank angle. The evaluation of the different factors is discussed below.

Proportionality constant C : This factor is constant during the whole combustion stroke. It includes a number of experimental parameters like collection efficiency, window transmission, camera sensitivity, etc. In principle, this factor will be the same for every position (x, y) , except for a small amount of vignetting at the margin of the observation window.

Local laser intensity $I_L(x, y)$: The intensity of the laser beam is attenuated on its way through the combustion chamber due to scattering off and absorption by particulates and fuel and oil droplets. For the present purpose the procedure outlined in chapter 3 to reconstruct the laser attenuation from a single elastic scattering image is followed.

Fluorescence attenuation $A_F(x, y)$: The induced fluorescence, like the laser radiation, suffers attenuation on its way to the observation window due to absorption and scattering. As the induced fluorescence (208 nm) is at almost the same wavelength as the laser radiation (193 nm), it is assumed that the average attenuation coefficient derived for the laser radiation can also be used for the fluorescence. Because this attenuation coefficient was found to be rather homogeneous over the field of view (chapter 3), it can be expected that the attenuation of the fluorescence on its way to the top window will be more or less the same for the whole image.

Additionally, $A_F(x, y)$ includes attenuation caused by the top window itself. However, these losses will be the same for every position (x, y) since the top window is burned clear by the combustion and no localised dirt is seen on it.

Boltzmann factor $f_{v,J}(T)$: The fractional population of the probed states ($v''=1, J=26.5/32.5$) depends strongly on temperature. Although it can be calculated using the well established spectroscopic data of the NO electronic ground state [83], the appropriate temperature, however, is difficult to determine. The latter may depend on the position (x, y) , and, since the $v''=1$ state is probed, small variations in temperature will have a relatively large effect on the population. In general, therefore, the Boltzmann factor cannot be expected to be uniform over the whole image. This point will be discussed further below.

Stern-Vollmer factor $\wp(T, P)$: The Stern-Vollmer factor, describing the competition between the radiative and non-radiative decay channels, is given by

$$\wp(P, T) = \frac{A_{v'v''}}{\sum_{v''} A_{v'v''} + Q} \approx \frac{A_{v'v''}}{Q}, \quad (5.2)$$

in which the non-radiative decay rate, Q , is assumed to be much larger than all radiative decay rates $A_{v'v''}$ under the conditions prevalent in the engine [30]. The radiative decay rate can be estimated from the radiative lifetime of the D-state ($\tau=18$ ns [84]) and the Franck-Condon factor for the monitored fluorescence transition $D(v'=0) \rightarrow X(v''=3)$ at 208 nm (0.165, calculated using a model of Nicholls [85] and the spectroscopic data for NO [83]). The non-radiative decay rate is caused by intermolecular collisions, including both Electronic Energy Transfer (EET; $D \rightarrow C$ and $D \rightarrow A$) and quenching ($D \rightarrow X$) (see section 2.3.2). After EET radiative decay can still occur from the NO A- or C-state, but that will be at wavelengths outside the detection system bandwidth. In contrast to the NO A-state, for which data on quenching are available in literature [71, 86], only little is known for the D-state. In general, Q can be written as $Q = \sum_{\text{col}} \bar{v} n_{\text{col}} \sigma_{\text{col}}$, in which $\bar{v} = \sqrt{8kT/\pi\mu}$ is the mean relative velocity of the collision partners at a total density n_{col} ($\propto P/T$) and σ_{col} is a non-radiative collision cross section, that includes both EET and quenching. As a first approximation $Q \approx \bar{v} n_{\text{tot}} \sigma_{\text{eff}}$, in which n_{tot} is the total density and σ_{eff} an effective non-radiative collision cross section, so that

$$\wp(P, T) \propto \frac{\sqrt{T}}{P}. \quad (5.3)$$

The Stern-Vollmer factor, in general, will not be uniform over the field of view as it depends on the square root of the temperature which can vary with the position (x, y) . In addition, the

proportionality factor in equation 5.3 will vary with local variations in chemical composition (through σ_{eff}) over the field of view. This is discussed qualitatively in the Appendix.

Overlap integral $g(\nu_a(T, P), \nu_L)$: Assuming Gaussian profiles for both the laser emission line ($L(\nu - \nu_L)$) and the NO absorption line ($N(\nu - \nu_a)$), with central frequencies ν_L and ν_a , respectively, the overlap integral can be calculated analytically (see footnote page 100). A shift in the position of the lines need not be taken into account because the laser is tuned to resonance ($\nu_L = \nu_a$) before each measurement. This results in:

$$g(\nu_L, \nu_a) = \int_0^{\infty} L(\nu - \nu_L)N(\nu - \nu_a) d\nu \propto \frac{1}{\sqrt{\Delta_L^2 + \Delta_a^2(T, P)}}, \quad (5.4)$$

in which Δ_L and $\Delta_a(T, P)$ are the widths (FWHM) of the laser emission line and the NO absorption line, respectively. Δ_L is constant (1 cm^{-1}) but $\Delta_a(T, P)$ is affected by the changing pressure and temperature during the stroke and therefore depends on the position (x, y) as well as on the crank angle. Calculation of Δ_a requires information about the pressure broadening of the NO absorption lines in the $D(v'=0) \leftarrow X(v''=1)$ band under engine conditions. These data are not available in literature. For the present purpose the functional pressure and temperature dependence of the $A \leftarrow X$ band is taken [87, 88], in combination with a proportionality factor that is derived from own measurements on the $D \leftarrow X$ band in the engine (section 2.5.1, figure 2.14), yielding

$$\Delta_a(T, P) = 0.53 P \left(\frac{295}{T} \right)^{0.75} \text{ cm}^{-1}. \quad (5.5)$$

The temperature dependence of the linewidth of the NO absorption line may cause small non-uniformities in the overlap integral for different positions (x, y). The overlap integral will also vary as a result of variations in chemical composition over the field of view.

In order to arrive at a NO density distribution at a specific crank angle, only the spatial dependence of the factors in equation 5.1 is of interest, whereas for comparing densities at different crank angles also the crank angle dependence of the factors has to be taken into account. To compare the relative densities of the NO distributions at different crank angles the total intensity of the distributions is integrated. These integrated intensities are processed for all crank angle dependent factors resulting in a semi-quantitative value for the average density of NO, $\bar{\rho}_{NO}$, present in the probe volume as a function of crank angle. This crank angle dependence should be equal to that obtained from the NO density derived from the fluorescence yield of dispersed fluorescence spectra, only the probe volume is different (see chapter 4). On the assumption that the probe volume is representative for the whole cylinder, an in-cylinder NO content can be calculated by multiplication with the crank angle-dependent volume,

$$N_{NO}(\Theta) \propto \bar{\rho}_{NO} V(\Theta), \quad (5.6)$$

in which Θ denotes the crank angle.

5.3 Experimental setup

Measurements are performed on a one-cylinder, two-stroke, direct injection diesel engine, described in detail in chapter 2. In the present experiments the engine is steadily running (*i.e.* not skip-fired) on standard commercial diesel fuel. No additional oxygen was added to the (ambient) intake air. The engine is made optically accessible by mounting quartz windows in the cylinder head. Two rectangular side windows (W1 and W2, $25 \times 10 \text{ mm}^2$, thickness 25 mm) are placed diametrically in the cylinder wall and one cylindrical top window (W3, diameter 25 mm, thickness 35 mm) is placed centrally in the top of the cylinder head. In this way a laser sheet (oriented in a horizontal plane, that is, parallel to the piston upper surface) can traverse the combustion chamber through the side windows while the scattered light can be coupled out in a direction perpendicular to the laser sheet through the top window as shown in figure 5.1.

To excite the NO molecules a pulsed (10 Hz) tunable excimer laser (Compex 350T; Λ -Physik) running on ArF is used. It delivers a beam whose shape is rectangular ($25 \times 3 \text{ mm}^2$), with a pulse duration of 20 ns and a bandwidth of 1.0 cm^{-1} . The laser is synchronised to the position of the piston with an accuracy of 0.6 degree crank angle. With the excimer laser NO molecules are excited at the $R_1(26.5)/Q_1(32.5)$ transition in the $D^2\Sigma^+(v'=0) \leftarrow X^2\Pi(v''=1)$ band at 193.377 nm [55]. This transition was selected in order to minimise interference from vibrationally hot oxygen that also has several strong transitions within the tuning range of the excimer laser [63–66] (see section 2.5.1). As it is difficult to avoid O_2 excitation completely, it

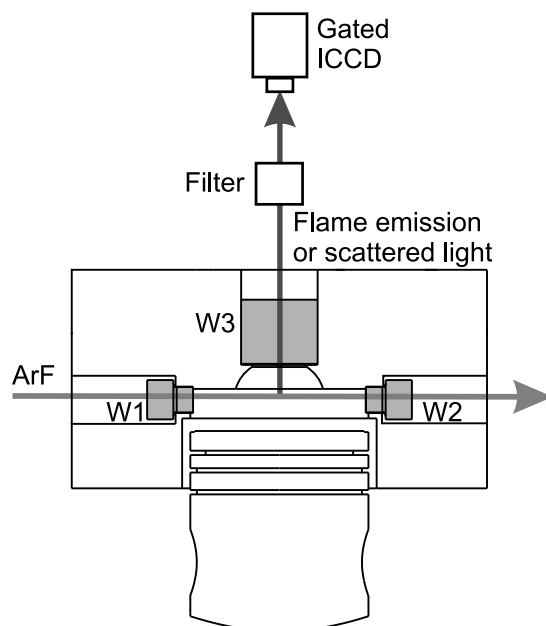


Figure 5.1: Schematic view of the modified two-stroke diesel engine and the optical setup. The engine is optically accessible by two windows in the side wall (side windows; W1,2) and one window in the top of the cylinder head (top window; W3). The ArF excimer laser beam traverses the combustion chamber through the side windows. The induced fluorescence, elastically scattered radiation or natural flame emission is detected through the top window by a gated CCD camera, positioned behind a filter.

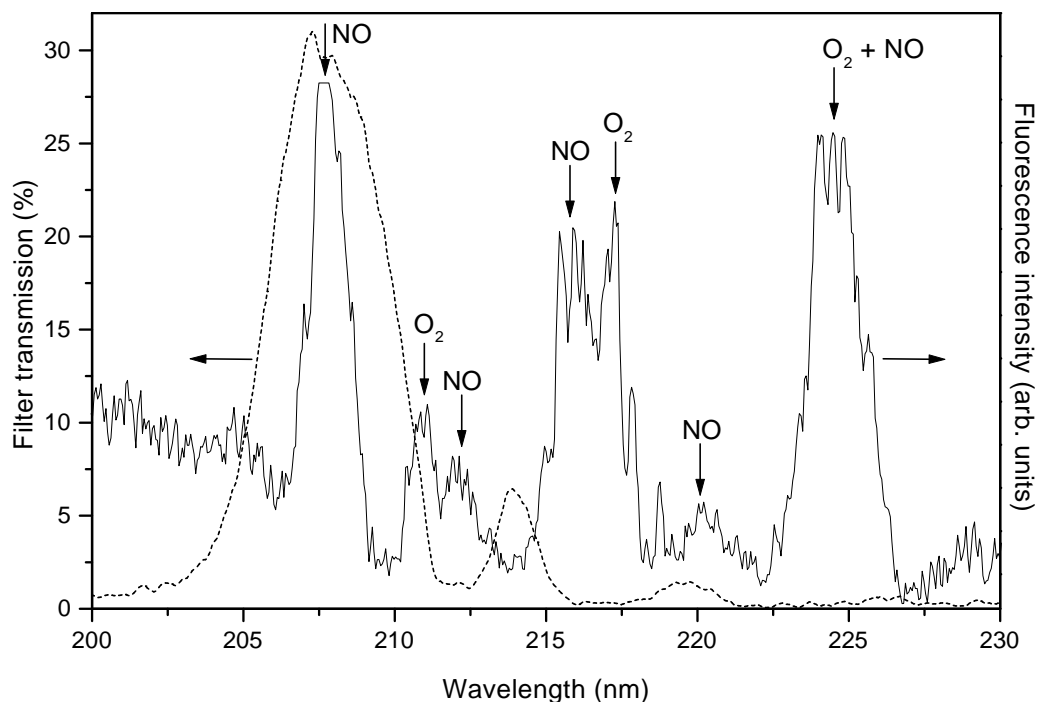


Figure 5.2: Dispersed fluorescence spectrum of NO, excited at the $R_1(26.5)/Q_1(32.5)$ transition in the $D^2\Sigma^+(v'=0) \leftarrow X^2\Pi(v''=1)$ band, obtained from the running engine at 25° aTDC (solid curve). NO fluorescence of the $D^2\Sigma^+(v'=0) \rightarrow X^2\Pi(v''=3,4,5)$ bands is seen at 208, 216 and 225 nm, respectively and of the $C^2\Pi(v'=0) \rightarrow X^2\Pi(v''=3,4)$ bands at 212.5 and 220 nm, respectively. At 211, 217 and 225 nm interfering fluorescence of O_2 is seen. NO and O_2 fluorescence coincide at 225 nm. Characteristic of the filter used to single out the $D^2\Sigma^+(v'=0) \rightarrow X^2\Pi(v''=3)$ fluorescence band of NO at 208 nm (dashed curve).

is necessary to use a filter to single out one specific fluorescence band of NO that is not overlapped by O_2 fluorescence. Spectra of the laser induced fluorescence, dispersed in its different wavelength components and recorded from the running engine, provide the information necessary to determine a fluorescence band of NO free from O_2 fluorescence (see section 4.3.2). A dispersion spectrum which clearly shows the interference between NO and O_2 , recorded at 25° aTDC by coupling in the laser beam through the top window and detecting the induced fluorescence through the top window as well, is given in figure 5.2 (solid curve). NO fluorescence is seen at 208, 216 and 225 nm from the directly excited $D^2\Sigma^+(v'=0)$ -state to the $X^2\Pi(v''=3,4,5)$ -states respectively, whereas O_2 fluorescence is seen at 211, 217 and 225 nm. At 225 nm the O_2 fluorescence coincides with the NO fluorescence. The fluorescence at 212.5 and 220 nm can be attributed to the $C^2\Pi(v'=0) \rightarrow X^2\Pi(v''=3,4)$ bands (the C-state is populated by collisional EET). This spectrum shows that the $D^2\Sigma^+(v'=0) \rightarrow X^2\Pi(v''=3)$ fluorescence band at 208 nm can be used for imaging because it is free of oxygen fluorescence and lies sufficiently far from the nearest O_2 fluorescence band seen at 211 nm. It should be noted that the intensity of the 208 nm peak in this spectrum is somewhat too large due to a narrow peak (0.5 nm FWHM) at 207.8 nm that interferes with the NO fluorescence band. However, this peak is an artefact of this particular setup in which the laser beam is coupled into the engine through the top window, caused probably by Raman scattering of the quartz top window. It plays no part when using side

window illumination, instead of top window illumination, as done in the experiments described below.

For the measurements of two-dimensional images the laser beam is oriented in a horizontal sheet (0.5 mm thick) parallel to the upper surface of the piston at TDC. It is coupled into the combustion chamber through the laser entrance window (W1) and coupled out through the exit window (W2) (see figure 5.1). The laser frequency is manually tuned to resonance with the NO transition before each measurement. The ensuing fluorescence is coupled out in a direction perpendicular to the laser sheet through the top window (W3), and detected by a gated (50 ns) intensified CCD camera (ICCD-576G/RB-E; Princeton Instruments) whose output is digitised and sent to a computer for further processing. When recording NO fluorescence distributions, a combination of a narrow-band filter consisting of four highly reflecting mirrors (Laser Optik) and a normal incidence 193 nm laser mirror is used in front of the camera to single out a narrow fluorescence wavelength band centred at 208 nm. The characteristic of this combination, also given in figure 5.2 (dashed curve), shows a transmission of 30% at its centre wavelength of 207 nm and a bandwidth of about 5 nm FWHM. The peaks at 214 and 219.5 nm are caused by other interference maxima in the reflection filter. In the case of recording two-dimensional elastic scattering distributions a filter transmitting 193 nm radiation is used. For the measurement of both distributions using a single laser pulse the images would have to be obtained simultaneously, because, due to the irreproducibility of the combustion, the distribution of NO molecules and scattering particles is expected to be different for every cycle. However, if images are averaged over several engine cycles, cycle to cycle variations are averaged out. Therefore, in case that fluorescence distributions and elastic scattering distributions are averaged they can be recorded directly after each other, as is done in the present experiment.

Additionally, distributions of the natural flame emission are obtained by recording the flame emission through the top window using a gate width of 200 ns.

5.4 Results and Discussion

5.4.1 NO fluorescence distributions

Raw data

Two-dimensional NO fluorescence distributions were recorded using the 208 nm filter described above by coupling in the laser beam through the side window and detecting the induced fluorescence through the top window, in a direction perpendicular to the laser beam. In addition, distributions of the elastically scattered laser radiation were recorded immediately after the NO fluorescence distributions, using a filter transmitting only the laser radiation. All images are averaged over 25 engine cycles and represent an area with a diameter of 25 mm; the probe volume amount to principle $25\varnothing \times 0.5 \text{ mm}^3$, located at the position of the piston upper surface at TDC. The illuminated part of the CCD camera corresponds to an area of 100×100 pixels, so the spatial resolution is $0.25 \times 0.25 \text{ mm}^2$. A series of eight NO fluorescence distributions recorded at different crank angles in the combustion stroke is given in figure 5.3. The distributions are presented in a linear grey scale ranging from black (minimum intensity) to white (maximum intensity) and each image is individually scaled. The laser beam travels from right to left and fuel is injected from the bottom of the images upwards.

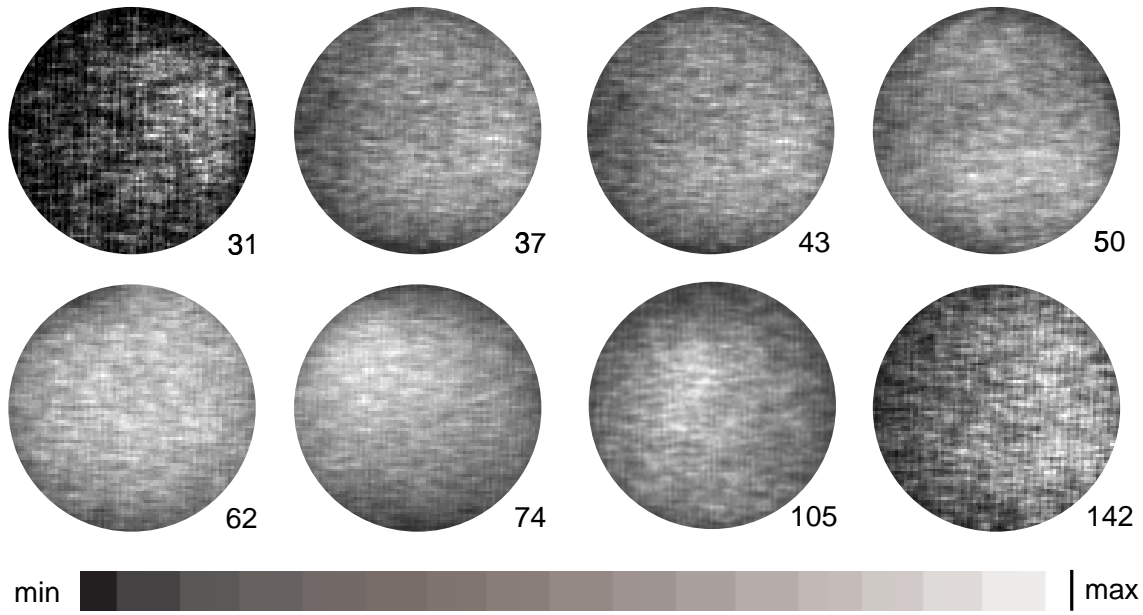


Figure 5.3: Measured NO fluorescence distributions averaged over 25 engine cycles recorded at different crank angles (indicated at the lower right of each image) during the combustion stroke. The images are presented in a linear grey scale ranging from black (minimum intensity), to white (maximum intensity), as indicated in the figure, and are individually scaled. The laser beam travels from right to left and fuel is injected from the bottom of the images upwards.

Although the raw data in figure 5.3 still have to be processed in order to derive density distributions from them, a few general observations can be made. Most images show a fairly uniform fluorescence distribution, which at least implies that sufficient laser intensity was available over the whole field of view. The increased noisiness of the images at 31° aTDC and 142° aTDC is due to weak signal approaching the detection limit. In case of the 142° aTDC image, the weak signal is very likely due to the NO being flushed out of the cylinder (outlet and inlet ports open at 105° aTDC and at 121° aTDC, respectively), whereas in the 31° aTDC image the decreasing optical transmission probably plays a major role, as discussed in chapter 3.

The question remains how much of the observed fluorescence is in fact due to NO. The characteristic of the transmission filter given in figure 5.2 shows that also some fluorescence of O_2 at 211 nm might be transmitted. However, the presence of possible O_2 fluorescence in the fluorescence distributions can be excluded on the basis of dispersed fluorescence spectra reported in chapter 4 (figure 4.2). The spectra show appreciable O_2 fluorescence only at crank angles $\lesssim 30^\circ$ aTDC, whereas the fluorescence distributions shown in figure 5.3 are recorded later in the stroke. Therefore, it can be concluded that the images of figure 5.3 (except perhaps for the 31° image) are free of O_2 fluorescence and due only to NO.

The fluorescence distributions recorded this way cannot immediately be interpreted as NO density distributions. Although the NO fluorescence is proportional to the NO density (equation 5.1), the different factors of the proportionality constant depend on the position (x, y) which results in a factor between the NO fluorescence and the NO density distribution that

in general will be different for each pixel. The majority of these inhomogeneities are caused by the non-uniform temperature distribution and the changing intensity of the laser beam over the observation area. The influence of both effects on the translation of the NO fluorescence distributions into NO density distributions is discussed below. Local variations in chemical composition are required to be of minor importance but will also be included in the discussion.

Laser intensity

The intensity of the laser beam decreases on its way through the combustion chamber due to scattering off and absorption by soot particles and oil and fuel droplets. The laser intensity decrease over the observation area is reconstructed from the distribution of the elastically scattered radiation, recorded just after the NO fluorescence distributions at every selected crank angle, and the total transmission through the engine, as described in chapter 3. Note that only the attenuation of the laser intensity over the observation area is corrected for. Therefore, in order to compare the local laser intensity for different crank angles, the intensity decrease in the first part of the combustion chamber, that cannot be seen, has still to be taken into account. Correcting the NO fluorescence distribution for the local laser attenuation results in a first order approximation to the density distribution of NO. These NO distributions are, for all measured crank angles, given in figure 5.4. However, it has to be taken into account that these distribu-

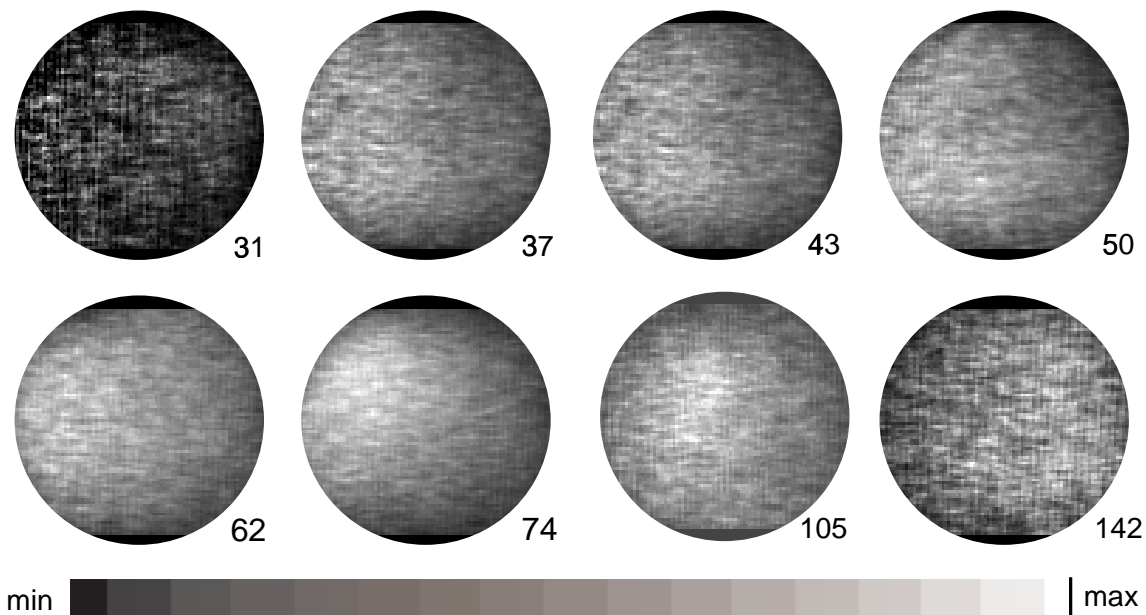


Figure 5.4: The NO fluorescence distributions, presented in figure 5.3 after processing for the decrease of the laser intensity over the field of view. These distributions represent a NO density distribution if it is assumed that all other factors in equation 5.1 are uniform over the field of view. The images are presented in a linear grey scale ranging from black (minimum intensity) to white (maximum intensity), as indicated in the figure, and are individually scaled. The laser beam travels from right to left and fuel is injected from the bottom of the images upwards.

tions represent NO density distributions only if the assumption that all factors (except the local laser intensity) in equation 5.1 are uniform over the field of view is valid.

Temperature

All temperature dependent factors in equation 5.1 (*i.e.* the Boltzmann factor, the Stern-Vollmer factor and the overlap integral) will depend on position within the probe volume. Therefore, they have to be analysed using the local temperature at a position (x, y) . The latter, however, is extremely difficult to obtain for a running diesel engine (if possible at all). Two-dimensional temperature distributions have been obtained in SI engines by Rayleigh scattering [77] and by using two-line tracer LIF [42]. For diesel engines the combustion is highly luminous as a result of the thermal radiation of soot particles at high temperatures. This high luminosity can be used to measure the local temperature in the cylinder by the two-colour method, described in detail in [33]. An interesting possibility might also be to use the fluorescence of the simultaneously excited O_2 for temperature determination (see chapter 6).

Although for the two-stroke engine the spatial distribution of temperature in the combustion chamber could not be measured, two spatially averaged crank angle dependent temperature curves were determined. An average temperature for the whole content of the cylinder, denoted as the mean gas temperature, was derived from the crank angle dependent pressure in and volume of the combustion chamber (section 2.2.2). Alternatively, a soot particle temperature was derived from the spectral distribution of the natural flame emission, largely arising from glowing soot particles, at the crank angles where flame emission can be seen. If the obtained flame emission spectra are fitted to a Planck black body radiation curve a temperature of the glowing soot particles can be determined (section 2.4.1). Both the soot temperature (■) and the mean gas temperature (dashed curve) are given in figure 5.5a. The solid curve is an extrapolation based on adiabatic expansion of an ideal gas during the later part of the stroke, matched to the intermediate part of the measured data. These two temperatures are not equal, the soot temperature being considerably higher than the mean gas temperature, and it is not evident which of the two (if any) most closely represents the local temperature at a position (x, y) and should be used in equation 5.1.

Some information on the spatial distribution of the soot temperature can be extracted from the distribution of the glowing soot particles, used to derive the soot temperature. This distribution can be obtained by recording the radiation of the glowing soot particles through the top window by a CCD camera (see figure 5.1). Here, it has to be taken into account that this results in an image that represents the flame emission integrated over the depth of the volume that is seen by the camera. Distributions of the natural flame emission averaged over 25 engine cycles, obtained using a gate width of 200 ns, are presented in figure 5.6; these images all have the same orientation as those in figures 5.3 and 5.4. The flame emissions are presented in a linear grey scale and individually scaled. Information about the relative intensity of the flame emission for the different crank angles is obtained by integrating the total intensity of the flame emission. This total integrated intensity is included in figure 5.6 (lower right). Flame emission is seen from about 19° bTDC till around 60° aTDC, and it is the most intense just before TDC. The locations where the first flame emission occurs are clearly seen in the images recorded in the beginning of the combustion. Two sites of intense luminosity can be distinguished (see arrows in figure 5.6), probably arising from two of the three sprays that can be seen through

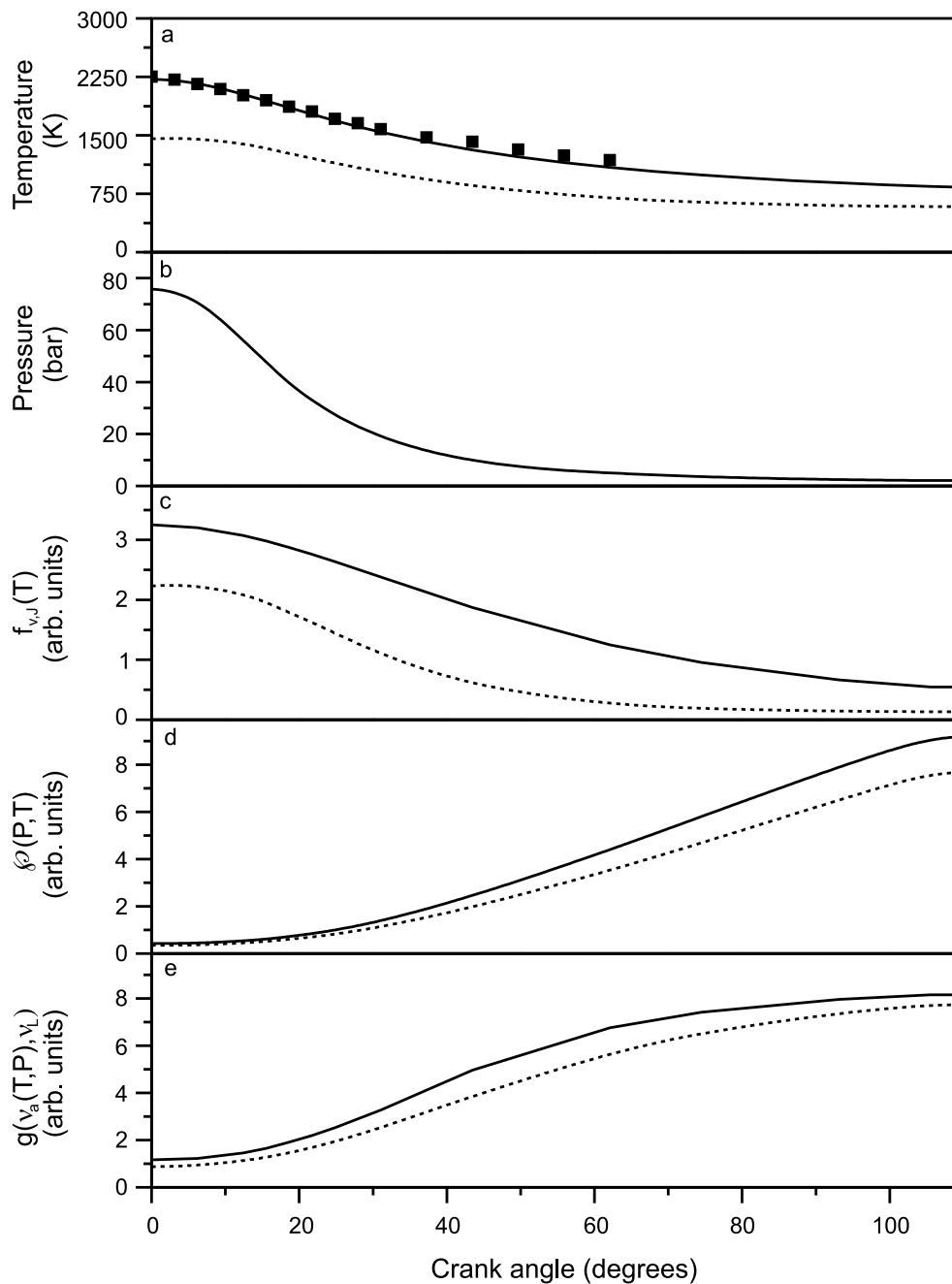


Figure 5.5: a) The mean gas temperature derived from the heat release (dashed curve) and the soot temperature derived from the spectral distribution of the natural flame emission (■). The solid curve is an extrapolation based on adiabatic expansion of an ideal gas during the later part of the stroke, matched to the intermediate part of the measured data. b) In-cylinder pressure as a function of crank angle for the running engine. c) Average Boltzmann factor, $f_{v,j}(T)$, for the $J''=26.5$ and $J''=32.5$ levels as a function of crank angle calculated for the soot temperature (solid curve) and the mean gas temperature (dashed curve). d) Stern-Vollmer factor, $\phi(T,P)$, as a function of crank angle calculated for the soot temperature (solid curve) and the mean gas temperature (dashed curve). e) Overlap integral, $g(v_a(T,P),v_L)$, as a function of crank angle calculated for the soot temperature (solid curve) and the mean gas temperature (dashed curve).

the top window. It is expected that the soot particles are located in the same region as where the combustion takes place and, therefore, the radiation used to determine the soot temperature originates from the places where the combustion actually takes place. Consequently, the distribution of the flame emission can be taken as an indication for the distribution of the soot temperature, which gives information on the regions in which the average temperature will be close to the soot temperature. It should, however, be taken into account that no conclusion can be drawn from the spatial intensity of the flame emission with respect to the exact local soot temperature, as the intensity of the emission is determined by the amount of soot along the line of sight as well. The distributions recorded in the beginning of the combustion clearly show an inhomogeneous distribution of the emission of soot particles, and they become more homogeneous during the combustion. For crank angles $\gtrsim 37^\circ$ aTDC, for which it was also possible to obtain NO fluorescence images, the flame emission is uniformly distributed.

The flame emission distributions in figure 5.6 support the expectation that the largest non-uniformities in temperature will be found around TDC, at the beginning of the combustion, where regions of high temperature arise from the start of the combustion in the relatively cold gas mixture. The soot temperature will be a better indication for the local temperature at the positions of the actual combustion (note that also the bulk of the thermal (Zeldovich) NO is expected to be formed there), whereas the mean gas temperature is probably a better estimate for the temperature at places away from the combustion. Thus, during the actual combustion regions of highly varying average temperatures will co-exist. Based on the temperature curves presented in figure 5.5a, at TDC for example, temperature variations between about 1500 and 2250 K can be expected. However, after the actual combustion the relatively large temperature differences will disappear due to mixing of the combustion gases with the unburned gas in the cylinder and the temperature distribution will become more homogeneous. Since the gases will cool down faster than the soot particles, the mean gas temperature will be a better estimate of the local in-cylinder temperature than the (extrapolated) soot temperature at the end of the stroke.

For the moment it is assumed that, for every crank angle, the most appropriate local temperature at the different positions (x, y) will be somewhere in between the two average temperatures. An indication of the variation of the different temperature dependent factors in equation 5.1 over the field of view can be derived by analysing them for both the soot temperature and the mean gas temperature. The pressure is taken constant over the image (that is, acoustical effects are neglected) and the used pressure curve as a function of crank angle measured in the running diesel engine is given in figure 5.5b. The Boltzmann factor, the Stern-Vollmer factor and the overlap integral as a function of crank angle are given in figure 5.5c, d and e, respectively, using both the soot temperature (solid curves) and the mean gas temperature (dashed curves) for their evaluation. The curves in figures 5.5d and e show that both the Stern-Vollmer factor and the overlap integral are not much influenced by the particular choice of the temperature. Therefore, it can be assumed that for the whole field of view these parameters will be more or less constant. However, the Boltzmann factor may change considerably if the local temperature changes. At TDC, where the average temperature over the field of view is expected to vary between about 2250 and about 1500 K the corresponding population changes by a factor of 1.4, whereas at the end of the stroke, with a temperature varying between 830 and 580 K, it is a factor of 4.2. This indicates that the population differences are lower at higher temperatures, which is favourable, as in the cylinder the largest spatial temperature fluctuations are expected at the start of the com-

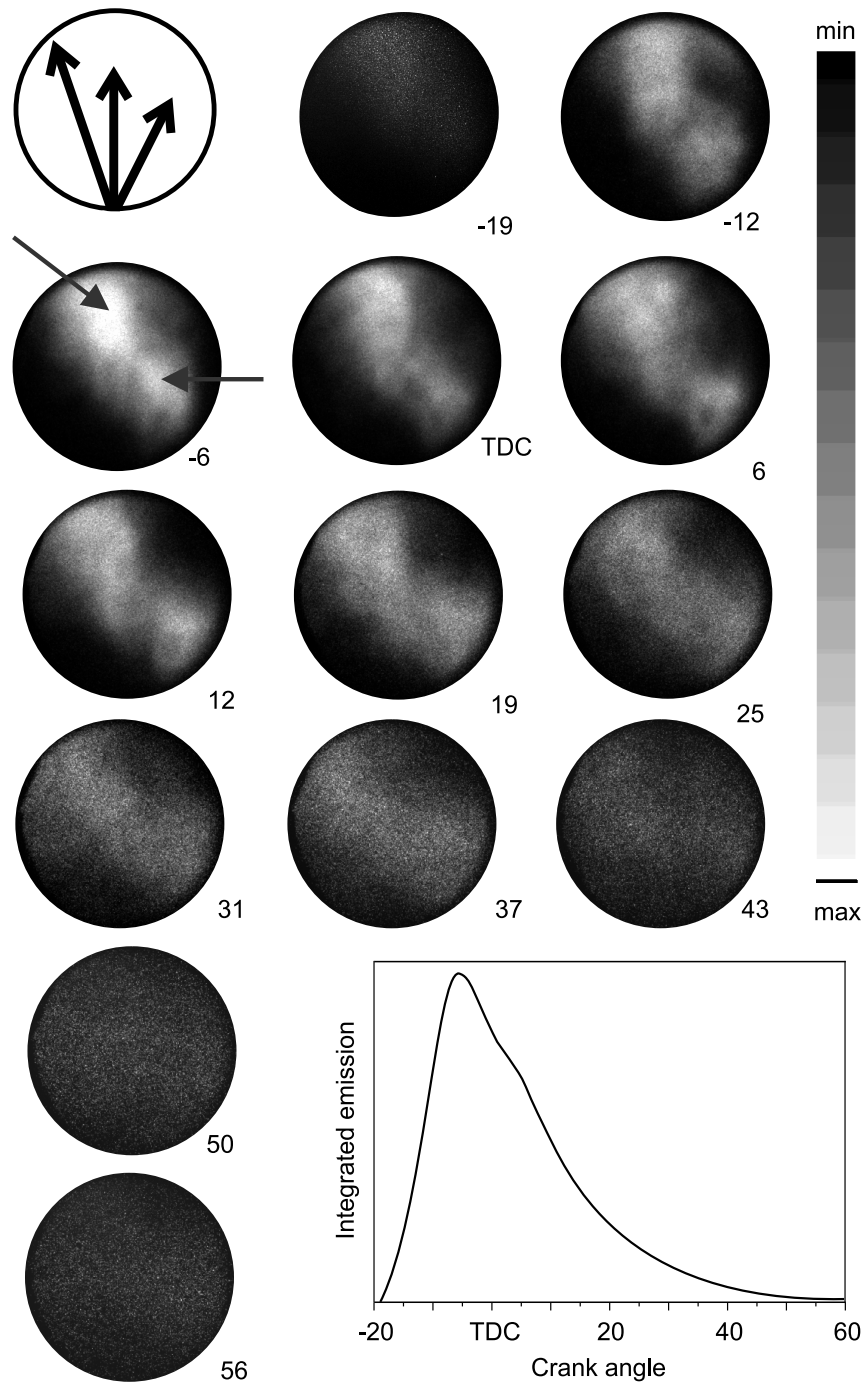


Figure 5.6: The (spectrally integrated) natural flame emission averaged over 25 engine cycles recorded through the top window using a gate width of 200 ns. Crank angles are indicated at the lower right of the images in degree crank angle where the minus sign refers to crank angles before TDC. The arrows in the image recorded at 6° bTDC indicate the two positions where the first flame emission occurs. In the upper left image the direction of the three fuel sprays, as seen through the top window, is indicated. The total intensity of the flame emission related to the crank angle is given in the lower right. All images are presented in a linear grey scale ranging from black (minimum intensity) to white (maximum intensity), as indicated in the figure, and are individually scaled.

bustion, where the temperature is highest. When the temperature drops, towards the end of the stroke, it is expected to become more homogeneous and to approach the mean gas temperature.

The fluorescence distributions in figure 5.3 are obtained late in the combustion stroke, after the actual combustion. Because the temperature is then expected to be more or less homogeneously distributed, it is assumed that temperature gradients over the field of view are of minor importance. Therefore, as a first approximation, a single uniform temperature is used for interpretation of the images. This assumption will be relaxed later on.

5.4.2 NO density distributions

When the assumptions are made that *i*) the temperature distribution over the field of view is uniform and *ii*) the fluorescence quenching is homogeneous, the NO fluorescence distributions processed for the laser attenuation over the field of view, as given in figure 5.4, can be interpreted as NO density distributions. The experimental error, determined from small scale fluctuations present in the distributions, is about 10%. By comparing the measured NO fluorescence distributions with the resulting NO density distributions only little difference is seen. The most conspicuous feature is that at almost all crank angles the most intense part of the distribution is shifted somewhat along the x -axis towards the side of the laser exit window. The noisy images at 31° and 142° aTDC, discussed above, will not be considered further. In most of the other NO density distributions in figure 5.4 a gradual increase in NO intensity over the field of view is seen along the x -axis going from right to left. The gradient of the intensity increase becomes larger going from the 37° aTDC image to the 74° aTDC image (*i.e.* with increasing crank angle). However, at 105° aTDC the highest intensity is shifted somewhat to the middle of the image. To get some feeling for the observed intensity differences over the field of view, the intensity differences of the distribution at 74° aTDC, which are relatively large, are analysed in more detail. The average intensity of this NO distribution differs by about 20% from the lowest and highest intensities that are seen at the side of the entrance and exit window, respectively. Similar, mostly somewhat lower, values result for the other density distributions. Within the approximation of a uniform temperature distribution it can be concluded that the NO density varies over the field of view by maximally 40%.

Before interpreting the NO density distributions, it is appropriate to get some insight in the errors that might be introduced by the assumptions made in the translation of the NO fluorescence distributions into NO density distributions. Firstly, it was assumed that the temperature be homogeneously distributed over the field of view. Secondly, the exact composition of the cylinder contents was supposed to be relatively unimportant. It would nevertheless be interesting to have an idea of the influence that a non-uniform temperature and/or composition of the cylinder contents would have on the obtained NO density distribution. In other words, to which extent can variations in NO fluorescence intensity be explained by variations in temperature and/or composition? To get some feeling about this, it is calculated what the variations in temperature or composition would have to be to fully explain the observed NO fluorescence distributions of figure 5.4 (which have already been processed for the laser attenuation) if the NO distribution would be uniform.

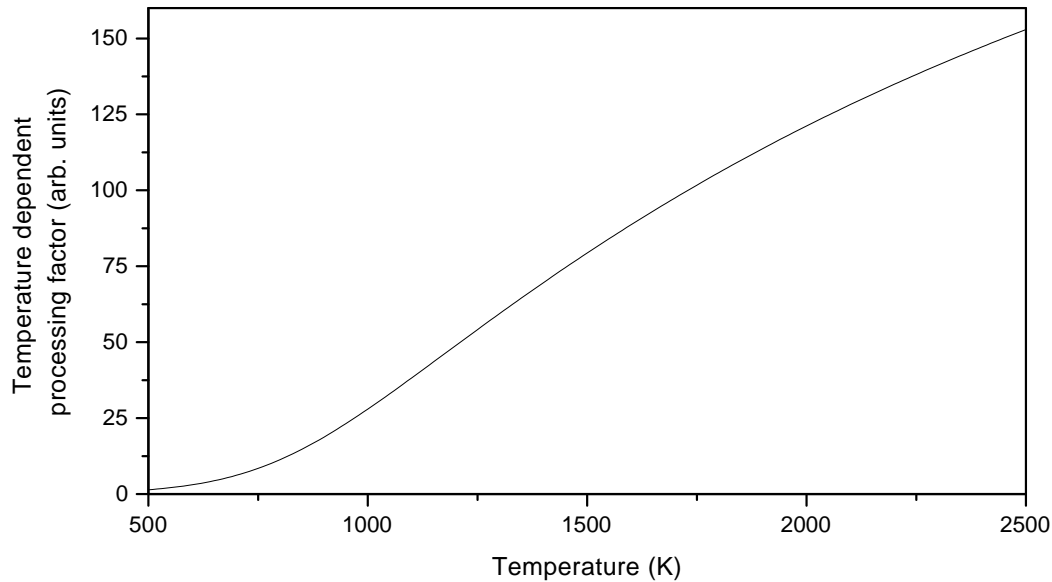


Figure 5.7: The factor, $H(T)$, resulting from the multiplication of the three temperature dependent factors in equation 5.1 (*i.e.* the Boltzmann factor, the Stern-Vollmer factor and the overlap integral) as a function of temperature, for temperatures relevant for the combustion in the engine.

Temperature distributions

First, the effect of a non-uniform temperature, $T(x, y)$, is analysed. To this end the three temperature dependent factors (*i.e.* the Boltzmann factor, the Stern-Vollmer factor and the overlap integral) are combined, resulting in a factor, $H(T(x, y))$, given by

$$H(T(x, y)) = \wp(T(x, y), P) g(\nu_a(T(x, y), P), \nu_L) f_{v,J}(T(x, y)), \quad (5.7)$$

which includes all temperature dependences of the different processing factors. $H(T(x, y))$ is given in figure 5.7, for the temperatures that are relevant for the combustion in the engine ($500 < T < 2500$ K). It is seen that $H(T)$ is approximately linear over a large temperature range. This, as a spin-off, also would justify the use of an average temperature for the calculation of spatially averaged results. Using $H(T(x, y))$ the NO fluorescence distribution (including correction for the change in laser intensity over the field of view), S'_{LIF} , can be written as

$$S'_{LIF}(x, y) \propto \rho_{NO}(x, y) H(T(x, y)), \quad (5.8)$$

if all other factors in equation 5.1 are constant over the field of view. This relation can be used to calculate the temperature distribution that would be required for a homogeneous NO density distribution to result in the corrected fluorescence distribution of figure 5.4.

These required temperature distributions are determined on the assumptions that *i)* the average temperature corresponds to the mean gas temperature and that *ii)* the mole fraction¹ of

¹The mole fraction is used instead of the NO density as in a closed volume with varying temperature (and constant pressure) the density cannot be constant in contrast to the mole fraction.

NO over the field of view is uniform. The results are presented in figure 5.8; all images have the same orientation as those in figures 5.3 and 5.4. For the 74° aTDC distribution (mean gas temperature 640 K) it is found that the average temperature at the side of the entrance window would have to be about 580 K whereas at the side of the exit window it would have to be about 690 K. That is, the variation in the corrected NO fluorescence intensity in the 74° aTDC image could be ascribed solely to a non-uniform temperature if a temperature gradient of somewhat more than 100 K would be present over the field of view (small scale variations are larger). For the other distributions the required average temperature variations over the field of view are found to be in the order of 100 K at large crank angles to 200 K for the distributions at the smallest crank angles. On a small scale the minimum and maximum temperatures, would have to vary to about 400 K. Such gradients in temperature over the field of view (25 mm diameter) are not expected in the cylinder for the studied crank angles late in the combustion cycle and are therefore unlikely to fully explain all fluorescence inhomogeneity.

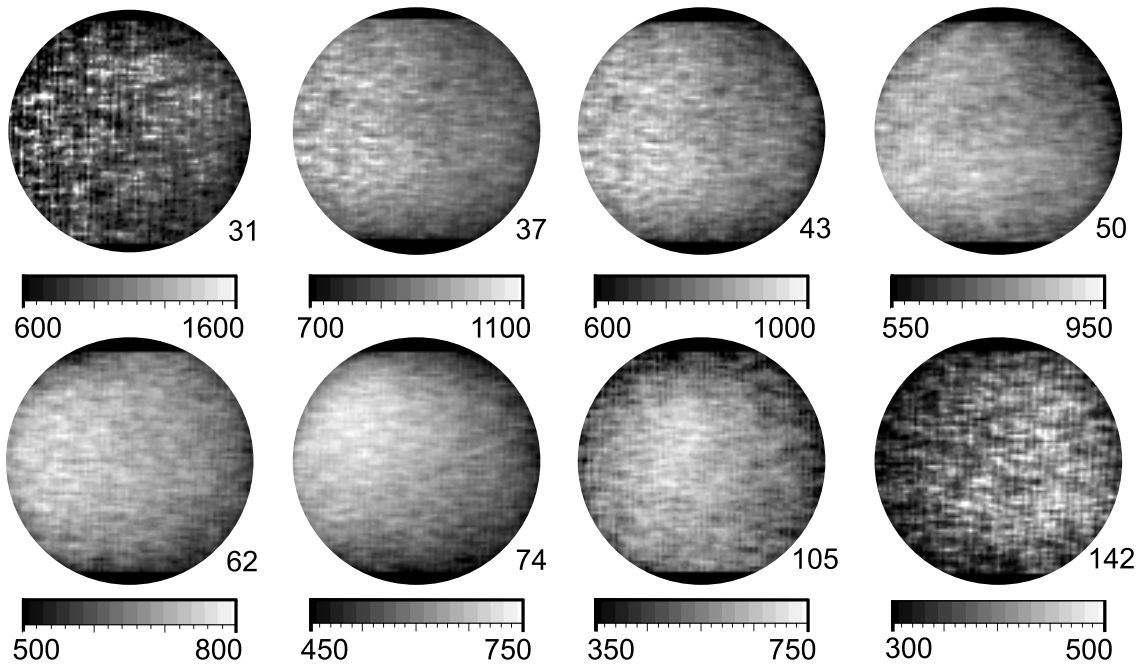


Figure 5.8: The temperature distribution over the field of view obtained from the NO fluorescence distributions processed for the local laser attenuation given in figure 5.4, on the assumption that the average NO density has an average temperature corresponding to the mean gas temperature and that the mole fraction of NO over the field of view is uniform. The images are presented in a linear grey scale ranging from black (lowest temperature) to white (highest temperature) as indicated below each image.

Collisional decay rate distributions

Besides the effect of an inhomogeneous temperature also the effect of an inhomogeneous chemical composition on the obtained NO density distribution is worth studying. Non-uniformities in gas mixture within the field of view would introduce non-uniformities in the Stern-Vollmer factor (due to variations in the non-radiative decay rate, Q) and, possibly, in the overlap integral (due to variations in the absorption linewidth). The non-radiative decay rate of the NO D-state is governed by EET and quenching processes, whereas the absorption linewidth (in the collision broadened limit) will probably be determined mainly by Rotational Energy Transfer (RET) in ground and excited state as well as by elastic (dephasing) collisions.

Assuming non-radiative decay of excited NO molecules to be much faster than radiative decay, the Stern-Vollmer factor can be approximated by A/Q , as in equation 5.2. For the conditions prevalent in the engine, the overlap integral, given in equation 5.4, will be dominated by the width Δ_a of the NO absorption line (*i.e.* $\Delta_a \gg \Delta_L$), which, if Doppler broadening is neglected, is given by the homogeneous collision rate constant Γ_H . Note that, in the present case, Q involves only quenching and EET processes, but will not be sensitive to excited state RET, because the fluorescence is not detected with rotational resolution. The collision rate Γ_H , on the other hand, is expected to be dominated by elastic (= phase changing) collisions as well as RET in the ground and excited states (the latter being the fastest inelastic process).

Taken together, the NO fluorescence yield (again corrected for laser attenuation) can be written as

$$S'_{\text{LIF}}(x, y) \propto \frac{\rho_{\text{NO}}(x, y)}{Q(x, y) \Gamma_H(x, y)}, \quad (5.9)$$

since, for the present purpose, all other factors in equation 5.1 are assumed constant (*i.e.* at a fixed temperature and pressure). By again assuming a uniform NO mole fraction over the field of view, distributions of the product $Q(x, y) \cdot \Gamma_H(x, y)$ that would be required to explain the variation in the NO fluorescence intensity of figure 5.4 can be determined. These distributions are shown in figure 5.9; all images have the same orientation as those in figures 5.3 and 5.4. Typical variations in the images stay within about $\pm 20\%$ of the average value.

The question remains, then, whether such variations in collision rates can reasonably be expected under conditions occurring in the engine. Both Q and Γ_H can be written in terms of collision cross sections as $\sum_j \bar{v}_j n_j \sigma_j$, with \bar{v} a mean relative velocity, n a density and σ a collision cross section; the summation extends over all possible collision partners and collision processes. Since pressure and temperature are held constant, \bar{v}_j and $\rho = \sum_j n_j$ are constant as well, and any fluctuation in Q and Γ_H must be attributed to changes in relative densities of species with different collision cross sections. In the absence of quantitative data on collision processes involving the NO states relevant to the present detection scheme, this subject will have to be addressed qualitatively and, to some extent, intuitively.

The most likely contributors to inhomogeneities in collisional rate constants will be the chemical majority species (N_2 , O_2 , fuel hydrocarbons, CO_2 , H_2O) and, perhaps, soot particles. Nitrogen is evidently the most abundant species at any crank angle, but, since it does not partake appreciably in the chemistry, it can hardly be expected to be non-uniformly distributed. Oxygen and fuel, on the other hand, are consumed locally by the combustion, and incorporated into CO_2 and H_2O . Soot particles, finally, can definitely be expected to be distributed non-uniformly, even later in the stroke. Also, their (geometrical) collision cross section can easily be 2 – 3 orders

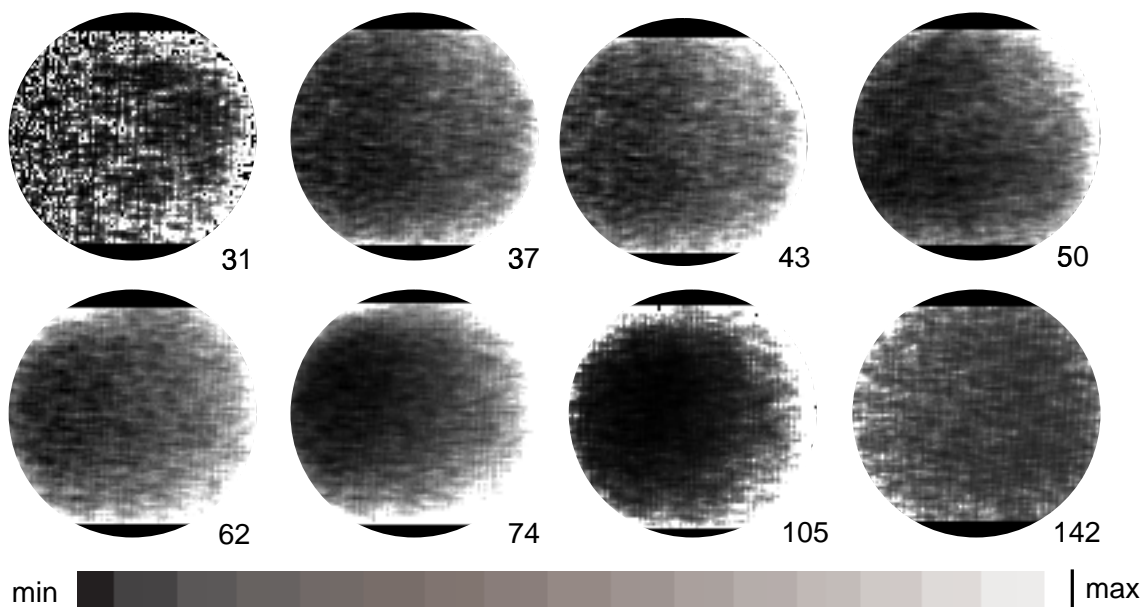


Figure 5.9: Distributions of the product $Q(x, y) \cdot \Gamma_H(x, y)$ over the field of view obtained from the NO fluorescence distributions processed for the local laser attenuation given in figure 5.4 using equation 5.9 on the assumption that the NO density distribution is uniform over the field of view. The images are presented in a linear grey scale ranging from black (minimum intensity) to white (maximum intensity), as indicated in the figure and individually scaled.

of magnitude larger than those typically associated with molecular collisions ($50 - 100 \text{ \AA}^2$). Nevertheless, since the soot particle density is so much lower (typically $\approx 10^{14} \text{ m}^{-3}$, calculated from data in [2]) than typical molecular number densities ($\approx 10^{25} \text{ m}^{-3}$ at 2 bars and 550 K), the contribution of soot particles to the total quenching rate will still be negligible. At 2 bars and 550 K, for example, the NO collision rate with soot particles is calculated to be about 12 sec^{-1} , whereas for collisions with H_2O (using a 5% mole fraction and the quenching cross section for the A-state) it amounts to ca. $4 \cdot 10^9 \text{ sec}^{-1}$.

In the Appendix a simple model is discussed which correlates non-uniformities in the densities of several of the majority species on the assumption that all such non-uniformities can be ascribed to non-uniform combustion. Assuming non-radiative decay (Q) and line broadening (Γ_H) to behave similarly, this model tends to predict unrealistically high relative cross sections for collisions with different chemical species, if *all* non-uniformity in the images of figure 5.9 were to be explained by non-uniform chemical composition. In fact, if a relative cross section $\sigma_{\text{H}_2\text{O}}/\sigma_{\text{O}_2} \sim 2 - 3$ is considered a realistic range, then only about 6% of the variation in figure 5.9 can be explained by chemical inhomogeneity, according to the model in the appendix.

Discussion

From the analysis of the effect of a non-uniform temperature or cylinder composition over the field of view it follows that the intensity differences of the NO fluorescence distributions of figure 5.4 cannot be ascribed solely to a temperature or composition variation and therefore

must arise, at least partly, from a non-uniform NO distribution. However, both effects will still have some influence on the observed NO density distribution. The combustion will introduce large non-uniformities over the field of view around TDC as can be seen in the observed flame emissions (figure 5.6). In regions where the combustion takes place the temperature will be relatively high and relatively large amounts of combustion products, including NO, will be present. Due to mixing, temperature and density differences over the combustion chamber will become smaller towards the end of the stroke, but still areas with a higher temperature and higher density of combustion products can exist. Thus, although the intensity differences seen in the NO density distribution indicate that regions exist with a somewhat higher or lower NO density, the density differences can be smaller or larger than observed in the distributions as due to temperature and composition variations the amount of NO can be under- or overestimated. In general, for most crank angles the NO density appears to be somewhat higher at the left side of the images where the probe volume intersects one of the fuel sprays (number 1 in figure 2.1).

5.4.3 Reproducibility

The series of NO density distributions presented in figure 5.4 is only one example, showing NO density distributions obtained between 31° aTDC and 142° aTDC during one engine run. To get some information about the reproducibility of the results, NO fluorescence distributions and corresponding elastic scattering distributions were obtained for several different engine runs at two successive days. These results were evaluated in the way described above in order to obtain density distributions of NO. Four representative series of NO density distributions, each consisting of distributions obtained at four different crank angles averaged over 25 engine cycles (62° , 74° , 105° and 142° aTDC) are presented in figure 5.10; all images have the same orientation as those in figures 5.3 and 5.4. It should be noted from the start that the distributions presented in figure 5.10 are recorded under different conditions (fuel, compression ratio, injector orientation) than those of figure 5.4.

By comparing the four series of figure 5.10 only little differences are seen, indicating that average distributions obtained from different engine runs reproduce well. Although it cannot be seen directly from the images, also the intensities of the images at a specific crank angle are of the same order of magnitude. The most conspicuous feature in almost all distributions is a slightly higher intensity at the right hand side of the image. The images do not show significant changes in the distribution of the NO density as a function of crank angle. The differences in the details of the images in each column can be attributed to the irreproducibility of the combustion itself. In principle these images represent a NO density distribution that is similar to the NO density distributions in figure 5.4.

Intensity differences over the field of view in these distributions are similar (maximally 20%) to those observed in the distributions of figure 5.4. Consequently, the variations in temperature or composition that are required to explain the observed NO distributions of figure 5.10 by a uniform NO distribution are similar to those found for the images presented in figure 5.4.

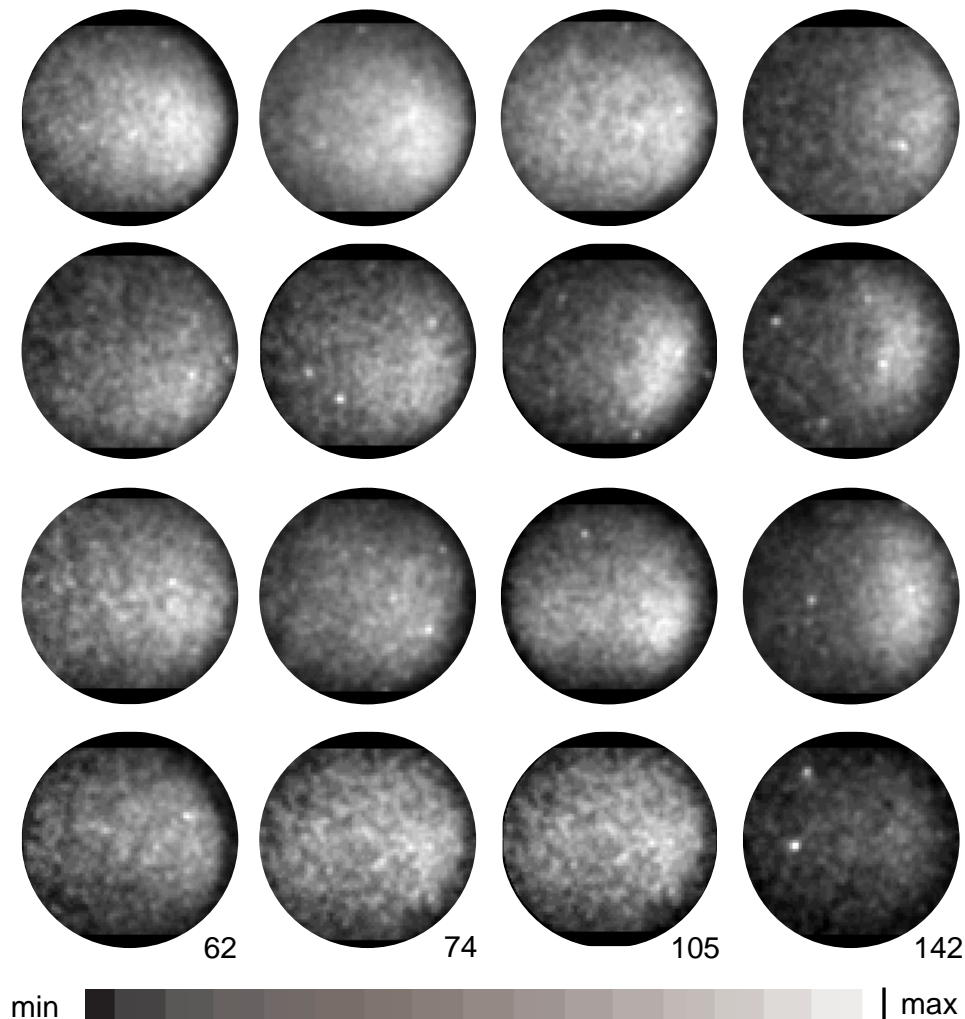


Figure 5.10: Four series of NO fluorescence distributions recorded at 62, 74, 105 and 142° aTDC and corrected for the decrease in laser intensity over the field of view. The images are presented in a linear grey scale ranging from black (minimum intensity) to white (maximum intensity), as indicated in the figure and individually scaled. The laser beam travels from right to left and fuel is injected from the bottom of the images upwards.

5.4.4 Integrated NO density

Although the NO densities within the distributions of figure 5.4 can be compared, the intensities still have to be processed for the crank angle dependent parameters in order to compare the relative NO density at different crank angles. To this end the intensity of the distributions is integrated and this NO fluorescence yield is given in figure 5.11a (Δ), as a function of crank angle. The fluorescence yields obtained from the density distributions for 31° and 142° aTDC are not included. At 31° aTDC the integrated intensity resulting from the low laser intensity that is left in the observation area, is too low for a reliable result. The low fluorescence yield at 142° aTDC, on the other hand, is reliable but at that time a lot of NO is already removed

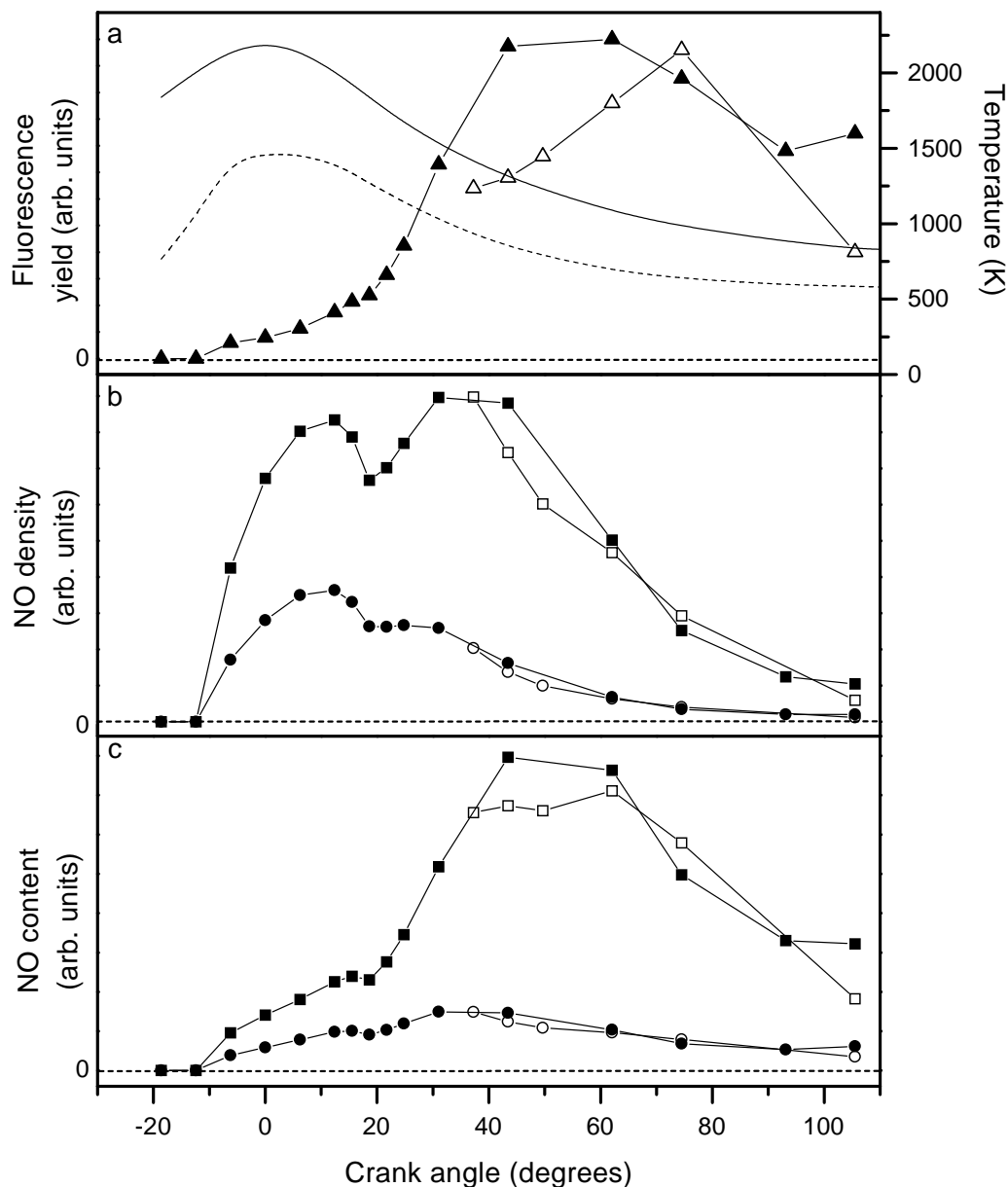


Figure 5.11: a) The integrated NO fluorescence yield obtained from the NO density distributions given in figure 5.4c (Δ). The mean gas temperature (dashed line) and the soot temperature (solid line) are also included. For comparison the fluorescence yield derived from the dispersed fluorescence spectra, given in section 4.3.3, is included in figure 5.11a (\blacktriangle). b) The corresponding NO density obtained by processing the NO fluorescence yield for all crank angle dependent factors as described in section 5.2, using either the mean gas temperature (\square) or the soot temperature (\circ). Also included are the NO density curves derived from the NO fluorescence yield of the dispersed fluorescence, using either the mean gas (\blacksquare) and the soot temperature (\bullet). c) Corresponding NO content obtained by multiplying the curves in b) by the (crank angle dependent) cylinder volume for the curves obtained from the fluorescence distributions (open symbols) as well as for the curves obtained from the spectra (solid symbols).

from the cylinder by the scavenging process. Although this fluorescence yield curve is obtained with a different setup including a different probe volume, it is similar to the fluorescence yield curve that is obtained by integrating the area below the NO fluorescence peaks in a dispersed fluorescence spectrum (see chapter 4). For comparison the fluorescence yield curve derived from the dispersed fluorescence spectra, given in chapter 4, (measured under nearly the same conditions) is included in figure 5.11a (▲).

Just comparing the fluorescence yield curves for the different crank angles is deceptive, as they are obtained from the NO distributions, which are only processed for the laser intensity decrease over the field of view. For a proper comparison the fluorescence yield curve has to be translated into an in-cylinder NO density curve, taking into account all crank angle dependent factors (including the laser intensity decrease in the first, invisible, part of the combustion chamber), as described in section 5.2. Most of the factors used in the translation are the same for both fluorescence yields, but the paths of the laser beam and induced fluorescence are quite different resulting in a different approach for the processing of the laser and fluorescence attenuation, even though the same extinction coefficient is used. In the processing both the mean gas temperature and the soot temperature are used. The effect of using an average temperature (rather than a local temperature) on the derived NO density will be discussed below. For comparison both temperature curves are included in figure 5.11a; the pressure curve is given in figure 5.5a. In figure 5.11b the NO density curve evaluated for both the mean gas temperature (□) and the soot temperature (○), is given. The NO content curves that are derived from the density curves under the assumption that the probe volume is representative for the whole cylinder content (equation 5.6) are given in figure 5.11c. In addition, the NO density and NO content curves for both the mean gas (■) and the soot temperature (●) resulting from the dispersed fluorescence spectra are also given for comparison in figures 5.11b and c, respectively. A comparison of the curves in figures 5.11b and c shows that the curves obtained from the NO fluorescence distributions (open symbols) are very similar to those obtained from the spectra (solid symbols). However, NO densities could not be obtained from NO fluorescence distributions for crank angles $\lesssim 35^\circ$ aTDC as the laser intensity left in the observation area is too weak.

The fact that the curves derived from the dispersed fluorescence spectra and from the 2D-distributions show about the same shape indicates that both methods yield consistent results for the in-cylinder NO density or content. The main advantage of the dispersed fluorescence spectra is that they can be recorded by coupling in the laser beam through the top window so that the laser beam enters the observation area immediately. Therefore, in-cylinder NO densities can be determined for all crank angles, whereas in the case of the images only NO fluorescence can be obtained for crank angles $\gtrsim 35^\circ$ aTDC because of the lack of laser intensity in the observation area at lower crank angles. In addition, for crank angles $\lesssim 30^\circ$ aTDC also some O₂ fluorescence will interfere in the images. On the other hand, the NO fluorescence distributions originate from a well defined plane inside the combustion chamber. Consequently, the fluorescence distributions contain spatial information about the NO molecules inside the combustion chamber, in contrast to the spectra that represent the integrated fluorescence of the probe volume. But to arrive at the NO density distribution both have to be processed for local differences in in-cylinder conditions which are mainly caused by the variation in laser intensity and the temperature gradients.

Before some conclusions are drawn from the shape of the curves in figure 5.11 about the

total NO density/content in the cylinder as a function of crank angle, it should be realised that neither the curve obtained from the mean gas temperature nor the curve from the soot temperature represents the 'real' NO density curve. Probably the most appropriate average temperature will be in between both temperatures and can even change from the soot temperature at TDC to the mean gas temperature at the end of the stroke. This leads to the conclusion that although both NO density curves have a similar shape, they gradually can change from one to the other when going to larger crank angles and so they can have a somewhat different shape. In addition, it is necessary to have an idea of the influence of the use of an average temperature instead of a local temperature in the processing of the integrated fluorescence yield. Because the temperature dependent factors in the proportionality factor between the fluorescence yield and the NO density (equation 5.1) are, in general, not a linear function of temperature, the use of an average temperature will introduce an error in the NO distribution or density.

Two different cases of temperature variations can be distinguished in dealing with this problem: *i*) relatively large temperature differences (typically in the order of 700 K) can be expected in the beginning of the combustion between areas where the actual combustion occurs and the areas of unburned gas, whereas *ii*) smaller fluctuations due to turbulence can be expected everywhere. For the processing of the integrated fluorescence yield the two cases in principle refer to yields obtained during the actual combustion (*i*) and after it (*ii*). However, although the local temperature during the actual combustion is expected to vary considerably, this does not necessarily imply that also the temperature at the positions where the NO is present, and thus fluorescence is obtained from, will vary by the same amount. The NO formation is expected to start at the relatively high temperature sites at the edge of the flame. After that it will mix with the colder air in the cylinder. Therefore, in the early part of the stroke, the presence of NO will be biased to areas at a relatively high temperature and the local temperature that is to be used will show smaller variations than the temperature differences that are expected for the whole cylinder content at that crank angle.

An estimate of the error that is made by using the average temperature in the translation of the NO fluorescence yield into a NO density can be derived from $H(T)$, the factor including all temperature dependences of equation 5.1, given in figure 5.7. This curve shows a more or less linear behaviour for temperatures between 800 and 2250 K. This indicates that in this temperature range the effect of using the average temperature on the total NO density will be small. It is estimated that in the case of variations of about 500 K in this temperature range, the total NO density, derived by using the average temperature, may locally be about 5% to 10% too low, for temperature variations of only 100 K it would be at most 2% too low. However, for temperatures below 800 K a variation of 100 K gives an error that can rise to about 10% for an average temperature of 500 K. (Note, that these errors are in the same order as the experimental error.)

This implies for the NO curves at the start of the combustion, where larger fluctuations are expected, that both the use of the soot temperature and the mean gas temperature as an average temperature are estimated to yield NO densities that are to be about 10% too low compared to the NO densities derived by using a local temperature. At the end of the combustion stroke only small temperature variations are expected. Using the soot temperature as average temperature instead of the local temperature would give almost no variation in the NO density. However, if the mean gas temperature, which is below 800 K for crank angles $\gtrsim 50^\circ$ aTDC, is used, it is estimated that the derived NO density is about 10% too low compared to the NO density that

would be derived by using a local temperature.

In the interpretation of the NO curves presented in figure 5.11 these remarks about the temperature should be taken into account. Assuming that in the beginning of the combustion the temperature will be closer to the soot temperature whereas at the end of the stroke it will be closer to the mean gas temperature, it can be concluded from the curves in figure 5.11b, that the NO density in the probe volume increases throughout the combustion stroke till somewhere between 20 and 50° aTDC. The end of the density increase depends on the temperature that is used in the derivation. The subsequent decrease in NO density in the probe volume is largely due to the expanding volume of the cylinder. This is illustrated by the NO content curves presented in figure 5.11c, which show an increase in the amount of NO up to about 50° aTDC after which it seems to decrease again. This however, might be somewhat misleading as it depends on the temperature used. A more extensive discussion about the shape of the curves in relation to the combustion process can be found in chapter 4, section 4.3.3.

5.5 Conclusion

Two-dimensional nitric oxide (NO) fluorescence distributions could be obtained for crank angles $\gtrsim 35^\circ$ aTDC, for lower crank angles the laser intensity left in the observation area is too low. The measured NO fluorescence distributions are processed for the change in laser intensity over the field of view, resulting in a first order approximation of the NO density distribution. By assuming all other factors involved in the relation between NO fluorescence and NO density to be constant over the field of view, these distributions can be interpreted as NO density distributions.

The results are discussed with an emphasis on the influence of an inhomogeneous distribution of temperature and/or chemical composition (quenching) over the field of view. It is argued that the intensity differences seen in the NO density distributions cannot be explained solely by a temperature or composition variation that might occur over the field of view, although they will have some influence on the observed NO density distribution. Therefore, the intensity differences that are found are ascribed to variations in the NO density, although they may be under- or overestimated due to temperature and/or composition variations.

The integrated intensity of the NO fluorescence distributions is used as a relative measure for the amount of NO present inside the cylinder. To compare the amounts of NO throughout the stroke they are processed for the changing in-cylinder conditions (pressure, temperature and laser radiation intensity) using two different temperature curves. The shape of the curves is discussed with an emphasis on the effect of the uncertainties in temperature. The resulting semi-quantitative NO density/content curves are compared to similar curves derived from NO dispersed fluorescence spectra (chapter 4). They show good agreement for the part of the stroke for which NO distributions could be obtained. This indicates that both methods yield consistent results on the amount of in-cylinder NO.

Appendix

Non-uniformities in the laser-induced NO fluorescence yield, that remain after the laser attenuation over the field of view has been corrected for, need not be due to a non-uniform NO distribution. Instead, they could arise from, for example, a non-uniform temperature distribution (discussed in the main text) or non-uniform collisional relaxation processes. This latter aspect will be discussed here.

Collisional energy redistribution enters the fluorescence yield in two ways (equation 5.1): via the Stern-Vollmer factor, \wp , and via the overlap integral, $g(\nu_a, \nu_L)$. For the case at hand, the non-radiative decay rate Q in the Stern-Vollmer factor is expected to be dominated by EET ($D \rightarrow A$), but the NO absorption linewidth $\Delta\nu_a$ will be determined mainly by RET in ground and excited states and by elastic collisions. (Note that, since the fluorescence is not detected with rotational resolution, RET and elastic collisions do not affect the Stern-Vollmer factor.) The efficiency of all these collision processes depends on the collision partners. Therefore, if the collision partners (other chemical species) are non-uniformly distributed, even a uniform NO density would give rise to an inhomogeneous fluorescence yield.

In order to isolate the effect of such an inhomogeneous collision partner distribution, it will here be assumed that temperature and pressure (and therefore also the total density, n_T) are uniform over the field of view. Writing²

$$Q = \sum_j \bar{v}_j n_j \sigma_j, \quad (5.10)$$

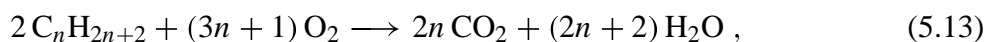
with \bar{v} the average relative velocity and the sum extending over all possible collision partners of a NO molecule, then $\sum_j n_j = n_T = \text{constant}$, and spatial variations in non-radiative decay rate must be due to varying chemical composition, involving species with different \bar{v}_j and/or σ_j . Since only an order-of-magnitude estimate is of interest here, variations in \bar{v}_j will be neglected (scale with $\sqrt{\text{reduced mass}}$) and

$$Q = \bar{v} n_T \sum_j f_j \sigma_j \quad \text{with } n_j = f_j n_T \quad (5.11)$$

(f_j is a volume fraction, with $\sum_j f_j = 1$). For the non-radiative decay only the most abundant chemical species will be of importance, that is, N_2 , O_2 , H_2O , CO_2 and ‘fuel’. Then

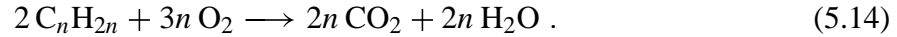
$$Q = \bar{v} n_T [f_{N_2} \sigma_{N_2} + f_{O_2} \sigma_{O_2} + f_{H_2O} \sigma_{H_2O} + f_{CO_2} \sigma_{CO_2} + f_{\text{fuel}} \sigma_{\text{fuel}}] . \quad (5.12)$$

Subsequently, it will be assumed that non-uniformities in chemical composition arise from the non-uniform nature of the combustion. If that is the case, then the local volume fractions of several chemical species will be correlated. For instance, if combustion locally reduces the amount of O_2 , the local concentrations of H_2O and CO_2 will be larger. Assuming complete combustion of an alkane fuel would imply



²The following discussion will be in terms of the non-radiative decay rate Q , but a similar reasoning holds for the effective collision rate Γ that determines the NO absorption linewidth.

or, for n not too small,



From this equation it follows that (taking $2C_nH_{2n} \sim 2nCH_2$)

$$f_{H_2O} = f_{CO_2} = f_{fuel}^{(i)} - f_{fuel} \quad \text{and} \quad f_{N_2} = f_{N_2}^{(i)}, \quad (5.15)$$

where the superscript (i) indicates an initial value (before combustion). f_{O_2} can be determined from the normalisation condition. Furthermore, it will be assumed that

$$\sigma_{H_2O} = \sigma_{CO_2} = \sigma_{fuel} = a\sigma_{O_2} \quad \text{and} \quad \sigma_{N_2} = \sigma_{O_2}. \quad (5.16)$$

This mainly serves to reduce the number of free parameters in the model, and is based on the idea that the number of internal degrees of freedom of the collision partner will provide a rough indication of its efficiency in collisional energy redistribution. For quenching of the NO A-state fluorescence, for example, $a \approx 2 - 3$ [71]³. With these assumptions it follows that

$$Q = \bar{v}n_T\sigma_{O_2} \left[f_{N_2}^{(i)} + f_{O_2} + 2a f_{fuel}^{(i)} - a f_{fuel} \right]. \quad (5.17)$$

Using the initial values $f_{CO_2}^{(i)} = f_{H_2O}^{(i)} = 0$, the normalisation condition $\sum_j f_j = \sum_j f_j^{(i)} = 1$ can be rewritten as $f_{fuel} = f_{O_2} - f_{O_2}^{(i)} + f_{fuel}^{(i)}$, (using relation 5.15) so that

$$Q = \bar{v}n_T\sigma_{O_2} \left[f_{N_2}^{(i)} + (1 - a)f_{O_2} + a(f_{fuel}^{(i)} + f_{O_2}^{(i)}) \right]. \quad (5.18)$$

This equation allows to relate differences in quenching rate to differences in oxygen volume fraction f_{O_2} : If $Q^{[2]} = \gamma Q^{[1]}$ then

$$f_{O_2}^{[2]} = \left(\frac{a}{1-a} + f_{N_2}^{(i)} \right) (\gamma - 1) + \gamma f_{O_2}^{[1]}. \quad (5.19)$$

Or, in other words, if a certain variation in NO fluorescence yield would have to be ascribed to a variation in non-radiative decay constant (rather than to a variation in NO density), this formula allows to relate the required variation in quenching cross section to a variation in oxygen volume fraction (under the assumptions of the model, of course). As an example, figure 5.12 shows $\Delta f_{O_2} = f_{O_2}^{[2]} - f_{O_2}^{[1]}$ as a function of the relative collision cross section $a = \sigma_{H_2O}/\sigma_{O_2}$ for several values of $\gamma = Q^{[2]}/Q^{[1]}$, for the initial conditions

$$f_{N_2}^{(i)} = 0.74, \quad f_{O_2}^{(i)} = 0.175 \quad \text{and} \quad f_{fuel}^{(i)} = 0.085. \quad (5.20)$$

$Q^{[1]}$ is understood to represent an average value over the field of view, and $f_{O_2}^{[1]} = 0.10$ is taken (typical oxygen content in the exhaust gases [2]). The vertical range in the figure has been limited to the possible range of $f_{O_2}^{[2]} \in (0; f_{O_2}^{(i)})$, but in practice the variation will probably stay

³Although for this example also $\sigma_{N_2} \ll \sigma_{O_2}$, this is not expected to be the case for non-radiative collisional decay of the NO D-state, since here $D \rightarrow A$ EET provides an additional decay channel for which N_2 has been shown to be very effective [82].

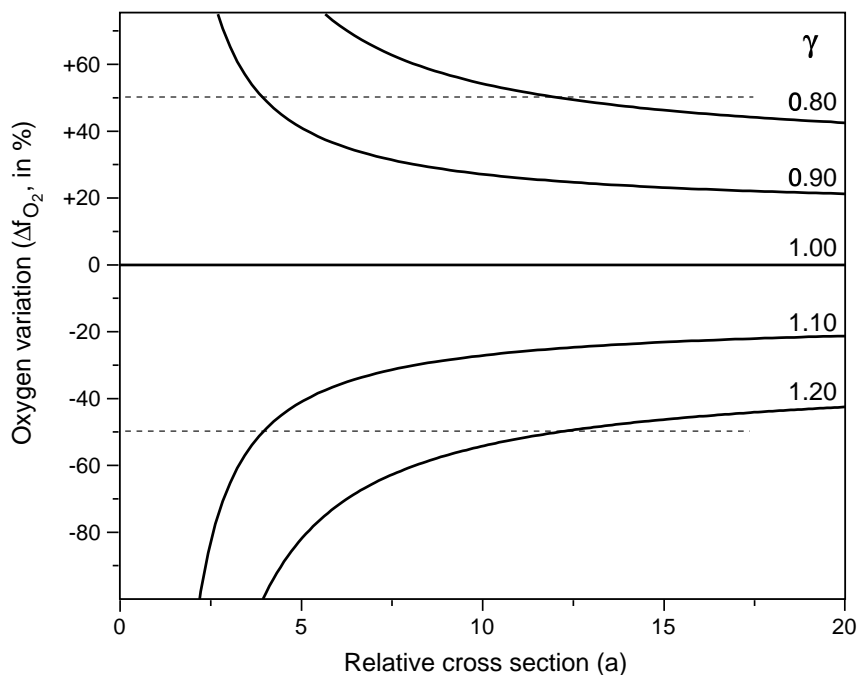


Figure 5.12: Variation in oxygen concentration required to produce a given variation in quenching rate constant (determined by the ratio $\gamma = Q/\langle Q \rangle$) as a function of relative collision cross section ($a = \sigma_{\text{H}_2\text{O}}/\sigma_{\text{O}_2}$).

within a smaller interval. For instance, if a 50% variation around $\langle f_{\text{O}_2} \rangle = f_{\text{O}_2}^{[1]}$ is considered acceptable, that is $0.05 \leq f_{\text{O}_2}^{[2]} \leq 0.15$, then to explain a variation in Q of 10% would require $a > 4$, and to explain a variation of 20% in Q would require $a \gtrsim 12$.

The question remains, of course, whether or not these values of a are deemed acceptable. In view of the available data on A-state quenching, and since σ_{N_2} for the D-state is already quite large, $a \lesssim 2 - 3$ seems a reasonable range.

Chapter 6

Summary and outlook

6.1 Summary

The main objective of the work described in this thesis is the development of a method to determine the nitric oxide (NO) density with both spatial and temporal resolution during the combustion inside the cylinder of a diesel engine by means of laser diagnostics. As a tool to observe the NO molecules the Laser Induced Fluorescence (LIF) technique is used. This non-intrusive technique allows to detect minority species in combustion with spatial and temporal resolution. The intensity of the fluorescence resulting from the NO molecules, that are excited by the laser radiation is a measure for the amount of NO present in the cylinder of the running engine.

The engine used is a one-cylinder, two-stroke, direct injection diesel engine which is described in section 2.2.1. The engine is made optically accessible by mounting two quartz windows in the cylinder wall through which the laser beam can traverse the combustion chamber. A third window is placed in the centre of the cylinder head and is used to detect the fluorescence. The engine was operated in steady-state, on standard commercial diesel fuel and non-oxygen enriched intake air, in contrast to most other experiments reported in literature. In previously described experiments the research engine was mostly operated in skip-fired mode on a substitute fuel and often extra oxygen was supplied to the intake air [17, 34–39].

The experiments reported in this thesis have shown that it is possible to observe NO inside the combustion chamber of the two-stroke diesel engine applying the LIF technique. Radiation of 193 nm, delivered by an excimer laser running on ArF, was used to excite NO molecules in the $D^2\Sigma^+(v'=0) \leftarrow X^2\Pi(v''=1)$ band. At higher temperatures and pressures it proved unavoidable to also excite oxygen (O_2) when exciting NO with 193 nm radiation and besides NO fluorescence interfering fluorescence from hot O_2 is observed. However, NO fluorescence can be spectrally separated from O_2 fluorescence by a proper choice of the excitation and detection wavelengths. To select the best wavelengths for excitation and detection of NO within the combustion chamber excitation/emission spectra recorded from the running engine are used (section 2.5.1).

To use the fluorescence yield as a measure for the NO density a linear relationship between the fluorescence yield and the laser intensity should exist and therefore the effect of saturation is investigated. Saturation of a transition generally occurs when the optical pumping is strong enough to induce 'considerable' changes in the equilibrium populations of the molecular levels

that are coupled by the pump. In molecules, Rotational Energy Transfer (RET) is the fastest process that maintains thermal equilibrium. Thus, as long as RET rates are faster than the pump rate, saturation effects will not be evident, even for laser fluences that would lead to considerable saturation if RET were absent. For the engine experiment, the fluorescence yield is shown to depend linearly on laser intensity. The effect of RET in ground and excited state has been estimated to increase the fluorescence yield by as much as a factor of 20. Furthermore, it has been shown that the weak field limit, which is usually assumed in the interpretation of fluorescence data, still gives reasonably accurate results far beyond the limits within which this approximation would be valid. This is due to the fact that, for the conditions of this experiment, RET rates compared to the pump rate are fast enough to keep the populations of the laser-coupled levels in thermal equilibrium.

Dispersed fluorescence spectra, obtained by excitation of NO at a wavelength that minimises O₂ interference show that it is possible to observe fluorescence from NO inside the combustion chamber throughout the whole combustion stroke starting around TDC (chapter 4). These measurements are done by coupling in the laser radiation through the top window, so that it enters the observation area immediately. All spectra, from the moment the combustion starts onwards, show spectral structure. This indicates that sufficient laser intensity is available to induce detectable amounts of fluorescence throughout the whole combustion stroke, even at TDC where pressure and temperature are high. For crank angles $\lesssim 20^\circ$ aTDC the spectra are dominated by fluorescence from vibrationally hot O₂ ($v''=2,3$), whereas this is almost absent in the spectra at crank angles $\gtrsim 40^\circ$ aTDC. Oxygen fluorescence peaks and NO fluorescence bands can be distinguished because they are partly at different spectral positions and they show different spectral features. The NO fluorescence bands are spectrally broad as a result of fluorescence out of many rotational levels, most of which are populated due to rapid RET in the excited state. The O₂ fluorescence peaks, on the contrary, are characterised by two closely spaced narrow lines (doublet structure) due to fast predissociation of the upper state, that results in dissociation of the excited O₂ molecules before RET has occurred. The intensity of the NO fluorescence bands in these spectra is proportional to the NO density in the measurement volume and can be used to determine the relative amount of NO present in the cylinder as a function of crank angle (chapter 4).

Spatial fluorescence distributions of NO are obtained for crank angles $\gtrsim 35^\circ$ aTDC (chapter 5). They are recorded through a somewhat involved narrow-band transmission filter (FWHM 5 nm) that only transmits the fluorescence within a narrow wavelength region centred around the NO fluorescence band at 208 nm which is free of O₂ fluorescence (see figure 5.2). The fluorescence intensity collected from a certain position is a measure for the local NO density inside the cylinder.

To compare the NO fluorescence intensities throughout the combustion stroke and at different positions in the probe volume the observed fluorescence signals have to be processed for the changing in-cylinder conditions in order to transform them into NO densities. The general relationship between fluorescence and density is well known. The NO fluorescence signal is proportional to *i*) the NO density in the volume irradiated by the laser beam and seen by the detector, *ii*) the fraction of molecules that is really excited and *iii*) the fraction of molecules that is detected. On its turn the fraction of molecules that is excited depends on *i*) the number of molecules in the right quantum state in the measurement volume, determined by the Boltzmann factor ($f_{v,J}(T)$), *ii*) the intensity of the laser radiation at the excitation position ($I_L(x, y)$) and

iii) the overlap of the laser line profile with the NO absorption spectrum ($g(\nu_a(T, P), \nu_L)$). Similarly, the fraction of molecules that is detected depends on *i*) the fraction of excited molecules that fluoresces at the right wavelength, determined by the Stern-Vollmer factor ($\phi(T, P)$) as well as *ii*) the attenuation of the induced fluorescence on its way to the detector ($A_F(x, y)$).

In general, therefore, although the NO fluorescence is proportional to the NO density the proportionality constant includes several spectroscopic and experimental factors that vary, both temporally and spatially, during the combustion. Mostly, these processing factors can be evaluated, but this results in expressions that depend on the local physical and chemical conditions in the combustion chamber. In general, these quantities, like pressure, temperature, laser intensity attenuation coefficient and gas mixture, are not known and difficult to assess. Furthermore, the processing factors involve molecular constants which are not always available from literature for the electronic state involved.

To obtain the required parameters additional experiments have been performed and some assumptions had to be made. The ways they are assessed and the approximations made thereby, are summarised shortly below. Of all quantities the in-cylinder pressure is most probably the easiest parameter to obtain. It is constant over the volume and its dependence as a function of crank angle is determined relatively easily and accurately by using a pressure transducer (section 2.2.2).

Measuring the in-cylinder temperature is a larger problem as it may vary with position. In fact, at the moment the local temperature cannot be determined. Two different measures of a temperature as a function of crank angle are obtained for the two-stroke engine, however, both of them not spatially resolved. The first one, called the mean gas temperature, is calculated from the heat release, which is obtained from the in-cylinder volume and measured in-cylinder pressure (section 2.2.2). This temperature represents an average temperature of the gas in the cylinder and will therefore be lower than the local temperature at those sites where the actual combustion occurs. The second temperature is derived from the spontaneous flame emission by fitting a Planck's curve to the dispersed emission spectrum (section 2.4.1). This represents the temperature of glowing soot particles, which is expected to more accurately represent the local temperature in the burning fuel/air mixture [56]. At any time, the measured NO fluorescence signal will contain contributions of newly formed and already existing NO which are not necessarily at the same place and temperature. Thus, it is not clear which temperature, if any, should be used. In addition, it should be noted that both temperatures are spatially averaged temperatures. In general a local temperature should be used because the temperature will generally not be uniform over the measurement volume.

Determination of the attenuation of the laser radiation due to scattering off and absorption by soot particles and oil and fuel droplets on its way through the combustion chamber is the next major problem. The attenuation of the laser radiation can be measured just by detecting the laser intensity that is left behind the exit window. In this case, however, the transmission losses through the windows, which are not known, are included. In addition, it only gives an average transmission and no information about the local laser intensity in the measurement volume. It has been shown that the local laser intensity attenuation can be assessed exactly using two distributions of elastically scattered laser radiation, recorded (virtually) simultaneously from two laser beams which traverse the engine along the same path, but in opposite direction (chapter 3; double image method). It is found that the attenuation coefficient is fairly homogeneously distributed over the field of view for the studied crank angles ($\gtrsim 30^\circ$ aTDC). This distribution

is used to reconstruct an image of the laser intensity decrease over the observation area. Furthermore, this experiment provides information about the attenuation of the laser radiation as a result of the contents of the combustion chamber only, independent of window losses. Although this method is exact, it requires a complicated experimental setup, and for this reason a more approximate method is also developed. Using this method the local laser intensity attenuation can be assessed from only one distribution of the elastically scattered laser radiation if the total transmission through the combustion chamber is known (chapter 3; single image method).

Besides attenuation of the laser radiation, attenuation of the induced fluorescence occurs as well. To estimate this attenuation it is assumed that the induced fluorescence behaves similar to the laser radiation as it has almost the same wavelength. Therefore, the same attenuation coefficient as found for the laser radiation is taken. It should be realized, however, that the distribution of scattering and absorbing particles in the beginning of the combustion is not uniform, so that differences in the attenuation of the fluorescence might occur.

The composition of the gas mixture in the cylinder is also of some importance for the interpretation of the NO fluorescence yield, as different molecules contribute differently to the fluorescence quenching. Besides knowledge of the molecules present in the mixture and their distribution, knowledge of the molecular constants that are involved in the calculation of the collision rates is necessary. However, in contrast to the NO A-state, for which data on quenching are available in literature [71, 86], only little is known for the NO D-state. To obtain some information about the quenching process and energy transfer processes of the NO D-state under pressure and temperature conditions present in the engine, measurements in a high pressure, high temperature cell are performed [82]. These measurements have shown that for the NO D-state nitrogen (N_2) is a very efficient collision partner, causing Electronic Energy Transfer (EET) to the NO A-state. As N_2 is always the majority species in the combustion chamber, it is assumed that N_2 collision induced EET dominates the non-radiative decay rate. This implies that the exact composition of the mixture in the cylinder is relatively unimportant. Therefore, for the moment, it is assumed that the non-radiative decay is caused by N_2 , homogeneously distributed over the cylinder. In addition, the molecules in the gas mixture are important for the determination of pressure broadening, of the NO absorption line. However, data about line broadening for the $D \leftarrow X$ transition of NO are also not available in literature. For the present purpose data of the $A \leftarrow X$ band are taken in combination with own measurements on the $D \leftarrow X$ band in the engine.

Under the conditions discussed above the processing factors can be determined as a function of crank angle and position. As it is not clear which temperature should be used, calculations have been performed both for the soot temperature and the mean gas temperature. Taking into account all processing factors the measured fluorescence yield, both from spectra and distributions, can be converted into a relative NO density as a function of crank angle and position (for the distributions). Thus, the resulting NO density distributions or curves can be compared throughout the stroke and over the observation area. In principle, they can be calibrated to give absolute values.

Nitric oxide density curves as a function of crank angle are derived from the integrated fluorescence yield of the NO dispersed fluorescence spectra. The density curves can be obtained for different engine conditions (load, fuel, compression ratio) and it is concluded that, as far as investigated, the engine operating conditions are of minor importance, as all NO density curves show the same features (chapter 4). Nitric oxide is seen first around TDC and its density in-

creases throughout the combustion stroke till somewhere between 20 and 50° aTDC, depending on the temperature used in the processing and the engine conditions. Hereafter, a decrease in NO density in the probe volume is seen, mainly due to the expanding cylinder volume. This result leads to the conclusion that the NO formation continues till late in the stroke and that the diffusion burning phase is important for the NO formation. Only little NO formation is seen during the fuel-rich initial premixed burn. This result is in agreement with experimental results from laser imaging techniques from other research groups [17, 39] as well as with theoretical calculations from the group of Peters [79].

The NO fluorescence distributions are transformed into NO density distributions under the assumptions of a uniform temperature distribution and a homogeneous fluorescence quenching over the field of view. The derived NO density distributions, obtained for crank angles $\gtrsim 35^\circ$ aTDC only, show a rather homogeneous distribution that varies gradually over the observation area; large fluctuations in the NO density are not seen (chapter 5). This can be expected as the distributions are obtained at crank angles late in the combustion process and the formed NO has already mixed with the cylinder contents. The remaining non-uniformity might to some extent also be explained by temperature or mixture variations. The integrated NO densities agree with the independently measured density curves from the dispersed fluorescence spectra.

6.2 Outlook

As stated above, the main goal of this thesis was to develop a method to measure density distributions of NO in the cylinder of an optically accessible diesel engine running on commercial diesel fuel by means of the LIF technique. In the determination of NO densities using the LIF technique two parts can be distinguished *i)* NO fluorescence has to be detected with temporal and spatial resolution and *ii)* the fluorescence yield has to be translated into a NO density taking into account the changing conditions in the combustion chamber. A summary of the way fluorescence of NO in the combustion chamber of the engine is detected, the assumptions made in the interpretation of the fluorescence yield and the most important results is given in section 6.1. In this outlook it will be discussed to what extent the results of the developed method meet the objective and what can be done to improve the method.

The experiments and results described in this thesis have shown that many of the problems arising by *i)* the detection of the NO fluorescence signal and *ii)* the interpretation of the NO fluorescence yield as a NO density are solved. Curves describing the relative NO density as a function of crank angle were obtained for the whole combustion stroke. In addition, relative distributions of the local NO density over the measuring volume were obtained, be it only for crank angles $\gtrsim 35^\circ$ aTDC and under the assumptions of a uniform temperature distribution and a homogeneous fluorescence quenching. In principle, both can be calibrated to give absolute values by measuring the amount of NO_x at the exhaust. In this case it is important to take into account that in the engine most NO_x is present as NO but at lower temperatures in the exhaust it can be converted to NO_2 . Therefore, both components should be measured at the exhaust. But it should be noted that a lot of assumptions have had to be made to assess the density curves and distributions, and some required quantities are still not, or only badly, known. The fact that density distributions are obtained only late in the combustion stroke and that uncertainties still exist in the interpretation of the fluorescence yield leads to the conclusion that the objective of

this work is not yet fully achieved. To use the LIF technique as a tool to obtain quantitative information about NO in the future, further refined developments are necessary. NO fluorescence distributions have to be obtained throughout the whole combustion stroke and to quantify the NO fluorescence more accurately, it will be necessary to develop methods to measure the badly known quantities locally. In addition, experiments are needed to obtain more information about the molecular constants of the NO molecule.

In this work local NO density distributions were not obtained throughout the whole combustion stroke but only for crank angles $\gtrsim 35^\circ$ aTDC because at smaller crank angles the laser intensity left in the observation volume was too low (the laser beam has to travel about 25 mm before reaching the observation area). If the laser intensity is sufficient, in principle, fluorescence distributions can be obtained at lower crank angles as well, in spite of the higher pressures¹. The problem of the travelling distance of the laser beam can be solved to some extent by mounting an observation window closer to the laser entrance window or using a larger window, so that the laser beam enters the observation area immediately. In addition, the fluorescence attenuation can be minimised if the laser beam passes the measuring area just below the observation window. However, although this way fluorescence signal can certainly be obtained from the edge of the combustion chamber it is no guarantee that NO fluorescence can be obtained from the whole plane in the combustion chamber.

A more fundamental problem in recording NO distributions at crank angles around TDC is the presence of O₂. At the high pressures and temperatures present around TDC it is unavoidable to also detect O₂ when spatial fluorescence distributions of NO are recorded using an excitation wavelength of 193 nm because the spectral positions of the fluorescence of both species lie too close together to separate by available 2D-filters. This, together with the fact that the attenuation of the 193 nm radiation is large, will probably preclude spatial fluorescence distributions of NO densities to be obtained throughout the whole combustion stroke using 193 nm laser radiation.

In an alternative detection scheme for LIF measurements that could be used to measure NO distributions 226 nm is used to excite the NO molecules in the $A^2\Sigma^+(v'=0) \leftarrow X^2\Pi(v''=0)$ band and fluorescence from the $A^2\Sigma^+(v'=0) \rightarrow X^2\Pi(v''=1-4)$ bands from 237 to 276 nm is detected. Experiments described in literature have already shown that this wavelength can also be used for detection of NO inside the combustion chamber of diesel engines [17, 37, 39]². It should be mentioned that, like in the case of using 193 nm radiation, O₂ is easily excited as well. However, if the laser used has a narrow bandwidth and excitation and detection wavelengths are selected carefully interference of O₂ fluorescence can be avoided even at high pressures and temperatures. An advantage of this detection scheme, compared to 193 nm excitation, is that molecules are excited from the vibrational ground state, whose population is more constant at the temperatures present during the combustion. This results in the fluorescence yield not depending so strongly on temperature as in the case of 193 nm excitation. Therefore, the temperature differences over the field of view, are less important for the evaluation of the local fluorescence yield. (Note that the local temperature is still important as it is not only involved in the Boltzmann factor, describing the population of the lower level, but also in the Stern-Vollmer factor and the

¹Note, that the high pressures around TDC, in itself, are no problem for measuring fluorescence distributions as can be seen from the dispersed fluorescence spectra where indeed fluorescence signal is obtained.

²The engines used in these experiments were all running on a low sooting fuel in order to increase the optical transparency of the combustion chamber.

overlap integral.) A second advantage is that the attenuation of the 226 nm laser radiation on its way through the combustion chamber is weaker than the attenuation of the 193 nm radiation (although this still has to be proven for real diesel fuel). The excited state is the $A(v'=0)$ -state that has the additional advantage that more information about molecular constants, like collision cross sections, is available in literature. A disadvantage, however, is that the composition of the cylinder contents is more important in calculating the non-radiative decay rate. As, in contrast to the D-state, the depopulation of the excited A-state is not dominated by collisions with the majority species, N_2 , the distribution and concentration of all species should be taken into account. The first experiments performed using 226 nm laser radiation in a realistic DAF six-cylinder DI diesel engine give promising results about the use of 226 nm radiation to obtain NO fluorescence distributions around TDC [82].

Besides 193 nm and 226 nm, also 248 nm laser radiation can be used to excite NO molecules in the $A^2\Sigma^+(v'=0) \leftarrow X^2\Pi(v''=2)$ band. With 248 nm the interference of O_2 can be avoided by a carefully chosen excitation and detection scheme. The advantage of using 248 nm radiation is that the attenuation of the 248 nm laser radiation is less than the attenuation of 193 and 226 nm laser radiation. However, an important disadvantage is that NO molecules are excited from the $X(v''=2)$ -state the population of which has an even stronger temperature dependence than that of the $X(v''=1)$ -state that is excited using 193 nm laser radiation. Therefore, the determination of a local temperature becomes increasingly important. Moreover, as the $X(v''=2)$ -state is populated only at higher temperatures this wavelength cannot be used for measurements late in the stroke. For this alternative detection scheme the excited state is also the $A(v'=0)$ -state and therefore the composition of the cylinder contents will be important like in the case of using 226 nm.

Once NO fluorescence distributions throughout the whole combustion process can be obtained successfully, still the question remains if the NO fluorescence yield can be interpreted as a NO density. As already mentioned in this work a number of assumptions were made in the processing of the NO fluorescence yield. For fluorescence distributions recorded in the beginning of the combustion process the assumptions of a uniform temperature distribution and a homogeneous fluorescence quenching will certainly not be valid. Therefore, it is required to have information about the local conditions in the combustion chamber.

At the moment the local in-cylinder temperature cannot be measured. Thus far, only two different spatially averaged temperatures as a function of crank angle are obtained for the two-stroke engine. Since both temperatures are not necessarily the appropriate ones for the interpretation of the NO fluorescence signal and do not give local information, as discussed above (section 6.1), it is of importance to develop a method to measure the local temperature. One possible way to determine this temperature is to use Laser Induced Predissociative Fluorescence (LIPF) of O_2 . As the excited states of O_2 have a fast predissociation rate fluorescence occurs only during the predissociation lifetime, in which no fluorescence is lost by collisions. Therefore, the Stern-Vollmer factor reduces to A/P , independent of the quenching rate. The fluorescence signal becomes proportional to the population of the lower state with a proportionality constant that does not depend on the local collision conditions. By measuring the relative population of two states, which are excited simultaneously, the temperature can be calculated via the Boltzmann expression for a population distribution in thermal equilibrium [89–91]. It should, however, be noted that laser intensity and RET in the lower state can have an effect on the ratio of the LIF signals from the two transitions and therefore also on the derived temperature [60]. Experiments are in progress to measure the local temperature using coinciding transitions from the $X(v''=2)$

and the $X(v''=3)$ in the Schumann-Runge band (a possibility could be the $R_1(17)$ transition of the $B(v'=10) \leftarrow X(v''=2)$ band and the $R_1(19)$ transition of the $B(v'=16) \leftarrow X(v''=3)$ band at 193.258 nm (51744.31 cm^{-1})).

The unknown composition of the gas mixture is another problem that has to be solved in order to correctly transform the NO fluorescence yield into a NO density. Till now the exact composition is assumed to be unimportant as the processes that influence the fluorescence yield and pressure broadening are assumed to be dominated by N_2 , as discussed above (section 6.1). However, for NO fluorescence distributions recorded in the beginning of the combustion by means of 226 nm laser radiation the direct environment of the NO molecule is an important parameter in the processing of the fluorescence yield. But, at the moment, it is impossible to measure the local composition of the gas mixture at the same position as the NO fluorescence is detected from. By applying the LIF technique to obtain quantitative information about the other species present the same problem arises again, as for the interpretation of their fluorescence yield the same information is required. To solve the problem of the fluorescence quenching Dec and co-workers [17] have assumed that the gas composition at the position and time NO is formed consists of the products of the combustion process and mixes with the rest of the cylinder contents during the latter part of the combustion stroke. This, however, is not a satisfactory solution as it requires knowledge about the combustion products of real diesel fuel as a function of crank angle and mixing rates, parameters that, again, are not well known. Other possible solutions in which the problem of fluorescence loss by quenching is circumvented are to choose a fast predissociating state (if that exists) or to choose a state in which the fluorescence loss is dominated by the majority species.

For the conversion of the NO fluorescence yield to a NO density more information about molecular constants of the NO molecule, like line broadening, quenching and EET cross sections, in a high pressure, high temperature environment as present in the combustion chamber, is required. Therefore, systematic experiments on NO in several known gas mixtures in a high pressure, high temperature environment will have to be performed. Information about line broadening can be obtained by recording excitation spectra of NO in different gas mixtures at several pressure and temperature combinations. By measuring the dispersed fluorescence as a result of laser excitation under controlled conditions quenching and EET rates can be derived. Furthermore, the importance of RET has to be assessed as this process refills the ground state that is depleted by the laser excitation. Therefore, it increases the fluorescence yield in such a way that it appears not saturated although the laser intensity is so high that all population out of the ground state can be removed. At the moment it is assumed that RET processes are unimportant as long as RET rates are faster than the pump rate and the fluorescence yield is linear with the laser intensity. Information about RET rates can be obtained by using double-resonance techniques. One laser frequency is used to populate a specific rotational level of a state. A second laser beam is used to probe the distribution of the molecules after delay times during which collisions may have transferred the population into other rotational levels of the prepared state.

Although it is not so important for the LIF technique in itself, it is worthwhile to mention that in almost all experiments reported in this thesis fluorescence signals are averaged over 25-100 engine cycles to increase the signal to noise ratio. Since the averaged information is found to reproduce, fluorescence distributions of different measurements recorded under the same engine conditions can be compared. In addition, relations between different quantities obtained

in separate measurements can still be demonstrated. A disadvantage of averaging is that information about (the differences between) individual combustion cycles cannot be obtained. To get information about individual combustion cycles cycle-resolved results also have to be obtained, *e.g.* by using a single laser pulse. However, in that case it is more difficult to compare NO densities obtained at different crank angles. For a good comparison a lot of single cycle measurements have to be obtained and analysed to get a sort of average value or distribution that can be compared. To relate different quantities and aspects of the combustion process that are obtained from only one engine cycle it is necessary to measure them simultaneously. This requires a more complicated setup as mostly two camera systems are necessary and sometimes two laser systems as well.

Information about the diesel combustion process and the formation mechanism of NO can also be obtained by measuring other molecular species present or formed in the combustion process. Interesting species are molecules that can be precursors of NO, like CH or CN involved in the prompt NO mechanism (section 1.4.2) or N₂O that can form NO via the ‘N₂O pathway’ (section 1.4.3). Other aspects of the combustion process can be studied by measuring molecular species that are characteristic for that specific aspect of the combustion. The flame front can be visualised by molecules like OH and CH which are confined to the flame front region [15, 92]. Species like, CN, OH and CH in combustion processes can be detected using the LIF technique [92, 93]. Soot is another important aspect of the combustion process that can be visualised using the LII technique [11, 12, 14]. Future measurements will also focus on the relation of NO to other aspects of the combustion process by measuring *e.g.* soot distributions and NO distributions, spontaneous flame emission and NO distributions or soot distributions and spontaneous flame emission simultaneously.

The question that still remains at the end of this outlook is whether the LIF technique in the future can be used as a tool to obtain quantitative NO density distributions with both spatial and temporal resolution in a diesel engine running on commercial diesel fuel throughout the whole combustion stroke. This question cannot yet be answered satisfactorily, but the problems that will have to be solved are outlined above. Much will, of course, depend on the amount of research that is put into it. But, in the end there is always the possibility that the development of alternatives to the diesel engine (or to the diesel fuel) will overtake the diesel engine itself. However this may work out, combustion optimisation will therefore remain an issue of considerable economical importance, and LIF-based diagnostics are definitively an extremely versatile tool in achieving this.

References

- [1] L. Bryant, "Rudolf Diesel and his rational engine", *Scientific American* **221**, 108-117 (1969).
- [2] J.B. Heywood, "Internal combustion engine fundamentals", McGraw-Hill, Singapore (1988).
- [3] A. Heintz and G.A. Reinhardt, "Chemie und Umwelt", Vieweg Verlag, Wiesbaden (1993).
- [4] A. Fisher-Riedman, "Environmental aspects of fine particles and soot", 2nd Symposium Towards clean diesel engines, Villigen (1998).
- [5] W.G. Agnew, "Room at the piston top: contributions of combustion science to engine design", Proc. 20th Symposium (Int'l) on Combustion, pp. 1-17 (1984).
- [6] G.M. Faeth, "Current status of droplet and liquid combustion", *Prog. Energy Combust. Sci.* **3**, 191-224 (1977).
- [7] J.E. Dec, A.O. zur Loye and D.L. Siebers, "Soot distribution in a DI diesel engine using 2D laser induced incandescence imaging", SAE paper no. 910224 (1991).
- [8] C. Espey and J.E. Dec, "The effect of TDC temperature and density on the liquid-phase fuel penetration in a DI diesel engine", SAE paper no. 952456 (1995).
- [9] C. Espey, J.E. Dec, T.A. Litzinger and D.A. Santavicca, "Quantitative 2D fuel vapor concentration imaging in a firing DI diesel engine using planar laser induced Rayleigh scattering", SAE paper no. 940682 (1994).
- [10] C. Espey, J.E. Dec, T.A. Litzinger and D.A. Santavicca, "Planar laser Rayleigh scattering for quantitative vapor-fuel imaging in a diesel jet", *Combustion and Flame* **109**, 65-86 (1997).
- [11] C. Espey and J.E. Dec, "Diesel engine combustion studies in a newly designed optical-access engine using high-speed visualisation and 2D laser imaging," SAE paper no. 930971 (1993).
- [12] J.E. Dec, "Soot distribution in a DI diesel engine using 2D imaging of laser induced incandescence, elastic scattering, and flame luminosity", SAE paper no. 920115 (1992).
- [13] J.E. Dec and C. Espey, "Ignition and early soot formation in a DI diesel engine using multiple 2D imaging diagnostics", SAE paper no. 950456 (1995).

- [14] J.E. Dec and C. Espey, "Soot and fuel distribution in a DI diesel engine via 2D imaging", SAE paper no. 922307 (1992).
- [15] J.E. Dec and E.B. Coy, "OH radical imaging in a DI diesel engine and the structure of the early diffusion flame", SAE paper no. 960831 (1996).
- [16] J.E. Dec, "A conceptual model of DI diesel combustion based on laser-sheet imaging", SAE paper no. 970873 (1997).
- [17] J.E. Dec and R.E. Canaan, "PLIF imaging of NO formation in a diesel engine", SAE paper no. 980147 (1998).
- [18] J.E. Dec and C. Espey, "Chemiluminescence imaging of autoignition in a DI diesel engine", SAE paper no. 982685 (1998).
- [19] J. Rife and J.B. Heywood, "Photographic and performance studies of diesel combustion with a rapid compression machine", SAE paper no. 740948 (1974).
- [20] H.H. Chui, H.K. Kim and E.J. Croke, "Internal group combustion of liquid droplets", Proc. 19th Symposium (Int'l) on Combustion, pp. 971-980 (1982).
- [21] "Bosch automotive handboek", 3rd ed., Robert Bosch GmbH, Stuttgart, Germany, worldwide distribution through the SAE, Warrendale, PA (1993).
- [22] J.A. Miller and C.T. Bowman, "Mechanism and modelling of nitrogen chemistry in combustion", Prog. Energy Combust. Sci. **15**, 287-338 (1989).
- [23] J. Olbregts, "Termolecular reaction of nitrogen monoxide and oxygen: a still unsolved problem", Int. J. Chem. Kin. **17**, 835-848 (1985).
- [24] J. Warnatz, U. Maas and R.W. Dibble, "Combustion", Springer Verlag, Berlin (1996).
- [25] M.C. Drake, J.W. Ratcliffe, R.J. Blint, C.D. Carter and N.M. Laurendeau, "Measurements and modeling of flamefront NO formation and superequilibrium radical concentrations in laminar high-pressure premixed flames", Proc. 19th Symposium (Int'l) on Combustion, pp. 387-395 (1990).
- [26] J. Wolfrum, "Bildung von Stickstoffoxiden bei der Verbrennung", Chemie-Ingenieur-Technik **44**, 656-659 (1972).
- [27] Ref. [2], p. 577-578.
- [28] H. Bockhorn (ed.), "Soot formation in combustion", Springer Verlag, Berlin (1994).
- [29] B.S. Haynes and H.G. Wagner, "Soot formation", Prog. Energy Combust. Sci. **7**, 229-273 (1981).
- [30] A.C. Eckbreth, "Laser diagnostics for combustion temperature and species", Abacus Press, Cambridge (1988).

- [31] K. Kohse-Höinghaus, "Laser techniques for the quantitative detection of reactive intermediates in combustion systems", *Prog. Energy Combust. Sci.* **20**, 203-279 (1994).
- [32] E.W. Rothe and P. Andresen, "Application of tunable excimer lasers to combustion diagnostics: a review", *Appl. Opt.* **36**, 3971-4033 (1997).
- [33] H. Zhao and N. Ladommatos, "Optical diagnostics for soot and temperature measurement in diesel engines", *Prog. Energy Combust. Sci.* **24**, 221-255 (1998).
- [34] Th.M. Brugman, "Laser-based diagnostics on NO in a diesel engine", Ph. D. Thesis, Applied Physics, University of Nijmegen (1999).
- [35] P. Andresen, G. Meijer, H. Schlüter, H. Voges, A. Koch, W. Hentschel, W. Oppermann and E. Rothe, "Fluorescence imaging inside an internal combustion engine using tunable excimer lasers", *Appl. Opt.* **29**, 2392-2404 (1990).
- [36] A. Arnold, F. Dinkelacker, T. Heitzmann, P. Monkhouse, M. Schäfer, V. Sick, J. Wolfrum, W. Hentschel and K.P. Schindler, "DI diesel engine combustion visualized by combined laser techniques", *Proc. 24th Symposium (Int'l) on Combustion*, pp. 1605-1612 (1992).
- [37] B. Alataş, J.A. Pinson, T.A. Litzinger and D.A. Santavicca, "A study of NO and soot evolution in a DI diesel engine via planar imaging", SAE paper no. 930973 (1993).
- [38] Th.M. Brugman, G.G.M. Stoffels, N. Dam, W.L. Meerts and J.J. ter Meulen, "Imaging and post-processing of laser-induced fluorescence from NO in a diesel engine", *Appl. Phys. B* **64**, 717-724 (1997).
- [39] H. Nakagawa, H. Endo, Y. Deguchi, M. Matsuhei, H. Oikawa and T. Shimada, "NO measurements in diesel spray flame using laser induced fluorescence", SAE paper no. 970874 (1997).
- [40] G. Josefsson, I. Magnusson, F. Hildenbrand, C. Schulz and V. Sick, "Multidimensional laser diagnostics and numerical analysis of NO formation in a gasoline engine", *Proc. 27th Symposium (Int,l) on Combustion*, pp. 2085-2092 (1998).
- [41] F. Hildenbrand, C. Schulz, V. Sick, G. Josefsson, I. Magnusson, Ö. Andersson and M. Aldén, "Laser spectroscopic investigation of flow fields and NO-formation in a realistic SI engine", SAE paper no. 980148 (1998).
- [42] S. Einecke, C. Schulz, V. Sick, A. Dreizler, R. Schiessl and U. Maas, "Two-dimensional temperature measurements in an SI engine using two-line tracer LIF", SAE paper no. 982468 (1998).
- [43] H. Kosaka, T. Nishigaki, T. Kamimoto, T. Sano, A. Matsutani and S. Harada, "Simultaneous 2D imaging of OH radicals and soot in a diesel flame by laser sheet techniques", SAE paper no. 960834 (1996).
- [44] J.A. Pinson, T. Ni and T.A. Litzinger, "Quantitative imaging study of the effects of intake air temperature on soot evolution in an optically accessible DI diesel engine", SAE paper no. 942044 (1994).

- [45] H. Fujimoto, K. Kurata, G. Asai and J. Senda, "OH radical generation and soot formation/oxidation in a DI diesel engine", SAE paper no. 982630 (1998).
- [46] G. Wiltalsky, W. Stolz, J. Köhler and C. Espey, "The quantification of laser induced incandescence (LII) for planar time resolved measurements of the soot volume fraction in a combusting diesel jet", SAE paper no. 961200 (1996).
- [47] J.D. Naber and D.L. Siebers, "Effects of gas density and vaporization on penetration and dispersion of diesel sprays", SAE paper no. 960034 (1996).
- [48] M. Suzuki, K. Nishida and H. Hiroyasu, "Simultaneous concentration measurements of vapor and liquid in an evaporating diesel spray", SAE paper no. 930863 (1993).
- [49] F. Rabenstein, J. Egermann and A. Leipertz, "Vapor-phase structures of diesel-type fuel sprays: an experimental analysis", SAE paper no. 982543 (1998).
- [50] M. Bakenhus and R.D. Reitz, "Two-color combustion visualization of single and split injections in a single-cylinder heavy-duty DI diesel engine using an endoscope-based imaging system", SAE paper no. 1999-01-1112 (1999).
- [51] P. Flynn, M. Mizusawa, O.A. Uyehara and P.S. Myers, "An experimental determination of the instantaneous potential radiant heat transfer within an operating diesel engine", SAE paper no. 720022 (1972).
- [52] S. Kobayashi, T. Sakai, T. Nakahira, M. Komori and K. Tsujimura, "Measurements of flame temperature distribution in DI diesel engine with high pressure fuel injection", SAE paper no. 920692 (1992).
- [53] X. Li and J.S. Wallace, "In-cylinder measurements of temperature and soot concentration using the two-color method", SAE paper no. 950848 (1995).
- [54] C. Arcoumanis, C. Bae, A. Nagwaney and J.H. Whitelaw, "Effect of EGR on combustion development in a 1.9L DI diesel optical engine", SAE paper no. 950850 (1995).
- [55] M. Versluis, M. Ebben, M. Drabbels and J.J. ter Meulen, "Frequency calibration in the ArF laser tuning range using laser-induced fluorescence of NO", *Appl. Opt.* **30**, 5229-5234 (1991).
- [56] Y. Matsui, T. Kamimoto and S. Matsuoka, "A study on the time and space resolved measurements of flame temperature and soot concentration in a DI diesel engine by the two-color method", SAE paper no. 790491 (1979).
- [57] H.G. Hottel and F.P. Broughton, "Determination of true temperature and total radiation from luminous gas flames", *Ind. and Engng. Chem.* **4**, 166 (1932).
- [58] Y. Matsui, T. Kamimoto and S. Matsuoka, "A study on the application of the two-color method to the measurement of flame temperature and soot concentration in diesel engines", SAE paper no. 800970 (1980).

- [59] N. Dam, S. Stolte and J. Reuss, "Rotational and vibrational relaxation in ethylene", *Chem. Phys.* **135**, 437-455 (1989).
- [60] J.W. Daily and E.W. Rothe, "Effects of laser intensity and of lower-state rotational energy transfer upon temperature measurements made with laser-induced fluorescence", *Appl. Phys. B* **68**, 131-140 (1999).
- [61] M. Kerker, "The scattering of light and other electromagnetic radiation", Academic Press (1969).
- [62] A.M. Wodtke, L. Huwel, H. Schlüter, G. Meijer and P. Andresen, "High-sensitivity detection of NO in a flame using a tunable ArF laser", *Opt. Lett.* **13**, 910-912 (1988).
- [63] P.H. Kruppenie, "The spectrum of molecular oxygen", *J. Phys. Chem. Ref. Data.* **1**, 423-534 (1972).
- [64] A.M. Wodtke, L. Huwel, H. Schlüter, H. Voges, G. Meijer and P. Andresen, "Predissociation of O₂ in the B-state", *J. Chem. Phys.* **89**, 1929-1935 (1988).
- [65] M.P. Lee and R.K. Hanson, "Calculations of O₂ absorption and fluorescence at elevated temperatures for a broadband argon-fluoride laser source at 193 nm", *J. Quant. Spectrosc. Radiat. Transfer* **36**, 425-440 (1986).
- [66] M. Shimauchi, T. Miura and H. Takuma, "Absorption lines of vibrationally excited O₂ and HF in ArF laser spectrum", *Jpn. J. Appl. Phys.* **33**, 4628-4635 (1994).
- [67] V. Sick, M. Decker, J. Heinze and W. Stricker, "Collisional processes in the O₂ B³Σ_u-state", *Chem. Phys. Lett.* **249**, 335-340 (1996).
- [68] E.W. Rothe, Y.W. Gu and G.P. Reck, "Laser induced predissociative fluorescence: dynamics and polarization. Implications for diagnostics", *Appl. Opt.* **35**, 934-947 (1996).
- [69] J. Luque and D.R. Crosly, "LIFBASE: Database and spectral simulation program (Version 1.3)", SRI International Report MP 98-021 (1998).
- [70] A.S. Sudbø and M.M.T. Loy, "Measurements of absolute state-to-state rate constants for collision-induced transitions between spin-orbit and rotational states of NO (X²Π, v=2)", *J. Chem. Phys.* **76**, 3646-3654 (1982).
- [71] M.C. Drake and J.W. Ratcliffe, "High temperature quenching cross sections for nitric oxide laser-induced fluorescence measurements", *J. Chem. Phys.* **98**, 3850-3865 (1992).
- [72] D. Stepowski, "Auto calibration of OH laser induced fluorescence signals by local absorption measurement in a flame", *Proc. 23rd Symposium (Int'l) on Combustion*, pp. 1839-1846 (1990).
- [73] M. Versluis, N. Georgiev, L. Martinsson, M. Aldén and S. Kröll, "2-D absolute concentration profiles in atmospheric flames using planar LIF in a bi-directional laser beam configuration", *Appl. Phys. B* **65**, 411-417 (1997).

- [74] S. Stoks, "Interpretation of 2D NO LIF images from a diesel engine", Internal report, University of Nijmegen (1999).
- [75] C.F. Bohren and D.R. Huffman, "Absorption and scattering of light by small particles", John Wiley & Sons, New York (1983).
- [76] J.G. Carter, R.H. Huebner, R.N. Hamm and R.D. Birkhoff, "Optical properties of graphite in the region 1100 to 1300 Å", *Phys. Rev. A* **137**, A639-A641 (1965).
- [77] C. Schulz, V. Sick, J. Wolfrum, V. Drewes, M. Zahn and R. Maly, "Quantitative 2D single-shot imaging of NO concentrations and temperatures in a transparent SI engine", *Proc. 26th Symposium (Int'l) on Combustion*, pp. 2597-2604 (1996).
- [78] A. Bräumer, V. Sick, J. Wolfrum, V. Drewes, M. Zahn and R. Maly, "Quantitative two-dimensional measurements of nitric oxide and temperature distributions in a transparent square piston engine", SAE paper no. 952462 (1995).
- [79] H. Pitsch, H. Barths and N. Peters, "Modellierung der Schadstoffbildung bei der dieselmotorischen Verbrennung", in A. Leipertz (ed.), "Berichte zur Energie- und Verfahrenstechnik", ESYTEC GmbH, Erlangen (Germany), **97.1**, pp. 139-163 (1997).
- [80] I.A. Voiculescu and G.L. Borman, "An experimental study of diesel engine cylinder-averaged NO_x histories", SAE paper no. 780228 (1978).
- [81] Ref. [2], p. 586-587.
- [82] E.J. van den Boom *et al.*, unpublished results.
- [83] K.P. Huber and G. Herzberg, "Molecular spectra and molecular structure IV. Constants of diatomic molecules", Van Nostrand Reinhold, New York (1979).
- [84] A.A. Radzig and B.M. Smirnov, "Reference data on atoms, molecules and ions", Springer Verlag, Berlin (1985).
- [85] R.W. Nicholls, "Approximate formulas for Frank-Condon factors", *J. Chem. Phys.* **74**, 6980-6981 (1981).
- [86] P.H. Paul, J.A. Gray, J.L. Durant Jr. and J.W. Thoman Jr, "A model for temperature-dependent collisional quenching of NO A²Σ⁺", *Appl. Phys. B* **57**, 249-259 (1993).
- [87] A.Y. Chang, M.D. DiRosa and R.K. Hanson, "Temperature dependence of collision broadening and shift in the NO A ← X (0,0) band in the presence of argon and nitrogen", *J. Quant. Spectrosc. Radiat. Transfer* **47**, 375-390 (1992).
- [88] M.P. Lee, B.K. McMillin and R.K. Hanson, "Temperature measurement in gases by use of planar laser induced fluorescence imaging of NO", *Appl. Opt.* **32**, 5379-5396 (1993).
- [89] G.A. Massey and C.J. Lemon, "Feasibility of measuring temperature and density fluctuations in air using laser-induced O₂ fluorescence", *IEEE J. Quant. Electr.* **20**, 454-457 (1984).

-
- [90] M.P. Lee, P.H. Paul and R.K. Hanson, "Quantitative imaging of temperature fields in air using planar laser-induced fluorescence of O₂" *Opt. Lett.* **12**, 75-77 (1987).
- [91] P. Andresen, A. Bath, W. Gröger, H.W. Lülff, G. Meijer and J.J. ter Meulen, "Laser-induced fluorescence with tunable excimer lasers as a possible method for instantaneous temperature field measurements at high pressures: checks with an atmospheric flame", *Appl. Opt.* **27**, 365-378 (1988).
- [92] R.J.H. Klein-Douwel, J.J.L. Spaanjaars and J.J. ter Meulen, "Two-dimensional distributions of C₂, CH and OH in a diamond depositing oxyacetylene flame measured by laser induced fluorescence", *J. Appl. Phys.* **78**, 2086-2096 (1995).
- [93] R.J.H. Klein-Douwel, J.J. Schermer and J.J. ter Meulen, "CN distributions in flame deposition of diamond and its relation to the growth rate, morphology, and nitrogen incorporation of the diamond layer", *Diamond and Related Materials* **7**, 1118-1132 (1998).

Samenvatting

Stikstofmonoxide in een dieselmotor: detectie met laserlicht en interpretatie

De dieselmotor, in 1897 uitgevonden door Rudolf Diesel, is wereldwijd nog steeds de meest gebruikte motor voor vrachtvervoer. Stikstofmonoxide (NO), gevormd tijdens dieselverbranding, is, naast roet, één van de meest vervuilende componenten in het uitlaatgas van de dieselmotor. Vanwege de schade die NO aanricht aan het milieu worden de eisen met betrekking tot de emissies steeds strenger. Om te kunnen blijven voldoen aan deze steeds scherper gestelde eisen is het van belang informatie te hebben over de vorming van NO gedurende het verbrandingsproces. Dit proefschrift gaat over de ontwikkeling van een methode om de hoeveelheid NO te meten met behulp van laserlicht in de cilinder van een optisch toegankelijke dieselmotor, die loopt op commerciële dieselbrandstof. Het doel is om te bepalen wanneer en waar in de verbrandingsproces NO gevormd wordt, door de dichtheid van NO als functie van het tijdstip in de verbrandingscyclus en de plaats in de cilinder te meten.

De experimenten zijn uitgevoerd in een één-cilinder, direct ingespoten tweetakt dieselmotor waarvan de verbrandingskamer optisch toegankelijk is gemaakt door kwarts vensters te monteren in de cilinderwand en in de cilinderkop. Bij de metingen is gebruik gemaakt van een verstembare gepulste excimeer laser; een bron die een lichtbundel met een goed gedefinieerde golflengte (energie, kleur) en richting uitzendt. Het licht van de laser, werkend in het ultraviolette (UV) gedeelte van het spectrum (193 nm), kan via één van de vensters de verbrandingskamer bereiken. De techniek die gebruikt wordt om NO moleculen zichtbaar te maken is de laser geïnduceerde fluorescentie (LIF) detectie. Deze meetmethode maakt gebruik van de eigenschap dat moleculen enkel licht kunnen absorberen en uitzenden met een voor het molecuul karakteristieke set van golflengtes. Als het laserlicht dat de verbrandingskamer binnenkomt de juiste golflengte heeft (in resonantie is met een energie-overgang in het NO molecuul) kan dit door de NO moleculen geabsorbeerd worden, die daardoor in een elektronisch aangeslagen toestand komen (excitatie). Deze toestand is echter niet stabiel en na korte tijd (enkele miljardste seconden) vallen de moleculen terug naar hun grondtoestand waarbij weer licht met dezelfde of een andere golflengte wordt uitgezonden (fluorescentie). Deze fluorescentie wordt via het venster in de cilinderkop gedetecteerd met een gevoelige camera (CCD camera). Door een filter te plaatsen voor de camera kan een specifieke golflengte geselecteerd worden. Een spectrum dat informatie bevat over de aanwezige golflengtes kan gemeten worden door met behulp van een monochromator de fluorescentie in de verschillende golflengtecomponenten te ontleden. Wanneer een lint van laserstraling wordt gebruikt en de fluorescentie in een loodrechte richting wordt gedetecteerd kunnen afbeeldingen (plaatjes) van de verdeling van moleculen in een tweedimensionaal vlak in de verbrandingskamer worden gemaakt.

De intensiteit van de uitgezonden fluorescentie, plaats- en tijdsopgelost gedetecteerd, is een

maat voor de hoeveelheid NO in de motor op een specifieke plaats en tijd tijdens het verbrandingsproces. De intensiteit van de fluorescentie is evenredig met de dichtheid van NO moleculen in het meetvolume. De evenredigheidsconstante bevat echter een aantal spectroscopische en experimentele factoren (Boltzmann factor, fluorescentie opbrengst en excitatie efficiëntie) die afhangen van de plaatselijke fysische en chemische omstandigheden waarin het NO molecuul zich bevindt. Deze omstandigheden, beschreven door grootheden als druk, temperatuur, laserintensiteit en gassamenstelling, veranderen gedurende de verbrandingscyclus en zijn meestal niet constant voor het gehele meetvolume. Om gemeten fluorescentiesignalen van NO te interpreteren als dichtheden, zodat metingen op verschillende tijdstippen en plaatsen in de verbranding met elkaar vergeleken kunnen worden, moet rekening gehouden worden met deze veranderende grootheden. In het algemeen zijn deze grootheden echter niet direct bekend en is het noodzakelijk ze via extra experimenten te achterhalen of, indien dat niet mogelijk is, ze zo goed mogelijk af te schatten.

Het eerste hoofdstuk is een algemene inleiding tot het verbrandingsproces zoals zich dat afspeelt in een dieselmotor. Na een korte beschrijving van de werking van de dieselmotor wordt het algemeen gangbare beeld van het dieselverbrandingsproces gegeven. Dit wordt gevolgd door enkele nieuwe ontwikkelingen in de theorie van dit proces naar aanleiding van recente, op lasertechnieken gebaseerde, experimenten. Tenslotte worden de verschillende mechanismen die kunnen leiden tot de vorming van NO in verbrandingsprocessen samengevat.

Hoofdstuk twee begint met een kort overzicht van een aantal laserdiagnostische methoden die gebruikt zijn voor de bestudering van verschillende aspecten van het verbrandingsproces in dieselmotoren in experimenten beschreven in de literatuur. De nadruk ligt hierbij op LIF-metingen voor de detectie van NO in motoren zoals die tot nu toe zijn uitgevoerd. Dit overzicht wordt gevolgd door een beschrijving van de optisch toegankelijk gemaakte dieselmotor en de experimentele opstelling. Om de metingen, aan een de dagelijkse praktijk zo goed mogelijk benaderend systeem, te verrichten, wordt de motor onder stabiele condities en op commerciële dieselbrandstof bedreven. Grootheden zoals de druk in de cilinder, de gemiddelde temperatuur van het gas in de cilinder, de temperatuur van de gloeiende roetdeeltjes en het warmteverloop tijdens het verbrandingsproces zijn bepaald. Verder worden de optische technieken beschreven die in dit proefschrift toegepast zijn. Naast de LIF-techniek zijn dat de detectie van het natuurlijke licht van de vlammen en de detectie van het laserlicht dat elastisch (zonder verandering van golflengte) verstrooid is (Mie verstrooiing). Aan het eind van dit hoofdstuk worden enkele meetresultaten gegeven, die het mogelijk maken om de meest geschikte excitatie- en detectiegolflengtes te bepalen om NO in de verbrandingskamer van de motor te meten met de LIF-techniek. Het is gebleken, dat het met het gebruikte laserlicht niet te vermijden is bij hoge temperaturen tevens 'warm' zuurstof (O_2) te exciteren, waarvan de fluorescentie interfereert met de fluorescentie van NO. Daarom is het noodzakelijk voor de excitatie een golflengte te kiezen die resulteert in een minimale O_2 fluorescentie en voor de detectie van NO een golflengte gebied dat geen overlap heeft met O_2 fluorescentie.

De intensiteit van het laserlicht in de verbrandingskamer neemt af als gevolg van verstrooiing aan en absorptie door roetdeeltjes en brandstof- en oliedruppels. Hoofdstuk drie beschrijft een experiment waarin een methode is ontwikkeld om de lokale verzwakkingscoëfficiënt voor het laserlicht te bepalen, die gebruikt kan worden om de lokale laserintensiteit te berekenen. Deze methode maakt gebruik van twee gelijktijdig opgenomen plaatjes van het elastisch verstrooide licht van twee laserbundels die in tegengestelde richting, maar via hetzelfde pad, de

verbrandingskamer doorkruisen. Beide plaatjes representeren dezelfde situatie in de verbrandingskamer, echter met een andere belichting. Via een aantal wiskundige bewerkingen kan het effect van de belichting uit de plaatjes geëlimineerd worden. Tevens kan uit de verzwakingscoëfficiënt de totale transmissie van het laserlicht door de verbrandingskamer bepaald worden. Omdat deze methode nogal omslachtig is, is een iets minder exacte methode ontwikkeld waarbij de lokale intensiteit van het laserlicht in de verbrandingskamer wordt gereconstrueerd uit één enkel plaatje van het resonant verstrooide laserlicht en de totale transmissie door de cilinder.

De resultaten van de eerste LIF-experimenten aan NO worden gepresenteerd in hoofdstuk vier. Hierin worden spectra gegeven van de fluorescentie, ontleed in de verschillende golflengtecomponenten, als een functie van het tijdstip in de verbrandingscyclus. Deze spectra tonen aan dat fluorescentie van NO gedetecteerd kan worden gedurende het totale verbrandingsproces, zelfs op het moment dat de zuiger zich geheel bovenin de cilinder bevindt en druk en temperatuur het hoogst zijn. De spectra gemeten in het begin van de verbranding laten naast NO fluorescentie interfererende fluorescentie van O₂ zien. De intensiteit van de NO fluorescentiepieken in de spectra is een maat voor de hoeveelheid NO die aanwezig is in het meetvolume. Het bewerken van het fluorescentiesignaal voor de veranderende condities in de verbrandingskamer resulteert in een curve die de relatieve dichtheid van NO als een functie van het tijdstip in de verbranding geeft. Relatieve dichtheidscurven van NO zijn bepaald voor verschillende motorcondities, zoals belasting en brandstoftype. Voor zover het is onderzocht is de invloed van de motorcondities en de brandstof op de hoeveelheid NO klein. Uit de gevonden curven kan de conclusie getrokken worden dat de vorming van NO langzaam op gang komt en dat het meeste NO relatief laat in de verbranding wordt gevormd. Dit suggereert dat de diffuse fase van het dieselverbrandingsproces een belangrijke rol speelt in het formatieproces van NO.

Fluorescentieverdelingen van NO gedurende het verbrandingsproces, gemeten door een smalbandig filter dat enkel de voor NO specifieke golflengte doorlaat, zijn gegeven in hoofdstuk vijf. In het begin van de verbranding konden geen verdelingen van NO gemeten worden als gevolg van de te lage laserintensiteit in het meetvolume. De gemeten fluorescentieverdelingen zijn bewerkt voor de afnemende intensiteit van het laserlicht. Deze verdelingen zijn geïnterpreteerd als dichtheidsverdelingen van NO onder de aannames van uniforme temperatuurverdeling en gassamenstelling. Deze aannames kunnen gemaakt worden aan het eind van de verbrandingscyclus waar de verbrandingsproducten redelijk homogeen verdeeld zijn. Om verdelingen, gemeten in het begin van de verbranding, goed te kunnen interpreteren is het echter noodzakelijk de lokale temperatuur en gassamenstelling te kennen. De gevonden dichtheidsverdelingen laten een redelijk uniforme verdeling van NO zien, wat te verwachten is aan het eind van de verbranding waar het gevormde NO reeds gemengd is met de rest van de cilinderinhoud. Tenslotte is een curve van de relatieve dichtheid van NO als functie van de tijd in het verbrandingsproces bepaald door de intensiteit in de dichtheidsverdelingen te integreren. Deze curve komt goed overeen met de curve bepaald uit de spectra.

In het afsluitende hoofdstuk zes worden de belangrijkste resultaten en aannames samengevat. Besproken wordt welke informatie gemist wordt of onvolledig is om de LIF-signalen van NO volledig te kunnen kwantificeren en welke experimenten gedaan zouden kunnen worden om deze informatie te verkrijgen. Tevens wordt bediscussieerd in hoeverre het haalbaar is in de toekomst ook daadwerkelijk kwantitatieve dichtheidsverdelingen van NO gedurende het gehele verbrandingsproces te bepalen met behulp van de LIF-techniek.

Curriculum Vitae

Op 5 november 1969 ben ik geboren te Wijchen waar ik ook de lagere school heb doorlopen. Hierna volgde de middelbare school periode op het Dominicus College te Nijmegen, die in 1988 werd afgesloten met het behalen van het VWO-diploma. Aansluitend ben ik natuurkunde gaan studeren aan de Katholieke Universiteit Nijmegen (KUN), waar ik na een jaar mijn propeuse behaalde. Op de afdeling Molecuul- en Laserfysica heb ik mijn afstudeerstage gedaan, begeleid door Adrian Marijnissen en Hans ter Meulen. Mijn afstudeerwerk betrof laserspectroscopie aan kortlevende moleculen gevormd in een gepulste ontlading. Na het behalen van het doctoraaldiploma in januari 1994, ben ik begonnen als onderzoeker in opleiding (OIO) onder begeleiding van Hans ter Meulen, Nico Dam en Leo Meerts bij Toegepaste Fysica, eveneens aan de KUN. Mijn promotieonderzoek bestond uit het ontwikkelen van een methode om stikstofmonoxide (NO) te detecteren in de verbrandingskamer van een dieselmotor met behulp van lasertechnieken en het interpreteren van de gemeten signalen als NO dichtheden. De resultaten van dit onderzoek vindt u terug in dit proefschrift. Tijdens mijn studie- en promotietijd heb ik eerste- en tweedejaars natuurkunde- en scheikundestudenten geassisteerd bij het practicum natuurkunde. Tevens ben ik werkcollege-assistent geweest bij het college Atoom- en Molecuulfysica. Ook heb ik in mijn onderzoekstijd studenten begeleid bij hun afstudeerwerk. In juli 1999 ben ik begonnen als postdoc onderzoeker aan de Technische Universiteit Delft (TUD).

Publications

- *Generation of 224 nm radiation by stimulated Raman scattering of ArF excimer laser radiation in a mixture of H₂/D₂.*
G.G.M. Stoffels, P. Schmidt, N. Dam and J.J. ter Meulen,
Applied Optics, 36, 6797-6801 (1997).
- *Imaging and post-processing of laser-induced fluorescence from NO in a diesel engine.*
Th.M. Brugman, G.G.M. Stoffels, N. Dam, W.L. Meerts and J.J. ter Meulen,
Applied Physics B, 64, 717-724 (1997).
- *In-cylinder measurements of NO in a running diesel engine by means of LIF diagnostics.*
G.G.M. Stoffels, Th.M. Brugman, C.M.I. Spaanjaars,
N. Dam, W.L. Meerts and J.J. ter Meulen,
in Challenges in Propellants and Combustion, 100 Years After Nobel,
Fourth International Symposium on Special Topics in Chemical Propulsion,
Begell house, New York, pp. 972-982 (1997).
- *Imaging of an underexpanded nozzle flow by UV laser Rayleigh scattering.*
N.J. Dam, M. Rodenburg, R.A.L. Tolboom, G.G.M. Stoffels,
P.M. Huisman-Kleinherenbrink and J.J. ter Meulen,
Experiments in Fluids, 24, 93-101 (1998).
- *In-cylinder measurements of NO formation in a diesel engine.*
G.G.M. Stoffels, E.J. van den Boom, C.M.I. Spaanjaars, N. Dam,
W.L. Meerts, J.J. ter Meulen, J.C.L. Duff and D.J. Rikeard,
SAE paper no. 1999-01-1487 (1999).
- *Laser diagnostics of nitric oxide inside a DI two-stroke diesel engine.*
G.G.M. Stoffels, E.J. van den Boom, C.M.I. Spaanjaars,
N. Dam, W.L. Meerts and J.J. ter Meulen,
to be published in Laser Techniques Applied to Fluid Mechanics,
Selected Papers from the 9th International Symposium,
Lissabon, Portugal, 13-16 July, 1998, Springer Verlag, Berlin (1999).

- *Methods to correct planar LIF distributions for local non-uniform laser attenuation.*
G.G.M. Stoffels, S. Stoks, N. Dam and J.J. ter Meulen,
submitted to Applied Optics (1999).
- *Planar LIF measurements of NO distributions in a realistic diesel engine,
in relation to temperature and chemical composition inhomogeneities.*
G.G.M. Stoffels, C.M.I. Spaanjaars, N. Dam and J.J. ter Meulen,
submitted to Applied Physics B (1999).
- *Nitric oxide densities in a realistic diesel engine measured by
planar and backscatter LIF.*
G.G.M. Stoffels, C.M.I. Spaanjaars, N. Dam and J.J. ter Meulen,
in preparation.